université
de BORDEAUX

COMENIUS
UNIVERSITY
BRATISLAVA

THÈSE EN COTUTELLE PRÉSENTÉE

POUR OBTENIR LE GRADE DE
DOCTEUR DE

L'UNIVERSITÉ DE BORDEAUX

ÉCOLE DOCTORALE SCIENCES PHYSIQUES ET DE L'INGÉNIEUR

SPÉCIALITÉ ASTROPHYSIQUE, PLASMAS, NUCLÉAIRE

ET DE

L'UNIVERSITÉ COMENIUS DE BRATISLAVA

FACULTÉ DE MATHÉMATIQUES, PHYSIQUE ET INFORMATIQUE

SPÉCIALITÉ PHYSIQUE NUCLÉAIRE ET SUBNUCLÉAIRE

Par **Veronika PALUŠOVÁ**

**Monte Carlo Simulations of Detectors Background and Analysis of
Background Characteristics of the SuperNEMO Experiment in the Modane
Underground Laboratory**

Sous la direction de : **Pavel POVINEC et Fabrice PIQUEMAL**

Soutenue le 04/11/2021

Membres du jury :

M. J. GASCON	Professeur	Université de Lyon	Rapporteur
M. D. FRANCO	Directeur de recherche	Université de Paris	Rapporteur
M. Š. GMUCA	Chargé de Recherche	Acad. des Sciences de la Rép. Slovaque	Rapporteur
M. D. DUMORA	Professeur	Université de Bordeaux	Président
Mme. C. NONES	Ingénieure	CEA Paris-Saclay	Examinatrice
Mme. M. SETTIMO	Chargée de Recherche	Université de Nantes	Examinatrice
M. J. MASARIK	Professeur	Université Comenius de Bratislava	Examinateur
M. V. NEČAS	Professeur	Université Technique de la Rép. Slovaque	Examinateur

Declaration of Authorship

I, Mgr. Veronika Palušová, declare that this thesis titled, "Monte Carlo Simulations of Detectors Background and Analysis of Background Characteristics of the SuperNEMO Experiment in the Modane Underground Laboratory" and the work presented in it are my own. I confirm that this work was done wholly or mainly while in candidature for a research degree at both universities and that this thesis has been composed by myself with the help of my supervisors. I have acknowledged all main sources of help.

Signed:
_____

Date:
_____

Monte Carlo Simulations of Detectors Background and Analysis of Background Characteristics of the SuperNEMO Experiment in the Modane Underground Laboratory

Abstract

Presented dissertation thesis is focused on Monte Carlo simulations of background induced by high energy gamma rays in the SuperNEMO experiment.

The discovery of neutrino masses through the observation of neutrino oscillations renewed the interest in neutrinoless double beta decay searches. They can probe lepton number conservation and investigate the nature of the neutrinos - Dirac or Majorana - and also probe their absolute mass scale. SuperNEMO experiment aims to search for the signal of neutrinoless double beta decay. It utilizes a tracking approach by separating the source isotope from the detector, while combining tracker and calorimetry techniques to detect emitted electrons independently. The first module of the experiment, the Demonstrator, is located in Modane underground laboratory. Its background suppression technique is based on rejection method by reconstructing the topology of events and on background suppression by selecting radiopure materials used in detector construction and passive shielding.

Part of the thesis is dedicated to evaluation of different sources of background, namely ambient background sources in the Modane underground laboratory that are unavoidable to all experiments operating here, and radiogenic sources of neutrons produced in fission processes of uranium and thorium, and in (α,n) reactions. This part represents an important component of inputs used for Monte Carlo simulation of the background induced by high energy gamma rays. A problem with simulation of gamma cascades emitted after thermal neutron capture in the software package along with the solution of this problem is discussed.

Another part is dedicated to simulations of attenuation of radiation passing through different shielding configurations and geometries. This study helps to optimize the final design of passive shielding used for the Demonstrator module.

All these parts are then used as inputs for the final Monte Carlo simulations of external background in the SuperNEMO experiment. The main goal of this task is to study and to identify events that mimic the 2 electron topology of neutrinoless double beta decay.

Keywords: Neutrino, SuperNEMO, Neutrinoless double beta decay, Monte Carlo simulations, Background, Underground laboratory

Monte Carlo simulácie pozadia detektorov a analýza pozaďových charakteristík SuperNEMO experimentu v podzemnom laboratóriu v Modane

Abstrakt

Predložená dizertačná práca je zameraná na Monte Carlo simulácie pozadia vyvolaného vysokoenergetickým gama žiarením v experimente SuperNEMO.

Objav hmotnosti neutrín pozorovaním neutrínových oscilácií obnovil záujem o hľadanie existencie bezneutrínovej dvojitej beta premeny. Pomocou tohto procesu je možné skúmať zachovanie leptónového čísla a povahu neutrín - Diracovská alebo Majoranovská - a tiež skúmať ich absolútnu hmotnostnú škálu. Cieľom SuperNEMO experimentu je hľadanie signálu bezneutrínovej dvojitej beta premeny. Experiment využíva trekovací prístup, čím oddeľuje zdrojový izotop od detektora, pričom ale kombinuje techniku dráhových detektorov a kalorimetrie na detekciu emitovaných elektrónov. Prvý modul experimentu, Demonštrátor, sa nachádza v podzemnom laboratóriu v Modane. Technika potlačenia pozadia je založená na metóde odmietnutia eventov, pomocou rekonštrukcie ich topológie, a na potlačení pozadia, výberom rádioaktívne čistých materiálov použitých pri konštrukcií detektora, a takisto použitím pasívneho tienenia.

Časť práce je venovaná zhodnoteniu rôznych zdrojov pozadia, konkrétne zdrojov pozadia v podzemnom laboratóriu v Modane, ktoré su neodstrániteľné pre všetky experimenty, ktoré v tomto laboratóriu operujú, a rádiogénnych zdrojov neutrónov produkovaných štiepnymi procesmi uránu a tória a (α, n) reakciami. Táto časť predstavuje dôležitú súčasť vstupov pre Monte Carlo simulácie pozadia vyvolaného vysokoenergetickým gama žiarením. Takisto je v tejto časti diskutovaný problém so simuláciou gama kaskád emitovaných po záchyte neutrónov v softvérovom balíku spolu s riešením tohto problému.

Ďalšia časť je venovaná simuláciám potlačenia žiarenia prechádzajúceho cez rôzne konfigurácie a geometrie tienenia. Táto štúdia pomáha optimalizovať konečný návrh pasívneho tienenia použitého pre Demonštrátor.

Všetky tieto časti sú potom použité ako vstupy pre simulácie externého pozadia v SuperNEMO experimente. Hlavným cieľom tejto úlohy je študovať a identifikovať udalosti, ktoré napodobňujú dvojelektrónovú topológiu dvojitej bezneutrínovej beta premeny.

Kľúčové slová: Neutríno, SuperNEMO, Bezneutrínová dvojitá beta premena, Monte Carlo simulácie, Pozadie, Podzemné laboratórium

Simulation Monte Carlo du bruit de fond des détecteurs et analyse des caractéristiques du fond de l'expérience SuperNEMO dans le laboratoire souterrain de Modane

Résumé

La découverte récente d'une masse non-nulle pour les neutrinos avec l'observation des oscillations renouvelle l'intérêt de rechercher de la décroissance double bêta sans émission de neutrino. Il s'agit de la meilleure approche expérimentale pour sonder la nature de neutrinos - Dirac ou Majorana - et leur échelle de masse. SuperNEMO est une expérience basée sur l'utilisation d'un trajectographe et d'un calorimètre afin de détecter individuellement les deux électrons émis lors de la décroissance. Le premier module démonstrateur de SuperNEMO se trouve au Laboratoire Souterrain de Modane. Sa technique de réjection du bruit de fond repose sur la reconstruction de la topologie des évènements ainsi qu'un suppression en amont des bruits de fond par une sélection de composants radiopurs et l'utilisation d'un blindage passif.

Une partie de cette thèse est dédiée à l'estimation du bruit de fond radioactif environnant au Laboratoire Souterrain de Modane, dont les neutrons radiogéniques produit par fission des isotopes d'uranium et de thorium, ainsi que par réaction (α, n). Ces derniers sont un ingrédient important pour les simulations Monte Carlo du bruit de fond induit par les rayonnements gamma de haute énergie. Un problème de simulation des cascades gamma par capture radiative de neutron est notamment discuté avec la mise au point d'une solution.

Une autre partie du travail porte sur des simulations d'atténuation de rayonnements à travers différente configurations et géométries de blindage passif, afin d'optimiser le blindage finale du module démonstrateur de SuperNEMO.

Ces travaux permettent une modélisation du bruit de fond dite externe de l'expérience SuperNEMO, par l'étude et identification des évènements imitant la topologie "deux électrons" de la décroissance double bêta sans émission de neutrinos.

Acknowledgements

Throughout the writing of this dissertation I have received a great amount of assistance and support.

Firstly, I would like to express my sincere gratitude to my supervisors, Pavel Povinec and Fabrice Piquemal, for their continuous support of my PhD study, motivation, and all of their advice. I would like to express my deepest appreciation to Emmanuel Chauveau, for his guidance, valuable consultations, and his unparalleled knowledge in the field. They all continuously provided encouragement and they were always willing to assist in any way they could throughout this research project.

My appreciation goes to the CENBG team for accepting me into the institute and for providing me with the opportunity to join their research group. Without their support, it would not have been possible to conduct this work.

I would also like to thank the following people who have helped me undertake this research: a collaboration member and a friend, Miroslav Macko from IEAP CTU in Prague, whose expertise was invaluable and whose insightful suggestions provided me with the tools that I needed to choose the right direction and successfully complete my dissertation. Róbert Breier from FMPH CU in Bratislava for his insightful feedback and who was always willing to offer a helping hand. Cheryl Patrick from UCL for all the thoughtful comments and recommendations she provided me with during these academic years. Stanislav Valenta from FMP CUNI in Prague for providing me with important inputs and outputs from the DICEBOX software and for all his advice on the related research topic. I also have had the support and encouragement of Christine Marquet from CENBG who always gave me constructive comments.

I wish to acknowledge the rest of the SuperNEMO collaboration and the staff of LSM - the meetings and conversations were vital for the completion of this thesis.

To conclude, I cannot forget to thank my family and friends for all the unconditional support in this time.

Dissertation Goals

This PhD work is carried out within the context of the SuperNEMO experiment, an ultra-low radioactive background experiment in the Modane underground laboratory, looking for Majorana nature of neutrino by searching for the neutrinoless double beta decay.

The application of the Monte Carlo simulations in nuclear and particle physics is vast. Monte Carlo simulations of detector background characteristics have been important prerequisites when working in underground laboratories. They help design detectors, understand their behaviour, compare experimental data to theory and investigate and predict the origin of the background.

The main goals of the PhD thesis are as follows:

- Simulation and analysis of the external background of the SuperNEMO experiment, specifically:

  - to quantify contributions to the background of the SuperNEMO detector operating in the LSM underground laboratory, which due to residual cosmic radiation and radioactive contamination of materials produce high energy gamma rays.

  - to quantify contributions to the SuperNEMO detector background from spontaneous fission neutrons and from (alpha, n) reactions originating in contaminated construction materials.

- Study of gamma ray and neutron attenuation by different shielding components also affected by radioactive contamination of construction materials.

- Participation in data collection and data analysis from the Demonstrator module without external shielding, and comparison of data and simulation. Namely, participation in data analysis of measurement with neutron source taken during calorimeter commissioning stage and comparison of experimental data with Monte Carlo simulation to validate the simulation method used to estimate neutron induced background rate.

- Direct participation in the completion of the Demonstrator module and its commissioning in the LSM.

Contents

List of Figures

List of Tables

Introduction

Since the 1930s many discoveries and theories providing an insight into the structure of matter have been made. It was found to be, that the observable matter and radiation in the Universe are made from elementary subatomic particles ad their composite particles and antiparticles. These fundamental particles are bound together by three fundamental forces - electromagnetic, weak, and strong. This knowledge and understanding of how these fundamental particles and three forces relate are contained in the Standard Model of particle physics. To this day, our understanding of the world of leptons and quarks is quite vast and remarkable. However, we know it to be incomplete. Although the Standard Model of particle physics agrees well with experiments, many questions remain unanswered. Why do neutrinos have small masses? What is the neutrino mass? Are there additional neutrino types? What is the dark matter made out of? What is the origin of the asymmetry between matter and antimatter? Answers to these questions and more pose an important factor to our knowledge of nature. Study and observation of extremely rare processes may lead us to these answers.

Investigation of neutrino properties is currently one of the most essential interests for particle physics and for better understanding the evolution of our Universe. Crucial missing information in this field could be provided by the observation of neutrinoless double beta decay ($0\nu\beta\beta$), a rare decay that violates total lepton number by two units which makes it forbidden in the Standard Model of particle physics. If observed, it would prove neutrinos are their own antiparticles - Majorana particles - and they could be the key to the matter-antimatter asymmetry problem.

But the only hope of seeing such rare events is shielding the experiment from any background radiation that might swamp the signal. Deep underground laboratories provide the necessary low radiation background to search for very rare nuclear phenomena that happen at extremely low rates.

In order to understand the origin of induced background, or to evaluate the background before the construction of a detector, a background spectrum can be obtained with *Monte Carlo simulations*. They became a key tool for studying problems intractable by an experimental approach only. Monte Carlo simulations have been widely applied in studying physical processes and interactions to explain measured background spectra or to predict detector background and to evaluate individual background contributions [1]. That makes them an excellent tool to study detector background before the system is built and to optimize background characteristics for planned experiments. They are also useful for optimizing the shielding design (material, thickness, etc.) necessary to reduce the background to a desirable level.

This thesis is focused on Monte Carlo simulations of the background characteristics of the SuperNEMO experiment. SuperNEMO is a one-of-a-kind experiment searching for neutrinoless double beta decay in the Modane underground laboratory. The thesis consists of 7 chapters.

Chapter 1 describes the history of neutrino physics, neutrino properties, and its place within and outside of the Standard Model. It contains insight into the physics of experimentally observed two-neutrino double beta decay and theoretically predicted neutrinoless

double beta decay. It also summarizes the status of experimental search for $0\nu\beta\beta$ signal of current experiments and next-generation experiments.

Chapter 2 focuses solely on the SuperNEMO experiment, its design, goals and detection technique.

Chapter 3 discusses background sources in underground laboratories that are common to deep underground experiments: cosmic rays and environmental radioactivity and radioactive contamination of materials. There is also a brief review of background sources in the Modane underground laboratory from available literature.

In *Chapter 4*, possible neutron sources are described. It contains a section with a theoretical overview of processes that lead to neutron production, such as spontaneous fission and (α,n) reactions, but also results of calculations and simulations of neutron yields, production rates, and their energy spectra. In the last part of this section, I use these results to evaluate the contributions from neutron background sources in the SuperNEMO Demonstrator.

The last part of this chapter is dedicated to neutron capture gamma cascades. It contains results of gamma cascades from thermal neutron capture on iron and copper isotopes from a separate simulation that are later used as input for the SuperNEMO simulation software.

In *Chapter 5*, the results of Monte Carlo simulation of external background in the SuperNEMO experiment induced by high energy gamma rays are presented. It is divided into two main sections. One is dedicated to ambient gamma ray induced background and the second one is dedicated to neutron induced background. The details of simulation software and analysis method are described here. Each of these parts also contains a subsection dedicated to the analysis of attenuation of ambient radiation by shielding.

Chapter 6 is dedicated to comparison of measured experimental data with our Monte Carlo based model used throughout the analysis of the external background. Part of this chapter is dedicated to the simulation of Americium-Beryllium (AmBe) neutron source which is used for comparison of simulation with experimental data taken with weak AmBe source during commissioning phase with the Demonstrator. And another part is focused on comparison of measured and simulated high energy spectra above 4 MeV in the LSM with the Demonstrator.

Conclusions of this work are summarized in the final *Chapter 7*.

Chapter 1

Neutrinoless Double Beta Decay

1.1 Neutrino Properties and Reactions

The Standard Model represents the most precise and widely accepted model of fundamental particles and three of the four known fundamental forces in the Universe up to date. All particles of the Standard Model, grouped into two categories of matter and force-carrier particles, are in Figure 1.1. The building blocks of matter come in two basic types called quarks and leptons. Within the lepton group, there are six particles arranged in three generations - the *electron (e$^-$)* and the *electron neutrino (ν_e)*, the *muon (μ^-)* and the *muon neutrino (ν_μ)*, and the *tau (τ^-)* and the *tau neutrino (ν_τ)*. Similarly, the six quarks are also paired in three generations - *up* and *down*, *charm* and *strange*, *top* and *bottom*. Additionally, every particle is associated with its own antiparticle[1]. The strong, weak and electromagnetic forces all have its own corresponding force-carrying particles in the Standard Model, which belong to a broader group called *bosons*.
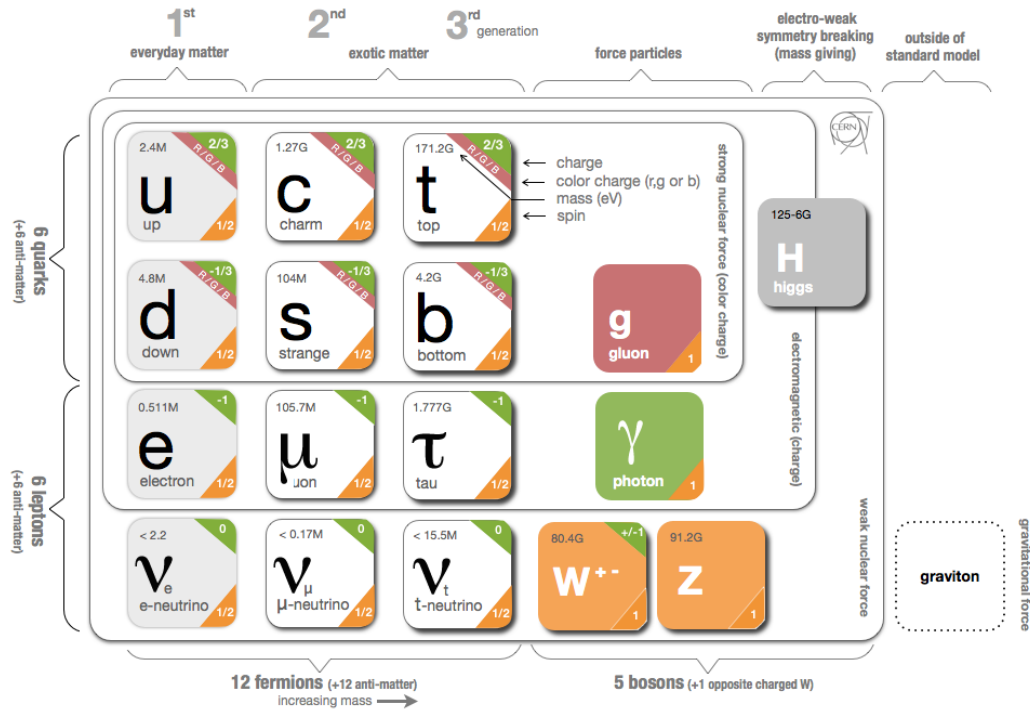
FIGURE 1.1: Elementary particles of the Standard Model - 3 generations of matter, gauge bosons and Higgs boson [2]

---

[1]Some particles, for instance the photon, are their own antiparticle.
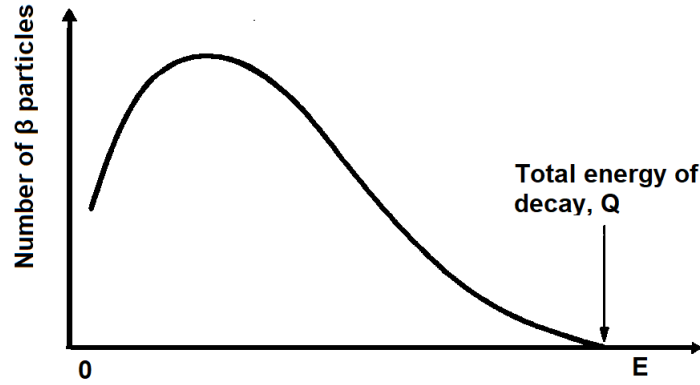
FIGURE 1.2: Continuous energy spectrum of β-decay

Neutrinos are fundamental particles created in diverse processes in nature, from nuclear reactions in the stars, particle decays, and star explosions to accelerators and nuclear power plants. Out of all known massive particles, they are the most abundant particles in the universe. Neutrinos are often called the most elusive particles of the Standard Model of nuclear physics as they are difficult, but not impossible, to detect.

1.1.1   Brief History of Neutrinos

The first indirect physical evidence of neutrino existence was provided by the study of β^--decay at the beginning of the 20th century. Back then, it was believed that in the process of β^--decay a nucleus undergoes a transition, where one neutron is transformed into a proton with emission of an electron:

$$^A_Z X \rightarrow ^A_{Z+1} Y + e^-$$ (1.1)

Experiments, performed by Otto Hahn and Lise Meitner in 1911 and by James Chadwick in 1914, showed that the kinetic energies of these electrons had a continuous spectrum, that is - electrons are emitted from a source with a distribution of energies that extends from zero up to a maximum energy of the reaction (Q value) (Fig. 1.2), which was in contradiction to the law of conservation of energy. By this law, the emitting electron should have an energy equal to the difference of the parent and daughter nuclear masses, Q. Wolfgang Pauli came with a solution, proposing the emission of another particle that escaped undetected. In this case, the sum of the energy of the electron and the new proposed particle should be equal to the Q value. Pauli called this particle "neutron" and in 1931 Enrico Fermi renamed Pauli's "neutron" to neutrino. In 1934, Enrico Fermi had developed his famous theory of beta decay including neutrino in this process.
Number of constraints were put on the properties of neutrino so the existing conservation laws were satisfied. The reaction in Equation 1.1 is already balanced with respect to electric charge, so neutrino must be neutral. The observed energies of electrons were up to the maximum allowed Q value of the decay, so neutrino mass must be smaller than instrumental uncertainties. From the lepton number[2] conservation in order to compensate for the creation of a particle, emitted neutrino must be antiparticle and therefore antineutrino.

---

[2]Quantum number that is assigned to all leptons and is 1 for electrons and neutrinos and -1 for their respective antiparticles.
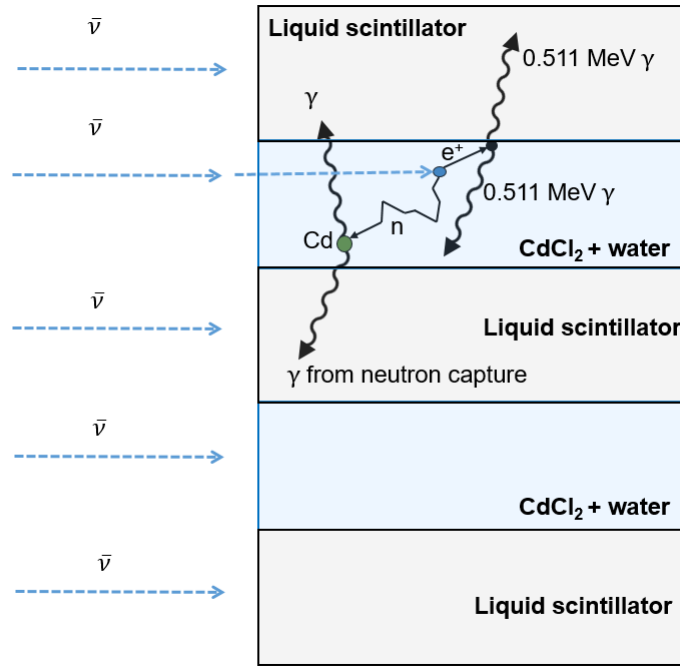
FIGURE 1.3: Scheme of the Cowan-Reines neutrino experiment

And final constraint is that neutrino/antineutrino must have a half-integer spin and be a fermion in order to couple the total angular momentum to the initial spin of ½ $\hbar$. The Equation 1.1 can be then rewritten accordingly:

$$^A_Z X \rightarrow^A_{Z+1} Y + e^- + \bar{\nu} \tag{1.2}$$

Direct Detection of Neutrinos

Due to its elusiveness, it took more than 20 years to directly detect neutrino. The first experiment that lead to the detection and confirmation of neutrino's existence was the Cowan-Reines neutrino experiment in 1956 [3]. The potential of this experiment comes from the nuclear reaction known as inverse beta decay, in which a proton captures an antineutrino, resulting in neutron and positron production:

$$\bar{\nu}_e + p^+ \rightarrow n^0 + e^+ \tag{1.3}$$

A nuclear reactor was used as a source of antineutrinos and the detector consisted of 2 water tanks (a huge number of potential proton targets of the water) with dissolved cadmium chloride, $CdCl_2$ (detection of the neutron from the neutrino interaction due to large cross-section of neutron capture by Cd), sandwiched between 3 tanks filled with a liquid scintillator (Fig. 1.3). Chain of events after antineutrino interaction is then two 0.511 MeV gamma rays from the positron annihilation, followed by the gamma rays from the disintegration of the nucleus after the neutron absorption by cadmium several microseconds later. The signatures of the interaction are thus unique making this rare process detectable. Their result was rewarded with the Nobel Prize in 1995.

   The antineutrino discovered by Cowan and Reines in 1956 is the antiparticle of the electron neutrino. In 1962, the first detection of the muon neutrino interactions was performed

by Leon M. Lederman et al. [4] and the first detection of tau neutrino interactions was announced in 2000 by DONUT[3] collaboration [5]. Up to now, we recognize three neutrino flavours- ν_e, ν_μ, ν_τ named after their partner leptons in the Standard Model.

1.1.2 Neutrinos in the Standard Model and Beyond

Neutrinos had to undergo a revision in the formulation of the Standard Model. Originally, neutrinos were believed to be massless, came in three flavours, and were clearly distinct from their antiparticles - all neutrinos are left-handed, helicity = -1, all antineutrinos are right-handed, helicity = 1, and the lepton number is strictly conserved. However, in recent years neutrino experiments have shown convincing evidence of the existence of neutrino oscillations, which is a consequence of neutrino masses and flavour mixing.

Neutrino Flavour Mixing and Oscillations

We know now, that there are three neutrinos[4] that participate in weak interactions and couple to W and Z bosons: ν_e, ν_μ, ν_τ[5], and the electroweak eigenstates of these neutrinos are linear combinations of their mass eigenstates: ν_1, ν_2, ν_3 [6]:

$$|\nu_f\rangle = \sum_i U_{fi} |\nu_i\rangle \tag{1.4}$$

where f denotes the flavour state, i denotes the mass state and U_{fi} is the unitary neutrino mixing matrix or Pontecorvo-Maki-Nakagawa-Sakata (PMNS) matrix. Equation 1.4 can be rewritten in matrix form:

$$\begin{pmatrix} |\nu_e\rangle \\ |\nu_\mu\rangle \\ |\nu_\tau\rangle \end{pmatrix} = U_{fi}^{PMNS} \begin{pmatrix} |\nu_1\rangle \\ |\nu_2\rangle \\ |\nu_3\rangle \end{pmatrix} \tag{1.5}$$

Such mixing between mass and flavour states is leading to the oscillation phenomenon, a periodical variation of the flavour in the function of time during the propagation of neutrinos.

Let's consider the simpler case of the mixing of only two neutrino flavors, ν_e and ν_μ. The relation between flavour and mass eigenstates is as follows [7]:

$$\begin{pmatrix} |\nu_e\rangle \\ |\nu_\mu\rangle \end{pmatrix} = \begin{pmatrix} cos\theta & sin\theta \\ -sin\theta & cos\theta \end{pmatrix} \begin{pmatrix} |\nu_1\rangle \\ |\nu_2\rangle \end{pmatrix} \tag{1.6}$$

where θ is the mixing angle. The two mass components of the neutrino have energies E_1 and E_2 given by:

$$E_i = \sqrt{p^2 - m_i^2} \simeq E + \frac{m_i^2}{2E} \tag{1.7}$$

---

[3]Direct Observation of NU Tau

[4]Number of light particles that have the standard properties of neutrinos with respect to the weak interactions, and does not apply to sterile neutrinos.

[5]These neutrinos are often called "active flavour neutrinos".

Initial state of neutrino ν_e at $t = 0$ is:

$$|\nu_e\rangle = cos\theta \, |\nu_1\rangle + sin\theta \, |\nu_2\rangle \tag{1.8}$$

After a period of time t, the state can be described by:

$$|\nu_e(t)\rangle = e^{-iE_1t}cos\theta \, |\nu_1\rangle + e^{-iE_2t}sin\theta \, |\nu_2\rangle \tag{1.9}$$

The phase difference between the two components results in flavour evolution of the neutrino, because the amplitudes of different mass components evolve differently with space and time, acquiring different quantum mechanical phases. The probability of finding the neutrino with the muon flavour is [7]:

$$P(\nu_e \to \nu_\mu, t) = |\langle\nu_\mu|\nu_e(t)\rangle|^2 = sin^2(2\theta)sin^2\left(\frac{\Delta m^2}{4E}t\right) \tag{1.10}$$

and $\Delta m^2 = m_2^2 - m_1^2$. For relativistic neutrinos, when approximating $L \simeq t$, the transition probability in Equation 1.10 can be written in the form:

$$P(\nu_e \to \nu_\mu, t) = sin^2(2\theta)sin^2\left(1.27\frac{\Delta m^2}{E}L\right) \tag{1.11}$$

where L is the flight path in km and E is the energy in GeV. Thus neutrinos oscillate between different flavours along their path of flight. From Equations 1.10 and 1.11 it is seen that if neutrinos have equal (zero) masses then there are no oscillations, and that the neutrino oscillations are only possible if at least one of the mass eigenstates would be non-zero.

The idea of neutrino oscillations was predicted by Bruno Pontecorvo in paper [8] in 1967 where he discussed the possibilities of neutrino oscillations in the case of two flavour neutrinos and neutrino oscillations were later discovered in 1998 with neutrinos produced in the atmosphere in Super-Kamiokande experiment [9], and later also in solar SNO [10] and neutrinos from nuclear reactor in KamLAND [11] experiments.

Helicity, Chirality and Antineutrino

The discovery of neutrino oscillations implies that neutrinos are not massless particles, and hence, it also has implications on two particle properties - helicity and chirality.

The helicity of a particle represents the projection of the particle's spin along its direction of motion. The helicity operator is given by projecting the spin operator onto the unit momentum vector:

$$\hat{h} = \frac{\hat{\vec{S}}\vec{p}}{|\vec{p}|} \tag{1.12}$$

We can measure the eigenvalue of this operator as helicity. When the spin and momentum of a particle are parallel, meaning the helicity eigenvalue is positive, we call the particle right-handed. If the helicity eigenvalue is negative, we say the particle is left-handed. If a particle is massless, then its helicity has a fixed value in all reference frames, on the other

hand for a massive particle, the sign of its helicity depends on the frame of reference[6] and thus helicity is no longer an intrinsic property.

Another particle property is chirality. It is Lorentz invariant and is defined through the operator γ^5 (Dirac matrix, product of the four gamma matrices). The left-handed chiral state is projected by projection operator P_L and the right-handed chiral state by P_R:

$$P_L = \frac{1}{2}(1 - \gamma^5), \ P_R = \frac{1}{2}(1 + \gamma^5) \tag{1.13}$$

Any particle can be written in terms of left-handed and right-handed components. For massless particles, the chirality and helicity are the same. A massless left-chiral particle also has left-handed helicity. However, in the case of massive particles chirality and helicity don't coincide and a massive particle has a specific chirality. For relativistic particles chirality almost coincides with helicity, meaning that the left- and right-handed chirality fields approximately coincide with those of negative and positive helicity, respectively.

The corresponding antiparticle to neutrino (ν) is antineutrino ($\bar{\nu}$) which also carries no electric charge and has half-integer spin, but has opposite chirality. It has been observed that all neutrinos in nature are left-handed, while the antineutrinos are right-handed, meaning we only see interactions of left-handed neutrinos ν_L and right-handed antineutrinos $\bar{\nu}_R$.

Neutrino Mass and Mass Hierarchy

While within the Standard Model neutrinos are precisely massless, consequently we say, that one must go beyond the Standard Model to generate neutrino's mass. The underlying physics that lies behind neutrino masses and their mixing may contain neutrino mass terms of two different kinds: Dirac and Majorana [12].

Particles like quarks and charged leptons derive their masses from an interaction with the Standard Model Higgs field and are called Dirac particles. Conceivably, the neutrinos could derive their masses in the same way but with a certain extension of Lagrangian by including left-handed and right-handed neutrino fields to generate neutrino masses.

For simplicity, let's neglect flavour mixing. A non-zero Dirac mass requires a particle to have both a left- and right-handed chiral state and once the right-handed neutrino field has been introduced, the Dirac mass term has the form:

$$\mathcal{L}_D = -m_D \bar{\nu}_R \nu_L + h.c^7 \tag{1.14}$$

where m_D is the Dirac neutrino mass.

Since the neutrino and antineutrino are both neutrally charged particles, the origin of their masses could involve a Majorana mass. This would mean neutrinos are Majorana fermions, which can only occur when both the particle and antiparticle are identical, meaning the antineutrino and neutrino are simply right-handed and left-handed versions of the same particle. Since the mass term in the Lagrangian couples left- and right-handed neutrino chiral states, in a Majorana mass term, one of the two coupled neutrino fields is simply the charge conjugate of the other, such that the right-handed component is $\nu_L^C = C\bar{\nu}_L^T$. A Majorana mass term may be constructed out of ν_L alone, in which case we have the left-handed Majorana mass (Eq. 1.15), or out of ν_R alone, in which case we have

---

[6]*An observer moving faster than the particle will see its helicity in the opposite direction.*
[7]h.c means the Hermitian conjugate
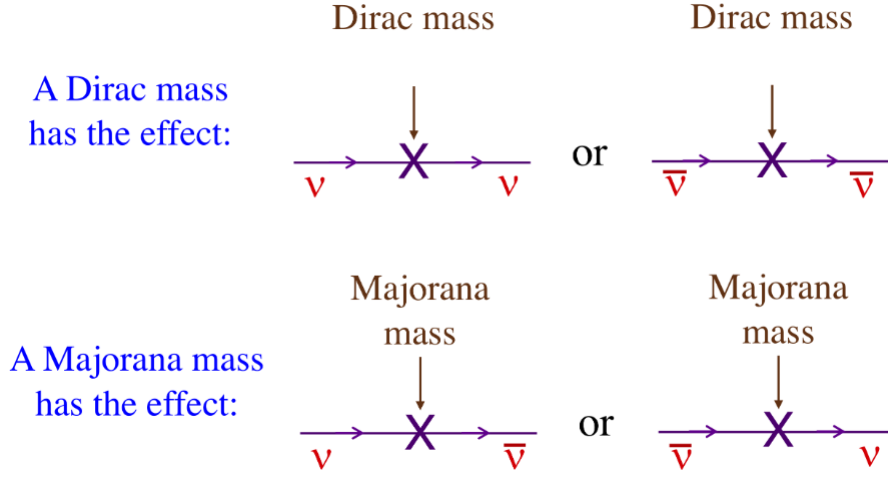
FIGURE 1.4: The effects of Dirac and Majorana mass terms in the Lagrangian [6]

the right-handed Majorana mass (Eq. 1.16) [12]:

$$\mathcal{L}_{M_L} = -\frac{1}{2}m_L\overline{(\nu_L)^C}\nu_L + h.c \tag{1.15}$$

$$\mathcal{L}_{M_R} = -\frac{1}{2}m_R\overline{(\nu_R)^C}\nu_R + h.c \tag{1.16}$$

and m_L, m_R are positive, real constant mass parameters.

The different effects of Dirac and Majorana mass terms in the Lagrangian are depicted in a simplified scheme in Figure 1.4. In contrast to Dirac mass, Majorana mass term does not conserve the lepton number and when it acts on a ν, it turns it into a $\bar{\nu}$, and vice versa.

There's also a possibility of mechanism that combines both Dirac and Majorana terms (e.g. See-Saw mechanism) and any model that includes Majorana masses predicts that the neutrino mass eigenstates will be Majorana particles [6].

So far, the mechanism by which neutrinos acquire mass and the mass of neutrino itself are unknown. Experiments observing the oscillations of neutrinos, that measure $sin^2(2\Theta)$ (Eq. 1.10), are sensitive only to the difference in the squares of the masses m_1, m_2 and m_3. While the differences are well determined, the absolute values of these masses are less certain. Results also show that the mixing matrix contains two large mixing angles and a third angle that is not exceedingly small, therefore we cannot associate any particular state $|v_i\rangle$ with any particular lepton flavour [13].

In general, there are two mass ordering hierarchies:

- The normal hierarchy: $m_1 < m_2 < m_3$

- The inverted hierarchy: $m_3 < m_1 < m_2$

The way these masses are ordered is shown in Figure 1.5. The difference in the squares of the neutrino masses $\Delta m_{21}^2 = 7.39^{+0.21}_{-0.20} \times 10^{-5} eV^2$ comes from solar neutrino observations and $|\Delta m_{31}^2| \sim |\Delta m_{32}^2| \sim 2.45^{+0.032}_{-0.030} \times 10^{-3} eV^2$ comes from atmospheric neutrino observations [13].

Direct Neutrino Mass Measurements and Cosmological Constraints on Neutrino Masses

Additional constraints can be obtained from the kinematics of weak decays. From energy-momentum conservation relation in reactions in which a neutrino or an antineutrino is involved, we can measure the limits on the mass of the flavour neutrino states, which we label as $m_{\nu_e}^{eff}$, $m_{\nu_\mu}^{eff}$, $m_{\nu_\tau}^{eff}$.

For example, it is possible to measure the neutrino masses using beta decays of nuclei with small Q value and short decay life-time by measuring the end part of the beta spectra [6]. Such conditions are satisfied in the tritium nucleus, with Q = 18.6 keV and $T_{1/2}$=12.3 y, which decays via beta decay to ^{3}He:

$$^{3}H \to\, ^{3}He + e^{-} + \bar{\nu}_e \qquad (1.17)$$

If E_0 is the mass difference between the initial and final nucleus, then the maximum kinetic energy of the electron is:

$$T_{max} = Q = E_0 - m_e \qquad (1.18)$$

However, in reality, due to a non-vanishing neutrino mass, Q value will be reduced by the neutrino mass [13]:

$$T_{max} = Q - m_{\nu_e}^{eff} \qquad (1.19)$$

This then provokes a distortion at the end point of the beta spectrum which can be probed by experiments. The most recent result on the kinematic search for neutrino mass in ^{3}H decay is from KATRIN experiment which sets an upper limit of $m_{\nu_e}^{eff} < 1.1$ eV [14].

Due to the unique role of relic neutrinos in the evolution of the Universe and in the formation of large scale structures, observations of matter clustering allow us to probe the neutrino mass sum Σm_i [14]. But these model dependent methods are heavily influenced by the selection of data, and the choice of how the neutrino is modelled for cosmological purposes significantly affects current upper bounds for the sum of the neutrino masses [15]. The most important probes for neutrino mass in cosmology are anisotropies in the cosmic microwave background (CBM) and large scale structure (LSS) formation. The bounds can be tightened by adding information within the framework of a cosmological model ΛCDM[8], such as BAO[9] or supernovae data, etc [13]. Recent constraints on Σm_i from *Planck* measurements of the cosmic microwave background anisotropies, combining information from the temperature and polarization maps and the lensing reconstruction, range from < 0.54 eV to < 0.11 eV [16].

Summary of general neutrino properties and current limits are presented in Table 1.1.

Mentioned experiments, however, do not distinguish between Dirac or Majorana neutrinos, as the ultra-relativistic neutrino behaviour is almost completely insensitive, under almost all circumstances, to whether it is a Dirac particle or a Majorana one [6]. The most sensitive experimental probe of whether the neutrino is Majorana fermion is the rate of neutrinoless double beta decay.

---

[8]Cosmological-constant (Lambda - Λ) Cold Dark Matter (CDM) model
[9]Baryon Acoustic Oscillation
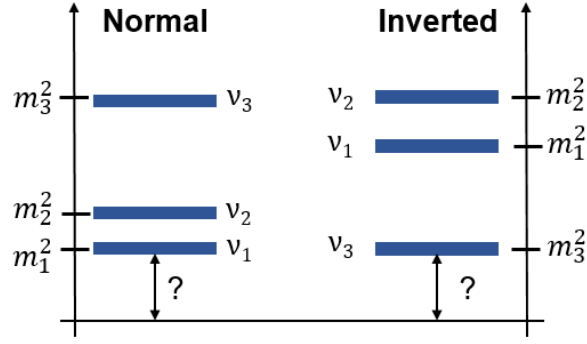
FIGURE 1.5: Ordering of neutrino mass states for the normal and inverted hierarchies

TABLE 1.1: Neutrino properties and limits obtained from global analysis of neutrino data [13, 17]

Property		Comment
Charge	0 e	neutral
Spin	$\frac{1}{2}$	fermion
Light neutrino flavours	ν_e, ν_μ, ν_τ	in association with charged lepton
Interactions	weak and gravitation	gravitational interaction is extremely weak
If ν mass = 0	neutrinos in one helicity state: left-handed, ν_L	antineutrinos in one helicity state: right-handed, $\bar{\nu}_R$
If ν mass >0	dirac fermion	particles: ν_L, ν_R, antiparticles: $\bar{\nu}_L$, $\bar{\nu}_R$,
	majorana fermion	two neutrino states: ν_L, ν_R
Mass limits		**Oscillations**
Δm^2_{21}	$7.39^{+0.21}_{-0.20} \times 10^{-5} eV^2$	solar neutrino observations
$\|\Delta m^2_{31}\| \sim \|\Delta m^2_{32}\|$	$\sim 2.45^{+0.032}_{-0.030} \times 10^{-3} eV^2$	atmospheric neutrino observations
		Kinematics of weak decays
$m^{eff}_{\nu_e}$	<1.1 eV (90% CL)	^{3}H$\rightarrow^3$He +e$^-$+ $\bar{\nu}_e$
$m^{eff}_{\nu_\mu}$	<190 keV (90% CL)	$\pi^- \rightarrow \mu + \bar{\nu}_\mu$
$m^{eff}_{\nu_\tau}$	<18.2 MeV (95% CL)	$\tau^- \rightarrow n\pi + \nu_\tau$
		Cosmology: CMB alone
Σm_i	< 0.54 eV (95% CL)	Planck 2018 data
		Cosmology: CMB + background evolution + LSS
Σm_i	< 0.12 eV (95% CL)	Planck 2018 data + BAO
Σm_i	< 0.11 eV (95% CL)	Planck 2018 data + BAO + supernovae data

1.2 Double Beta Decay and Neutrinoless Double Beta Decay

$(A, Z) \rightarrow (A, Z+2) + 2e^- + 2\bar{\nu}_e$ $(A, Z) \rightarrow (A, Z+2) + 2e^-$
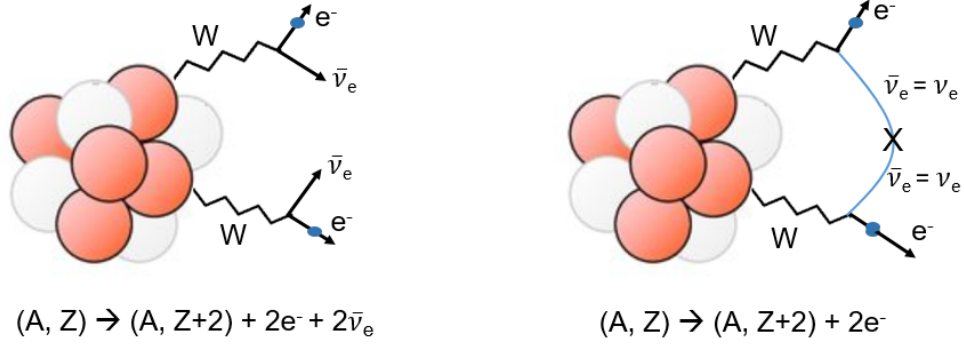
FIGURE 1.6: Simplified schemes of double beta decay (left) and neutrinoless double beta decay (right)

After the development of Enrico Fermi's theory of beta decay, the idea of double beta decay ($2\nu\beta\beta$) was first proposed by Maria Goeppert-Mayer in 1935 [18]. $2\nu\beta\beta$ is a nuclear transition in which two neutrons are simultaneously transformed into two protons inside an atomic nucleus and two electrons and two electron antineutrinos are emitted from the decaying nucleus:

$$\ _Z^A X \rightarrow\ _{Z+2}^A Y + 2e^- + 2\bar{\nu} \tag{1.20}$$

A necessary requirement for double beta decay to occur is that the mass of (Z,A) is greater than the mass of (Z + 2,A) [19]. The possibility of such transformation is due to the presence of a pairing interaction between nucleons in the nucleus. This causes an even-even nucleus with an even number of protons and neutrons to be more stable than the neighbouring odd-odd nucleus. In this case, the ordinary beta conversion of the even-even nucleus (A,Z) into the odd-odd nucleus (A,Z+1) is energetically forbidden and the only possible disintegration channel is the double beta decay. Just like in the standard beta decay, the energy spectrum of the emitted electrons is continuous. This process, however, is very rare. Calculations predict the half-life by the following equation:

$$(T_{1/2}^{2\nu})^{-1} = G^{2\nu}|M^{2\nu}|^2, \tag{1.21}$$

where $G^{2\nu}$ is phase-space factor, and $|M^{2\nu}|$ is the nuclear matrix element of the transition. Half-life periods of $\sim 10^{18}$ - 10^{21} years have been observed [20]. Double beta decays have been experimentally observed for several isotopes, including ^{48}Ca, ^{76}Ge, ^{82}Se, ^{96}Zr, ^{100}Mo, ^{116}Cd, ^{150}Nd and others. Table 1.2 shows the transitions of these isotopes along with half-lives of this process, Q values and their natural abundances.

In 1937, Italian physicist Ettore Majorana demonstrated that results of beta decay theory remain the same if neutrino was its own antiparticle - a Majorana particle. In 1939, Wolfgang Furry then proposed that a double beta decay without emission of antineutrinos ($0\nu\beta\beta$) could occur in $\beta\beta$ emitting nuclei, if neutrinos are Majorana particles in the following form:

$$\ _Z^A X \rightarrow\ _{Z+2}^A Y + 2e^- \tag{1.22}$$

TABLE 1.2: Examples of $\beta\beta$ emitters [19]

Transition	Q value [keV]	Half-life* [y]	Natural abundance [%]
$^{48}_{20}Ca \rightarrow ^{48}_{22}Ti$	4271	4.4×10^{19}	0.187
$^{76}_{32}Ge \rightarrow ^{76}_{34}Se$	2039	1.5×10^{21}	7.8
$^{82}_{34}Se \rightarrow ^{82}_{36}Kr$	2995	0.9×10^{20}	9.2
$^{96}_{40}Zr \rightarrow ^{96}_{42}Mo$	3350	2.3×10^{19}	2.8
$^{100}_{42}Mo \rightarrow ^{100}_{44}Ru$	3034	7.1×10^{18}	9.6
$^{116}_{48}Cd \rightarrow ^{116}_{50}Sn$	2802	2.8×10^{19}	7.5
$^{150}_{60}Nd \rightarrow ^{150}_{62}Sm$	3367	8.2×10^{18}	5.6

* From [20]

The process can be mediated by an exchange of a light Majorana neutrino, or by an exchange of other particles. In the first case, it can be seen as two subsequent steps: first, a neutron decays under the emission of a right-handed neutrino which is absorbed in the second vertex as a left-handed neutrino [19]. Other models which can provide alternative mechanisms to trigger this decay include, for example, Majoron emission or right-handed (RH) weak current, or even more exotic models, such as R-parity violating Supersymmetry (SUSY), or an extra dimensions model. The light neutrino exchange mechanism is, however, the most commonly postulated decay mode, since it involves the least deviation from the SM. In this work, the following summary of sensitivities and limits are given for this mechanism.

Formula for the inverted half-life is given by:

$$(T^{0\nu}_{1/2})^{-1} = G^{0\nu}|M^{0\nu}|^2|\langle m_{\beta\beta}\rangle|^2, \tag{1.23}$$

where $m_{\beta\beta}$ is the effective Majorana mass of the electron neutrino. Under the hypothesis that only the known three light neutrinos participate in the process, the effective mass equals to:

$$m_{\beta\beta} = \sum_{i=1}^{3} m_i U_{ei}^2, \tag{1.24}$$

U_{ei} are the elements of mixing matrix.

This process has not yet been experimentally observed. The decay violates total lepton number by two units and its observation would imply neutrinos are Majorana fermions no matter what the underlying mechanism is.

In $0\nu\beta\beta$ decay, the two electrons carry away all of the decay energy. This would lead to a summation peak at the end of the combined electron energy spectrum (Fig. 1.7). Thus, the signal for neutrinoless double beta decay is a peak in the spectrum of the sum of the emitted electrons at the Q-value of the transition.
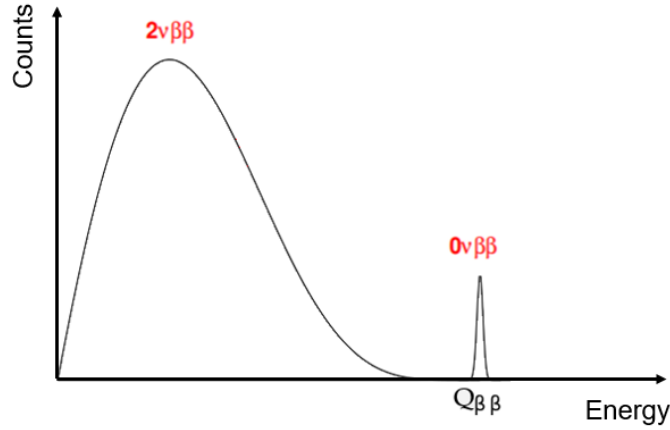
FIGURE 1.7: Plot of the sum energy spectrum of the emitted electrons for $0\nu\beta\beta$ decay

1.2.1 Experimental Investigations of Neutrinoless Double Beta Decay

In the following section, a brief review of some ongoing and next generation experiments is given, with the description of relevant parameters contributing to the experimental sensitivity.

Experimental Sensitivity

Experiments searching for the $0\nu\beta\beta$ signal are sensitive to the half-life of the process. From the law of radioactive decay, the $0\nu\beta\beta$ half-life can be evaluated as [21]:

$$T_{1/2}^{0\nu} = ln2 \cdot t \cdot \epsilon \frac{N_{\beta\beta}}{N_{peak}}, \tag{1.25}$$

where t is the measuring time, ϵ is the detection efficiency, $N_{\beta\beta}$ is the number of decaying nuclei, and N_{peak} is the number of observed decays in the region of interest[10]. This formula is valid for the case of a positive signal where the peak shows up in the spectrum.

If there is no signal (no peak) detected, the sensitivity of an experiment[11] is estimated as a half-life corresponding to the maximum signal that could be hidden in the background n_b, for which the expression can be written as [21]:

$$S^{0\nu} = ln2 \cdot t \cdot \epsilon \frac{N_{\beta\beta}}{n_b} \tag{1.26}$$

Considering real experimental conditions, an estimation for $S^{0\nu}$ as a function of the experimental parameters can be written as:

$$S^{0\nu} = ln(2) \frac{\epsilon N_A}{W} \sqrt{\frac{Mt}{b\Delta E}}, \tag{1.27}$$

---

[10]A particular relevant range in the measurement.

[11]Often called also "factor of merit".

where M is the mass of the $\beta\beta$-emitting isotope, W is its molar mass, N_A is the Avogadro constant, ΔE is the energy resolution and b is the background rate per unit mass, time, and energy. This is valid under assumption of Poisson statistics, when $n_b = \sqrt{b \cdot \Delta E \cdot t \cdot M}$. If the background level is so low that the expected number of background events in the ROI is of order of unity (or close to zero), n_b is a constant, Equation 1.27 is no longer valid and the sensitivity is given by [21]:

$$S^{0\nu} = ln(2) \frac{\epsilon N_A}{W} \frac{Mt}{N_s}, \tag{1.28}$$

where N_s is the number of observed events in the region of interest.

Equations 1.27 and 1.28 emphasize the role of the experimental parameters that constrain the experimental sensitivity. Neutrinoless double beta decay is an extremely rare process and therefore, its experimental research requires features such as large source masses, long measurements, good energy resolution and low radioactive background. Of particular interest is the case when Equation 1.28 is valid, when the background rate is very low and sensitivity scales linearly with the sensitive mass M and the measurement time t, and not with the square root of M and t.

The experimental search for $0\nu\beta\beta$ is extremely challenging, experimental difficulties are matched by the theoretical ones and all previous searches failed to find a positive signal setting only the best current half-life limits of $>10^{26}$ years (Table 1.3) [22].

Source Isotope Selection

Because of the uncertainties related to the theoretical considerations (nuclear matrix elements, mechanism behind the $0\nu\beta\beta$) and experimental techniques, it is important to pursue the searches with various isotopes. Not all $\beta\beta$ isotopes are suitable as candidate isotopes as the source isotope selection must be based on maximizing the $0\nu\beta\beta$ signal over the background events. Therefore isotope candidates must have a long $2\nu\beta\beta$ half-life, high Q value and a large phase space factor (because $(T^{0\nu}_{1/2}) \sim (G^{0\nu})^{-1}$) [23]. The isotopic abundance also plays a key role as the source mass influences the sensitivity of an experiment.

A Brief Review of Experiments

There are two main types of neutrinoless double beta decay detectors. The majority of the experiments searching for neutrinoless double beta decay exploits a homogeneous approach, which means that the detector coincides with the source. They often measure only the sum energy of the two electrons, but the electrons themselves are never observed directly. A different approach consists of separating the source from the detector, where the two electrons are detected independently using tracking and calorimeter techniques. The energy of electrons is measured with ionization, scintillation or phonon detectors, or a combination of two techniques.

Semiconductor experiments

In this type of experiment, the source material is some form of a semiconductor and the isotope under investigation is part of the source. Signal that can be measured comes from a cascade of electron-hole pairs that originate from ionization of the semiconductor by emitted electrons from a double beta decay event. The advantage of such detectors

TABLE 1.3: $T^{0\nu}_{1/2}$ and $\langle m_{\beta\beta}\rangle$ limits (90% CL) determined for various isotopes

Isotope	Experiment	$T^{0\nu}_{1/2}$ limit [y]	$\langle m_{\beta\beta}\rangle$ limit [eV]
^{48}Ca	ELEGANT VI [24]	$>5.8 \times 10^{22}$	<3.5 - 22
^{76}Ge	Majorana [25]	$>1.9 \times 10^{25}$	<0.24 - 0.52
	GERDA [26]	$>1.4 \times 10^{26}$	<0.079 - 0.18
^{82}Se	NEMO-3 [27]	$>2.5 \times 10^{23}$	<1.2 - 3.0
	CUPID-0 [28]	$>2.4 \times 10^{24}$	<0.376 - 0.77
^{100}Mo	NEMO-3 [29]	$>1.1 \times 10^{24}$	<0.3 - 0.9
^{116}Cd	Aurora [30]	$>2.2 \times 10^{23}$	<1.0 - 1.7
^{130}Te	CUORE [31]	$>3.2 \times 10^{25}$	<0.075 - 0.35
^{136}Xe	PandaX-II [32]	$>2.4 \times 10^{23}$	<1.3 - 3.5
	EXO-200 [33]	$>1.8 \times 10^{25}$	<0.15 - 0.40
	KamLAND-Zen [34]	$>1.07 \times 10^{26}$	<0.061 - 0.165
^{150}Nd	NEMO-3 [35]	$>2.0 \times 10^{22}$	<1.6 - 5.3

is that the energy resolution is usually extremely good since the number of electron-hole pairs is proportional to the energy of the emitted electrons.

Among the different semiconductor detector technologies, ^{76}Ge-enriched high-purity germanium (HPGe) detectors provide the best sensitivity and are the most promising for scaling to a tonne-scale experiment [22]. HPGe detectors are intrinsically clean, as impurities are removed in the detector crystal-growing process [22], however, the $Q_{\beta\beta}$ value of germanium is only 2039 keV, and so it lies in a region where contamination from many external background sources is still possible.

HPGe detectors are used by collaborations such as GERDA[12] and Majorana. Recently, LEGEND[13] experiment was formed to pursue a tonne-scale ^{76}Ge-based experiment and aims to increase the sensitivities for ^{76}Ge in the first phase to 10^{27} years and in the second phase up to 10^{28} years [36]. The phase of the experiment called LEGEND-1000 plans the exposure of 10 $t.y$ by operating 1000 kg of detectors for 10 years. So far, an initial baseline design has been established with bare germanium detectors operating in liquid argon. The active liquid argon (LAr) veto tags external backgrounds depositing energy in the LAr that subsequently scintillates.

Besides germanium detectors, other semiconductor technologies exist which can potentially provide competitive results, such effort being made by COBRA[14] experiment using a large array of CdZnTe semiconductors.

Bolometer experiments

Bolometers are calorimeters operating at milli-kelvin temperatures that can measure the energy released in the crystal by interacting particles through their temperature rise. Bolometer absorbers can be grown from a variety of materials, those including $\beta\beta$ emitters

---

[12]The Germanium Detector Array
[13]Large Enriched Germanium Experiment for Neutrinoless Double Beta Decay
[14]Cadmium Zinc Telluride 0-Neutrino Double-Beta

are, for example, $^{nat/130}TeO_2$, $^{116}CdWO_4$, $Zn^{82}Se$ or $^{40}Ca^{100}MoO_4$. Excellent counting statistics in the phonon channel make bolometers energy resolution comparable to that of semiconductor detectors but working at extremely low temperatures increases the technical difficulty of building large detectors [22]. Experiments exploiting these techniques are CUORE[15], CUPID[16] and AMoRE[17].

Scintillator experiments

Scintillator experiments place the $\beta\beta$ emitting candidate isotope inside a scintillating medium where the emitted particles excite the scintillator atoms and the light is usually detected by an array of photomultiplier tubes.

Typical isotope candidates for these experiments are ^{136}Xe, which can be dissolved in liquid scintillators or used as gas, or ^{48}Ca build in crystal scintillators.

Two large experiments have searched for $0\nu\beta\beta$ in Xe: EXO-200[18], which has used Xe in a time projection chamber, thus combining the ionization and scintillation light for signal detection, and KamLAND-Zen[19], where it has been dissolved as a passive $\beta\beta$ source in a liquid scintillator detector. Detectors for ^{48}Ca double beta decay measurements are the ELEGANT VI system and its scale-up detector CANDLES[20] using inorganic CaF_2 scintillators. Another example of these experiments is the SNO+ experiment [37] that selected ^{130}Te as its $\beta\beta$ emitting isotope by using tellurium loaded liquid scintillator.

Tracking experiments

The approach of tracking experiments consists of separating the source from the detector but combining tracker and calorimetry techniques. They usually sacrifice the source mass for extremely good background rejection which is based on reconstructing the topology of measured events. The separation between source and detector also implies that any isotope candidate can be studied. It is currently the only detector technology capable of measuring full $\beta\beta$ kinematics (individual electron energy, opening angle between the two electrons) which can lead to distinguishing certain underlying mechanisms for $0\nu\beta\beta$ decay [22]. The most noteworthy tracker-calorimeter experiments are the NEMO-3[21] experiment and its successor SuperNEMO. NEMO-3 detector had been operating in the Modane Underground Laboratory from 2003 to 2011. It installed foils of the source isotope between tracking detectors and plastic scintillator calorimeters (Figure 1.8). This technique can detect each electron as it is emitted from the source foil, measure its energy and angular distribution and, thanks to a magnetic field, its charge. The two isotopes with the largest masses were ^{100}Mo (6.914 kg) and ^{82}Se (0.932 kg) with smaller amounts of ^{48}Ca, ^{96}Zr, ^{116}Cd, ^{130}Te and ^{150}Nd. Another experiment with the capabilities for calorimetry and tracking is the NEXT[22] [38] experiment using high-pressure xenon gas time projection chambers.

---

[15] Cryogenic Underground Observatory for Rare Events
[16] CUORE Upgrade with Particle Identification
[17] Advanced Molybdenum Based Rare Process Experiment
[18] Enriched Xenon Observatory
[19] Based on KamLAND experiment in the Kamioka underground neutrino observatory in Japan
[20] Calcium fluoride for the study of Neutrinos and Dark matters by Low Energy Spectrometer
[21] Neutrino Ettore Majorana Observatory
[22] Neutrino Experiment with a Xenon TPC
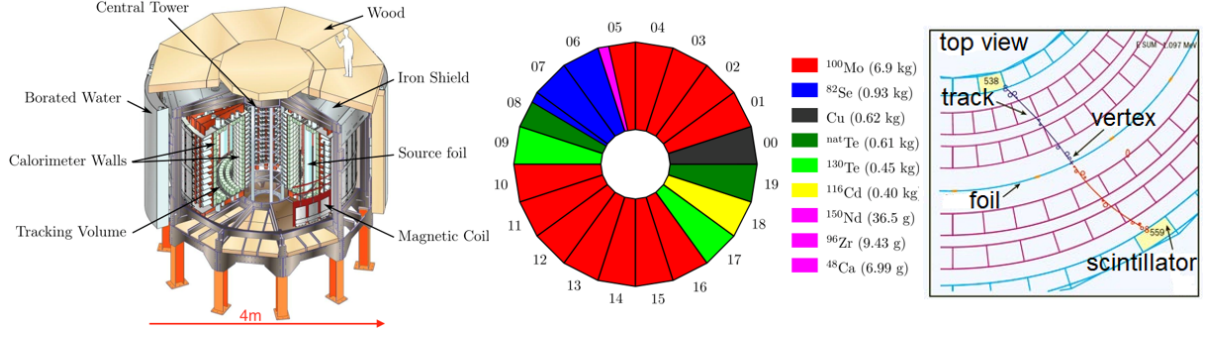
FIGURE 1.8: **Left:** Design of the NEMO-3 experiment. **Middle:** Source distribution. **Right:** NEMO-3 $2e^-$ event reconstruction.

Future Experimental Prospects

Many criteria need to be considered when optimizing the design of future experiments. The desirable features are a well performing detector, with good energy resolution, giving the maximum information on decay kinematics, large isotopically enriched source mass and very low background. Unfortunately, it is impossible to optimize these features simultaneously in a single detector and one has to find the best compromise between incompatible requests. As of today, there is no clear experiment that satisfies all criteria.

Currently, there is R&D towards improved detectors in all detection techniques aiming for better sensitivity for the $0\nu\beta\beta$ decay. Many of these next generation experiments will be sensitive to $\langle m_{\beta\beta} \rangle \sim 75$ meV, or even ~ 10 meV for tonne scaled experiments, and they will offer the potential of a discovery at $T_{1/2}^{0\nu}$ exceeding 10^{28} years [22]. Thus, from the predictions on effective Majorana mass $m_{\beta\beta}$ as a function of the lightest neutrino mass shown in Figure 1.9, they will be able to explore the Majorana neutrino mass if neutrinos have the inverted mass hierarchy [39]. Probing the Majorana neutrino mass through $0\nu\beta\beta$ decay assuming normal mass hierarchy would require multi-tonne-scale detectors and very high background suppression.
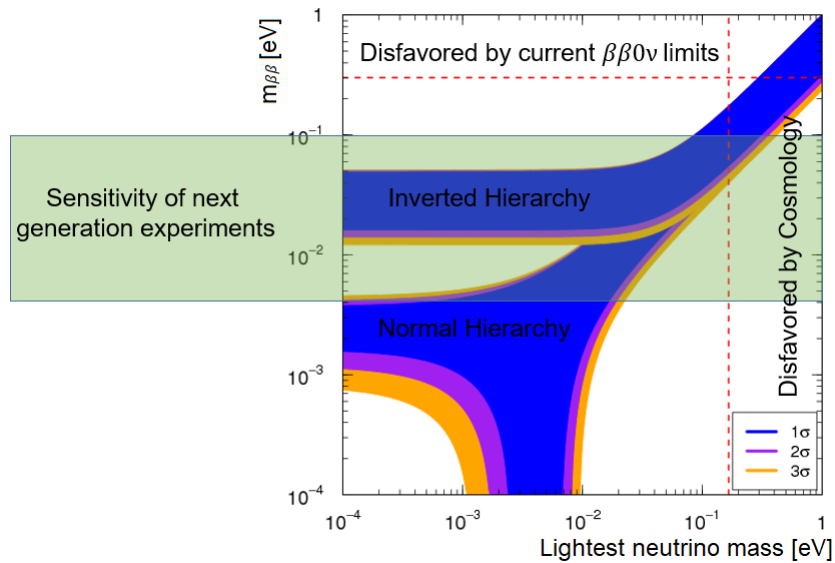
FIGURE 1.9: The dependence of $m_{\beta\beta}$ on the absolute mass of the lightest neutrino

Chapter 2

SuperNEMO Experiment

The SuperNEMO experiment is a next generation neutrinoless double beta decay experiment building on the successes of its predecessor NEMO-3, using the same tracker-calorimeter technology. The first module of the detector, the Demonstrator, is located at the Laboratoire Souterrain de Modane (LSM), in the middle of Fréjus road tunnel in the French Alps near Modane. The baseline design of the detector consists of 20 such modules each containing approximately 5-7 kg of enriched and purified $\beta\beta$ emitting isotope deposited on a thin supporting foil, which, unlike NEMO-3, are planar in geometry. It aims for half-life sensitivity of 10^{26} years, corresponding to an effective neutrino mass of 50-100 meV. The baseline isotope currently used in the Demonstrator is enriched ^{82}Se. The source isotope is placed in between trackers that are surrounded by calorimeter walls on both sides, which makes this unique tracking and calorimetry technique, along with an extremely radio-pure detector and surrounding materials, sufficiently eliminating background events by full reconstruction of event topology. Each module is completed with a magnetic field followed by the installation of passive shielding against gamma rays and neutrons (Fig. 2.1). The ultimate goal is to observe the experimental signature of $0\nu\beta\beta$, which are two electrons originating in the same location on the source foil, with the energy sum equaling the Q value of the decay. The full three-dimensional reconstruction of charged particle tracks, as well as energy measurements also makes it possible to analyze both the angular and electron energy distributions, which are two quantities that may provide a method to distinguish between different mechanisms of $0\nu\beta\beta$.

2.1   SuperNEMO Design

The design of the experiment is not solely a scaled-up version of NEMO-3, but to meet required ultralow levels of background, a considerable amount of R&D was dedicated to source foil production and to tracker and calorimeter development.

2.1.1   Source Foils

The ^{82}Se source isotope selection was based on maximizing the $0\nu\beta\beta$ signal over the $2\nu\beta\beta$ background events as they are indistinguishable from those in the $0\nu\beta\beta$ mode in the energy region of interest (ROI). Isotope candidate must therefore have a long $2\nu\beta\beta$ half-life. ^{82}Se also has a high $Q_{\beta\beta}$ value, equal to 2.995 MeV, to avoid common backgrounds that can deposit energy extraneously within the ROI. Another important factor for selection is the natural abundance of the isotope and a possible (and relatively easy) enrichment and purification process.
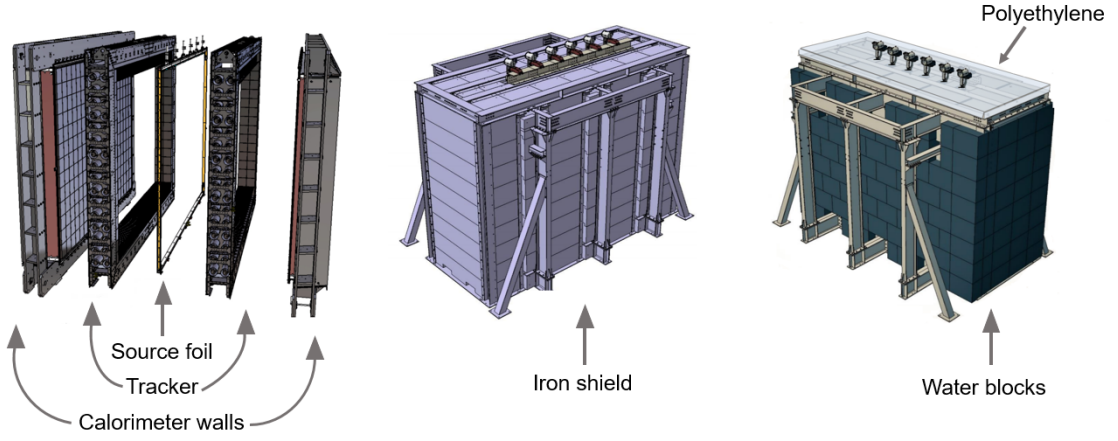
FIGURE 2.1: Design of the Demonstrator module and proposed shielding

In essence, the foils are composed of enriched ^{82}Se isotope with 10% PVA glue (polyvinyl alcohol as a binder) of an average thickness of 286 μm ($\sim 40 mg/cm^2$), in a thin Mylar plastic envelope (12 μm thick) for mechanical strength. The foils are 2.7 m long and 13.5 cm wide. Keeping the foils thin increases the chance that emitted electrons will escape the foil into the tracker. In total, the Demonstrator has 34 selenium foils installed side by side in a frame with total ^{82}Se mass of $\sim$7 kg. As it is important to have a very clean and radiopure detector, the selenium source was purified by teams at Tomsk and Dubna in Russia, to remove contamination from naturally-occurring beta decaying elements. The required radiopurity is ^{208}Tl < 2 μBq/kg and ^{214}Bi < 10 μBq/kg to achieve the sensitivity $T_{1/2}(\beta\beta0\nu) > 10^{26}$ years.

2.1.2 Tracker

The tracker used in SuperNEMO is a wire-chamber tracker with octagonal drift cells operating in Geiger mode (operating voltage of around 1800 V). Cells are formed of a 2.7 m long, 40 μm diameter, stainless steel anode wire, surrounded by 8 grounded cathode wires (50 μm in diameter). The gas mixture used as the drift gas is He with addition of 1% of Ar and 4% of ethanol used as a quencher. Each cell consists of a central anode wire that is surrounded by field shaping wires, and a cathode at each end to pick up the signal (Figure 2.2).

When a charged particle passes through the cell the ionized gas mixture yields approximately 6 electrons per 1cm. These electrons then drift toward the anode with different drift time depending on whether they were produced close or far away from the anode wire because the layout of the field and ground wires establishes a varying electric field within each cell. In the high field region close to the wire, further ionisation produces UV light which induces new ionisation further out. This sets up a chain reaction, and gas of ionised plasma spreads out from the initial track point, parallel to the wire [40].

The time difference between the Geiger discharge arriving at each end of the cell provides the longitudinal location of the track and the time for the resulting electron shower to drift to the anode tells us the particle's distance from the center of the cell [41]. This way, the full three-dimensional track reconstruction of charged particles is possible.

There are 2034 such cells assembled into cassettes and a total of 113 cassettes are built on both sides of the source foils.
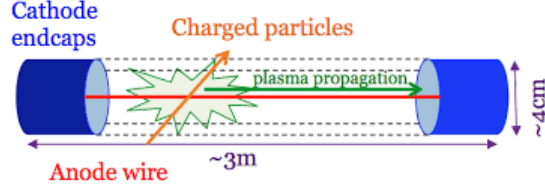
FIGURE 2.2: SuperNEMO tracker cell scheme

To reach the target sensitivity the radon concentration inside the tracking volume must be < 0.15 mBq/m^3.

2.1.3 Calorimeter

The SuperNEMO calorimeter is a scintillator based detector divided into two main walls on the outside of the detector to measure the energy of particles that reach the edge. Each calorimeter wall consists of 260 optical modules - each module is a large volume plastic scintillator block (256 mm x 256 mm with a minimum thickness of 141 mm and a hemispherical cutout) coupled to an 8-inch photomultiplier tube (PMT) (Fig. 2.3). Each module is covered by individual iron shielding.
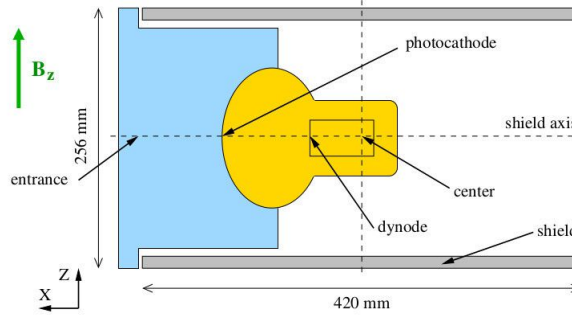
FIGURE 2.3: Individual optical module and its iron shield

The calorimeter is segmented into walls to measure the individual energy of each particle and each scintillator block is thick enough to fully absorb the electrons that are produced in $0\nu\beta\beta$-decay and to efficiently identify gamma rays. In the final stage, optical modules are also positioned above, below and to the sides of the tracker, giving a total of 720 such modules fully enclosing the geometry.

The main requirement of the calorimeter is to provide good time-of-flight measurements and energy resolution for low-energy electron detection and to detect incoming electrons simultaneously originating from the same vertex in the source foil [42]. The calorimeter requires a scintillator that has a high light yield, low electron backscattering, which is proportional to Z^2, high radiopurity, good timing and a relatively low cost. An R&D program was undertaken with Czech manufacturer NUVIA CZ to improve the performance of the plastic scintillator. This improved scintillator, known as enhanced PS, has a composition of 1.5% p-Terphenyl (p-TP) and 0.05% POPOP [42]. Energy resolution better than $8\%/\sqrt{E}$ (FWHM) has been reached and in order to increase the light collection, the blocks are

TABLE 2.1: SuperNEMO calorimeter parameters [42]

Geometry and dimensions	
	$256 \times 256 \times 194$ mm
Composition of plastic blocks	1.5% p-Terphenyl (p-TP) + 0.05% POPOP (1.4-bis(5-phenyloxazol-2-yl) benzene)
PMT reference	Hamamatsu R5912MOD
Energy resolution	8% (FWHM) at 1 MeV
Time resolution	< 400 ps at 1 MeV
PMT radiopurity	$A_{40_K}=$ 150 mBq/kg $A_{214_{Bi}}=$ 65 mBq/kg $A_{208_{Tl}}=$ 4 mBq/kg
Scintillator radiopurity	$A_{40_K}=$2.2 mBq/kg $A_{214_{Bi}} < 0.3$ mBq/kg $A_{208_{Tl}} < 0.1$ mBq/kg

wrapped in 600 μm Teflon on the sides followed by 12 μm aluminised Mylar on all the faces [43].

Table 2.1 summarizes selected SuperNEMO calorimeter parameters. The activity levels of radioisotopes of the plastic scintillators selected for SuperNEMO are negligible compared to the PMTs, and in particular, the PMT glass, which are the main source of contamination.

To ensure radiopurity, all components of the optical module, particularly the PMT components and glass, were analysed using high purity Germanium (HPGe) detectors.

The core assembly of source foils, tracker and main calorimeter walls of the SuperNEMO module is shown in Figure 2.4.

2.1.4 Magnetic Field and Shielding

To aid in particle identification inside the tracker, a solenoid coil will be placed around the detector producing a magnetic field of ~ 25 Gauss with direction orientation along z axis, $+z$, parallel to the tracker drift cells. This way it is possible to distinguish between electrons and positrons based on their track curvature in the tracker chamber.

The successful completion of the Demonstrator module will be followed by the installation of passive shielding. Since external radioactivity has a big impact on the detector background, which might influence the experiment, the task to define and optimize the shielding materials and thickness becomes important. The collaboration carried out R&D regarding the choice of materials and thickness in order to suppress significantly intrinsic
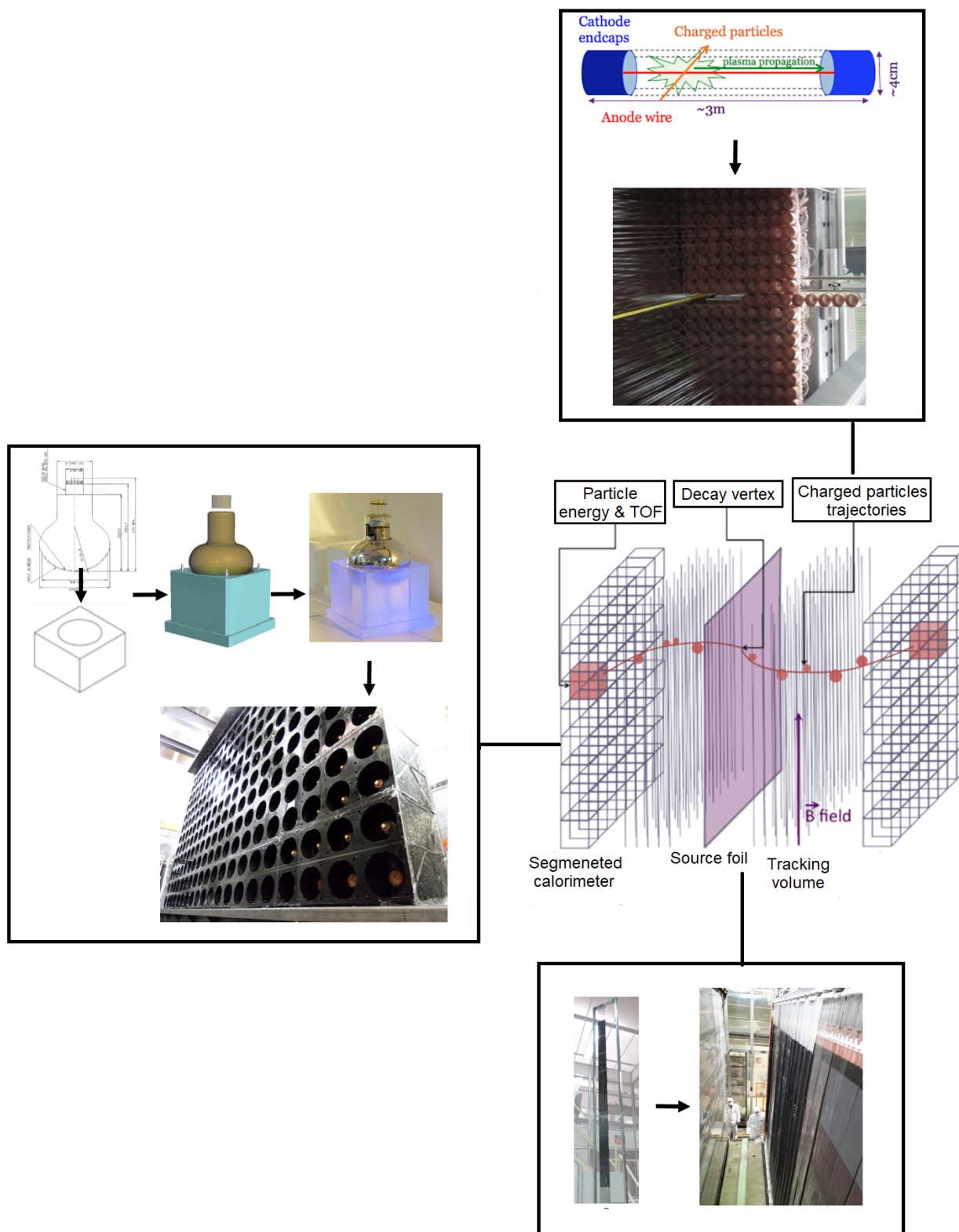
FIGURE 2.4: The core assembly of SuperNEMO module

background including ambient external gamma rays and neutrons.

The best shielding against gamma rays is achieved with a substance that has a high density of electrons (which correlates with a high mass density) and also a high atomic number Z. For shielding against gamma rays radiopure iron is considered.

Neutron shielding materials are typically constructed from low atomic number elements (hydrogen, carbon, and oxygen) with high scattering cross sections that can effectively moderate or thermalize incident neutrons. In SuperNEMO experiment water and polyethylene (also with the possible addition of boron) are considered.

2.1.5 Event Reconstruction and Selection

As it was mentioned before, one of the strengths and advantages of combining the calorimetry and tracking techniques is that we are able to obtain charged particle trajectories in the tracker, and energy and time-of-flight (TOF) information from the calorimeter.

Alpha particles can be identified as short and straight tracks. Electrons can be identified via track with negative curvature due to the magnetic field associated with calorimeter hit. Positrons can be identified via tracks with opposite curvature to that of an electron. Gamma particles are identified as calorimeter hits that are not associated with tracks. The conceptual scheme of this approach is shown in Figure 2.5.

Tracks can be extrapolated into the foil to determine appropriate event vertex. This allows us to identify particles and to isolate true $0\nu\beta\beta$ events. Given these conditions, a strict set of selection rules can be applied for double beta decay events - two electrons with a common vertex in the foil:

- Events must include only two negatively charged particles each associated with one calorimeter hit - in a magnetic field pointing upwards when the initial velocity of the electron is forwards, then the electron acceleration will point to the left, corresponding to a negative track curvature

- Event vertices must be traced to originate within the source foil and the tracks must have a common vertex - the vertex separation precision the detector will have in operation is ~ 3.2 cm

- The TOF of the electrons in the detector must be consistent with the hypothesis of the electrons originating in the source foil

- Maximum of two calorimeter hits with energy deposited in individual calorimeter blocks above 50 keV are allowed, with at least one of the hits being above 150 keV - to avoid flooding the event trigger with noise

- The number of delayed Geiger drift cell hits due to α particles must be zero

- There are no hits in the γ-veto detectors with energy > 50 keV and zero calorimeter hits not associated with a track

- For $0\nu\beta\beta$ the total energy of the event is between 2.8 and 3.2 MeV - this energy interval is the region of interest (ROI) for ^{82}Se, the optimal window for the best $0\nu\beta\beta$ sensitivity
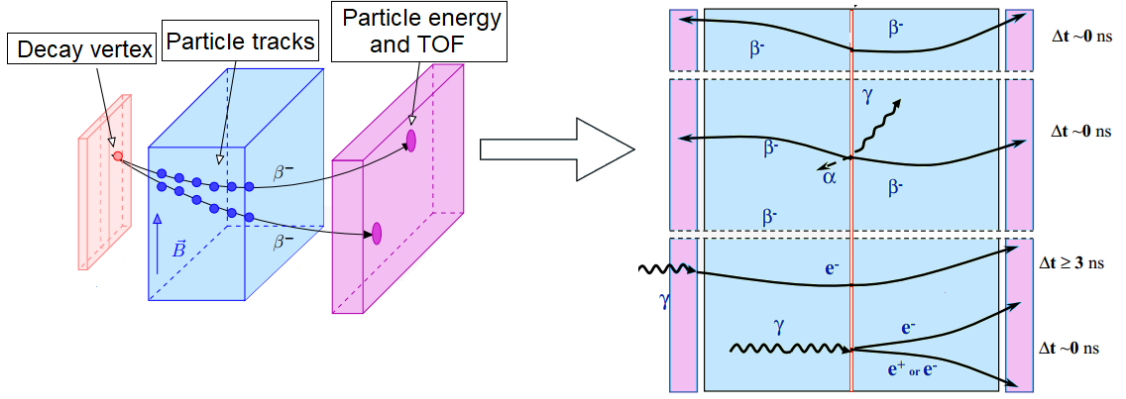
FIGURE 2.5: Reconstruction of the event topology and particle identification

Internal and External Probabilities

In order to establish the origin of the event, whether the event is internal or external (from an external source), the time-of-flight information plays a key role. For example, an event that has one electron crossing the foil can mimic an event that has two electrons coming from the foil. To discriminate those events, internal and external TOF probabilities are calculated.

The calculations go as follows: We assume that two particles are emitted from a common origin inside the foil and at least one particle leaves a track and we have two different calorimeter hits with associated times t_i^{meas} (i=1,2). TOF of a particle to travel the distance l_i is:

$$t_i^{tof} = \frac{l_i}{\beta_i}. \tag{2.1}$$

Where β_i for electrons is:

$$\beta_i = \sqrt{\frac{E_i(E_i + 2m_e)}{E_i + m_e}}, \tag{2.2}$$

and E_i is calibrated energy deposited in the calorimeter and m_e is electron rest mass. The time of emission of each particle t_i^{int} is:

$$t_i^{int} = t_i^{meas} - t_i^{tof} = t_i^{meas} - \frac{l_i}{\beta_i}. \tag{2.3}$$

The time distributions are approximately Gaussian and so a χ^2 test may be used with an appropriate χ^2 variable:

$$\chi^2 = \frac{[(t_1^{meas} - \frac{l_1}{\beta_1}) - (t_2^{meas} - \frac{l_2}{\beta_2})]^2}{\sigma_{t_1^{int}}^2 + \sigma_{t_2^{int}}^2}. \tag{2.4}$$

$\sigma_{t_i^{int}}^2$ is the variance of the emission timing measurement which is dominated by contributions from uncertainties on the measurement time $\sigma_{t_i^{meas}}$, σ_{β_i} and σ_{l_i}.
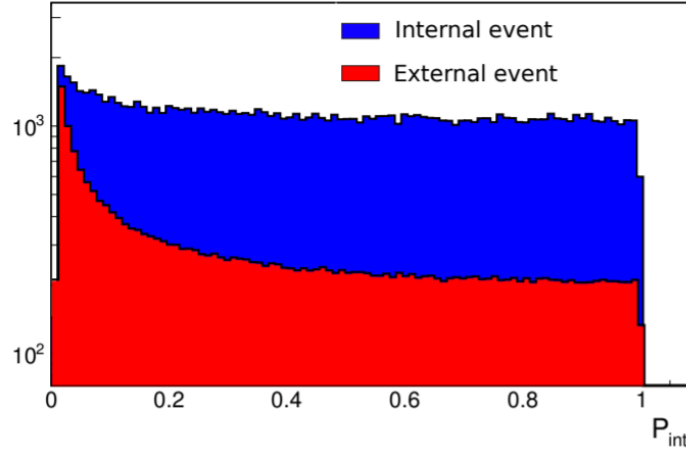
FIGURE 2.6: Internal probability distribution for an internal 2e event and for an external event [44]

If we assume that an incident photon interacts in the first PMT and causes either a crossing electron or an external $1e1\gamma$ event, TOF of the particles is then given[1]:

$$t^{tof} = \frac{l_1}{\beta_1} + \frac{l_2}{\beta_2}.$$ (2.5)

In this case, the χ^2 variable is constructed as:

$$\chi^2 = \frac{[(t_2^{meas} - t_1^{meas}) - (\frac{l_1}{\beta_1} + \frac{l_2}{\beta_2})]^2}{\sigma_{t_1^{int}}^2 + \sigma_{t_2^{int}}^2}.$$ (2.6)

To convert the χ^2 values into a probability, following equation can be used:

$$P(\chi^2) = 1 - \frac{1}{\sqrt{2\pi}} \int_0^{\chi^2} x^{-1/2} e^{-x/2} dx.$$ (2.7)

For an internal event the internal probability distribution is expected to be equally distributed from 0 to 1, while it is expected to be peaked for an external event (Fig. 2.6). The standard SuperNEMO cuts that maximize signal over background are: $P_{internal} > 4\%$ and $P_{external} < 1\%$.

2.2 Timescale and Sensitivity

The goal of the Demonstrator module is to demonstrate that the background target level can be reached and to explore the prospects of the combination of calorimetry and tracking techniques. The Demonstrator contains up to 7 kg of target isotope reaching half-life sensitivity 6.5×10^{24} years with 2.5 years of data (17.5 kg·y exposure), which is close to the limit already set by this generation $0\nu\beta\beta$ experiments. However, if the signal were discovered by one of these experiments in the near future, the Demonstrator could prove useful in confirming the result.

---

[1]For a photon accompanied with the emission of an electron, $\beta = 1$

TABLE 2.2: Summary of detector properties and target levels
of SuperNEMO experiment

Detector property	Demonstrator	Full scale
Isotope	^{82}Se	^{82}Se / ^{150}Nd / ^{48}Ca.
Source mass	7 kg	100 kg
$T_{1/2}^{\beta\beta0\nu}$ sensitivity	$\sim 10^{24}$ years	$> 10^{26}$ years
$\langle m_{\beta\beta} \rangle$ sensitivity	0.2 - 0.4 eV	0.05 - 0.1 eV
Energy resolution	8% (FWHM) @ 1 MeV, 4% @ 3 MeV	
Time resolution	< 400 ps at 1 MeV	
Foil radiopurity	^{208}Tl < 2 μBq/kg , ^{214}Bi < 10 μBq/kg	
Tracker radon concentration	< 0.15 mBq/m^3	
PMT radiopurity	^{40}K= 150 mBq/kg, ^{214}Bi= 65 mBq/kg, ^{208}Tl= 4 mBq/kg	
Scintillator radiopurity	^{40}K= 2.2 mBq/kg, ^{214}Bi< 0.3 mBq/kg, ^{208}Tl< 0.1 mBq/kg	

The modular design of the experiment allows it to be scaled up to reach higher sensitivities, as the mass can be increased in a straightforward manner. Full-scale SuperNEMO of 20 modules could contain 100 kg of source isotope.

It also provides the means to discriminate different underlying mechanisms for the neutrinoless double beta decay by measuring the decay half-life and the electron angular and energy distributions. Using the experimental selection criteria summarized in the previous section the signal efficiency was found to be 28.2% for the light neutrino exchange mechanism and 17.0% for the right-handed current mechanism in ^{82}Se [45]. $0\nu\beta\beta$ half-lives that SuperNEMO is expected to exclude are up to 10^{26} years assuming the light neutrino exchange mechanism and 10^{25} years assuming the right-handed current mechanism for ^{82}Se [45]. SuperNEMO detector properties and target levels are summarized in Table 2.2.

2.3   Background of the Experiment

A serious concern of all neutrinoless double beta decay experiments is the background. Experiments detect the electrons of $0\nu\beta\beta$ signal in the final state - the sum of the electron energies will be a peak at the $Q_{\beta\beta}$ value. The decay rate is extremely low and the peak is expected to be very small.

Background events to the SuperNEMO experiment is reduced to all events in topologies that could mimic the topology of the two electrons emitted from a common vertex in the source foil in the energy region of interest. The energy region of interest is around the $Q_{\beta\beta}$ value of ^{82}Se (2.995 MeV). This energy region is shared by the natural radioactivity contamination present in the detector materials and environment surrounding the detector. Only two natural radio-isotopes have Q_{β} value greater than 3 MeV - ^{214}Bi from ^{238}U decay chain, and ^{208}Tl from ^{232}Th decay chain, see Table 2.3. Their simplified decay schemes showing the strongest transitions are in Figures 2.7 and 2.8. In both decays, the beta
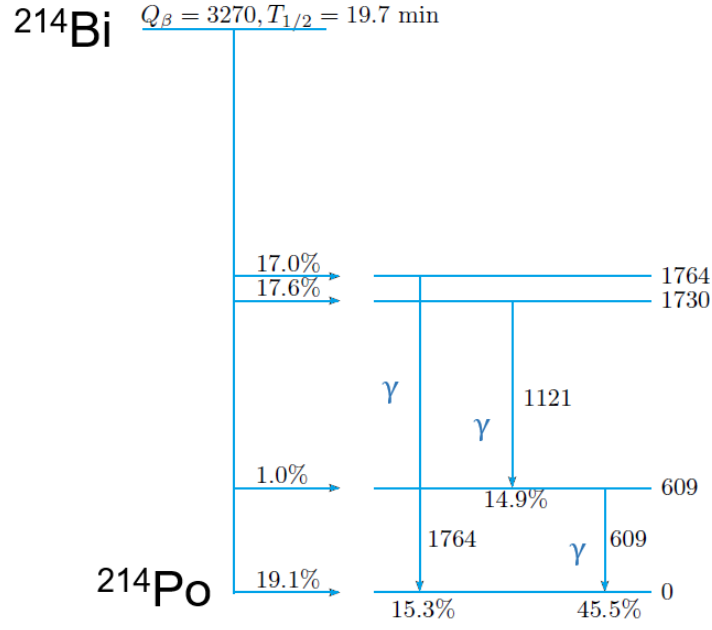
FIGURE 2.7: Decay scheme for the beta decay of ^{214}Bi showing the strongest gamma transitions (energies are in keV)

decay can proceed via an excited state which is accompanied by the emission of photons. Both beta decay and beta + gamma decay can mimic two electron events via mechanisms described in the next section.

TABLE 2.3: Isotopes with Q$_\beta$ value greater than 3 MeV

Isotope	Decay chain	Half-life [min]	Q$_\beta$ [MeV]
^{214}Bi	^{238}U	19.7	3.272
^{208}Tl	^{232}Th	3.05	5.001

Thanks to the unique tracking-calorimeter technique, SuperNEMO is able to identify and reconstruct different particles and obtain topological information. We distinguish background according to their origin, either internal or external to the source foil.

2.3.1 Internal Background

Internal background originates from radioactive contaminants inside the source foil. Inseparable background from the $0\nu\beta\beta$ signal is the tail of $2\nu\beta\beta$ decay distribution. Attenuation of the $2\nu\beta\beta$ background depends on the energy resolution of a calorimeter. A relatively slow $2\nu\beta\beta$ rate also helps to control this background.

Internal background events also come from beta decays of ^{214}Bi and ^{208}Tl, which are present in the source foil at some level. Mechanisms by which they can mimic the $0\nu\beta\beta$ signal are:

- Beta decay accompanied by an electron conversion

- Beta decay followed by Møller scattering of beta particles in the source foil
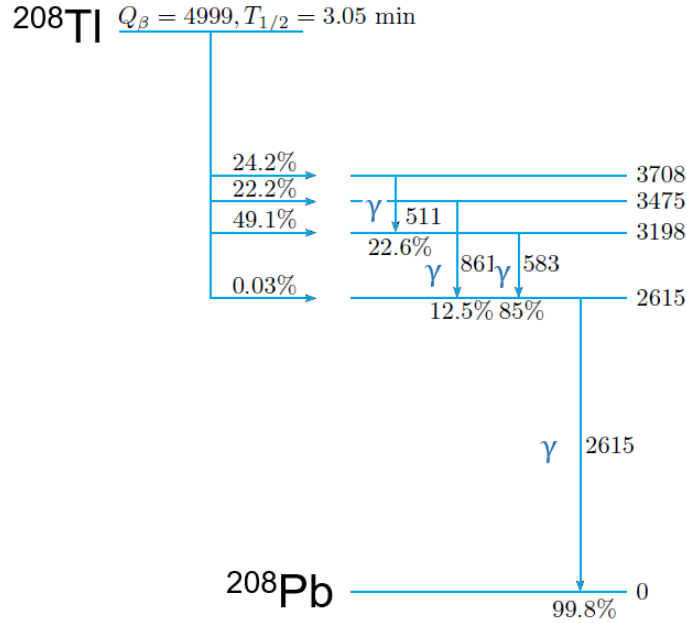
FIGURE 2.8: Decay scheme for the beta decay of ^{208}Tl showing the strongest gamma transitions (energies are in keV)

- Beta decay to an excited state, deexcitation by emitting a gamma ray followed by Compton scattering

2.3.2   External Background

External background originates from radioactive contaminants outside of the source foil, which interact with the detector. These events can be produced by crossing electrons or by gamma ray interactions (if an external γ ray is not detected by a scintillator) by:

- e^-e^+ pair creation - if the two photons from a subsequent positron annihilation remain undetected or the sign of the positron track curvature is incorrectly reconstructed

- Double Compton scattering

- Compton scattering followed by Møller scattering

Figure 2.9 depicts the scheme of these different mechanisms.

There is also a possibility of an external crossing electron background event when γ hits the first scintillator block from outside and then creates an electron by Compton scattering within the last few millimetres of the scintillator closest to the tracking detector. This Compton electron crosses the detector through the foil before hitting the second scintillator, depositing its entire energy (Fig. 2.10).

Another background contribution comes from the radon (^{222}Rn) contamination in the tracking chamber, namely from β-decay of ^{214}Bi in the immediate vicinity of the source foil (Fig. 2.11). Although the origin of these backgrounds is external, radon progenies can be deposited on the source foil surfaces, thus providing a continuous input of ^{214}Bi contamination.

Potential sources of these background contributions in underground laboratories will be discussed in detail in the following chapter.
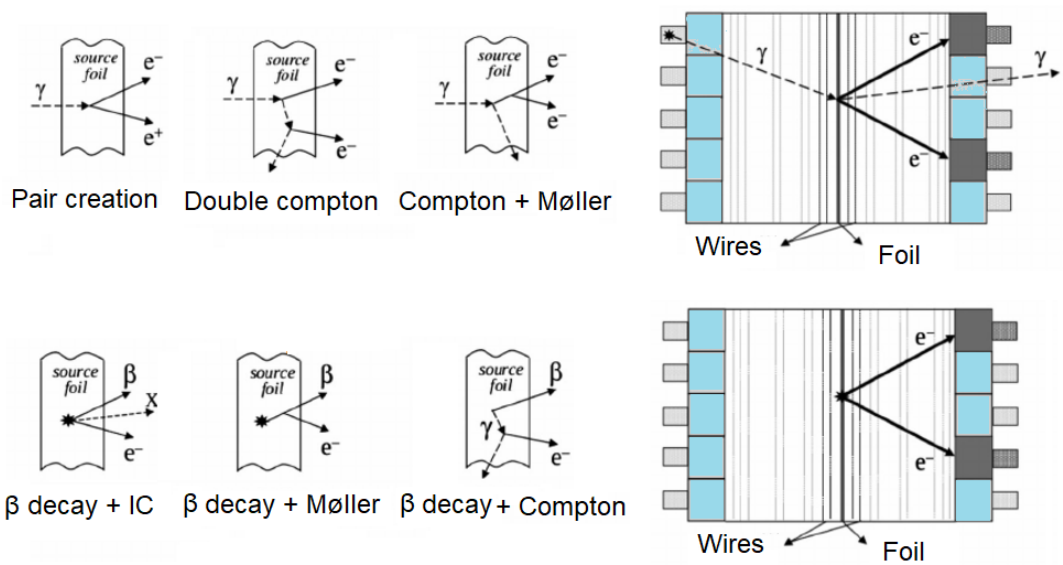
FIGURE 2.9: Mechanisms of internal (bottom) and external (top) background events production
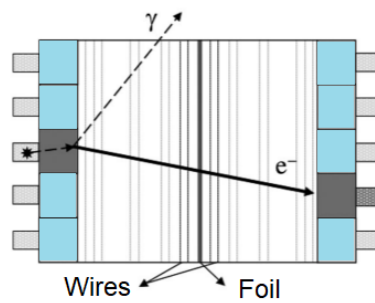
FIGURE 2.10: Crossing electron event
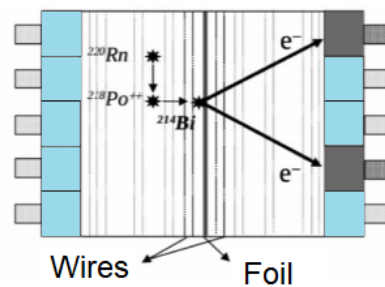
FIGURE 2.11: Radon background event from the radon contamination inside the tracking detector

2.3.3 Assessment of Background Sources of the SuperNEMO Demonstrator

The number of expected events for backgrounds after baseline cuts for 2.5 year exposure time of the Demonstrator was analysed by the collaboration from several sources. Dominant sources include the tail of the $2\nu\beta\beta$ signal, internal background from ^{208}Tl and ^{214}Bi contamination of source foil bulk, radon contamination of source foil surface and tracker wire bulk and surface, and external background from PMT contamination. The number of expected events in the ^{82}Se ROI, for all internal and external backgrounds currently investigated[2], are summarized in Table 2.4.

TABLE 2.4: Number of expected events after 2.5 years of exposure

Background source	Number of expected background events
$2\nu\beta\beta$	0.03 ± 0.02 (stat)
^{208}Tl internal	0.82 ± 0.02 (stat) ± 0.16 (syst)
^{214}Bi internal	1.41 ± 0.07 (stat) ± 0.01 (syst)
^{208}Tl external	0.60 ± 0.42 (stat) ± 0.06 (syst)
^{214}Bi external	0.10 ± 0.01 (stat) ± 0.01 (syst)

The background rate from $2\nu\beta\beta$ signal is reduced mainly due to its relatively long half-life.

^{214}Bi is a progeny of ^{222}Rn that can deposit on the source foils or on tracker cells close to the foil, where it decays to ^{214}Po via β-decay. To identify and reject events from ^{214}Bi, it is possible to use the short half-life of ^{214}Po, which decays via α-decay ($T_{1/2} = 164.3$ μs), to identify this type of bismuth-polonium (BiPo) event by searching for a prompt electron track from ^{214}Bi β-decay followed by a delayed alpha track originating from the same location from ^{214}Po α-decay (Fig. 2.11). And thus, in a $0\nu\beta\beta$ search, events, where there are any number of delayed Geiger hits close to the electron vertex, are removed.

Similarly, events where an electron is accompanied by gamma candidates, out of which at least one is of high energy, are rejected to remove ^{208}Tl background events (according to its decay scheme in Figure 2.8 there is almost always a 2.61 MeV gamma).

Time of flight (TOF) information plays an important role in establishing the origin of an event, as it is possible to tell whether an electron crosses the foil or whether there are two electrons that both originated within the foil. Crossing electron events from β-decays outside of the source foil (Fig. 2.10) or events where an external photon interacts in the calorimeter and the source foil (Fig. 2.9 (top)) are suppressed by TOF cuts. In the case of photon interaction via pair production in the foil, the outgoing positron and electron have different track curvatures in the magnetic field. However, at higher energies of β particles, the tracks are less curved and thus the curvature of positron might still be miss-reconstructed.

---

[2]Preliminary internal analysis of the collaboration

There are currently additional analysis techniques under investigation to further remove external and internal background events without a significant reduction in sensitivity to $0\nu\beta\beta$, such as BDT[3] or other machine learning techniques.

Other sources of external background are predominantly due to radioactive decays within the rock surrounding the laboratory, and neutron captures. Contributions of flux from the surrounding rock and from neutron captures are expected to be small compared to the radioactivity of components of the detector. If the gamma incident on the detector is ambient, in order for it to produce a background event, it must not be detected by a scintillator and furthermore, it must have high enough energy to produce background event in the energy ROI[4]. Then, if its interaction in the foil happens through e^-e^+ pair production, the sign of the positron track curvature must be incorrectly reconstructed. The estimation of this external background for the Demonstrator was missing for the latest design of the module and is investigated in this work, with a beforehand complete review of environmental background sources, fluxes and energy spectra in the LSM. Thus, these contributions are further investigated in this work to complete the external background model to include the flux incident on the detector.

---

[3]Boosted Decision Trees

[4]High energy gammas interact mainly via pair production and excess energy of the pair-producing gamma ray is given to the electron-positron pair as kinetic energy, therefore its energy should be at least 1.02 MeV + Q$_{\beta\beta}$ (2.99 MeV).

Chapter 3

Background Sources in Underground Experiments

The very first underground experiments date back to the 1960s when they were performed in deep mines. Scientists have come a long way since then building underground laboratories of different depths and sizes all across the world. Important characteristics of underground laboratories are: the laboratory depth, as the cosmic ray flux decreases with increasing depth; surface and heights of laboratory halls with thick enough layers of overburden rock; horizontal access to the laboratory is preferred over vertical access; geology of the site must be suitable for excavation of stable cavities; and funding and capital investment are another important factors, etc. The depth of underground laboratories is usually expressed in meter water equivalent (m w.e. or mwe). It is a standard measure of cosmic ray attenuation in underground laboratories making them easier to compare to each other in terms of how shielded they are from cosmic rays.

Deep underground laboratories shield sensitive detectors from cosmic radiation and this allows us to search for and to study the rarest phenomena and processes in nuclear and particle physics. The challenge towards greater sensitivities in underground experiments turns into a fight against background induced by radioactive contamination of surroundings. In order to design and build a system with the lowest possible background, there is a need for understanding individual sources of background and the estimation of each component.

Although each deep underground experiment has different physics goal, sensitivity and detection techniques, there are several common background components coming from the underground environment. In general, three main components are contributing to the detectors background:

- Cosmic rays

- Environmental radioactivity and radioactive contamination of materials

- Electric noise and disturbances

3.1   Cosmic Rays

There are primary and secondary cosmic rays. Primary cosmic rays originate somewhere in the universe (from supernovae or active galactic nuclei) and enter the Earth's atmosphere. More than 90% of them are individual protons, the rest are alpha particles, heavier nuclei of other elements and high energetic electrons. Secondary cosmic rays are produced in
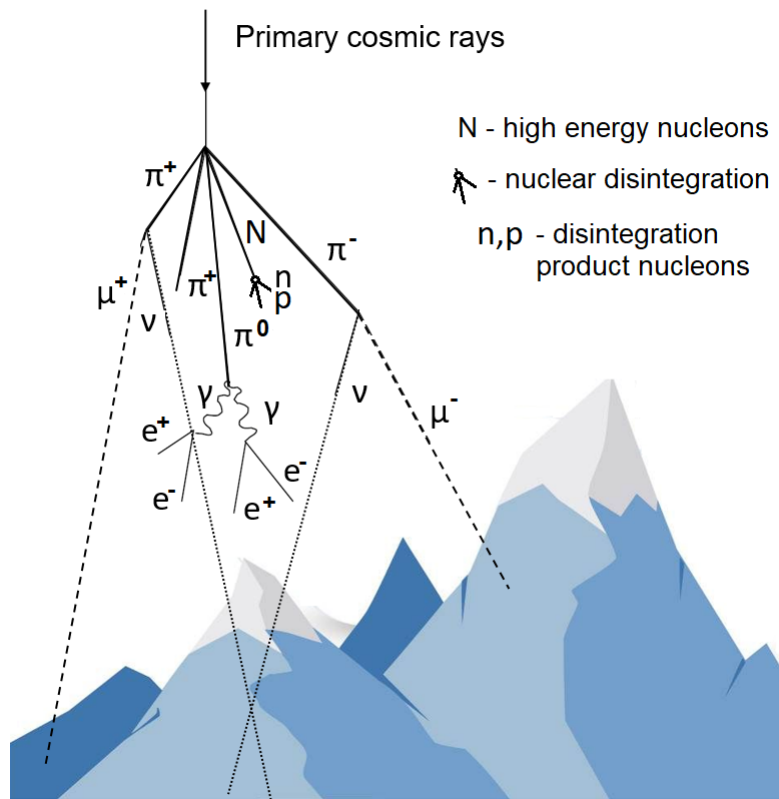
FIGURE 3.1: Cosmic ray shower in the atmosphere

interactions of primary cosmic rays with the atmosphere. The cascade of particles that this collision produces via electromagnetic and hadronic cascades is known as an air shower. Particles produced in such showers are protons, alpha particles, electrons and positrons, neutrons, muons, pions, photons and neutrinos. We can divide secondary cosmic ray particles into three categories:

- Soft component (electrons, positrons, γ-rays)

- Hard component (muons)

- Nucleonic component (hadrons)

The soft component originates from electromagnetic showers and consists of electrons, positrons and photons, and the hard component originates from hadronic showers and consists of muons. The penetration ability of the muon component is higher. At sea level, both components are observable, but only a small fraction of these particles can penetrate the rock overburden. Figure 3.1 shows a simple scheme of a cosmic ray shower in the atmosphere and its penetration underground.

In fact, by going underground, it is possible to shield most of the cosmic radiation, thus if detectors operate in deep underground laboratories, the cosmic ray component should be negligible [1, 46], as all components of cosmic ray induced background are substantially decreased by surrounding rock and only muons and neutrinos reach the underground laboratories. Once the majority of cosmic ray component has been reduced, these remaining cosmic background sources become dominant:

- Residual high energy muons produced in the decay of pions and kaons induced by interactions of high energy cosmic rays in the upper atmosphere

- Cosmogenic neutrons produced in cosmic ray muon reactions with rock nuclei and experimental setup components

Cosmic Ray Muons

High energy cosmic muons are able to penetrate deeply and can reach any underground location. Muons energy loss, as they travel through overburden rock and material, happens through ionization, pair production, bremsstrahlung, and photoproduction [46]. Through these interactions, muons can produce electromagnetic and hadronic showers accompanied by the production of high energy gammas and neutrons which can contribute to the overall background. Consequently, the residual muon intensity and angular distribution of high energy cosmic muons are key parameters in site selection and in evaluation of the sensitivity of underground experiments. Accurate measurements of muon energy spectra underground are very difficult to obtain and one has to often rely on simulations taking as an input the muon energy spectrum at surface [47].

Gaisser's parametrization of the muon flux at sea level can be used reliably for representing and describing the muon flux for ground experiments [48]:

$$\frac{dI_\mu}{dE_\mu} = 0.14 E_\mu^{-\gamma} \left(\frac{1}{1 + \frac{1.1 E_\mu cos\Theta}{\epsilon_\pi}} + \frac{0.054}{1 + \frac{1.1 E_\mu cos\Theta}{\epsilon_K}} \right), \tag{3.1}$$

where the differential flux is in units of $cm^{-2}s^{-1}sr^{-1}GeV^{-1}$, E_μ is the muon energy in GeV, γ is the spectral index, Θ is the zenith angle and ϵ_K=850 GeV, ϵ_π=115 GeV. Equation 3.1 is valid for flat Earth approximation - the curvature of Earth is neglected ($\Theta < 70°$). This parametrization is often coupled to a software package for transporting the surface muons through the rock overburden profile of the site to obtain muon flux or muon energy and angular spectra underground. Similarly, several models exist that fit the experimental data to a Depth-Intensity-Relation to obtain muon intensity and energy and angular distributions corresponding to the slant-depth of the laboratory. For example, prediction of muon flux from [49] has a form:

$$I_\mu(h_0) = 67.97 \times 10^{-6} e^{\frac{-h_0}{0.285}} + 2.071 \times 10^{-6} e^{\frac{-h_0}{0.698}}, \tag{3.2}$$

where h_0 is the vertical depth in km.w.e. and $I_\mu(h_0)$ is in units of $cm^{-2}s^{-1}$.

The muon energy spectrum discussed in [48] and [49] in a form of:

$$\frac{dN}{dE_\mu} = A e^{-0.4 h_0 (\gamma - 1)} (E_\mu + 693(1 - e^{-0.4 h_0}))^{-\gamma}, \tag{3.3}$$

where A is a normalization constant, can be used to approximate local muon energy spectra at different slant-depths. Figure 3.2 shows the total muon flux measured at various underground laboratories as a function of the equivalent vertical depth[1] with a fit to Eq. 3.2, and Figure 3.3 shows calculated local muon energy spectrum for various underground

---

[1]Data collected from available literature
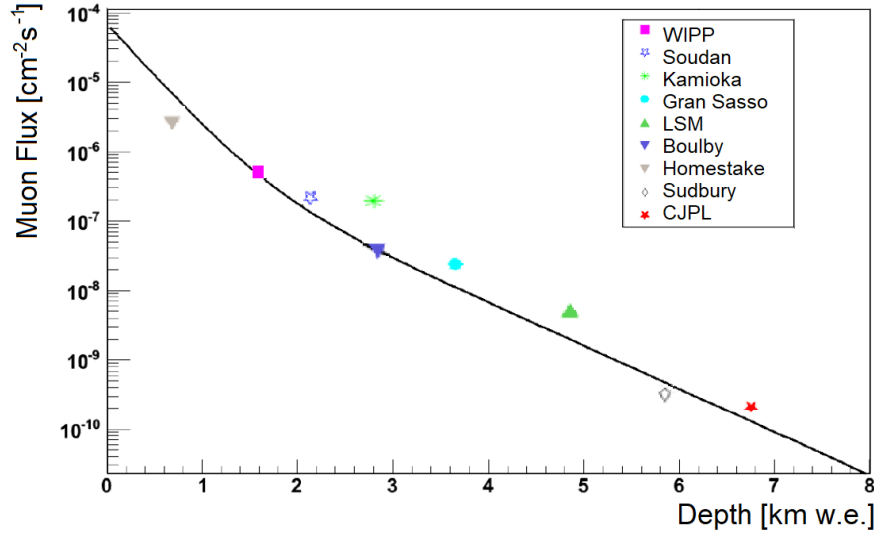
FIGURE 3.2: Total muon flux as a function of the equivalent vertical depth
for different underground sites [50]

laboratories. In Figure 3.2, a typical decrease of muon intensity with the depth of the underground laboratory can be seen. Although several other parametrizations exist, to have more detailed descriptions of the muon fluxes and their spectra, Monte Carlo simulations are often needed.

Incident muons by themselves, when interacting directly with a detector, do not contribute by a significant amount to the background of underground experiments. They are either vetoed or easily identified and distinguished. However, there are muon-induced background events, caused by spallation products created by high energy muons, dangerous to the background of low-energy experiments. Especially dangerous can be secondary neutrons produced in the detector itself or construction and surrounding materials, such as overburden rock, shielding, etc.

Cosmogenic Neutrons

Cosmogenic neutrons are produced by hadronic and electromagnetic interactions in matter, especially in high Z materials, by incident cosmic ray muons. Cosmogenic neutrons can be characterized by [51]:

- the neutron yield $Y_n(A, E_\mu)$ $[n\mu^{-1}(g/cm^2)^{-1}]$ that presents the ability of matter to produce neutrons under the effect of muons

- the production rate $R_n(h) = I_\mu(h) Y(E_{avg,\mu})$ $[ng^{-1}s^{-1}]$

- the neutron flux $\Phi_n = R_n(h) l_n \rho$ $[ncm^{-2}s^{-1}]$,

where $E_{avg,\mu}$ is the average muon energy at depth h, $I_\mu(h)$ is the itensity of muons , $l_n \rho$ is an attenuation length for neutron flux.

In deep underground laboratories, the yield Y_n is mainly the sum of these processes that contribute to the overall production: neutron yield from neutron production in hadronic showers, yield of photoneutrons from photo-nuclear reactions associated with electromagnetic showers, and muon interactions via virtual photon (muon spallation). Additionally,
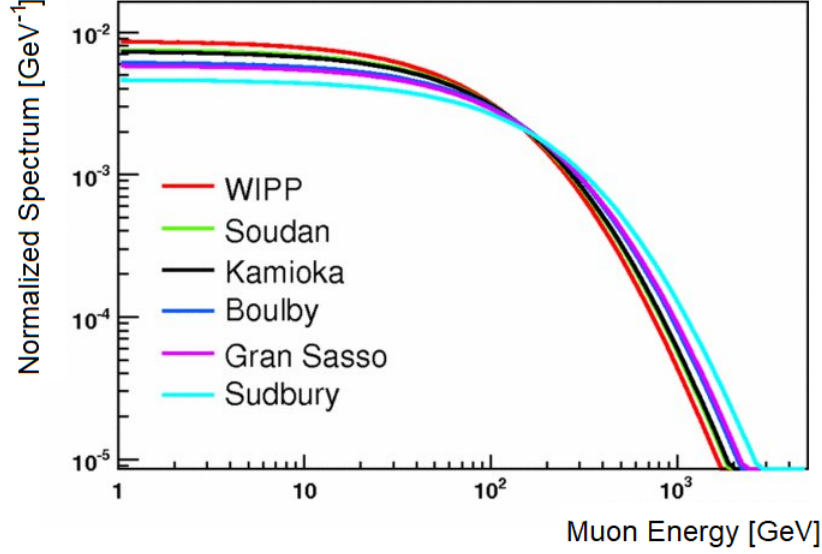
FIGURE 3.3: Local muon energy spectrum at various underground sites
normalized to the vertical muon intensity [49]

secondary neutron production may arise from neutrons produced in mentioned processes. The energy spectrum of these neutrons can extend up to several hundred MeVs or even GeVs.

Establishing the shape of the spectrum and the overall yield is, however, difficult. The calculations performed in recent years for various materials using software packages are often in disagreement and there is only a limited number of measurements with significant errors, which are not always consistent between each other or with calculations. The reason for this inconsistency lies in the difficulty of experimental measurements due to the low muon flux underground and the complexity of measuring neutron energies over a wide range.

Similarly to the situation of cosmic ray muons in underground laboratories, various parametrizations or Monte Carlo simulation tools are established and widely used for cosmogenic neutron yields calculations. For example, empirical universal formula obtained by fitting to experimental and calculated data but derived from the phenomenology of muon energy loss has a form of [51]:

$$Y_n^{UF} = 4.4 \times 10^{-7} E_\mu^{0.78} A^{0.98}, \tag{3.4}$$

where it can be seen that the neutron production rate increases with the average atomic weight A of the material and muon energy E_μ. This dependence can roughly be seen in Figure 3.4, where neutron yields from available data in literature in different targets (Al, Cd, Fe and Pb) at different averaged muon energies are plotted.

Often, only a scaling law for neutron yield versus the atomic mass A, $Y_n \propto A^{0.8}$ or $Y_n \propto (\frac{Z^2}{A})^{0.92}$, is used [47, 49].

Following convenient parameterizations of the neutron energy spectra based on fitting functions of simulated data are often used- the parameterization from Wang et al. [56]:

$$\frac{dN}{dE_n} = A\left(\frac{e^{-7E_n}}{E_n} + B(E_\mu)e^{-2E_n}\right), \tag{3.5}$$
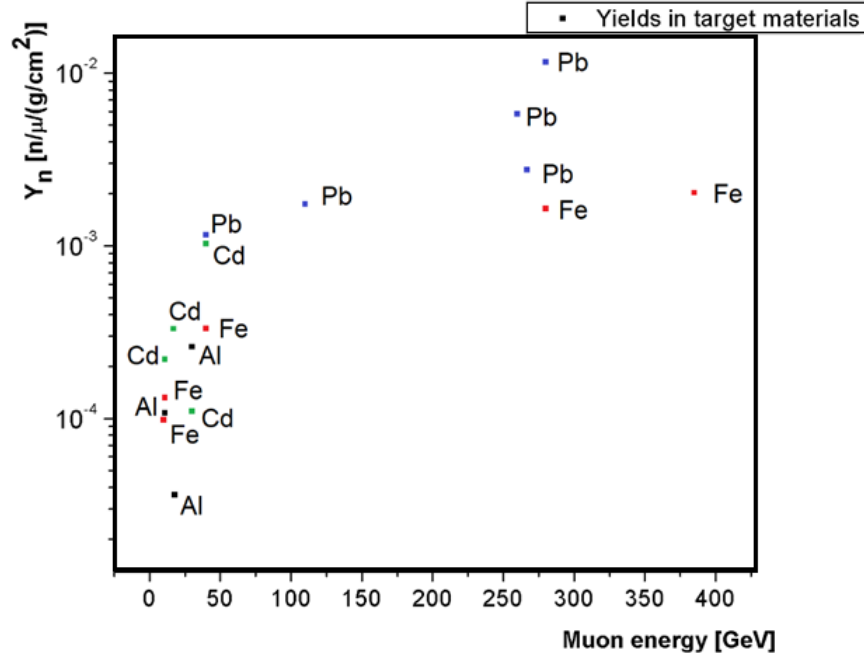
FIGURE 3.4: Dependence of cosmogenic neutron yield on the muon energy in target materials (data from [52, 53, 54, 55])

where A is a normalization factor and $B(E_\mu) = 0.52 - 0.58e^{-0.0099E_\mu}$, or the Mei-Hime parameterization [49]:

$$\frac{dN}{dE_n} = A(\frac{e^{-a_0 E_n}}{E_n} + B(E_\mu)e^{-a_1 E_n}) + a_2 E_n^{-a_3}, \qquad (3.6)$$

where a_i are fit parameters and $B(E_\mu) = 0.324 - 0.641e^{-0.014E_\mu}$.

Simulated differential energy spectra for muon-induced neutrons at various underground sites coming from the rock overburden with fitting functions from Equation 3.6 are shown in Figure 3.5.

Since high-A targets, such as lead or iron that are used for passive γ-ray shielding, have higher cosmogenic neutron yields, they behave like a neutron source under muon irradiation [47]. This means that a passive shield made of high Z material designed to suppress gamma radiation of environmental radionuclides turns itself into a source of background, especially for experiments observing recoiling nuclei since muon-induced neutrons have a very hard energy spectrum and can interact via elastic scattering.

Neutrinos

Neutrino interactions are an irreducible source of background since no detector can be shielded from the ambient flux of incident neutrinos. These include neutrinos produced in fusion reactions in the Sun, anti-neutrinos produced in radioactive decays in the earth's mantle and core, neutrinos and antineutrinos from general atmospheric phenomena, and neutrinos produced during the births, collisions, and deaths of stars, particularly the explosions of supernovas. Neutrinos interact only by the weak force and gravity, hence the reaction cross sections are much smaller than those of other particles. However, it has been
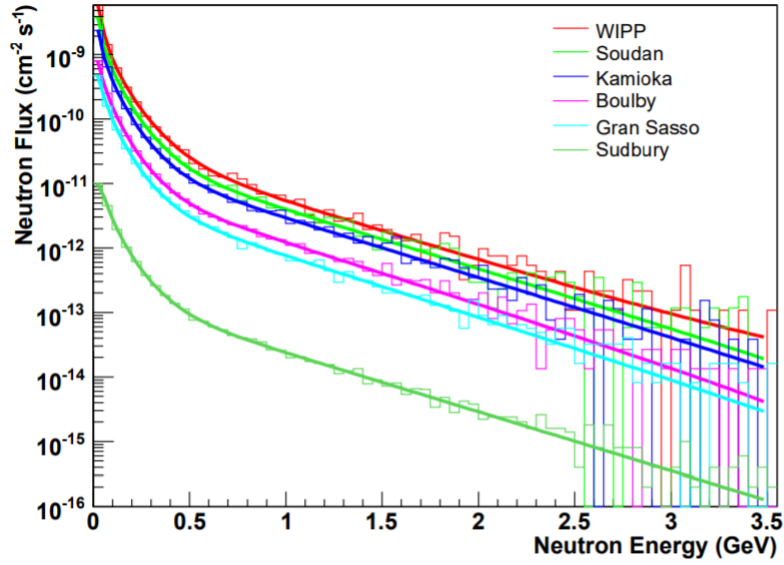
FIGURE 3.5: Muon-induced neutrons at the various underground sites [49]

pointed out that neutrino-nucleus coherent elastic scattering is a background to direct dark matter detection. Direct detection dark matter experiments search for $\chi N \to \chi N'$ scattering, a very rare signal process which is identified by observing recoiling nuclei N'. The $\nu N \to \nu N'$ cross section can be as large as 10^{-39} cm^2, producing nuclear recoils with kinetic energies up to tens of keV [57].

3.2 Environmental Radioactivity

Major contributions to the background come from primordial, cosmogenic and anthropogenic radionuclides present in the environment. Dominant sources are:

- Contributions from radioactive contamination and radioactive impurities of the detector and its surroundings (laboratory walls concrete, shielding, electronics, etc.)

- Radon contamination of the laboratory air

- Neutrons produced in fission processes of uranium and thorium, and in (α,n) reactions

The next section focuses on radionuclides and their decay products present in the underground environment. Radiogenic neutron background sources are discussed in detail in Chapter 4.

Primordial Radionuclides

Radioactivity is a natural and common process occurring everywhere in nature. Primordial radionuclides are those persisting in the Earth since the Earth was formed and which have not completely decayed due to their long decay half-lives ($\sim 10^9$ years or more). These nuclides occur in construction materials for a variety of reasons: the material itself may be made out of an element that has one of the very long-lived isotopes, materials could have been contaminated while in the ground or during the manufacturing or transport process.

Radioactive contamination of construction materials and surroundings is mostly represented by decay products in the ^{238}U, ^{235}U and ^{232}Th decay chains, and by primordial ^{40}K [1, 46]. Figure 3.6 shows decay series of ^{238}U, ^{235}U and ^{232}Th. Beta and alpha decays and de-excitations of these radionuclides and their daughter products produce high energy photons, electrons or alpha particles that constitute serious backgrounds for almost all experiments.
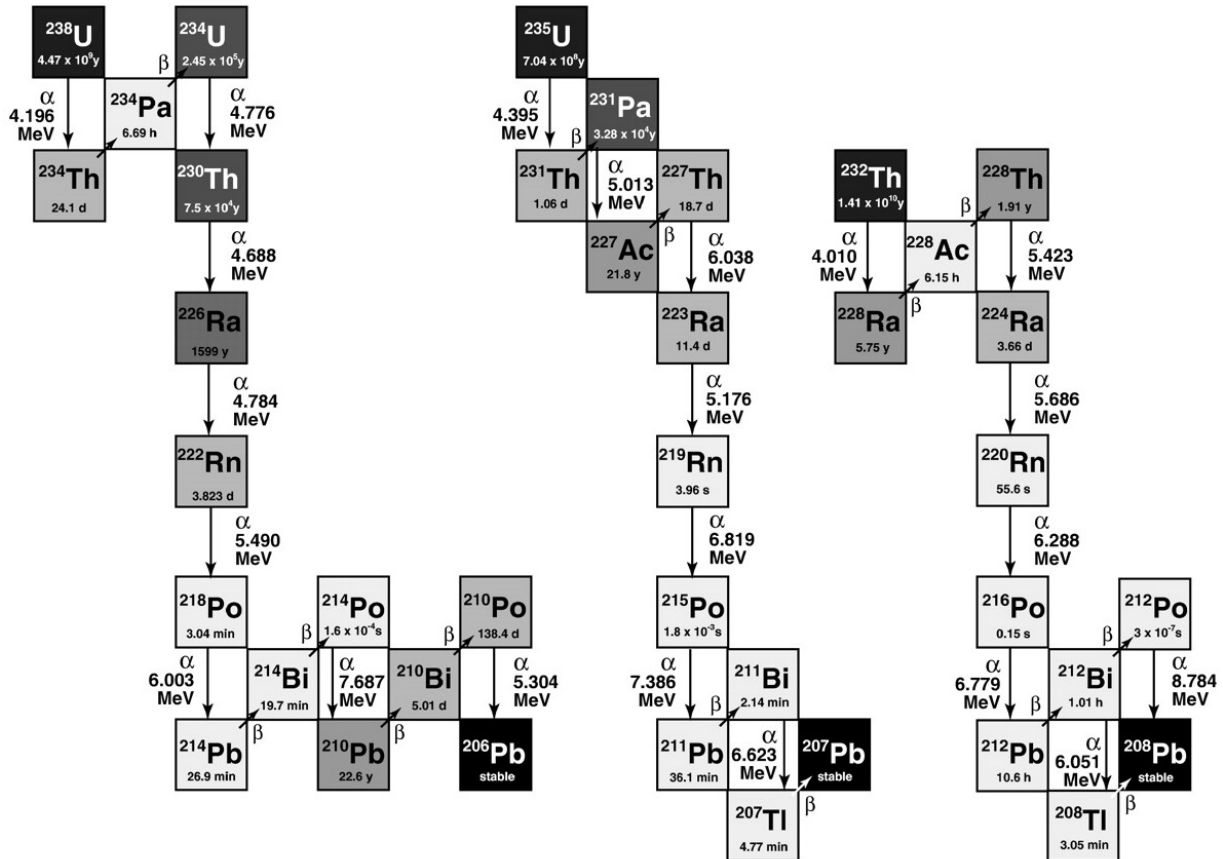
FIGURE 3.6: Decay chains of ^{238}U, ^{235}U and ^{232}Th

A naturally occurring radioactive isotope ^{40}K is another major source of the background gamma radiation. ^{40}K has a very long half-life of 1.3×10^9 years comparable to that of uranium and thorium. The decay scheme of this isotope is, however, far less complex, approximately 89% of the time it undergoes beta decay to stable ^{40}Ca, but about 10.7% of the time it decays to ^{40}Ar* by electron capture, with the subsequent emission of a 1.46 MeV gamma ray. A simple decay scheme of ^{40}K is shown in Figure 3.7.

Anthropogenic Radionuclides

Significant quantities of several radionuclides have been added to natural reservoirs due to human activities. Major anthropogenic sources that have contributed to the radionuclide contamination are: nuclear weapon testing (mainly in 1950s and 1960s), operation of nuclear power plants, mining of uranium, fuel reprocessing, nuclear waste repositories and nuclear accidents. ^{14}C and ^{3}H are two important radionuclides produced by both nuclear explosions and cosmic radiations. For their abundance, toxicity and mobility, ^{3}H, ^{14}C, ^{85}Kr, ^{90}Sr ^{137}Cs, ^{99}Tc, ^{129}I, ^{241}Am, as well as several uranium and plutonium
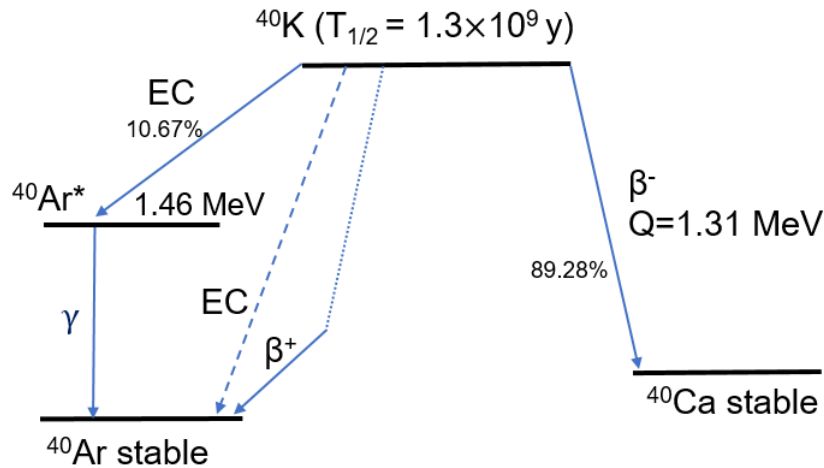
FIGURE 3.7: Decay scheme of ^{40}K

isotopes are of particular importance and interest. After the Chernobyl accident, almost all exposed surfaces became contaminated. It is therefore essential to screen all materials from regions where they could have been contaminated before using them in low-background experiments.

Cosmogenic Radionuclides

Cosmic ray particles contribute to the background also indirectly through the production of cosmogenic radionuclides. As primary and secondary particles of cosmic rays pass through the atmosphere and Earth's crust, they initiate nuclear reactions with various atoms of the atmosphere and surface rocks. The production rate of cosmogenic radionuclides strongly depends on energy-dependent cross sections and on the intensity of cosmic ray flux. For atmospheric production, the spallation reactions caused by high energy particles on O, Ar or N nuclei are one of the most significant processes. The main cosmogenic nuclides that are produced by cosmic rays in the atmosphere along with their half-lives and production reactions are listed in Table 3.1. Since protons are absorbed by the atmosphere, mainly neutrons and muons induce production in the lithosphere. Cosmic rays can also activate materials later used in detector construction. During transport in air, storage or manufacture, the activation by the hadronic component can reach higher radioactivity levels than the residual contamination from primordial nuclides [58].

In addition to purification techniques, activation can be avoided or kept under control by minimizing exposure and storing materials underground, avoiding flight transport of materials, and using shielding against cosmic rays during surface detector building and even during operation [58]. In low background experiments, even the short-living radionuclides are contributing to the background. A lot of studies have been dedicated to studying the production rates of cosmogenic nuclides in experiments, such as ^{49}V, ^{54}Mn, ^{55}Fe, ^{57}Co, ^{58}Co, ^{60}Co, ^{65}Zn, ^{68}Ge in germanium detectors; ^{32}Si in silicon medium in cryogenic detectors; several iodine, tellurium and sodium isotopes induced in NaI(Tl) crystals; xenon isotopes in xenon-based detectors; argon isotopes in liquid argon; cobalt isotopes in copper and stainless steel; lighter radionuclides (He, Li, B, Be, N, C) in organic scintillators and more [46, 58]. Table 3.2 summarizes some of these cosmogenic radionuclides commonly produced

TABLE 3.1: Cosmogenic radionuclides, their production rates in the atmosphere [59], and their decay modes of highest branching ratios [60]

Nuclide	Target	Reaction	Half-life	Production rate [atoms cm^{-2}s^{-1}]	Decay mode	Released energy [keV]
^{3}H	O,N	Spallation	12.34 y	0.28	β^-	E$_\beta$ = 18.59 (endpoint)
^{14}C	N	^{14}N(n, p)^{14}C	5730 y	2.02	β^-	E$_\beta$ = 156.48 (endpoint)
^{7}Be	O,N	Spallation	53.4 d	0.035	EC	E$_\gamma$ = 477.60
^{10}Be	O,N	Spallation	1.5×10^6 y	0.018	β^-	E$_\beta$ = 555.80 (endpoint)
^{26}Al	Ar	Spallation	7.17×10^5 y	1.4×10^4	EC$^+$,β^+	E$_\beta$ = 1173.42 (endpoint), E$_\gamma$ = 1808.65
^{36}Cl	Ar	Spallation	301 000 y	0.0019	β^-	E$_\beta$ = 708.60 (endpoint)
^{32}Si	Ar	Spallation	150 y	1.6×10^4	β^-	E$_\beta$ = 224.50 (endpoint)
^{22}Na	Ar	Spallation	2.6 y	5.4×10^5	EC$^+$,β^+	E$_\gamma$ = 1274.53

in an experimental setup of detectors, and their decay modes and released energies of the highest branching ratios.

Radon Contamination

Radon and its radioactive decay products form by far the strongest source of airborne radioactivity in many low-background experiments, as all radon isotopes are, under standard conditions, gaseous. Three naturally occurring isotopes of radon are created by the decay of radium isotopes that are a part of primordial decay chains (^{235}U, ^{238}U and ^{232}Th, see Figure 3.6). They are ^{219}Rn, ^{220}Rn and ^{222}Rn with half-lives of 3.96 *s*, 55.6 *s* and 3.82 *d* respectively. All of these isotopes emanate naturally from the ground and building materials wherever traces of uranium and thorium can be found. ^{219}Rn with its short half-life and low abundance of ^{235}U is negligible in most low-background experiments. Usually, the beta decaying isotopes within the decay chains of radon isotopes are crucial contributors to the background.

3.3   Background Sources in the Modane Underground Laboratory (LSM)

The next section describes and summarizes ambient background sources in the Modane underground laboratory that are present in underground environment and are common and unavoidable to all experiments operating here.

It is important to note and to remember, that following summarized fluxes, rates and yields of ambient radiation from available measurements are highly dependent on the materials placed near the detectors that measure them and contamination of the detectors themselves. Therefore, they do not represent ideal unaffected ambient fluxes. Such a bias is unfortunately unavoidable and should be considered when using these values for further studies of backgrounds of experiments.

TABLE 3.2: Cosmogenic radionuclides produced in experimental setup and their decay modes of highest branching ratios [60]

Nuclide	Half-life	Decay mode	Released energy [keV]
^{6}He	806.7 ms	β^-	$E_\beta = 3507.80$ (endpoint)
^{8}He	119.0 ms	β^-	$E_\beta = 9671.2$ (endpoint), $E_\gamma = 980.70$
^{8}Li	838 ms	β^-, $\beta^- 2\alpha$	$E_\beta = 12\,964.50$ (endpoint)
^{9}Li	178.3 ms	β^-	$E_\beta = 13\,606.30$ (endpoint)
^{8}B	770 ms	EC$^+$,β^+	$E_\beta = 17\,979.30$ (endpoint)
^{12}B	20.20 ms	β^-	$E_\beta = 13\,368.90$ (endpoint)
^{11}Be	13.81 s	β^-	$E_\beta = 11\,506.00$ (endpoint)
^{9}C	126.5 ms	EC$^+$,β^+	$E_\beta = 16\,497.90$ (endpoint)
^{10}C	19.255 s	EC$^+$,β^+	$E_\beta = 2929.46$ (endpoint), $E_\gamma = 718.30$
^{11}C	20.39 m	EC$^+$,β^+	$E_\beta = 1982.50$ (endpoint)
^{12}N	11.0 ms	EC$^+$,β^+	$E_\beta = 17\,338.10$ (endpoint)
^{32}Si	150 y	β^-	$E_\beta = 224.50$ (endpoint)
^{54}Mn	312.3 d	EC$^+$,β^+	$E_\beta = 542.24$ (endpoint), $E_\gamma = 834.85$
^{57}Co	271.79 d	EC	$E_\gamma = 122.06$, $E_\gamma = 136.47$
^{60}Co	5.27 y	β^-	$E_\beta = 318.13$ (endpoint), $E_\gamma = 1173.24$, $E_\gamma = 1332.50$
^{65}Zn	244.26 d	EC$^+$,β^+	$E_\beta = 1351.90$ (endpoint), $E_\gamma = 1115.55$
^{68}Ge + ^{68}Ga	270.8 d + 67.63 m	EC + EC$^+$,β^+	$E_\gamma = 1077.35$

3.3.1 LSM
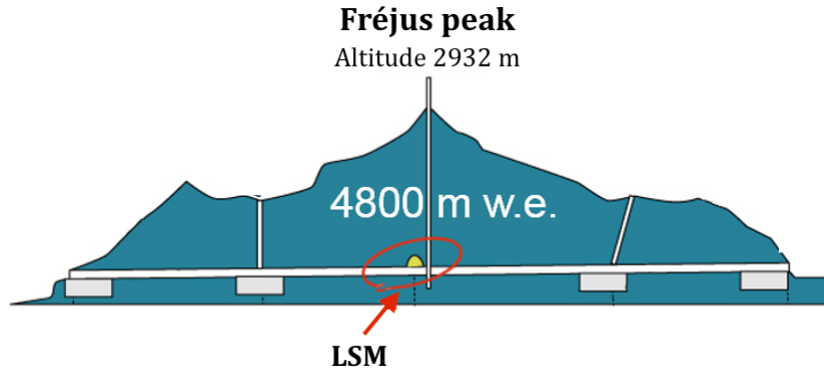
FIGURE 3.8: Location of the Modane underground laboratory

The Modane underground laboratory (Laboratoire Souterrain de Modane, LSM) is located in the middle of the 13 km long Fréjus road tunnel, under the Savoie Alps in France. The tunnel is connecting Modane in France to Bardonecchia in Italy. It sits below the Fréjus Peak with a rock overburden of approximately 1700 m, which corresponds to 4800 m w.e., and is currently the deepest underground laboratory in Europe. It has been in operation since 1982 and it serves as an interdisciplinary platform for several experiments in nuclear and particle physics, astrophysics and environmental physics.

The geological composition of rock surrounding the LSM is generally considered to be homogenous and uniform. The rock is constituted of metamorphic rocks called glossy schists [61, 62], which are characterized by having plenty of mineral constituents. In the past, LSM rock and concrete samples have been collected and analyzed by spectrometry methods to determine the chemical composition and the content of major compounds in % by weight is summarized in Table 3.3.

TABLE 3.3: Major compound composition of LSM rock and concrete (in %)
[61]

Compound	LSM rock	LSM concrete
SiO_2	14.9	5.8
Al_2O_3	5.0	1.1
FeO_3	2.8	0.74
MnO	0.038	0.008
MgO	1.4	1.3
CaO	42.8	51.5
TiO_2	0.12	0.17
K_2O	0.25	0.02
Na_2O	0.6	0.02
P_2O_5	0.15	0.15

The uranium and thorium content of rocks and walls, that contribute to overall low-radioactivity of laboratory environment, has also been measured in [61] and [62] and the results are summarized in Table 3.4.

TABLE 3.4: LSM rock and concrete activity

	^{238}U				^{232}Th				^{40}K	
	from [61]		from [62]		from [61]		from [62]		from [61]	from [62]
	[ppm]	[Bq/kg]	[ppm]	[Bq/kg]	[ppm]	[Bq/kg]	[ppm]	[Bq/kg]	[Bq/kg]	[Bq/kg]
Rock	0.84	10.4*	0.95	11.8	2.45	9.9*	2.48	10.2	213	182
Concrete	1.9	23.5*	1.83	22.8	1.4	5.7*	1.63	6.7	77	91

*calculated using conversion factors

3.3.2   Muon Flux in LSM

The local muon flux at LSM is related to the muon flux at sea level and muon energy before and after it transverses the LSM rock overburden. LSM muon flux measured by the Fréjus collaboration [63] was:

$$\Phi_{LSM} = (5.47 \pm 0.10) \times 10^{-5} m^{-2} s^{-1} \tag{3.7}$$

meaning that the LSM overburden attenuates the muon flux down to approximately 5 μ m^{-2} d^{-1}, and the mean energy of LSM muons was determined as [64]:

$$\langle E_{\mu,LSM} \rangle = (255.0 \pm 4.5) GeV \tag{3.8}$$

3.3.3   Gamma Background in LSM

To overall gamma background contributes mainly radioactive contamination of laboratory environment and detector surroundings, that is mostly represented by decay products in the ^{238}U, ^{235}U and ^{232}Th decay series, and by primordial ^{40}K. Other sources of high energy gamma rays include gammas from neutron captures in materials surrounding the detectors (e.g. 2.223 MeV γ from neutron capture on H and higher energies from neutron captures on metals) or even muon bremsstrahlung from weak residual muon flux in the laboratory.

Ambient gamma ray fluxes in the LSM have been studied and measured in work [62] at two locations by a coaxial HPGe detector and in [65] using a large volume sodium iodide (NaI) scintillator. Results of both investigations of gamma fluxes from peaks of several radionuclides and ambient high energy fluxes in 5 energy intervals from 4 - 10 MeV are presented in Table 3.5.

3.3.4   Radon Background in LSM

The measured values of radon (^{222}Rn) activity in LSM air are between 5-20 Bq/m^3 [66] and the mean value of thoron (^{220}Rn) activity measured in the LSM cavity is 10 Bq/m^3 [67]. This radon level is kept thanks to a ventilation system that is renewing the entire laboratory air. Experiments often require advanced systems that can reduce radon concentration at least by a factor of 1000 due to short-lived radon decay products and their deposition on surfaces and subsequent irradiation of sensitive volumes by alpha particles [68]. Moreover, radon is a noble gas with high penetrating power and can diffuse into materials. Therefore, further reduction of the radon level to just a few mBq/m^3 in experiments is often achieved by a radon trapping facility.

TABLE 3.5: Gamma ray fluxes measured in LSM

γ energy [MeV]	γ-ray flux [γcm^{-2}s^{-1}]
0.352 (^{214}Pb)	6.04 $\times 10^{-3}$ *
	2.10 $\times 10^{-3}$ *
0.609 (^{214}Bi)	5.26 $\times 10^{-3}$ *
	1.78 $\times 10^{-3}$ *
0.911 (^{228}Ac)	1.31 $\times 10^{-3}$ *
	6.10 $\times 10^{-4}$ *
1.46 (^{40}K)	1.00 $\times 10^{-1}$ #
	3.55 $\times 10^{-3}$ *
	2.40 $\times 10^{-3}$ *
2.204 (^{214}Bi)	4.53 $\times 10^{-4}$ *
	2.02 $\times 10^{-4}$ *
2.61 (^{208}Tl)	4.00 $\times 10^{-2}$ #
	1.00 $\times 10^{-3}$ *
	4.78 $\times 10^{-4}$ *
4-6	3.8 $\times 10^{-6}$ #
6-7	1.5 $\times 10^{-6}$ #
7-8	1.6 $\times 10^{-6}$ #
8-9	0.07 $\times 10^{-6}$ #
9-10	0.05 $\times 10^{-6}$ #

* from [62] - fluxes at 2 different locations

from [65]- given measurement errors $\sim$30%

3.3.5 Neutron Background in LSM

In general, we can divide the ambient neutron flux into thermal and fast neutron fluxes. The fast ambient neutron flux in the LSM originates mainly from the radioactivity of the rock and walls - from spontaneous fission and neutrons induced by (α,n) reactions, or from muon induced reactions. Subsequently, these neutrons transverse the rock overburden and materials present in the laboratory where they get moderated and they thermalize. In the past, many studies have been dedicated to estimating the LSM neutron flux and the next section summarizes the results of two publications ([61, 69]), where calculations and measurements of neutron fluxes and neutron energy spectra were provided.

In [69], to monitor the ambient thermal neutron flux at different locations at LSM, a setup of proportional counters filled with ^3He gas was installed. The thermal neutron flux at LSM may vary by up to a factor three from one location to another and near the experimental setup of NEMO-3 experiment (predecessor of SuperNEMO in the same location), the flux was measured to be:

$$\Phi_{n,thermal} = (2.9 \pm 0.4) \times 10^{-6} neutrons\ s^{-1} cm^{-2}, \qquad (3.9)$$

under the assumption that the neutron spectrum below 0.3 eV is Maxwell-Boltzmann distribution:

$$f_{MB} = \frac{E_n}{(kT)^2} e^{-\frac{E_n}{kT}}, \qquad (3.10)$$
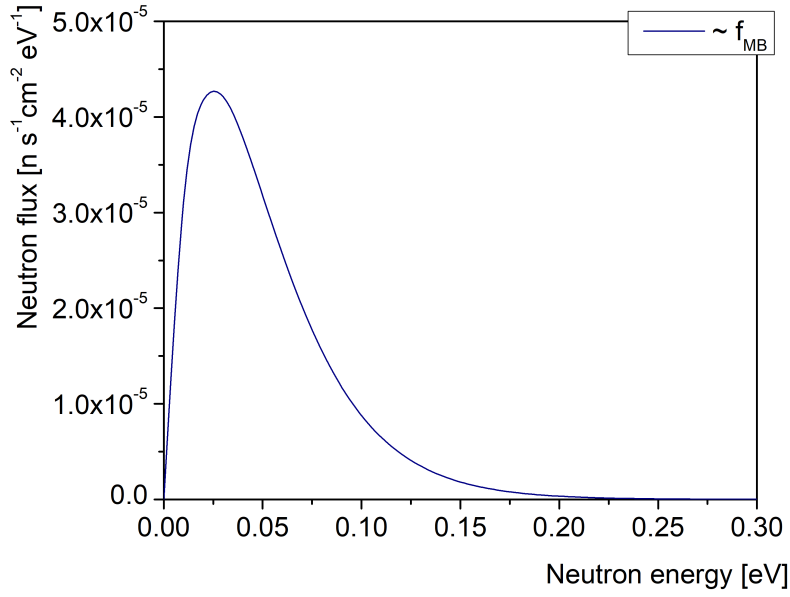
FIGURE 3.9: Thermal neutron spectrum in the LSM

where k is the Boltzmann constant and $T = 293K$, and that thermal neutron flux is fully isotropic (4π). Thermal neutron energy spectrum plotted according to this spectrum and normalized to flux in Equation 3.9 is shown in Figure 3.9.

Similarly, thermal neutron flux was measured in [61] where they obtained flux of $(1.6\pm0.1)\times10^{-6}$ n s^{-1}cm^{-2}.

In [61], results of measurement of fast LSM neutron flux using ^{6}Li loaded scintillator are reported as:

$$\Phi_{n,fast} = (4.0 \pm 1.0) \times 10^{-6} neutrons\ s^{-1}cm^{-2}, \qquad (3.11)$$

with energies between 2-6 MeV. A Monte Carlo simulation was also performed and compared to experimental result. The simulation was performed by propagating estimated neutron spectrum from spontaneous fission and (α,n) reactions from LSM rock's U and Th activity (Table 3.3) through rock. This way neutron spectrum with 1 MeV threshold corresponding to flux 1.0×10^{-6} n s^{-1}cm^{-2} was obtained which was in reasonable agreement with the experimental result. This spectrum is shown in Figure 3.10. It can be easily normalized to flux in Equation 3.11. This way a somewhat realistic fast neutron energy spectrum can be assessed.

Summary of neutron fluxes given in available literature is given in Table 3.6.
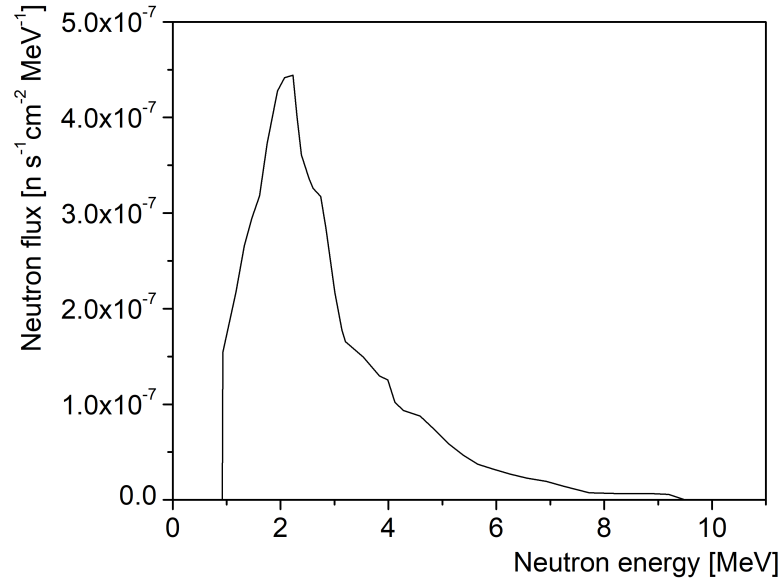
FIGURE 3.10: Fast neutron spectrum in the LSM above 1 MeV threshold [61]

TABLE 3.6: Summary of LSM neutron fluxes

Neutron flux $[\times 10^{-6} \text{ n s}^{-1}\text{cm}^{-2}]$	Neutron energy*	Technique	Reference
4.0 ± 1.0	fast, 2-6 MeV	Slowing down neutrons + $n_{th} +^6 Li \rightarrow \alpha +^3 H$ reaction	[61]
1.0	>1 MeV	MC simulation	[61]
1.6 ± 0.1	Thermal	^3He detectors, $n +^3 He \rightarrow T + p$ reaction	[61]
(2.0 ± 0.2)-(6.2 ± 0.6)	Thermal	^3He proportional counters	[69]

* as given in reference

Chapter 4

Neutron Background Sources

Neutrons from local radioactivity dominate the overall neutron production in underground laboratories. These neutrons are called radiogenic neutrons as they are produced in a process of radioactive decay. Dominant mechanisms are direct fission of uranium and thorium, and (α,n) reactions. The neutron energy spectrum and production rate from natural radioactivity depend on the specific concentrations of uranium and thorium present in the surrounding materials, and in the case of the (α,n) reactions also on the exact composition of the materials [70]. These neutrons dominate neutron scattering events in underground experiments, and the capture of thermal neutrons also leads to secondary radioactivity [70].

This chapter is dedicated to the calculation and simulations of radiogenic neutron production rates and their energy spectra, and to secondary radioactivity of neutron capture reactions.

4.1 Spontaneous Fission Neutrons
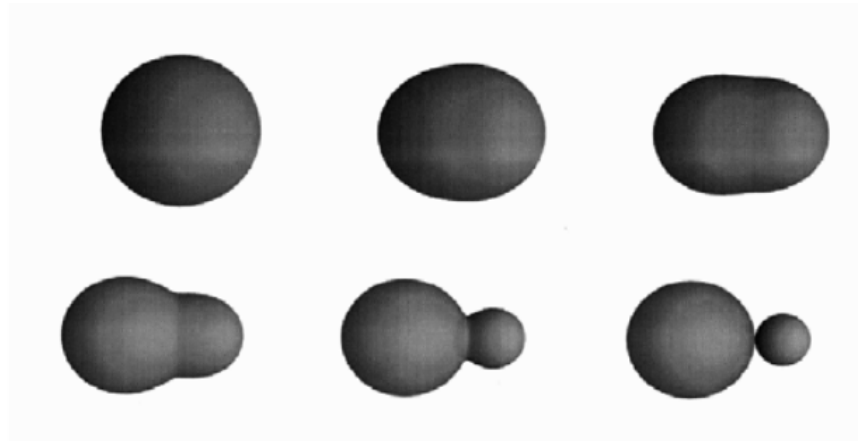
FIGURE 4.1: Liquid Drop Model of fission [71]

The process of fission was first interpreted by Meitner and Frisch in 1939 (the same year that it was discovered by Hahn and Strassmann), when they proposed that the uranium nuclei following neutron capture are highly unstable and they fission or split nearly in half [72]. In fact, the two fragments produced by a nucleus are governed by a statistical distribution and typically, both fragments will end up with different but relatively similar masses. When nuclear fission occurs without the nuclei having been previously hit by a neutron or other particle the process is called spontaneous fission. Fission fragments
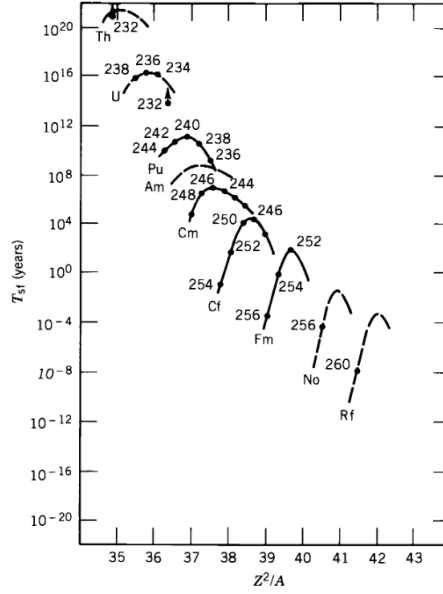
FIGURE 4.2: Half-lives for spontaneous fission [72]

are usually left with high excitation energy and they will frequently emit neutrons via evaporation processes to cool down.

The fission rate is a very sensitive function of atomic number Z and atomic mass A [73]. Mathematically, a parameter that serves as an indicator, whether a nucleus can fission spontaneously is [72]:

$$\frac{Z^2}{A} > 47 \tag{4.1}$$

This criterion is derived from the liquid drop model, but does not account for quantum mechanical barrier penetration and furthermore, the model is not very accurate for the heaviest nuclei. Nevertheless, the larger the value of Z^2/A, the shorter is the half-life for spontaneous fission (Fig. 4.2) [72].

In underground laboratories, the fission neutron flux is the result of spontaneous fission of naturally occurring primordial radionuclides ^{232}Th, ^{235}U and ^{238}U. The fission rate for thorium and uranium is, however, low compared to the rate of their decay by alpha particle emission, which dominates the total half-life (Table 4.1).

TABLE 4.1: Spontaneous fission (SF) parameters for ^{232}Th, ^{235}U and ^{238}U

	^{232}**Th**	^{235}**U**	^{238}**U**
$\mathbf{T}_{1/2}$ **[y]**^{a}	1.40×10^{10}	7.04×10^8	4.47×10^9
$\mathbf{T}_{1/2}$ **(SF) [y]**^{a}	1.20×10^{21}	9.80×10^{18}	8.20×10^{15}
Average multiplicity $\nu_k(SF)^b$	2.14	1.86	2.01
Branching ratio $BR_k(SF)$	1.17×10^{-11}	7.18×10^{-11}	5.45×10^{-7}
Neutron yield $R_k(SF)$ **[n/decay]**	2.50×10^{-11}	1.34×10^{-10}	1.09×10^{-6}
Watt parameter a [MeV]^c	0.796	0.7747	0.827
Watt parameter b [MeV^{-1}]^c	4.755	4.852	4.445

^{a} from [74], ^{b} from [75], ^{c} from [76] and [77]

4.1.1 Calculations of Neutron Yields and Energy Spectra from Spontaneous Fission

Let's assume that spontaneous fission of nuclide k is accompanied by the emission of a number of neutrons equal to the average neutron multiplicity $\nu_k(\text{SF})$. Given the spontaneous fission decay constant of nuclide k, $\lambda_k(SF)$, the fraction of nuclide k decays that are spontaneous fission events is given by the spontaneous fission branching ratio:

$$BR_k(SF) = \frac{\lambda_k(SF)}{\lambda_k} = \frac{T_{1/2}}{T_{1/2}(SF)} \tag{4.2}$$

and λ_k is the total decay constant of nuclide k and $T_{1/2}$, $T_{1/2}(SF)$ are corresponding half-lives. The neutron rate $R_k(\text{SF})$ or the average number of spontaneous fission neutrons emitted per decay of nuclide k is [78]:

$$R_k(SF) = BR_k(SF)\nu_k(SF) = \nu_k(SF)\frac{T_{1/2}}{T_{1/2}(SF)} \quad [\frac{n}{decay}] \tag{4.3}$$

This yield for individual isotopes is the same for all materials and depends only on the concentration of the fissioning isotope [79].

Many Monte Carlo neutron transport codes[1] randomly sample fission neutron energies, E, according to a Watt spectrum [76, 78, 82, 83], which is one of two (along with Maxwellian) most frequently used forms given in the literature to describe the experimental fission neutron energy distributions [84]. The Watt spectrum has a following form [85]:

$$N_W(E) = \frac{1}{\sqrt{T\pi E_f}}e^{-\frac{E_f}{T}}e^{-\frac{E}{T}}sinh(\frac{1}{T}\sqrt{EE_f}), \tag{4.4}$$

where E is the neutron energy, T is the thermodynamic temperature of the residual nucleus and E_f is the kinetic energy of the fission fragment.

The Watt spectrum used for calculation of the neutron spectra is, however, often defined using the given simplified analytical function [82]:

$$f_{Watt}(E) = Ce^{-E/a}sinh(\sqrt{bE}), \tag{4.5}$$

where E is the neutron exit energy [MeV], a, b are nuclide dependant Watt spectrum parameters[2], and normalization constant C is:

$$C = \frac{2e^{\frac{-ab}{4}}}{\sqrt{b\pi a^3}} \tag{4.6}$$

The parameters a and b are usually determined by fitting the Watt formula to the experimentally measured fission spectrum data and are available in literature for many radionuclides undergoing nuclear fission [83].

---

[1]Such as SOURCES-4A [78], MCNP [80] and NEDIS [76]. Additionally, fission spectra in the Evaluated Nuclear Data Library (ENDL) [81] are defined by Watt spectrum [75].

[2]In the case of induced fission, these parameters also depend on the energy of an incident neutron.

TABLE 4.2: Properties of gamma rays from spontaneous fission of ^{238}U [86]

Isotope	Total energy [MeV]	Average number of γs	Average γ energy [MeV]
^{238}U	6.06 ± 0.03	6.36 ± 0.47	0.95 ± 0.07

Thus, spontaneous fission neutron spectrum for nuclide k has the form of [78]:

$$\chi_{k,SF}(E) = R_k(SF)f_{Watt}(E) = R_k(SF)\frac{2e^{\frac{-ab}{4}}}{\sqrt{b\pi a^3}}e^{-E/a}sinh(\sqrt{bE}) \qquad (4.7)$$

Figure 4.3 shows calculated spontaneous fission neutron energy spectra for ^{232}Th, ^{235}U and ^{238}U according to Equation 4.7. The spontaneous fission rates and neutron yields of these isotopes are very low (Table 4.1), the highest contribution is mostly due to spontaneous fission of ^{238}U. Therefore, these processes contribute to neutron background only in materials with high contamination levels.

Spontaneous fission is also a source of γ-rays emitted by the excited fragments after the end of neutron evaporation [73]. When a nucleus undergoes fission and the excitation energy falls behind the neutron binding energy, prompt γ-rays take over and carry away the remaining energy and in principle, spontaneous fission events can thus be tagged in some detectors due to the simultaneous emission of several neutrons and γ-rays [73, 79]. There is a positive correlation between the number of neutrons produced in a spontaneous fission event and the total amount of energy carried away by γ-rays [86]. The P(n) distribution for fission neutron multiplicity can be well fitted by a Gaussian distribution [87, 88]. In [87], the P(n) distribution of neutron multiplicity of ^{238}U spontaneous fission was measured by using a large liquid scintillation neutron detector, the data are presented in Figure 4.4 (left) along with Gaussian fit with the mean value matching the average multiplicity for ^{238}U presented in Table 4.1.

An empirical formula relating the total prompt gamma ray energy to the mass (A) of fissioning isotope and the number of neutrons from fission ν is given in the form of [86]:

$$E_{\gamma,total}(\nu, Z, A) = (2.51 - 1.13 \times 10^{-5}Z^2\sqrt{A})\nu + 4, \qquad (4.8)$$

where the constant terms were obtained from experimental data.

Similarly, the average prompt gamma ray energy was found to obey [86]:

$$E_{\gamma,avg} = -1.08 + 106.9\sqrt[3]{Z}/A, \qquad (4.9)$$

where the constants were obtained from a fit to data. Then the average number of gamma rays produced in fission is approximated as $E_{\gamma,total}/E_{\gamma,avg}$. The total and average energy of gamma rays from the spontaneous fission of ^{238}U and the average number of γs produced are shown in Table 4.8. Figure 4.4 (right) shows the mean number of γ-rays produced in spontaneous fission of ^{238}U as a function of the neutron multiplicity.
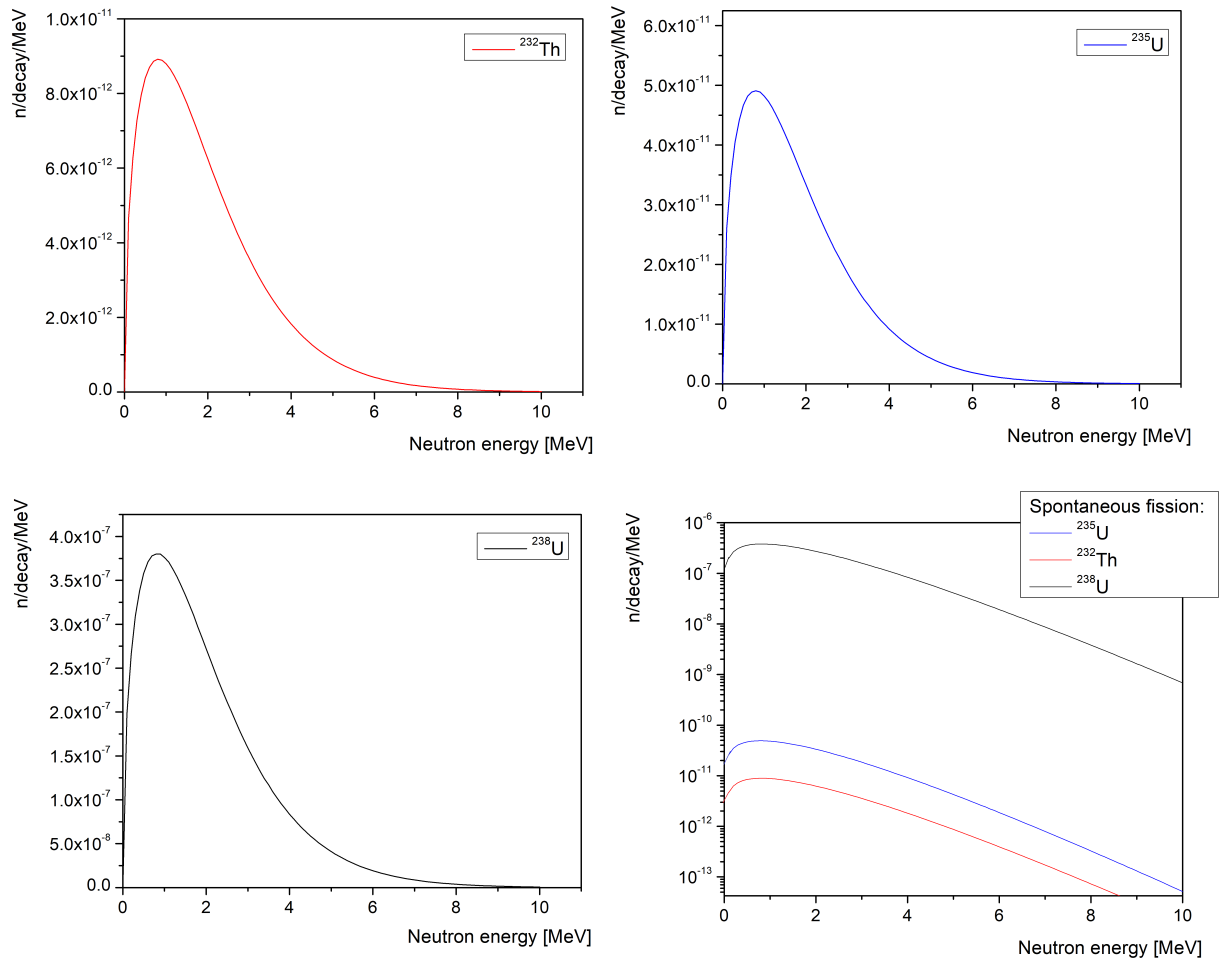
FIGURE 4.3: SF neutron energy spectra of ^{232}Th, ^{235}U and ^{238}U
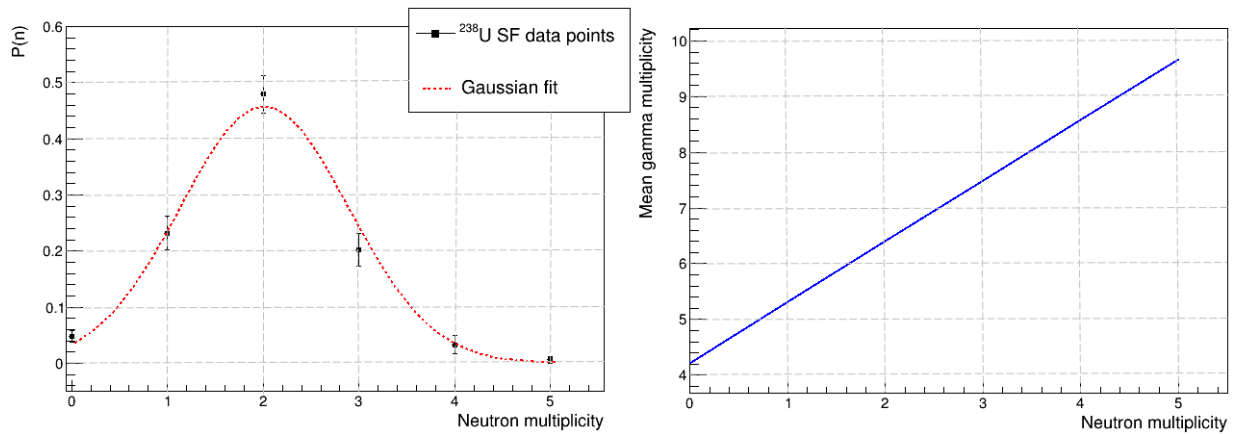
FIGURE 4.4: **Left**: Distribution of neutron multiplicity of spontaneous fission of ^{238}U (data points from [87]) with Gaussian fit with mean of 2.01 $\pm$ 0.06 and standard deviation of 0.99 $\pm$ 0.05. **Right**: The mean number of γ-rays produced in the spontaneous fission of ^{238}U as a function of the neutron multiplicity

4.2 Neutrons from (α,n) Reactions

$$\ _{Z}^{A}X +\ _{2}^{4}He \longrightarrow\ _{Z+2}^{A+3}Y +\ _{0}^{1}n$$
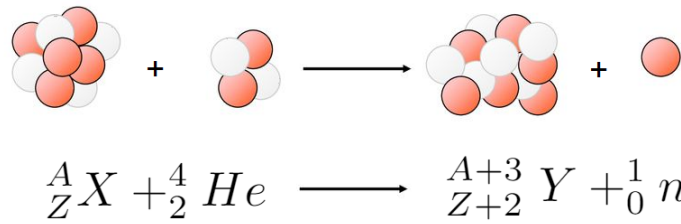
FIGURE 4.5: (α,n) reaction scheme

Many heavy nuclei, naturally occurring in the radioactive decay chains, decay through a nuclear disintegration process that emits alpha particles, called alpha decay. The α particle is a very stable and tightly bound structure of two protons and two neutrons (helium nucleus $_{2}^{4}He$), emission of which brings energetically unstable nuclei against α decay to a more stable configuration [72]. Alpha decay, like spontaneous fission, is a quantum tunnelling process that occurs despite the presence of the Coulomb potential repulsion barrier. However, the Coulomb barrier is often high enough to make alpha decay unlikely for all but the heaviest nuclei [72, 73]. These nuclei, if present in a material, can produce α particles with energies in order of MeVs that further interact with the nuclei in a thick target of light elements and yield neutrons through the (α,n) reactions. For heavier elements, the cross-section of (α,n) reaction is suppressed by the Coulomb barrier (thus, unlike the spontaneous fission, the neutron yield from (α,n) reaction is material dependant). In lower α particle energy ranges (< 10 MeV) the mechanism of the reaction can be described by the compound nucleus model when an intermediate state of a particle-target system is formed. The compound nucleus is excited by the kinetic energy of the α particle and is usually left in an unstable state and further decays to a daughter nucleus. This process is governed by the nuclear state of the compound nucleus (energy levels, spin, and parity of given excited state) and the structure of the daughter nucleus, and one of the possibilities of this decay is neutron emission. Higher energy α particle will excite the compound nucleus to a higher energy part of the nucleus's energy level and it may also undergo decay to the first excited state accompanied by the emission of γ-rays as well. At higher energies of α particles, it is possible for the compound nucleus to emit multiple neutrons. In underground environments and experiments, the ^{235}U, ^{238}U, ^{232}Th radioactive decay chains are responsible for neutron production, tough the contribution of ^{235}U is relatively small due to a small abundance [79]. α particle energies in these decay chains are low (< 9 MeV) making (α,Xn) reactions with emission of several neutrons processes very rare.

4.2.1 Example Case of ^{13}C(α,n)^{16}O

An example of common (α,n) reaction is a well known and studied ^{13}C(α,n)^{16}O reaction:

$$^{13}C + \alpha \rightarrow\ ^{17}O^* \rightarrow\ ^{16}O^{(*)} + n \tag{4.10}$$

where $^{17}O^*$ is the compound nucleus and ^{16}O is the residual nucleus. This reaction is of high importance for several reasons. Although the abundance of ^{13}C in natural carbon is
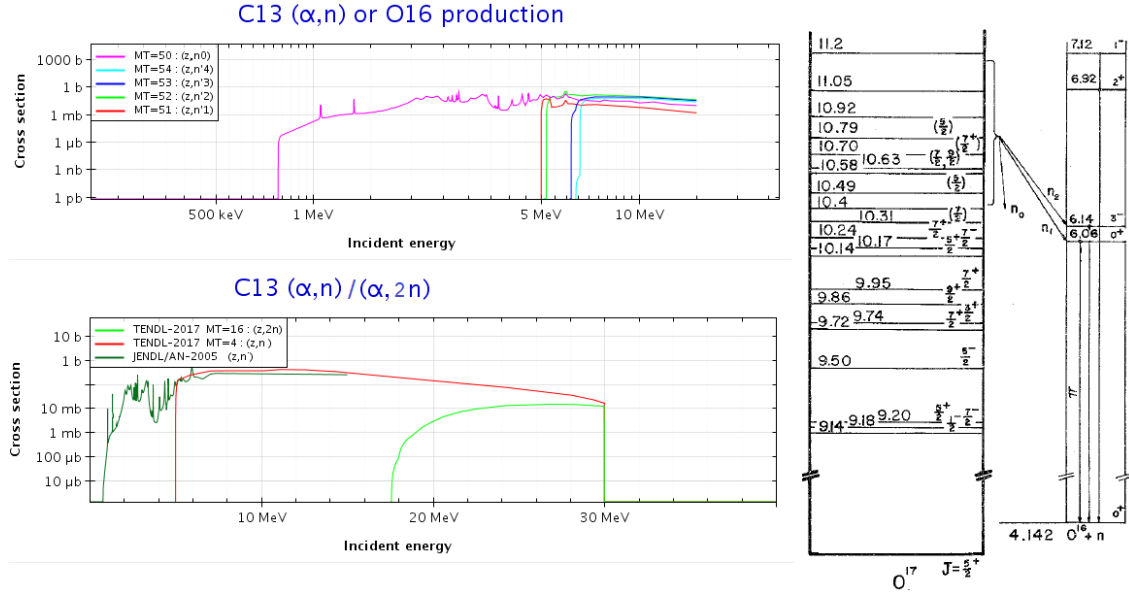
FIGURE 4.6: **Left**: cross-sections for $^{13}\text{C}(\alpha,\text{Xn})^{16}\text{O}$ reactions [92] (z - incident particle (α), (z,n) - production of one neutron in the exit channel, (z,2n) - production of two neutrons, (z,n0-4) - production of a neutron, leaving the residual nucleus in the ground state, 1st, 2nd, 3rd and 4th excited state). **Right**: Energy level diagram showing the states in ^{17}O and excited states of ^{16}O observed in $^{13}\text{C}(\alpha,\text{n})^{16}\text{O}$ [93]

relatively low (1.07 %), it has a significant (α,n) yield, and tends to produce a prominent peak in the neutron energy spectrum whenever carbon is present, thus contributing to the background of experiments. From the point of view of astronomy, it is also the most important neutron source for the main component of the s-process (slow neutron capture process), responsible for the production of most of the nuclei in the mass range 90<A<208 inside the helium-burning shell of asymptotic giant branch stars [89, 90]. Moreover, it has been used as a source of 6.1 MeV gamma-rays from the de-excitation of the second excited state of ^{16}O [91]. α energies needed for the production of one or two neutrons in the exit channel and for leaving the residual nucleus in the excited state can be seen from the reaction cross-sections in Figure 4.6 along with excited states of ^{16}O. This shows that only some neutrons are accompanied by a γ-ray, and most of these neutrons have a multiplicity of 1, making these neutrons harder to veto.

4.2.2   Calculations of Neutron Yields and Energy Spectra from (α,n) Reactions

Overall, the neutron yield of (α,n) reaction depends on the alpha activity of the alpha-emitting isotopes present in a given material, the cross-section of the reaction, the alpha energy loss in a given material (the stopping power of alpha particles), the alpha particle's energy (alpha decay energy spectra), the reaction Q values, and also on the degree of mixing (due to the short range of the alpha particle) [73, 78, 79, 94, 95].

(α,n) reaction neutrons are not monoenergetic due to many discrete α groups of decay,

the slowing down of α particles in any material[3] and the probability that residual nucleus is left in an excited state after the reaction [72].

Over a number of years, a lot of studies have been dedicated to modelling and calculation of the neutron emission processes, neutron yields from (α,n) reactions and their energy spectra and this topic has been discussed by many authors [76, 79, 94, 95, 96, 97, 98, 99] (and see also references therein). As a result, there are presently various codes dedicated and specifically developed for neutron yield and energy spectra calculations, such as SOURCES-4A (and updated version SOURCES-4C) [78], NeuCBOT (Neutron Calculator Based On TALYS) [100], the USD code (developed by the University of South Dakota in the USA) [95], NEDIS [76] or SaG4n (Geant4 [101] code with modifications included in the Geant4.10.6 version) [99]. Development of all above-mentioned codes has required accumulation and evaluation of not only measured experimental data, but also the calculation of reaction cross-sections, stopping powers of α particles, decay constants, energy spectra of the initial α particles, angular neutron distributions for the individual levels of the residual nucleus, etc [76, 102].

This shows that nuclear data work on (α,n) reactions constitutes a specific field of study but basic nuclear data and information on the source spectrum for sensitivity studies are sparse and highly discrepant [98, 102], which means that further improvements are desirable in all cases[4].

In general, a theoretical approximation of the neutron yield adopted by several authors and used in above-mentioned codes (except for the SaG4n code [99]) gives the following expression for the thick-target neutron production function [78, 95, 96, 98, 99]:

$$p_i = \frac{N_i}{N} \int_0^{E_\alpha} \frac{\sigma_i(E)}{\varepsilon(E)} dE, \tag{4.11}$$

where p_i is probability that the α particle with initial energy E_α will undergo an (α,n) reaction with element i in which it has the atomic stopping cross-section $\varepsilon(E)$. N_i is atom number density of target nuclide i, N is total atom number density and $\sigma_i(E)$ is the neutron production cross-section at an α particle energy E.

A decay chain consists of several α decays and we have to consider that a fraction of the decays of a radionuclide within the material is due to α emission. The neutron yields in the ^{232}Th and ^{238}U decay chains can be determined by the sum of the yields induced by each α particle in given decay chain [95], weighted by the intensity $F_{i'}$ which is a fraction of the decays of a radionuclide i' within the material due to α emission [78, 98]. This fraction can occur with the emission of one of N' possible discrete α-energies of intensity $f_{i'}(E_{\alpha,j})$ $(j = 1, ..., N')$ [98], and thus, the fraction of decays resulting in (α,n) neutron yield in a thick target material containing k target elemental constituents is [78, 98]:

$$R_{i'}(\alpha, n) = F_{i'} \sum_{i=1}^{k} p_i = \sum_{j=1}^{N'} f_{i'}(E_{\alpha,j}) \sum_{i=1}^{k} p_i \tag{4.12}$$

---

[3]The energy of emitted neutron depends on the energy that the α particle has at the moment of collision and the Q value of the reaction [73].

[4]Such as independent comparisons, data validation, measurements and benchmarks, proper modelling of resonance behaviour which has been experimentally observed, etc.
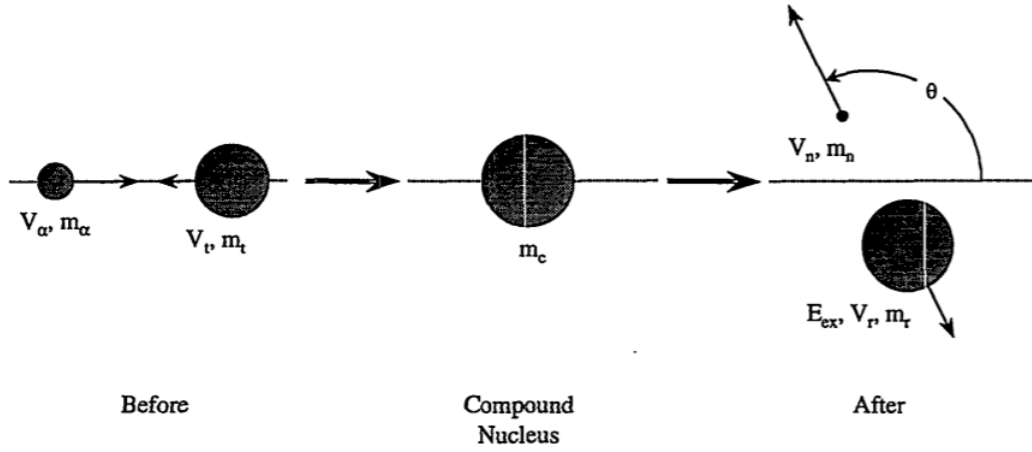
FIGURE 4.7: Center of mass system for (α,n) reaction [78]

In the theory of the neutron energy spectra the assumption of an isotropic neutron angular distribution in the center-of-mass system (CMS) (see Fig.4.7) is often made [98, 99, 103]. The neutron energy distribution for the target nuclide i is then given as [98]:

$$\frac{dQ_i}{dE_n} = \int_{X_{En}}^{Y_{En}} \frac{\sigma_i^m(E)}{\varepsilon(E)(E_{n+}^m - E_{n-}^m)} dE, \qquad (4.13)$$

where m marks discrete number of excited state of the residual nucleus, $E_{n+/-}^m$ are the maximum and minimum permissible neutron energies[5] and integration limits are determined by the kinematics of the reaction [76].

Isotope-dependent cross-sections of (α,n) reactions can be calculated, for example, by the TALYS [104] or some versions of EMPIRE [105], or can be taken from experimental measurements, for example, the JENDL/AN-2005 (JENDL[6] (alpha,n) Reaction Data File 2005) [106] in ENDF format. Additionally, the TENDL[7] library [107] can also be used in ENDF[8] format that contains cross-sections calculated through the determination of nuclear models implemented in TALYS. For the stopping powers of α particles in materials, codes like ASTAR [108] or SRIM[9] [109] are often used. The knowledge of all elemental constituents is needed (often user-defined) and a homogeneous mixture is often considered.

Unlike the other codes, which utilize some form of evaluation of aforementioned equations, Geant4 performs an explicit transport of the incident α particles through the material and resulting neutrons are generated consequently as the (α,n) reaction takes place [99]. The Geant 4.10.6 based code SaG4n takes advantage of the ParticleHP module incorporated in Geant4, which allows using data libraries written in ENDF-6 format (such as JENDL/AN-2005 or TENDL), that contain information on reaction cross-sections and production of secondary particles. Electromagnetic, elastic and non-elastic nuclear interactions are modelled using the G4EmStandardPhysics option4, G4HadronElasticPhysics

---

[5]E_{n-}^m for $\theta = \pi$ and E_{n+}^m for $\theta = 0$, θ is the neutron emission angle in the CMS. Energy of neutron in laboratory system and $cos\theta$ are coupled by the expression that depends on the reaction Q_m value, the incident α particle energy, and masses of the nuclides involved in the kinematics of reaction [98, 103].

[6]Japanese Evaluated Nuclear Data Library

[7]TALYS-based evaluated nuclear data library.

[8]Evaluated Nuclear Data File

[9]Stopping and Range of Ions in Matter

and the G4ParticleHP packages, respectively [99]. There are several advantages of using Geant4 based code compared to others, as it allows [99, 110]:

- users to build complicated geometries of studied systems

- to bias a particular process and ultimately reduce the computing time

- for the production of γ decays in the same nuclear process (in the (α,γn) reactions), provided that the used data libraries contain that information

- to store position and momentum of the generated α particles and of the produced neutrons (and γ rays) and their weight.

In this case, given that N_n is the number of neutrons produced in the simulation, ω_i is the weight of each of them, and N_α is the number of simulated alphas, the resulting neutron yield per α can be calculated as [110]:

$$Y_n = \frac{1}{N_\alpha} \sum_{i=1}^{N_n} \omega_i \ [n/decay] \tag{4.14}$$

Recommended data library is the JENDL/AN-2005, that contains neutron production cross-sections for alpha-particle induced reactions of 17 nuclides (^{6,7}Li, ^{9}Be, ^{10,11}B, ^{12,13}C, ^{14,15}N, ^{17,18}O, ^{19}F, ^{23}Na, ^{27}Al, ^{28,29,30}Si) [106], combined with TENDL-2017 elsewhere, where information is not available [110]. The evaluation of neutron emission data of (α,xn) reactions in JENDL/AN-2005 was performed on the basis of available experimental data and nuclear model calculations [106]. TENDL-2017 is the 9th version of TENDL library which provides the output of nuclear models implemented in TALYS [107, 111]. Comparison of cross-sections and differences between the two libraries for some selected isotopes can be seen in Figure 4.8. In most cases, the cross-sections in TENDL are higher than in JENDL and TENDL does not reproduce the resonance behaviour. The difference is most likely due to the calculation of cross-sections with the TALYS nuclear code which uses a statistical model or model parameters that are not accurate for light elements[10]. This shows that theoretical models could be quite far from reality and it highlights the importance of experimental data. The neutron yields could be, in most cases, overestimated when using the cross-sections from TALYS. This trend is seen in works that compare results of different calculation codes between each other and with experimental data, for example in [99] or [94].

---

[10]This is suggested, for example, in [112]. In [113], some parameters in the TALYS were adjusted to obtain good agreement between calculated total and partial cross sections and experimental data for the mass range of 19<A<210. And in [114], some discrepancies of the neutron yield induced by proton and deuteron bombardment are also attributed to the inaccurate cross sections calculated with the TALYS for light elements.
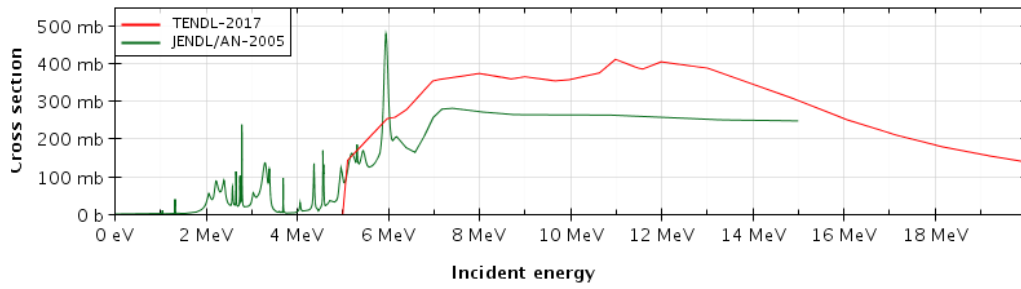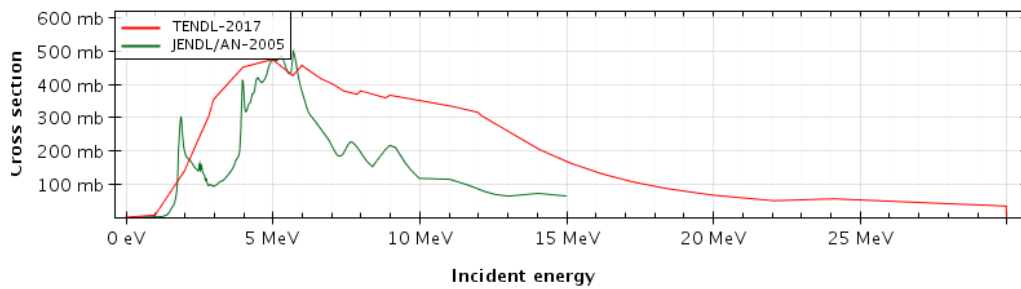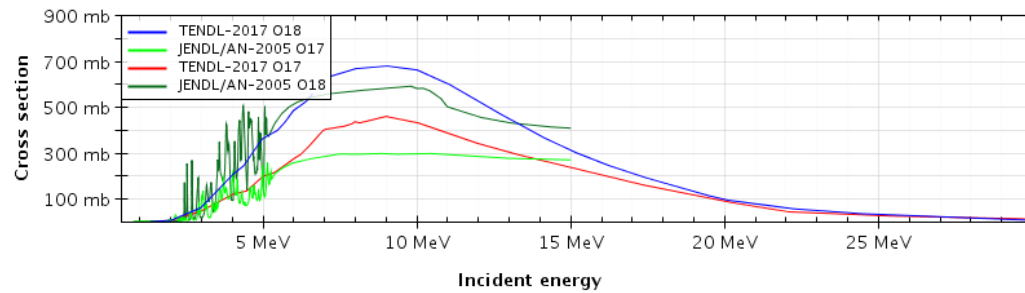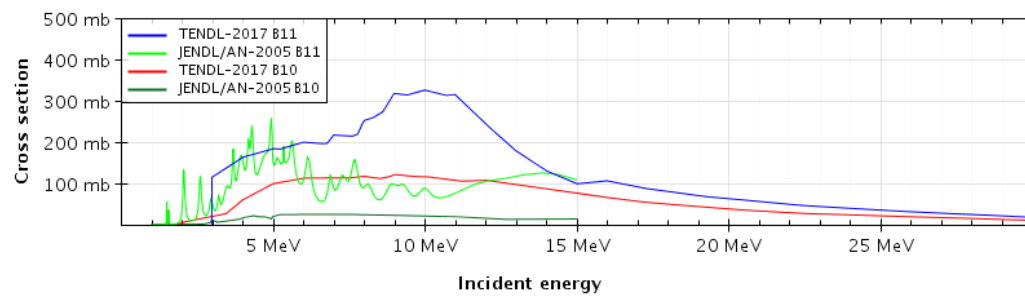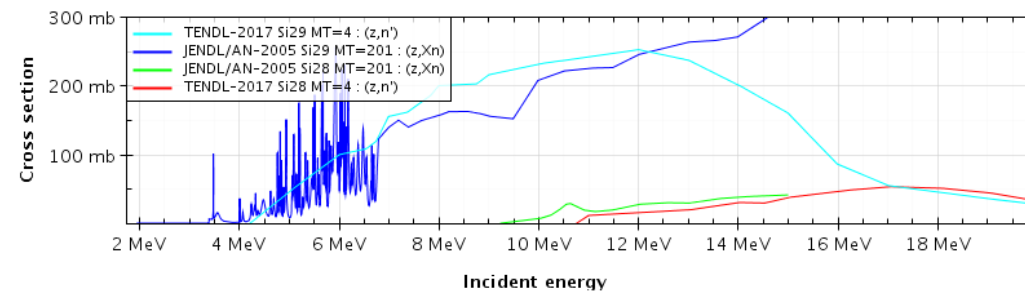
FIGURE 4.8: Comparison of cross-sections for (α,n) reactions of selected isotopes [92]

4.2.3 Estimation of (α,n) Reactions for SuperNEMO

(α,n) reaction energy spectra and neutron yields were studied in materials with the highest ^{238}U and ^{232}Th contamination and in materials with a large mass that can contribute significantly to overall neutron yield. In the SuperNEMO detector, it is mainly the shielding (considered materials are water, pure polyethylene, 5% borated polyethylene against neutrons and iron against gammas), borosilicate glass which is the most commonly used window material in photomultiplier tubes and pins on feedthrough connectors that are made out of copper-beryllium alloy (containing 3% of Be, Fig. 4.9). Due to the purification and demineralization process, there is no expected contamination of water shielding and no alpha particles are able to travel through the iron shield to water to initiate (α,n) reaction. Thus, the neutron yield from water is neglected.
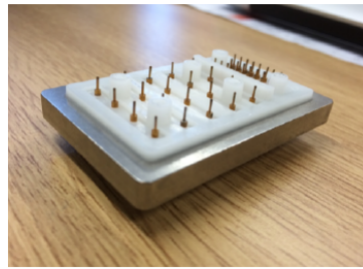
FIGURE 4.9: Feedthrough with copper-beryllium alloy pins used in the Demonstrator

Simulations were performed using Geant 4.10.6. with suited recommended combined data library, JENDL/AN-2005 + TENDL-2017. Energies of α particles along with their intensities in ^{238}U and ^{232}Th decay chains used in simulation are listed in Appendix A in Tables A.2 and A.3, respectively. The α energies range from 3.72 to 8.78 MeV. The chemical composition of shielding materials, Cu-Be alloy and borosilicate glass used in calculations is defined in Table 4.3 with the isotopic abundances of each element defined in Table A.1 (Appendix A). Secular equilibrium was assumed in both decay chains. The geometry of shielding in Geant4 was defined according to Figure 4.10.

Neutron Yields and Energy Spectra Results

In general, the magnitude of the total cross-section of (α,n) reaction determines the total neutron yield in a material. All cross-sections from corresponding data libraries for the most common isotopes defined in the composition of selected materials are plotted in Appendix A in Figure A.1.

Results for neutron and gamma energy spectra in individual materials are shown in Figures 4.13 - 4.16 and yields given in Table 4.4 were calculated by integrating over the spectra. The highest yield is obtained from Cu-Be alloy pins that contain beryllium, which has a very high neutron yield. Relatively higher neutron rates are also in materials containing boron, PMT glass and borated polyethylene, due to a large cross-section for (α,n) reactions in ^{11}B (Fig.4.8) and its large abundance in ^{nat}B (Table A.1). The results of neutron yields also show that the largest contribution to neutron yield comes from ^{232}Th decay chain. It can be explained by the fact that ^{232}Th decay chain has more α particles above the threshold energy for the (α,n) reactions to occur. Statistical uncertainties are ~1% for

TABLE 4.3: Composition of materials used in simulations

Material	Density [g/cm^3]	Element	Mass Fraction [%]	Abundance [%]
Polyethylene, (CH$_2$)$_n$ (PE)	0.93	H	14.3	66.54
		C	85.7	33.46
Borated PE (5% PE(B))	0.96	H	61.2	27.61
		C	11.6	62.36
		O	22.2	7.52
		B	5.0	2.51
Iron	7.87	Fe	100	100
Cu-Be alloy	8.36	Be	0.44	3.0
		Cu	99.56	97.0
Borosilicate glass (PMT)	2.23	Si	39.13	27.26
		O	55.98	68.46
		B	0.41	0.75
		Na	2.93	2.49
		K	0.34	0.17
		Al	1.2	0.87
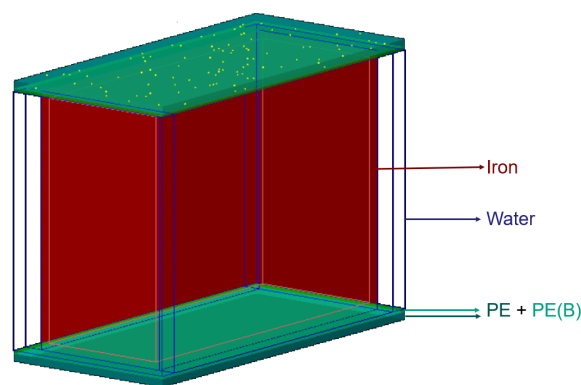
FIGURE 4.10: Simplified geometry of SuperNEMO shielding used in (α,n) simulation. Iron (red) enclosing the whole detector, PE and PE(B) (green) on top and bottom, water (blue frame, transparent fill) on front, back, left and right sides. Yellow dots - example of α source positions in top PE.

TABLE 4.4: Calculated neutron and gamma yields from (α,n) and (α,γn) reactions in shielding and PMT materials

Material + decay chain	n/decay	γ/decay
Fe ^{232}Th	3.06 $\times 10^{-7}$	9.34 $\times 10^{-8}$
Fe ^{238}U	6.06 $\times 10^{-8}$	7.15 $\times 10^{-9}$
PE ^{232}Th	1.37 $\times 10^{-7}$	8.42 $\times 10^{-8}$
PE ^{238}U	7.49 $\times 10^{-8}$	3.60 $\times 10^{-8}$
PE(B) ^{232}Th	1.09 $\times 10^{-6}$	2.79 $\times 10^{-7}$
PE(B) ^{238}U	8.04 $\times 10^{-7}$	1.48 $\times 10^{-7}$
Cu-Be alloy ^{238}U	4.15 $\times 10^{-6}$	2.96 $\times 10^{-6}$
Borosilicate glass ^{232}Th	6.06$\times 10^{-7}$	1.43 $\times 10^{-7}$
Borosilicate glass ^{238}U	3.42$\times 10^{-7}$	8.02$\times 10^{-8}$

neutron yields and $\sim$5% for gamma yields. The biggest source of systematic uncertainty is assumed due to the uncertainty in the radioisotope contamination and component masses, which will be discussed later in the chapter.

Generally, the contribution of the excited states of residual nuclei, that are energetically accessible, determines the shape of the neutron energy spectrum. Smaller values of neutron energies correspond to higher excited states of residual nuclei. For gamma spectra, only gammas from ^{232}Th decay chain are plotted, as from ^{238}U decay chain the spectra are the same but with different γ yields. Gamma spectra for lighter elements have characteristic gamma lines from excited states of residual nuclei where the states are well separated, and γ spectra for heavier elements, like Ni (from iron) and Ga (from copper), form more of a continuum. Energy level diagrams showing the excited states observed in (α,n) reactions of some light compound nuclei are plotted in Figure A.2 (Appendix A). Plotted γ spectra also give an insight to how many energy levels are populated in the (α,γn) reactions.

Iron

The composition of the iron shield is straightforward and contains only one element - Fe. The reactions that take place are: ^{54}Fe(α,n)^{57}Ni, ^{56}Fe(α,n)^{59}Ni, ^{57}Fe(α,n)^{60}Ni and ^{58}Fe(α,n)^{61}Ni. The biggest difference in the contribution to the neutron yield between the two decay chains is seen in this case of iron (Fig. 4.11 (left)). Figure 4.12 shows the cross-sections for Fe isotopes for (α,n) reaction. For the two most abundant Fe isotopes, ^{56}Fe and ^{54}Fe, the α energy thresholds are above 5.8 and 7 MeV, and there are five prominent αs of significant intensities with energy larger than these thresholds in ^{232}Th decay chain (from ^{220}Rn, ^{216}Po, ^{212}Bi and ^{212}Po) compared to only two such αs in ^{238}U decay chain (from ^{218}Po and ^{214}Po) (see Tables A.2 and A.3).

The total γ-ray yield to the total neutron yield ratios from the ^{232}Th and ^{238}U decay chains are 0.3 and 0.1 respectively.

The cross-section of these reactions was taken from the TENDL library, where we have seen from the discussion in the previous section, that they tend to be overestimated. The obtained values of neutron yields for iron can be considered conservative, however, from the point of view of experiment's sensitivity, it could be considered better to overestimate the background model rather than underestimate it.
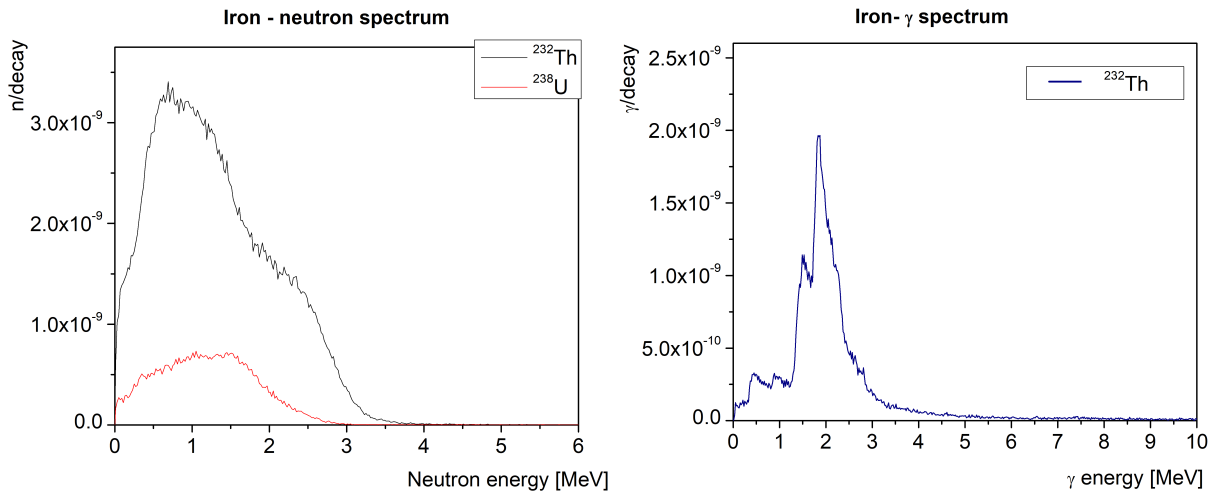
FIGURE 4.11: **Left:** Neutron energy spectra from (α,n) reactions in iron from ^{238}U and ^{232}Th decay chains. **Right:** Gamma energy spectrum from (α,γn) reactions in iron from ^{232}Th decay chain.
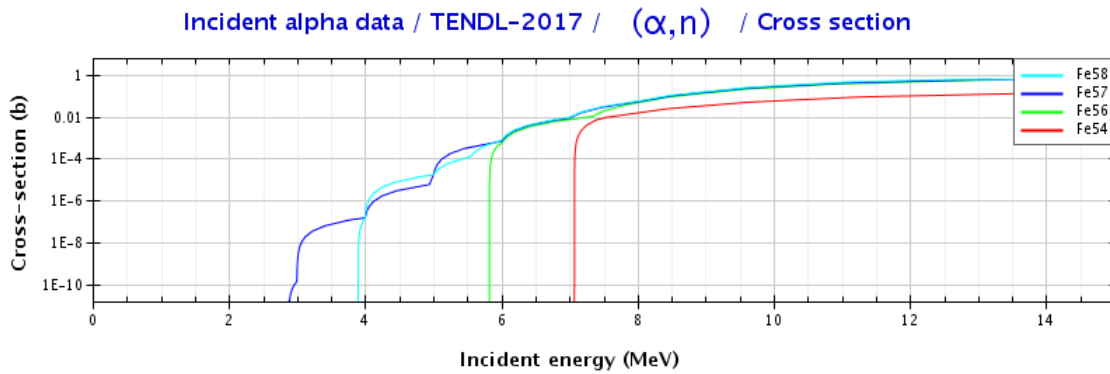
FIGURE 4.12: cross-sections for (α,n) reactions in Fe isotopes [92].

PE and PE(B)

In polyethylene (Fig. 4.13 (left)), the neutron energy spectrum has two prominent broad peaks. These neutrons come only from reaction on ^{13}C, $^{13}C(\alpha,n)^{16}O$, since the α energies in ^{238}U and ^{232}Th decay chains are not high enough to evoke (α,n) reaction in ^{12}C. However, the energies are sufficient for leaving the residual ^{16}O nucleus in an excited state, as it was shown in the previous section (Fig. 4.6). From Figure 4.6 (right) it can be seen that there is a big dip between the excited states in the residual ^{16}O nucleus, and also between its ground state and the excited states. Therefore, there must also be a big dip in the neutron energy spectrum. Observed gamma rays in Figure 4.13 (right) come from the excited states of ^{16}O: 6.1, 6.14, 6.92 and 7.12 MeV.

There is a noticeable difference in spectra and yields between PE and PE(B) (Fig. 4.14 (left)) which have similar composition and densities, but the yield for PE(B) is almost nine times higher. This can be explained by the contributions of boron and oxygen to the total neutron yield in PE(B) and a large cross-section for (α,n) reactions in ^{11}B. The additional reactions that take place in PE(B) are $^{10,11}B(\alpha,n)^{13,14}N$ and $^{17,18}O(\alpha,n)^{20,21}Ne$. There is no contribution from $^{16}O(\alpha,n)^{19}Ne$ as the threshold alpha energy for this reaction is > 10

MeV. In PE(B) gamma spectrum (Fig. 4.14 (right)), we can observe, for example, 3.95 and 2.31 MeV gammas from ^{14}N*, or lower energy gammas of 0.35 and 1.12 MeV from ^{21}Ne*, and more.

The total γ yield from PE(B) is approximately 3.5 times higher compared to the pure PE. However, overall fewer neutrons from (α,γn) reactions in PE(B) are accompanied by γ-rays, with the γ to neutron yield ratios of 0.26 and 0.18 from the ^{232}Th and ^{238}U decay chains respectively, compared to the ratios of 0.61 and 0.48 in PE. This means that (α,n) reactions on additional elements, present in the PE(B), feed mostly the ground states of the final compound nuclei.
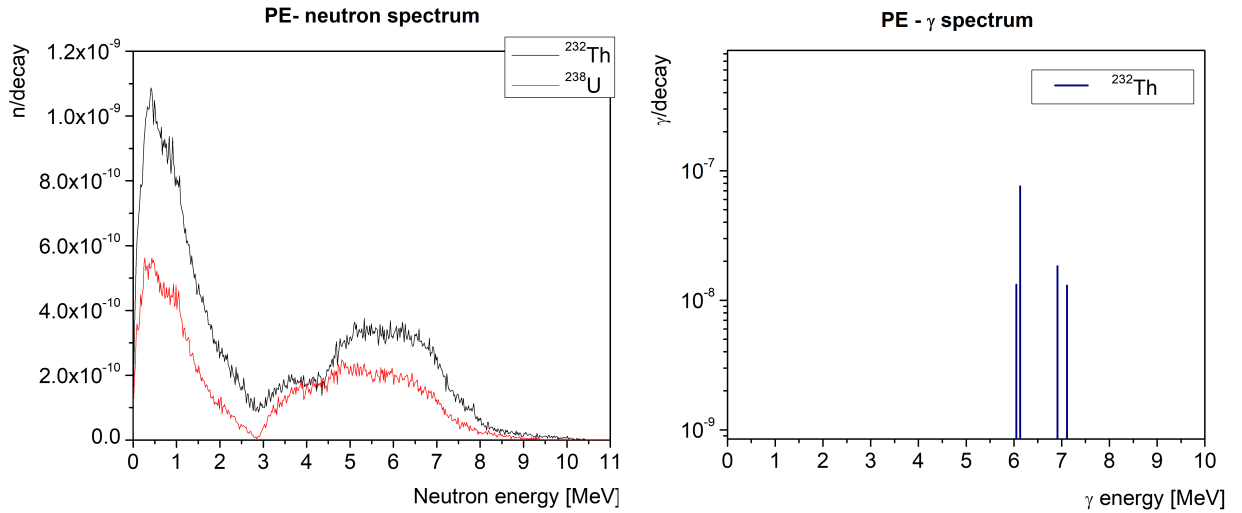
FIGURE 4.13: **Left:** Neutron energy spectra from (α,n) reactions in polyethylene from ^{238}U and ^{232}Th decay chains. **Right:** Gamma energy spectrum from (α,γn) reactions in polyethylene from ^{232}Th decay chain.

FIGURE 4.14: **Left:** Neutron energy spectra from (α,n) reactions in borated polyethylene from ^{238}U and ^{232}Th decay chains. **Right:** Gamma energy spectrum from (α,γn) reactions in borated polyethylene from ^{232}Th decay chain.

FIGURE 4.15: **Left:** Neutron energy spectra from (α,n) reactions in PMT glass from ^{238}U and ^{232}Th decay chains. **Right:** Gamma energy spectrum from $(\alpha,\gamma n)$ reactions in PMT glass from ^{232}Th decay chain.

Borosilicate Glass

The composition of this type of glass usually consists of several oxides, out of which the SiO_2 is the most dominant with smaller contributions of Al_2O_3 and B_2O_3. The neutron energy spectrum of the borosilicate glass (Fig. 4.15) consists of contributions from several reactions according to its composition defined in the simulation: $^{28,29,30}Si(\alpha,n)^{31,32,33}S$, $^{10,11}B(\alpha,n)^{13,14}N$, $^{17,18}O(\alpha,n)^{20,21}Ne$, $^{23}Na(\alpha,n)^{26}Al$, $^{27}Al(\alpha,n)^{30}P$, and $^{39,41}K(\alpha,n)^{42,44}Sc$. Based on the magnitude of the cross-sections and abundance of elements defined in the material composition, the biggest contribution to the total yield comes from boron, oxygen, sodium and silicon. The least contributing element is potassium. In comparison with PE(B), the boron content of borosilicate glass is significantly lower, therefore, the broad peak with a maximum around 3 MeV, coming from the $B(\alpha,n)N$ reaction, is suppressed. Due to the influence of other elements present in this material, the overall shape of the spectrum is smoother.

Because the cross-sections of (α,n) reactions leaving the residual nucleus in the excited state on oxygen and boron isotopes start already at relatively low α energies (< 3 MeV), gammas from the de-excitations of Ne and N isotopes dominate in the γ spectrum (Fig. 4.15 (right)). The most prominent gammas are 0.35, 1.12, 1.39 and 2.5 MeV gammas from the $^{18}O(\alpha,n)^{21}Ne$ reaction. The alpha energies in both ^{232}Th and ^{238}U decay chains are high enough for these reactions to occur and the total gamma to neutron yield ratios are similar, 0.24 and 0.23 respectively.

Cu-Be Alloy

For the Cu-Be alloy, only the yield from the ^{238}U decay chain has been investigated[11]. The main contributor to the copper-beryllium alloy neutron yield is from the beryllium: $^{9}Be(\alpha,n)^{12}C$. Not only it has a high cross-section for this reaction to occur, but its isotopic abundance in the material is also 100%. The final nucleus ^{12}C can be in the ground state or the 4.44, 7.65 or 9.64 MeV excited energy levels and the total neutron spectrum

---

[11]The contamination of ^{232}Th of these pins has not been estimated.

results from combining spectra corresponding to these different populated levels. Therefore, several peak-like features and dips can be observed in the neutron spectrum in Figure 4.16 (left). The less common reactions are ^{63,65}Cu(α,n)^{66,68}Ga which also contribute to the total yield and influence the spectrum shape.

This material has the highest neutron yield out of all materials and additionally, it also yields the highest number of γ-rays, with the γ-ray to total neutron yield ratio of 0.71. The majority of these γs (almost 87%) have energy of 4.44 MeV, and they come from the de-excitations of both the first and second excited states of ^{12}C (Fig. A.2 (Appendix A)).
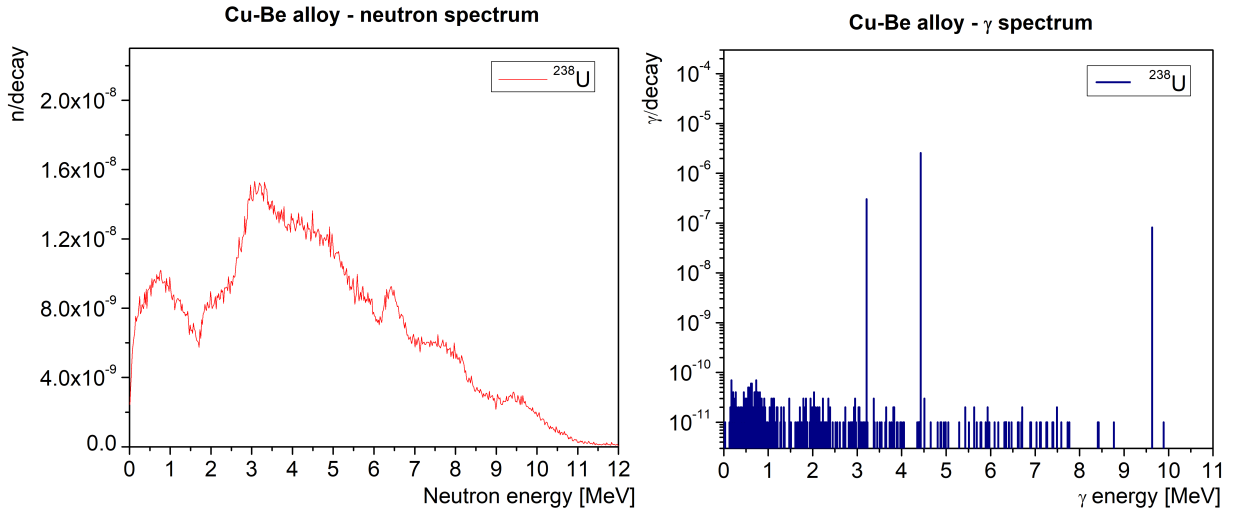
FIGURE 4.16: **Left:** Neutron energy spectra from (α,n) reactions in Cu-Be alloy from ^{238}U decay chain. **Right:** Gamma energy spectrum from (α,γn) reactions in Cu-Be alloy from ^{238}U decay chain.

It is clear, that the total yield in all materials depends on the material's total activity of ^{232}Th and ^{238}U. In some cases (Cu-Be pins, PMT glass) the activities were measured, otherwise activity limits were put on materials yet to be purchased by the collaboration. Section 4.3 is dedicated to the overall estimation of neutron contributions of the Demonstrator.

4.3 Neutron Contributions to the Background of the SuperNEMO Demonstrator

Based on the summary of the neutron sources in previous sections, we can now estimate the total neutron contribution for the Demonstrator from the ambient neutron fluxes, and radiogenic and cosmogenic neutrons.

4.3.1 Radiogenic Neutrons

To calculate overall neutron production rates from spontaneous fission and from (α,n) reactions in the Demonstrator, one needs to know the activity of ^{232}Th and ^{238}U of contaminated components and their mass. Measured activities of PMT glass, CuBe pins and polyethylene bricks, and iron activity limits are summarized in Table 4.5 along with their masses.

TABLE 4.5: Measured activities and activity limits of contaminated Demonstrator components

Component	Mass [kg]	^{232}Th activity [Bq/kg]	^{238}U activity [Bq/kg]
PMT glass bulb*	0.65	0.390±0.098	0.86±0.22
Iron shield	230 000	<0.0005 **	<0.001 **
Feedthroughs CuBe pins	1.36	-	13.5±0.8
PE brick	1.33	<0.00151	<0.00226
PE(B) brick	1.33	0.012± 0.002	0.207± 0.005

*Number of 8" PMTs=440, **target limit

These values can be used in a straightforward manner to normalize neutron yields obtained from calculations from Table 4.1 (SF) and MC simulations from Table 4.4 ((α,n) reactions) to obtain contributions from individual neutron sources.

Several assumptions were taken into account while calculating neutron production from contaminated materials: the mass, volume and surface of PE and PE(B) bricks is assumed to be the same and thickness of 1 brick is 8 cm[12]. Currently[13], the design of SuperNEMO shielding considers 18 cm of iron against gammas on each side of the detector with the addition of water on all lateral sides and polyethylene bricks on top and bottom or polyethylene bricks on the back side of the detector instead of water. This way, we can estimate that approximately 1539 bricks and 992 bricks of polyethylene are needed to cover the top and back sides respectively. The surface of the top and bottom shielding is also assumed to be the same.

Calculations of total radiogenic neutron production from contaminated materials are summarized in Table 4.6. For the CuBe alloy pins, it also shows γ production from excited states of $^{12}C^*$ after (α, n) reactions out of which the majority, $\sim$1536 γs/year, are above 4 MeV (see γ spectrum from Fig. 4.16). Other γ contributions from $(\alpha, n\gamma)$ reactions can be neglected, as they either do not reach high yields for relevant energies (e.g. PMT glass, iron) or they are expected to get shielded by their subsequent attenuation by the iron shield (the case of PE and PE(B)).

In all cases, spontaneous fission dominates the neutron production, except for the CuBe alloy feedthrough pins where the cross-section for (α, n) on beryllium is high enough to take over.

Uncertainties in the (α,n) calculations can come from several sources and are still widely discussed and investigated within the scientific community as they are not well understood. They can come from the definition of material composition where the exact composition is often vaguely provided by the supplier and whether or not an element (or isotope)

---

[12]These are the dimensions of bricks currently under consideration.
[13]In the time of writing this thesis.

TABLE 4.6: Contributions to neutron production from contaminated materials under investigations

Material	Total mass/Surface	Process	n/year, γ/year[#]
PMT glass	286 kg	(α, n) Th	2133.0
		(α, n) U	2654.9
		SF U	8460.3
CuBe pins	1.36 kg	(α, n) U	2406.8
		SF U	631.1
		(α, n) γs from $^{12}C^*$	1714.0[#]
Iron shield	230 000 kg	(α, n) Th	1110.5
		(α, n) U	439.8
		SF U	7911.3
PE bricks	Top side $\sim$31m^2	(α, n) Th	13.4
		(α, n) U	10.9
		SF U	159.1
	Back side $\sim$20m^2	(α, n) Th	8.6
		(α, n) U	7.0
		SF U	102.5
PE(B) bricks	Top side $\sim$31m^2	(α, n) Th	844.8
		(α, n) U	10749.7
		SF U	14573.6
	Back side $\sim$20m^2	(α, n) Th	544.4
		(α, n) U	6926.5
		SF U	9390.4

appears in the material at all can make a big difference. There is also some variance in reported natural abundances of elements used in calculations. Another uncertainty can come from stopping power calculations of α particles in matter and reaction cross-sections, where theoretical predictions disagree significantly with measurements, and uncertainties on measurements are typically large (often 10-20%). Moreover, some measurements of cross-sections of the same isotopes are in disagreement. This should all be taken into account when predicting radiogenic neutron production, however, as there are a lot of complex systematics in these measurements and calculations it is not easily predicted. Therefore, the biggest contribution to overall uncertainty is assumed to come from the uncertainty of material activity and often only this is considered.

It is important to note again that understanding the radiogenic neutron production is essential in rare event searches and that it is very much an evolving research field with many future plans to reduce the uncertainty in the sensitivity of next generation experiments. Such plans include a thorough review of the existing tools for (α,n) yield calculations and the available cross-section databases, plans to improve the accuracy of the estimates and novel ideas for (α,n) cross-sections measurements. This is outside of the scope of this work, but it represents a new potential approach in future, where this work may serve as a reference point. In summary, evaluating the systematics associated with backgrounds in underground laboratories by analytical or Monte Carlo methods is currently at an early stage.

TABLE 4.7: Muon induced neutron yields and production rates in Fe for different mean muon energies

Fe density [g cm^{-3}]	Fe thickness [cm]	Interaction length [g cm^{-2}]	μ flux [μm^{-2}d^{-1}]
7.87	18	141.66	$\sim$5
Average μ energy [GeV]	μ induced n yield in Fe* [n μ^{-1}(g cm^{-2})$^{-1}$]	Production [n μ^{-1}]	Muon induced n flux [n cm^{-2}s^{-1}]
10	9.10×10^{-5}	0.013	7.46×10^{-11}
11	1.32×10^{-4}	0.019	1.08×10^{-10}
12	5.40×10^{-5}	0.008	4.43×10^{-11}
17.8	1.69×10^{-4}	0.024	1.39×10^{-10}
20	9.80×10^{-5}	0.014	8.03×10^{-11}
40	1.30×10^{-4}	0.018	1.07×10^{-10}
40	3.31×10^{-4}	0.047	2.71×10^{-10}
80	1.70×10^{-4}	0.024	1.39×10^{-10}
150	3.30×10^{-4}	0.047	2.71×10^{-10}
280**	1.64×10^{-3}	0.232	1.34×10^{-9}
385	2.03×10^{-3}	0.288	1.66×10^{-9}

*Dependance of neutron yield in Fe (data from [51, 52])

**Closest measured mean energy to E$_{\mu,LSM}$= 255.0(45) GeV

4.3.2 Cosmogenic Neutrons in Iron

In general, the flux of cosmogenic neutrons is considered to be negligible [61]. Very little data is available from measurements and simulations of muon induced neutron yields in LSM. It is generally accepted that the neutron production at a certain depth can be approximated by assuming that neutrons are produced by muons, all having mean energy corresponding to this depth. As it was described in Section 3.1, they are predominantly created in high Z materials such as lead or iron used for gamma shields. In SuperNEMO, iron shielding is considered. We can estimate the neutron yield in iron using available measurements for different muon energies in underground environments or by using the universal formula from Equation 3.4. Muon induced neutron yields and production rates in Fe from available literature for different mean muon energies are summarized in Table 4.7 and plotted in Figure 4.17.

Using the universal formula for iron and average muon energy from Equation 3.8 we get:

$$Fe(A = 56) : Y_n^{UF} = 1.71 \times 10^{-3} n\mu^{-1}(gcm^{-2})^{-1} \tag{4.15}$$

For 18 cm thick iron shield we can estimate the interaction length $\sim$ 141 cm, and use muon flux from Equation 3.7, which yields approximately 1.4×10^{-9} n cm^{-2}s^{-1}. This flux is by 3 orders of magnitude lower than fast and thermal ambient neutron fluxes and moreover, energies of these neutrons extend to high values, therefore we conclude that these neutrons do not contribute significantly to the background of the SuperNEMO experiment.
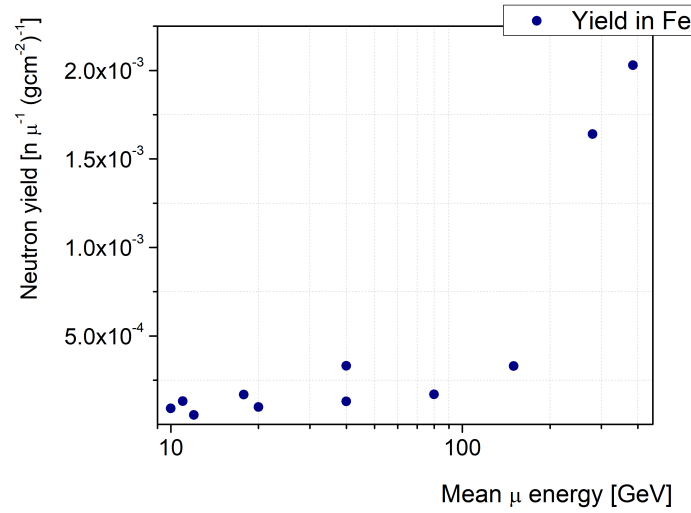
FIGURE 4.17: Dependance of muon induced neutron yield on the average
muon energy in Fe (data from [51, 52])

By far the biggest contributions constitute the ambient neutron fluxes. We can esti-
mate their contribution in *n/year* by taking into account the measured fluxes from Sec-
tion 3.3.5 and calculating the number of neutrons entering the surface of the detector which
is known. Figure 4.18 summarises the rate of different neutrons sources estimated in this
work, wherein radiogenic neutrons only neutrons from iron, PMTs, CuBe pins and pure
polyethylene bricks are accounted for[14]. Thus, the task to optimize the neutron shielding
in terms of its thickness becomes important.
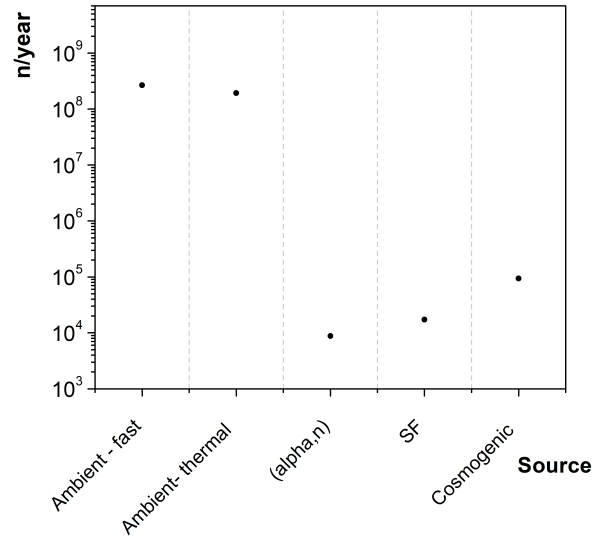
FIGURE 4.18: Contribution of neutrons from different neutron sources

---

[14]PE(B) bricks are excluded to see how low the neutron production can be achieved

4.4 Neutron Capture Gamma Cascades

Neutron induced background in the SuperNEMO experiment is expected to arise primarily from the (n,γ) reactions. However, SuperNEMO simulation software is based on Geant4 which has a known issue of not being able to reproduce (n,γ) reactions properly because correlations between gammas in individual gamma cascades in de-excitations are not taken into account correctly [115, 116, 117]. This prevents energy conservation in neutron capture events, which is crucial in many applications [115] and it can lead to rather unreliable results and difficulties when simulating electromagnetic calorimeters or overall detector response to neutron interactions.

This problem can be solved by separate simulation of gamma de-excitations using dedicated gamma decay software DICEBOX [118] to make sure cascades are generated according to the available data and that the correlations between γ-rays are correctly taken into account. Section 4.4 describes the basic theory and assumptions of neutron capture gamma cascades and the results of DICEBOX thermal neutron captures simulations on iron and copper (abundant metals used in SuperNEMO Demonstrator constructions materials) are discussed later in Section 4.4.3.

The work discussed in this section was done with collaboration with the DICEBOX software developers from Charles University in Prague.

4.4.1 Neutron Radiative Capture
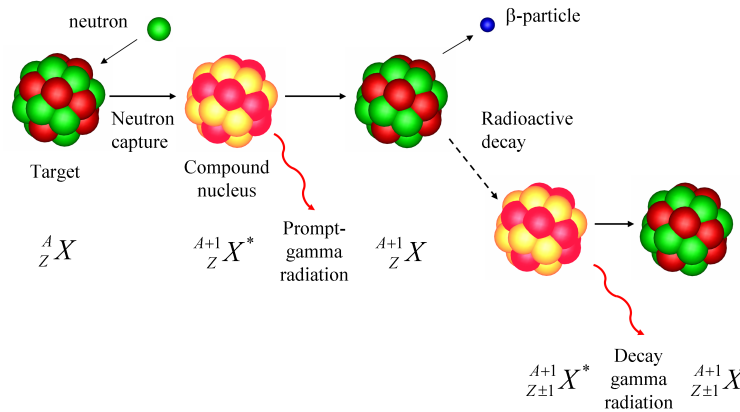
FIGURE 4.19: Scheme of (n,γ) reaction [119]

Neutron radiative capture, (n, γ) reaction, is the process when a target nucleus absorbs a neutron to form a heavier nucleus, which then de-excites by means of electromagnetic transitions, including emission of prompt γ-rays, internal conversion or internal pair production. The excited nucleus loses energy in a transition to a state lower in energy in the same nucleus. The de-excitations from the state with higher excitation energy to the state with lower excitation energy can generally proceed via a cascade of transitions with many intermediate levels [120]. Typical quantities that characterize the cascade γ emission are the energy of emitted γ-rays, γ-ray multiplicity and populations of individual levels [120].

The probability of a particular transition depends upon the quantum numbers of the state and the transition energy. In thermal neutron capture, the compound nucleus $^{A+1}$X
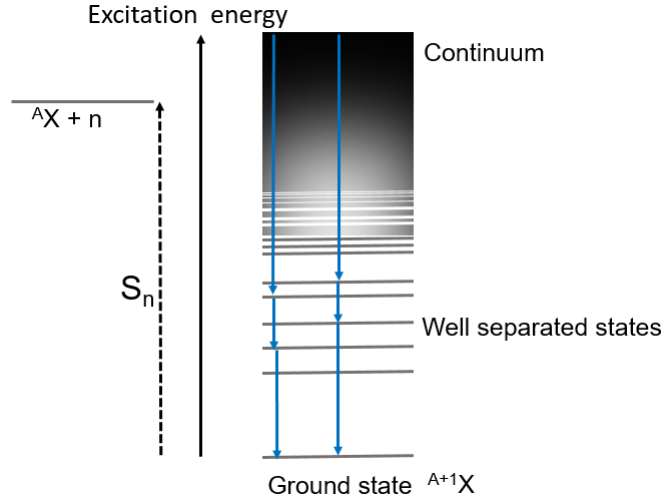
FIGURE 4.20: Simplified scheme of γ-ray transitions after neutron capture

is formed with excitation energy slightly above the neutron separation energy S_n threshold [121]. The excitation energy of the compound nucleus is equal to the sum of S_n and the neutron kinetic energy E_n. At the lowest excitation energy region, the individual levels in the nucleus are well separated, their energies, spins, parities and γ-ray de-excitations are known and can be predicted by nuclear models, but with increasing excitation energy, nuclear levels become more difficult to resolve and above some critical energy, E_{crit}, these levels form a continuum (simple scheme of nuclear level distribution is shown in Figure 4.20, with blue lines showing an example of possibilities of realization of γ-ray transitions) [120, 121]. With increasing excitation energy, the nature of these levels becomes complicated and the only way to describe the level density seems to be the use of a statistical model. During the de-excitation of a medium-heavy or heavy nucleus, a large number of levels in the energy range from zero to the S_n is populated and the spectrum of emitted γ-rays is thus very complex.

The two entities responsible for the emission of γ cascades in the neutron capture reactions are the level density (LD) and the photon strength function (PSF) [120]. The mean value of a partial radiative width, Γ_{if}^{XL}, of corresponding transition of γ-ray decay with an energy $E_\gamma = E_i - E_f$ is [121, 122]:

$$< \Gamma_{if}^{XL} > = \frac{f^{XL}(E_\gamma) E_\gamma^{2L+1}}{\rho(E_i, J_i, \pi_i)} \tag{4.16}$$

where XL[15] denotes the multipolarity of the transition, E_i, E_f are energies of initial and final states, f^{XL} is the photon strength function and $\rho(E_i, J_i, \pi_i)$ is the level density model depending on energy E, spin J and parity π of the initial state. Thus, Equation 4.16 can be rewritten for the PSF of type and multipolarity XL:

$$f^{XL}(E_\gamma) = \frac{< \Gamma_{if}^{XL} > \rho(E_i, J_i, \pi_i)}{E_\gamma^{2L+1}} \tag{4.17}$$

---

[15]X stands for type of transition, L stands for associated multipole moment ($X = E$ is electric and $X = M$ is magnetic multipole operator of given multipolarity L)
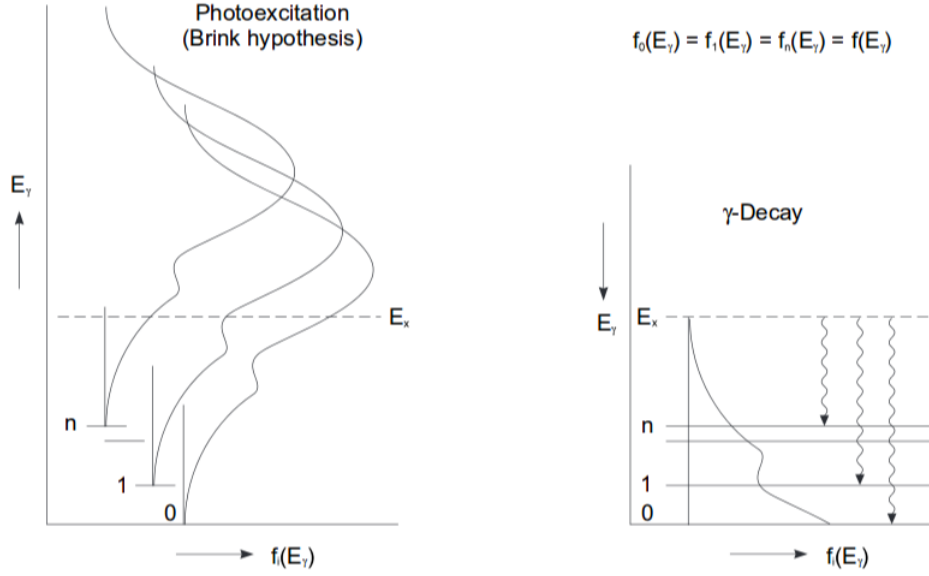
FIGURE 4.21: Representation of the Brink-Axel hypothesis for photoexcitation (photo-absorption) and neutron capture [123]

From Equation 4.17, it is seen that the PSF represents the distribution of average, reduced partial γ-transition widths, and so it describes the average probability to emit γ radiation with a given γ-ray energy.

While the strength function from Equation 4.17 is related to γ decay[16], a photo-absorption strength function[17] is determined by the average photo-absorption cross-section $< \sigma^{XL}(E_\gamma) >$ summed over all possible spins of final states [123]:

$$f^{XL}(E_\gamma, E_f, J_f, \pi_f) = \frac{< \sigma^{XL}(E_f, J_f, \pi_f, E_\gamma) >}{(2L+1)(\pi\hbar c)^2 E_\gamma^{2L+1}} \tag{4.18}$$

The basis of the treatment of γ-ray transition probabilities in the concept of PSF is the so-called Brink-Axel (BA) hypothesis [124, 125] that assumes that the total absorption cross-section depends only on transition energy E_γ and does not depend on other characteristics of the initial and/or final states [126]. In other words, the photo-absorption cross-section on an excited state will have the same shape as the photo-absorption on the ground state (Fig. 4.21), and so the strength function from Equation 4.18 can be used as a substitute for the strength function in Equation 4.17 [123].

Hence, PSFs can be evaluated from measurements of total photo-absorption cross-sections as well as from neutron radiative capture measurements, if data are available. Where the data are not available and the PSFs are not well known, theoretical models are usually proposed.

---

[16]Often reffered to as "downward" strength function (see Fig.4.21)

[17]Often reffered to as "upward" strength function (see Fig.4.21)

4.4.2 Internal Conversion (IC) and Internal Pair Production (IPP)

Internal conversion and internal pair production (conversion) are decay modes that compete with γ emission as a de-excitation process of excited nuclei.

IC results in the emission of an orbital electron of the same atom after absorbing the excitation energy of the nucleus. The kinetic energy of IC electron is equal to the energy of the transition between excited and lower energy states of nucleus minus the binding energy of the electron, $E_e = E_i - E_f - E_{binding}$.

An excited nucleus can also decay electromagnetically by emission of an electron-positron pair provided that the nuclear transition energy exceeds $2m_e c^2$ (1.022 MeV). The particles emitted in the IPP process share the available kinetic energy, $E_{transition} - 2m_e c^2$.

The conversion coefficients are defined as the ratio of the electron/electron-positron pair emission rate to the gamma emission rate. Knowledge of accurate IC and IPP coefficients is needed in the determination of total transition rates.

4.4.3 Gamma Cascades from Thermal Neutron Capture on Fe and Cu Isotopes

Results presented in this section were obtained by the DICEBOX γ-decay simulation code. Input data for selected studied isotopes (Table 4.8) include the knowledge of transitions, PSF and LD models, and IC and IPP conversion coefficients. DICEBOX generates the full level scheme of each isotope according to available data and any missing information is provided with the use of statistical model.

TABLE 4.8: Abundance of studied Fe and Cu isotopes and neutron separation energies for compound nuclei

Isotope	Abundance [%]	Reaction	S_n of CN [MeV]
^{54}Fe	5.85	^{54}Fe(n,γ)^{55}Fe	9.298
^{56}Fe	91.75	^{56}Fe(n,γ)^{57}Fe	7.646
^{63}Cu	69.17	^{63}Cu(n,γ)^{64}Cu	7.916
^{65}Cu	30.83	^{65}Cu(n,γ)^{66}Cu	7.066

The knowledge of transitions for all isotopes was adopted from corresponding ENSDF[18] files from the electronic database of evaluated experimental nuclear structure data [127, 128], and from reference [129] for Fe and reference [130] for Cu. IC and IPP coefficients were taken from the internal conversion coefficient database, BrIcc [131]. For Fe isotopes QRPA calculations were used for E1 a M1 transitions, single particle approximation for E2 transition and Constant Temperature Formula (CTF) for LD [132], this combination being relatively well tested for iron [129]. For Cu isotopes traditionally used models are standard Lorentzian for E1, M1 and E2 transitions and Back Shifted Fermi Gas model (BSFG) for level density [132]. PSF models for Fe and Cu are shown in Figures 4.22 and 4.23 respectively (E2 PSF is multiplied by the square of E_γ to ensure units comparable to M1 and E1 PSF. It is summed to M1 PSF, because M1 and E2 transitions have similar selection

---

[18]Evaluated Nuclear Structure Data File

rules - they do not change parity and can therefore occur between the same two levels, and mixed M1 + E2 transitions can be observed).
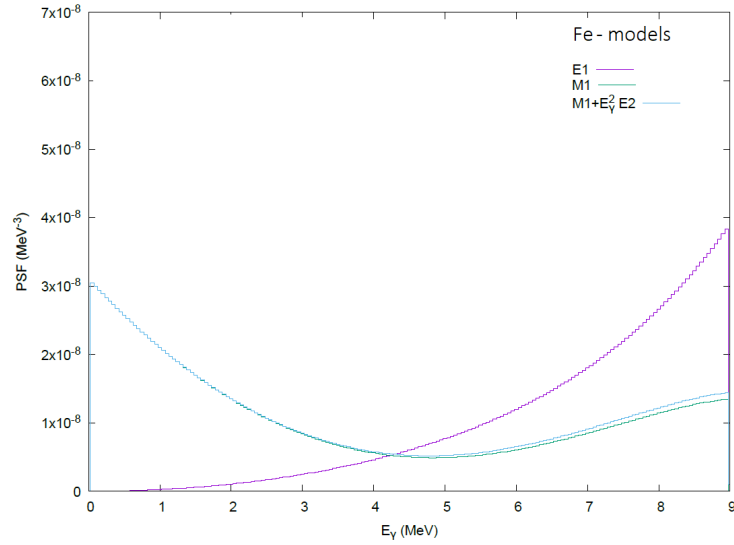
FIGURE 4.22: PSF models used in DICEBOX simulation for Fe isotopes: QRPA calculations for E1 and M1 transitions, single particle approximation for E2 transition and Constant Temperature Formula for level density.
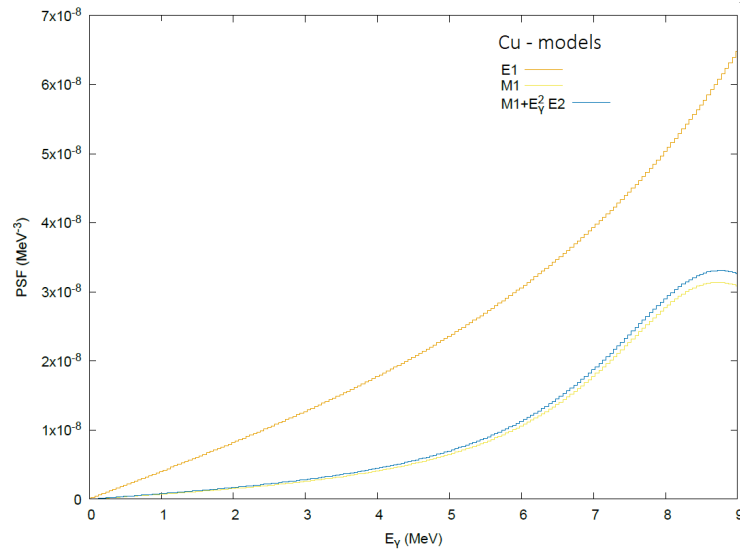
FIGURE 4.23: PSF models used in DICEBOX simulation for Cu isotopes: standard Lorentzian for E1, M1 and E2 transitions and Back Shifted Fermi Gas model for level density.

In DICEBOX, 100 000 thermal neutron captures were simulated. Obtained results for each isotope include γ spectra following thermal neutron capture, individual γs in cascades, lengths of individual cascades and contributions from de-excitation from IC and IPP. Results of 10^5 cascades in a nuclear realization simulated in DICEBOX are presented in Figures 4.24 - 4.26.

Figure 4.24 shows plots of sums of gammas in generated cascades. It can be seen that in all cases, the majority of events have energy equal to the neutron separation energy S_n of compound nucleus, the mean value is $\approx S_n$ (S_n values are in Table 4.8). Therefore, γ emission dominates all de-excitation modes. In other cases, the de-excitation process proceeds via γ emission in combination with IC and/or IPP, and so the electrons or $e^- - e^+$ pairs carry away the remaining energy.
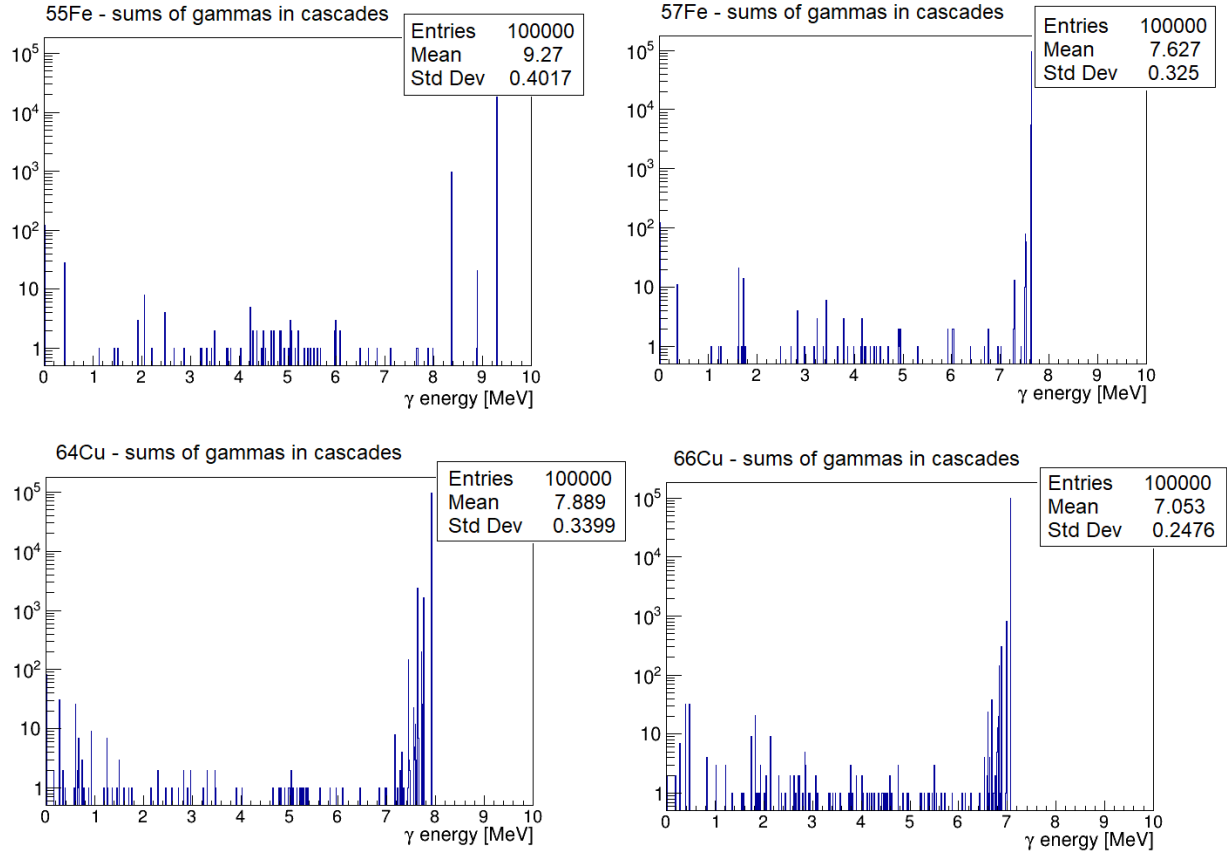
FIGURE 4.24: Sums of gammas in 100 000 generated neutron captures on Fe and Cu isotopes

Figure 4.25 shows the energy distribution of individual gammas in cascades, therefore the number of entries is always larger than 100 000. It can be seen that the de-excitations proceed via different transitions with many intermediate levels and the gammas cover a wide range of energies. Only for ^{55}Fe and ^{64}Cu, the de-excitation happens through the emission of gamma with energy equal to the S_n in most cases. This can also be seen from the length of gamma cascades in Figure 4.26, where the mean number of gammas in ^{55}Fe cascades is 1.6, and 2.2 in ^{64}Cu cascades. The biggest number of gammas is emitted in cascades of ^{66}Cu. In comparison to iron isotopes, in copper, there is a larger number of transitions proceeding to the low-lying excited states of the product nuclei. Namely γ-rays of 159.3 and 278.3 keV in ^{64}Cu, and γ-rays of 185.9 and 465.2 keV in ^{66}Cu have high intensities. For ^{66}Cu, the E_γ=185.9 keV is also the strongest transition. The strongest high energy transitions are: E_γ=9.23 and 8.88 MeV for ^{55}Fe, E_γ=7.64, 7.27, 6.02 and 5.92 MeV for ^{57}Fe, E_γ=7.91, 7.64, 7.31 MeV for ^{64}Cu, and E_γ=6.60, 6.68, 5.32 and 5.25 MeV for ^{66}Cu.
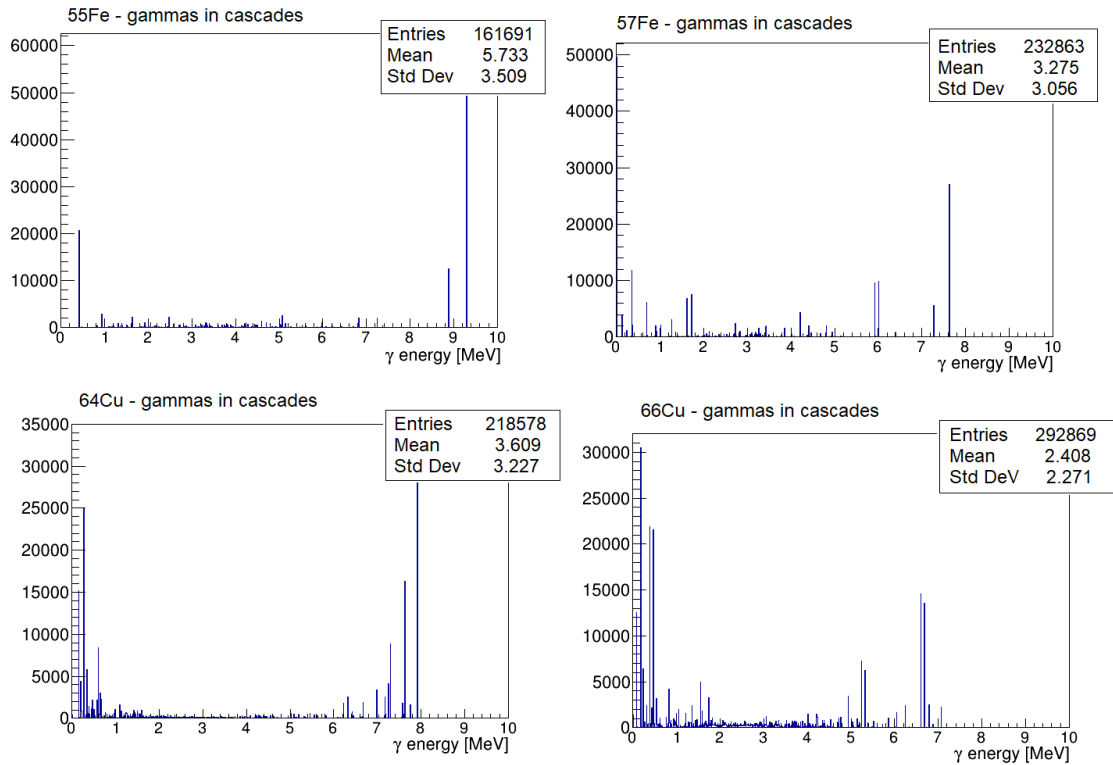
FIGURE 4.25: Individual gammas in 100 000 generated neutron captures on
Fe and Cu isotopes
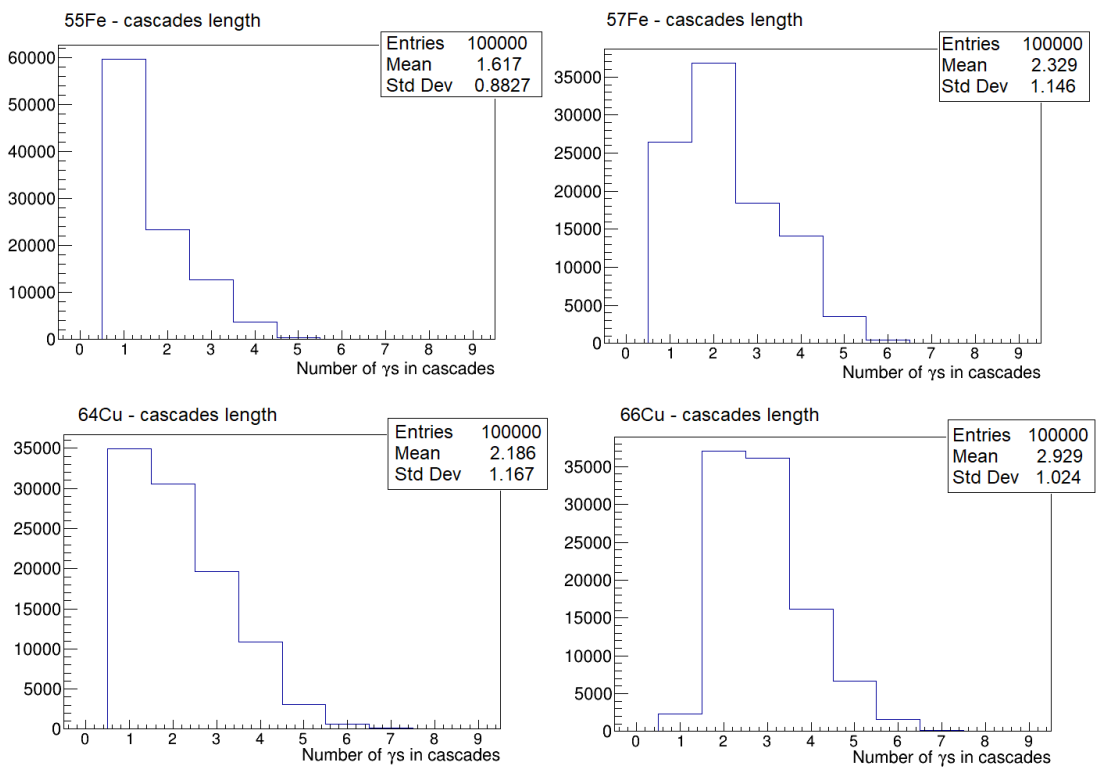
FIGURE 4.26: Lengths of cascades for Fe and Cu isotopes

Plots for IC (Fig. 4.27) show γ energies contributing to IC (energy absorbed by orbital electron[19]), the kinetic energy of the electron is then smaller by its binding energy. In all cases, IC is important for low energy nuclear transitions with the mean energies being lower than 1 MeV. This agrees well with the theory that internal conversion is favoured for low energy transitions [133]. The biggest IC contribution can be seen in ^{57}Fe for the lowest energies, which is most likely due to high IC coefficients for these transitions, for example, ICC=8.54 for E_γ=14.4 keV transition [129].
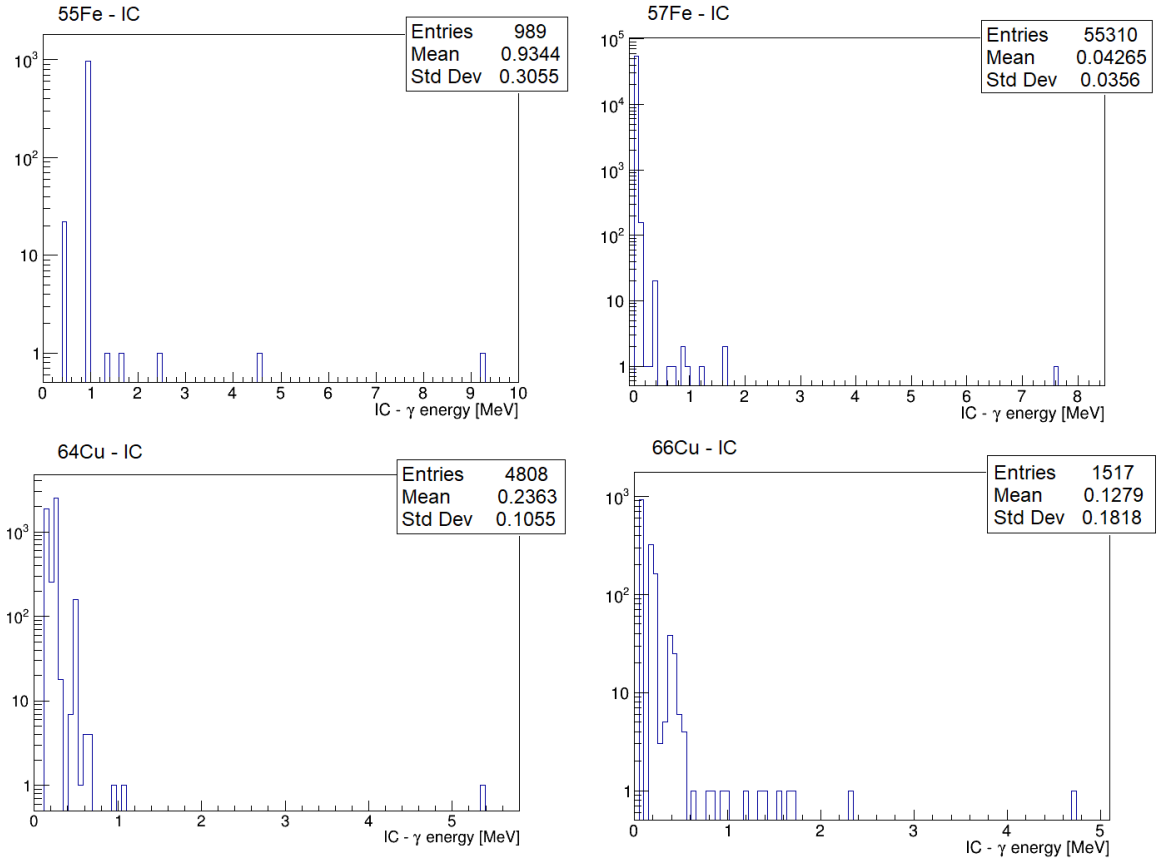
FIGURE 4.27: Results of IC

Plots for IPP (Fig. 4.28) show total energies of $e^- - e^+$ pairs, the kinetic energy of the pair is then smaller by $2m_ec^2$. A substantial amount of energy can be carried away by $e^- - e^+$ pairs with mean energies close to the value of S_n in most cases. However, the contribution of the IPP process is overall very small with the number of entries ranging only between 218 - 238.

---

[19]The exact quantum of energy lost by a nucleus.
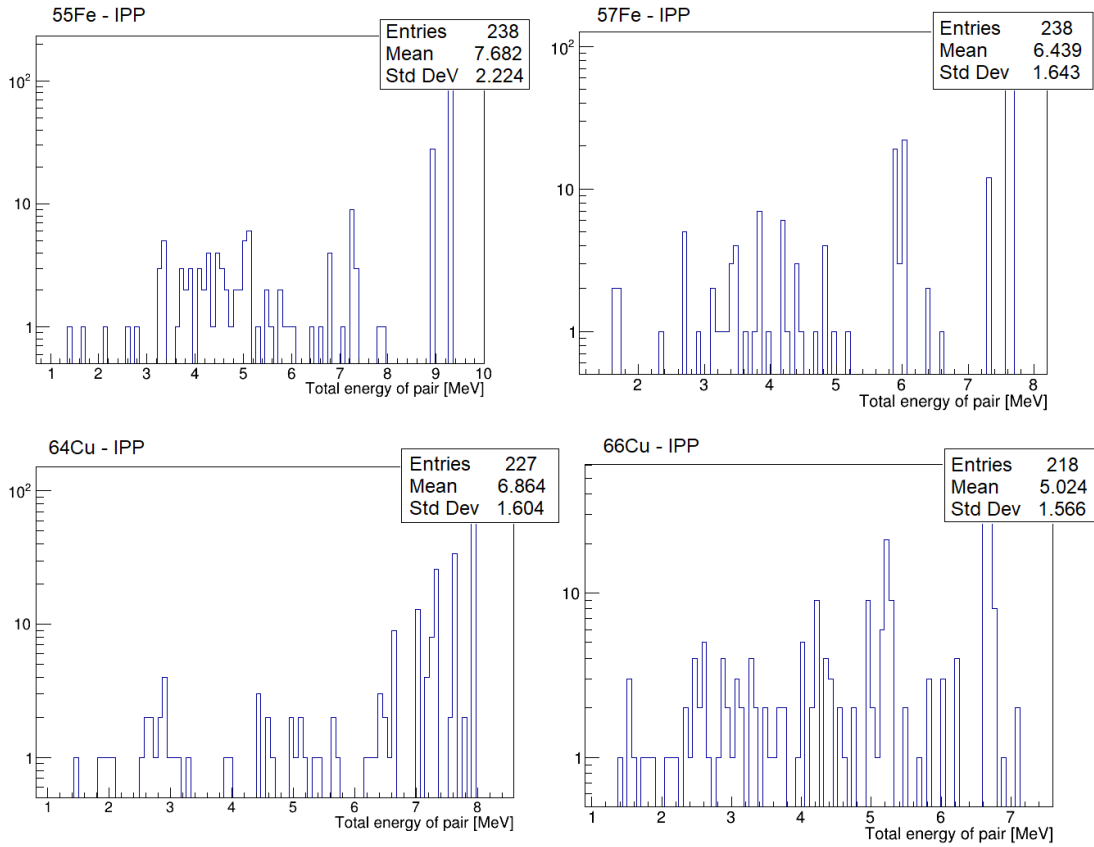
FIGURE 4.28: Results of IPP

4.5 Summary

The main objective of this chapter was to evaluate neutron production rates and their energy spectra from sources that could potentially contribute to the background of the SuperNEMO experiment. These sources include spontaneous fission of uranium and thorium isotopes, (α,n) reactions and muon induced neutrons.

Each radiogenic source has its dedicated section in the chapter which includes a short theoretical overview of the process and a summary of approaches and simulation tools to calculate the total neutron yields and their energy distributions. Based on extensive research in the available literature, I used the best performing tools, formulas and data libraries to calculate and evaluate these neutron contributions.

From spontaneous fission, only ^{238}U is of concern, due to its higher branching ratio for this process[20]. The number of spontaneous fission neutrons emitted per decay of ^{238}U is approximately 1.1×10^{-6}. In comparison, neutron yields from (α,n) reactions were found to be lower in most cases, except for a material containing ^{9}Be. For this reason, spontaneous fission dominates the neutron production for construction materials used in the Demonstrator.

The energy spectra of these neutrons are soft, extending to ~12 MeV, with mean energies centered around 1-2 MeV for SF and 1-5 MeV for (α,n) reactions in studied materials.

---

[20]Compared to ^{235}U and ^{232}Th.

For each process, also the average number of produced γ-rays was determined, as γ-rays and their interactions in the source foil may lead to the background event production. The average energy of these γ-rays is $\sim$1 MeV in the case of spontaneous fission. These energies are not of concern for the energy region of interest of the SuperNEMO experiment. The γ-ray energies can extend up to $\sim$10 MeV in the case of (α,n) reactions in studied materials, however, the gamma yields are relatively low in most cases.

Higher gamma yields may, however, arise from secondary radioactivity of neutron capture reactions. Therefore, gamma cascades from (n,γ) reactions in metals of high mass in the Demonstrator were studied in the last section of this chapter. Energies of γ-rays of the highest intensities from neutron captures on copper and iron isotopes, which are of concern for the energy ROI of the SuperNEMO experiment, extend from 4 to 9.3 MeV. Electrons and electron-positron pairs, associated with internal conversion and internal pair production[21], have negligible rates or energies compared to the γ-ray cascades.

We can conclude, that from the point of view of the high energy γ-ray induced background, the dominant sources, that should be investigated, are γ-rays from captures of radiogenic neutrons on Fe and Cu isotopes, and γ-rays from $(\alpha,n\gamma)$ reactions in CuBe alloy pins that reach higher yields for energies above 4 MeV. The study of these γ-rays in the geometry of the Demonstrator is the objective of the next chapter.

---

[21]De-excitation modes competing with γ-ray emission.

Chapter 5

Monte Carlo Simulation of External Background in the SuperNEMO Experiment Induced by High Energy Gamma Rays

Simulation of high energy γ induced background in the SuperNEMO Demonstrator consists of two parts:

1. Simulation of ambient high energy γ induced background

2. Simulation of neutron induced background

Each simulation has its own dedicated section in this chapter. Firstly, the SuperNEMO simulation software is described in Section 5.2. The method and results of external ambient γ-ray induced background simulation are presented in Section 5.3, and Section 5.4 is dedicated to the complex analysis of neutron induced background. Each of these parts also contains a subsection dedicated to the analysis of attenuation of ambient radiation by shielding.

5.1   High Energy External Background Sources of the SuperNEMO Experiment

As it was described in Section 2.3, the external background of the SuperNEMO detector originates from radioactive contaminants outside the source foil, and which interact with the detector. An important component of this background are high energy γ-rays ($>$ 4 MeV) coming from the LSM laboratory environment that can lead to 2 electron events (mainly through pair production when the sign of the positron track curvature is incorrectly reconstructed).

Another important source of high energy γ-rays are neutron capture reactions on metals in construction materials - primarily iron and copper due to their large mass present in the detector. Elastic scattering of fast neutrons doesn't contribute to 2 electron events and therefore mainly thermal neutron captures are of big concern, because they lead to gamma emission from excited nucleus which can then interact with the source foil:

$$n \rightarrow^A_Z X \rightarrow^{A+1}_Z X^* \rightarrow^{A+1}_Z X + \gamma... \ \ \gamma \rightarrow interaction \ in \ foil \rightarrow 2e^- \tag{5.1}$$

Chapter 5. Monte Carlo Simulation of External Background in the SuperNEMO Experiment Induced by High Energy Gamma Rays

80

These neutrons can be ambient - coming from the laboratory - or internal to the detector - originating from nuclear interactions in construction and shielding materials of the detector.

The aim of this work is to simulate and estimate the background contributions from high energy gamma rays coming from the underground environment and (n,γ) reactions that constitute a major source of background to almost all underground experiments.

The analysis method is based on simulating gamma and neutron fluxes from their source positions according to their energy spectra and analyzing the detector's response. Calculations or measurements of gamma and neutron yields and their energy spectra are important for establishing their contribution to the background of the experiment, as the total yield indicates the number of particles that enter the sensitive volume or that are produced in the target material, and their energy spectrum determines the total number of expected background events in the region of interest.

Where measurements are available these data on fluxes and energy spectra are used (summarized in Sections 3.3.3 and 3.3.5), otherwise, we rely on theoretical calculations and simulations exploiting various software and approaches described in Chapter 4.

5.2 SuperNEMO Simulation Software - Falaise

All Monte Carlo simulations of external background were performed using the Falaise software [134] and analyzed using ROOT [135] and Sensitivity Module [136] (Falaise pipeline module to process selected data) developed by a member of SuperNEMO collaboration.

Falaise is the software system developed for the SuperNEMO experiment based on Geant4. It provides the main computational environment for the simulation, processing and analysis of data. It includes the full geometry of the detector. The three main components of the software are:

- core library: libFalaise

- main detector simulation application: FLSimulate

- main reconstruction application: FLReconstruct

FLSimulate's task is to simulate the generation and passage of particles through the SuperNEMO detector, recording the detector response and writing this to an output file. FLReconstruct's task is to read data from an output file generated by the SuperNEMO simulation, perform reconstruction on each event in the data, and write the reconstructed data to an output file. Falaise also provides FLVisualize, which is the main detector/event viewer GUI used to display simulated and reconstructed events. Figure 5.1 displays the visualization of the main parts of the SuperNEMO demonstrator in the Falaise software from the top, side and front view.

The visualization of a simulated $0\nu\beta\beta$ event in Falaise with a common vertex in the source foil and two calorimeter hits each associated with a track with negative curvature is in Figure 5.2. The ultimate goal of simulation of the γ-ray induced external background is to study and to identify events that mimic the 2 electron topology of $0\nu\beta\beta$.

5.3 Ambient Gamma Ray Induced Background

The first important step in simulation is to have input data, which in this case means to have ambient LSM γ-ray fluxes.

Chapter 5.   Monte Carlo Simulation of External Background in the SuperNEMO Experiment Induced by High Energy Gamma Rays

81
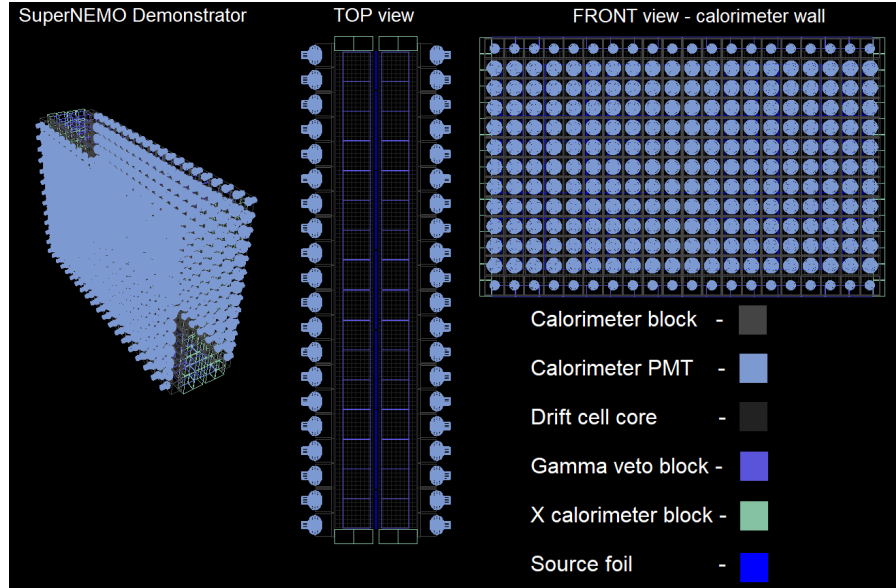
FIGURE 5.1: Visualization of the main parts of the SuperNEMO demonstrator in the Falaise software
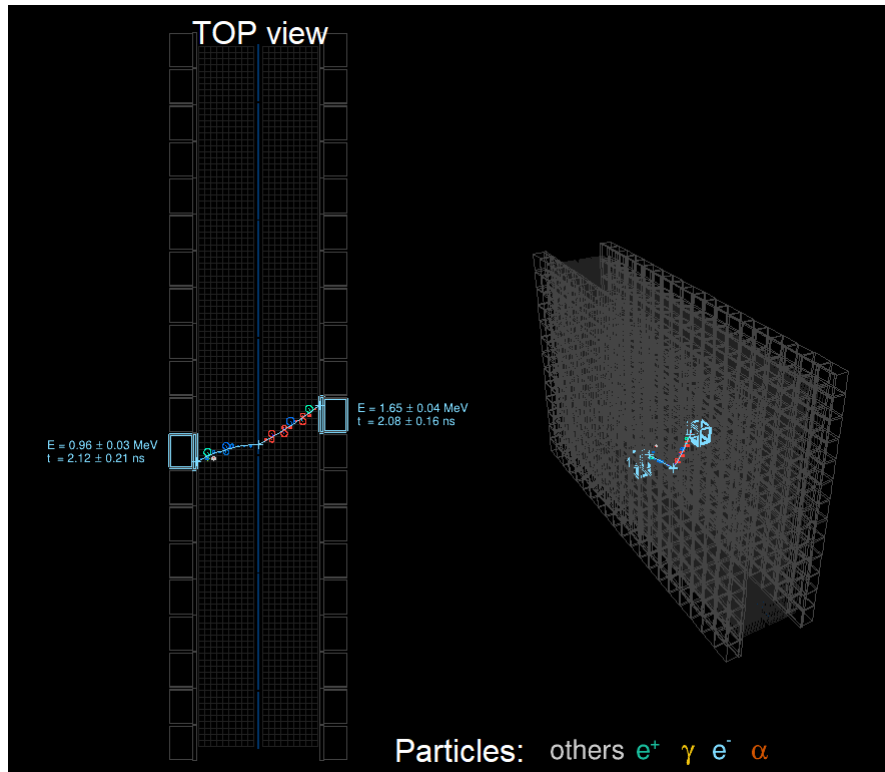
FIGURE 5.2: Visualization of a reconstructed $0\nu\beta\beta$ event simulated in the Falaise software

The extracted γ-ray fluxes measured in the LSM for each energy interval above 4 MeV summarized in Table 3.5 of Section 3.3.3 can be used for further investigations of the background of detectors operating in the LSM. A spectrum of these fluxes can be approximated by a flat spectrum in each interval, normalized to a measured value of flux, according to Figure 5.3.

Chapter 5. Monte Carlo Simulation of External Background in the SuperNEMO Experiment Induced by High Energy Gamma Rays

82
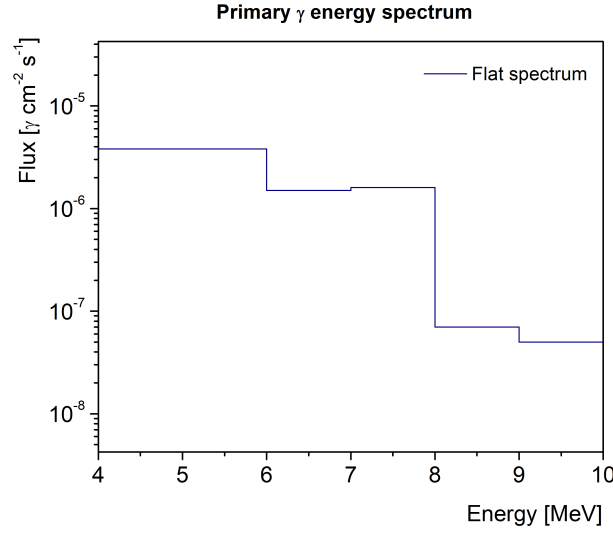
FIGURE 5.3: Generated flat primary LSM γ energy spectrum

The second step is to estimate the flux entering the detector after the installation of passive shielding.

5.3.1 Simulation of γ-ray Attenuation by Shielding

The main objective of this task has been to evaluate LSM γ-ray attenuation and investigate different shielding configurations for the SuperNEMO experiment. For this purpose, a simple Geant4 simulation has been used. Shielding of basic rectangular parallelepiped shape of given material was built around the detector and fluxes passing through the shield and reaching the detector were simulated. To stop the particles from backscattering and counting them more than once, each particle was killed after it reached the detector. LSM γ fluxes were shot towards the detector and attenuated fluxes for energy ranges 0-2, 2-4, 4-6, 6-7, 7-8, 8-9 and 9-10 MeV were extracted.

Following shielding materials and thicknesses were studied: 3, 6, 9, 12, 15 and 18 cm of iron, plus either 0, 1 or 2 cm of copper placed between the detector and the iron shield. These high Z materials are the main shielding materials against γ radiation.

Figure 5.4 shows the results of this simulation. The total γ-ray flux in LSM decreases with the thickness of the shielding material as expected. At 18 cm of iron, the influence of copper seems to be negligible as all fluxes have been asymptotically decreasing to the same value. This suggests that from the point of view of external γ-ray flux suppression, 18 cm of iron with no addition of copper is sufficient.

TABLE 5.1: Densities of studied materials

Material	Density [g/cm^3]
Iron	7.87
Copper	8.96
Polyethylene	0.941
Water	0.997

Chapter 5.   Monte Carlo Simulation of External Background in the SuperNEMO Experiment Induced by High Energy Gamma Rays

83

TABLE 5.2: Attenuated γ fluxes for different shielding configuration in each energy interval

| | Flux in energy interval $[\gamma\ \mathrm{cm^{-2}s^{-1}}]$ | | | | | | | |
	0-2 MeV	2-4 MeV	4-6 MeV	6-7 MeV	7-8 MeV	8-9 MeV	9-10 MeV	Total flux*
18 cm Fe	7.55×10^{-8}	2.00×10^{-8}	1.82×10^{-8}	6.02×10^{-9}	5.47×10^{-9}	2.57×10^{-10}	1.63×10^{-10}	1.26×10^{-7}
18 cm Fe + 50 cm H$_2$O	9.43×10^{-9}	3.05×10^{-9}	1.99×10^{-9}	5.60×10^{-10}	5.78×10^{-10}	3.38×10^{-11}	1.92×10^{-11}	1.57×10^{-8}
18 cm Fe + 20 cm PE	5.82×10^{-8}	1.99×10^{-8}	1.66×10^{-8}	5.62×10^{-9}	4.92×10^{-9}	2.66×10^{-10}	1.54×10^{-10}	1.06×10^{-7}

*LSM flux > 4 MeV:

$\Phi_\gamma = (7.02 \pm 2.10) \times 10^{-6} \gamma cm^{-2} s^{-1}$
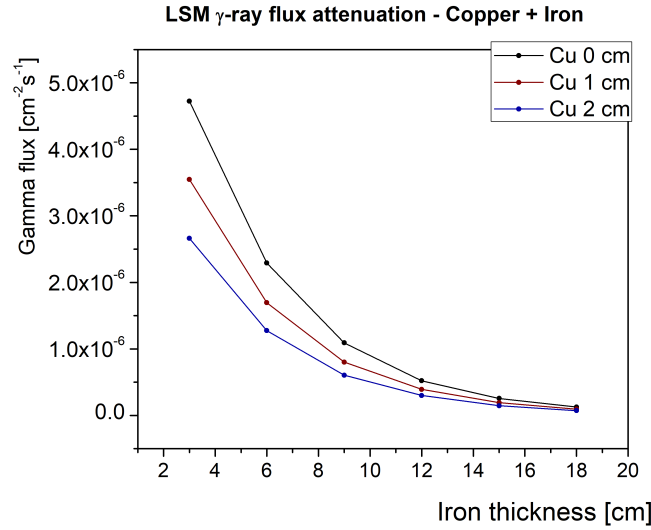
FIGURE 5.4: Simulation of attenuation of γ-ray fluxes in the LSM after passing iron and copper wall shielding

Additional attenuation is achieved with neutron shielding materials, although their attenuation power is lower due to lower density (Tab. 5.1):

- Combination of iron and water

- Combination of iron shield and polyethylene

Because the size of shielding is constraint due to limited space in the LSM laboratory, and price and installation are also key factors, maximal suggested thicknesses of water and polyethylene are 50 and 20 cm respectively. Each side of the detector may be covered by a wall of different shielding. Table 5.2 shows attenuated γ fluxes for different material configuration in each energy interval, which can be used to further investigate optimal detector shielding.

Shielding properties against neutrons will be discussed in Section 5.4 regarding neutron simulations.

5.3.2   Simulation of Ambient γ-rays in Falaise

Once all the input data for the Falaise software are available, the response of the Demonstrator detector can be investigated through Monte Carlo simulations. As a vertex generator

Chapter 5. Monte Carlo Simulation of External Background in the SuperNEMO Experiment Induced by High Energy Gamma Rays

84
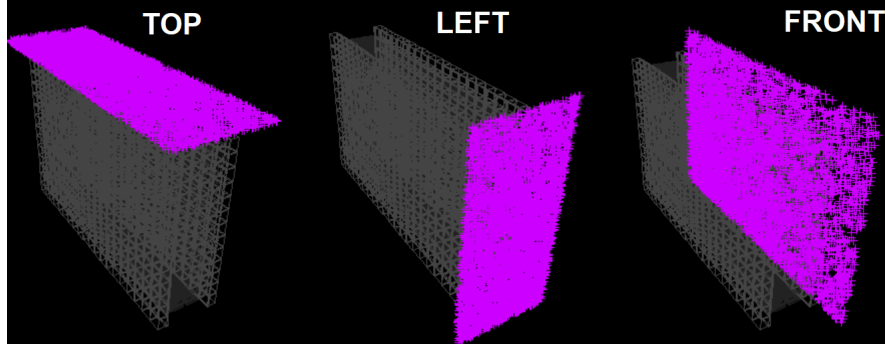
FIGURE 5.5: Example of Falaise visualization of vertices of generated γ particles from separate sides of the detector

(starting position of primary particles) so called "box model vertex generator" was used, since the external LSM γ flux comes from the surrounding environment of the detector. This generator fully encloses the detector from each side. Primary particle (γ) energies were generated from "flat energy generator" in each energy interval up to 10 MeV (0-2, 2-4, 4-6, 6-7, 7-8, 8-9 and 9-10 MeV). This generator randomly chooses the particle energy from the flat spectrum in a given energy range from E_{min} to E_{max}.

Since the attenuation of the fluxes depends on shielding configuration (material and its thickness) and each side of the detector will likely use a different configuration, the simulation in Falaise is divided accordingly: events were generated separately for each side of the detector in each individual energy interval. Figure 5.5 shows an example of simulated event vertices from the top, left and front sides of the detector. The total number of simulated events in each such category *"side+energy interval"* was 500 million making it 7×500 million, events = 3.5 billion events for each side.

All simulated data were then reconstructed using FLReconstruct. After simulation and reconstruction were complete, I looped through all events in ROOT to apply selection cuts to extract events in the desired topology.

Selection Cuts

For background events in 2 electron topology (2e$^-$), only electrons are allowed. Selection criteria used to extract background events mimicking the signal follow the reconstruction described in Section 2.1.5 in more detail. To briefly summarize the main criteria, they go as follows: event needs to have exactly 2 reconstructed calorimeter hits over 50 keV, of which 1 is over 150 keV. Electron is selected as a track with associated calorimeter hit with a negative curvature of the track[1]. Both electrons need to have a vertex on the source foil.

One of the main requirements for the signal is, that it must originate from inside the foils placed in the center of the detector, meaning the event must be internal. In establishing the origin of the event, whether the event is internal or external (from an external source), internal and external TOF probabilities are calculated.

---

[1]The tracks of charged particles are bent in the magnetic field.

Chapter 5. Monte Carlo Simulation of External Background in the SuperNEMO Experiment Induced by High Energy Gamma Rays

85

5.3.3 External High Energy γ Induced Background Events - Results

Results of the Falaise simulations were then normalized to time of one year, the corresponding surface of a side of the vertex generator and corresponding flux in each energy interval. The effect of flux attenuation by passive shielding can be seen in a comparison between deposited energy in calorimeter of all events without any selection cuts applied in Figure 5.6. In this case, the iron shield has a thickness of 18 cm, and the geometry of the neutron shield is 50 cm of water on lateral sides of the detector and 20 cm of polyethylene on top and bottom (Table 5.2). The drop in the spectrum without shielding in the energy range below 4 MeV is due to the fact that measured LSM γ fluxes were given from 4 MeV higher and only these fluxes were simulated. The LSM fluxes above 8 MeV are two orders of magnitude lower compared to fluxes from 4-8 MeV, therefore there is a drop in this region in the spectrum.
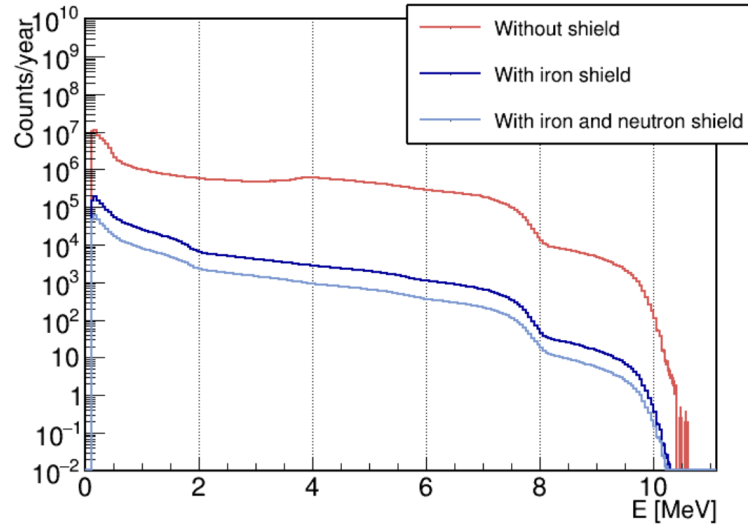
FIGURE 5.6: Comparison of deposited energy in calorimeter with and without passive shielding

Following histograms show the distributions of summed electron energies of events that passed the selection criteria of background topology. The region of interest (ROI) in the SuperNEMO experiment is the energy interval around the $Q_{\beta\beta}$ value of ^{82}Se, and that is the interval (2.8,3.2) MeV. The simulation was performed for each energy interval separately and it is, therefore, possible to see individual contributions to background events from these fluxes. This is plotted in Figure 5.7. The smallest contribution comes from fluxes above 8 MeV because the LSM fluxes in this energy region are two orders of magnitude lower compared to fluxes from 4-8 MeV (see Table 3.5). Moreover, the maximum of summed electron energies is shifted towards higher energies with a lower rate in the ROI around the $Q_{\beta\beta}$ value of ^{82}Se.

Similarly, we can also see contributions from individual sides, especially before and after shielding in Figure 5.8. The geometry of the Demonstrator is symmetrical and the results remain the same (within small statistical fluctuations) for opposite sides, and therefore the results are plotted for Top/Bottom, Left/Right and Front/Back sides. The biggest contribution after iron and neutron shield comes from the top and bottom sides, where the

Chapter 5. Monte Carlo Simulation of External Background in the SuperNEMO Experiment Induced by High Energy Gamma Rays

86
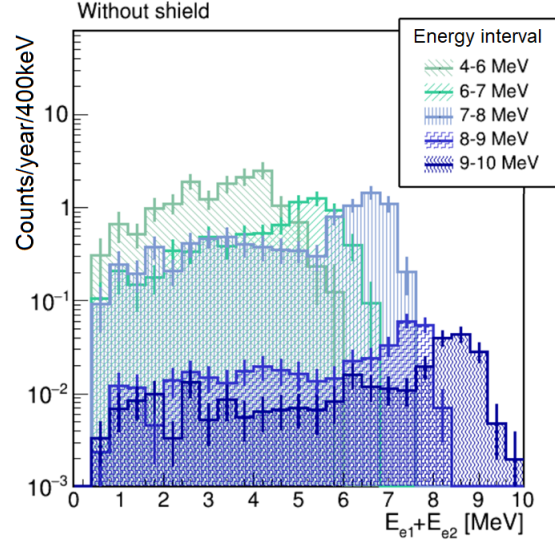
FIGURE 5.7: Background rate in the 2e⁻ channel coming from individual fluxes of each energy interval (simulation without shielding)
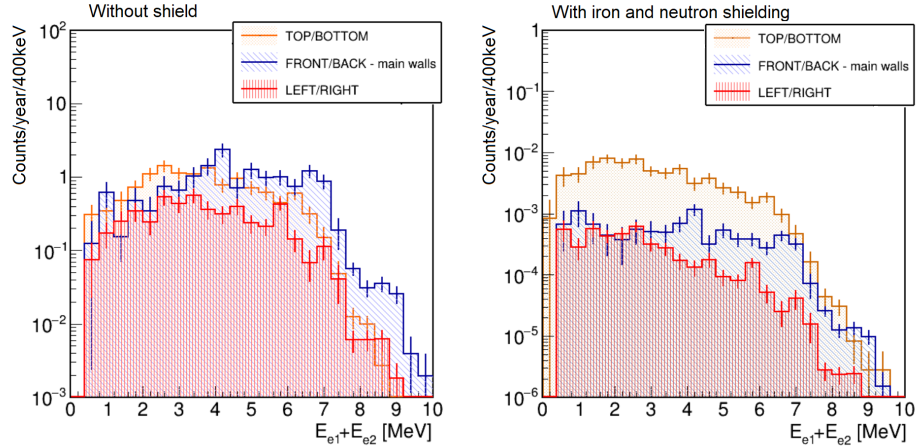
FIGURE 5.8: Background rate in the 2e⁻ channel coming from individual sides without any shielding (left) and with iron and neutron shield (right)

γ-flux is shielded the least due to the lower thickness of polyethylene used on these sides compared to water on other sides (Table 5.2).

Figure 5.9 shows the total external gamma induced background in the 2e⁻ channel. Total background rate in the 2e⁻ channel can be obtained by integrating the histograms and these results are given in Table 5.3.

The expected number of external gamma induced background events without the use of passive shielding is 3.01 ± 0.41 (stat) ± 0.91 (syst). This number is reduced down to 0.016 ± 0.002 (stat) ± 0.005 (syst) by using iron shield against γ-rays and even lower to 0.008 ± 0.001 (stat) ± 0.002 (syst) by a combination of iron and neutron shield. These results show, that with the use of the proposed shielding, no external gamma induced background event is expected in ROI after a year of running the experiment.

We can compare it with the expected number of background events from other external sources, described in Subsection 2.3.2, coming from ^{208}Tl and ^{214}Bi contamination of PMTs and radon contamination of source foil surface, tracker wire surface and field wire bulk.

Chapter 5.   Monte Carlo Simulation of External Background in the SuperNEMO Experiment Induced by High Energy Gamma Rays

87
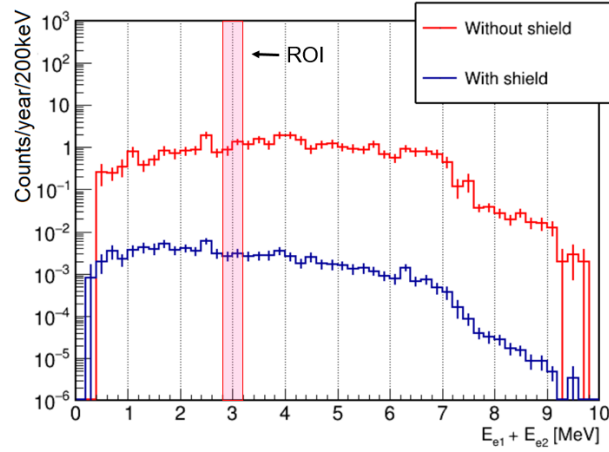
FIGURE 5.9: Background rate in the 2e⁻ channel - total external gamma induced background

TABLE 5.3: Number of expected background events in ROI

| Number of events in ROI /year | | |
No shield	Iron shield	Iron and neutron shield
3.01 ± 0.91	0.016 ± 0.005	0.008 ± 0.002

And from internal background sources - ^{208}Tl and ^{214}Bi contamination of source foil bulk. The number of expected events after 2.5 years of exposure planned for the Demonstrator from these sources is currently 2.93 ± 0.42 (stat) ± 0.17 (syst)[2]. Compared to these internal and external sources, the ambient gamma rays coming from the laboratory environment become negligible after the use of passive shielding.

---

[2]Preliminary internal analysis of collaboration

Chapter 5. Monte Carlo Simulation of External Background in the SuperNEMO Experiment Induced by High Energy Gamma Rays

88

5.4 Neutron Induced Background

To analyze the background induced by high energy gammas from neutron capture reactions, and to avoid the unreliable and undesirable cascade production in Geant4, the simulation was split into several steps:

1. Obtain input neutron energy spectra and neutron fluxes or neutron yields from available measurements or simulations

2. Generate input spectra in the Falaise software from their source positions

3. Extract neutron capture positions and fractions of captured neutrons on iron and copper isotopes in the detector from the Falaise simulation

4. Generate neutron capture gamma cascades from obtained capture positions

5. Analyze detector's response and obtain the expected number of background events in the 2 electron channel

Input energy spectra and neutron production rates, yields and fluxes from *step 1* are divided into two categories: ambient neutrons and neutrons internal to the detector from material contamination. The ambient neutrons were discussed in Section 3.3.5 and contributions of internal neutrons were summarized in Section 4.3 (their energy spectra are discussed in detail in Chapter 4). Simulations in *step 2* were then performed separately for thermal ambient neutrons, fast ambient neutrons and individually for radiogenic neutrons from each decay chain (^{238}U and ^{232}Th) - spontaneous fission neutrons and (α,n) reactions - for PMT glass bulbs, iron shield and CuBe alloy feedthrough pins. Only spontaneous fission of ^{238}U was considered as the contribution from other radionuclides is negligible in this decay mode. Vertices of source position of shielding materials were generated similarly to external γs - from box model generator enclosing the detector (Fig. 5.5) and for PMT glass and CuBe alloy pins from the bulk of the material according to Figure 5.10.
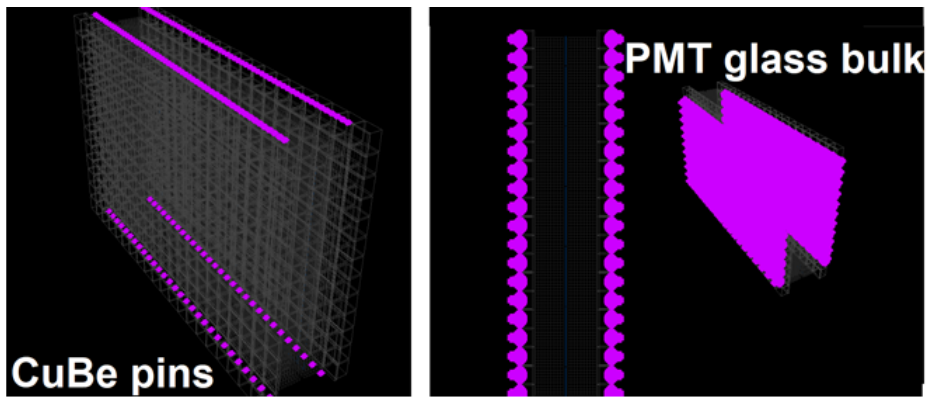
FIGURE 5.10: Example of Falaise visualization of vertices of generated neutrons from bulk of CuBe pins and PMT glass

In *step 3*, for each simulation of *step 2*, the capture positions were extracted for each of these isotopes: ^{54}Fe, ^{56}Fe, ^{63}Cu and ^{65}Cu. The fraction of neutron captures represents the number of captured neutrons on individual isotopes out of all generated neutrons. Physical processes are well implemented, tested and optimized in Geant4 for such task. This step

Chapter 5. Monte Carlo Simulation of External Background in the SuperNEMO Experiment Induced by High Energy Gamma Rays

89

is described again in Subsection 5.4.2 in more detail. The problem arises with subsequent (n,γ) reactions. The extracted positions were then used as vertex generators for gamma cascades obtained from the DICEBOX simulation in Section 4.4.3 in the *4th step*. In *step 5*, the background rate in the 2 electron channel was analyzed following the reconstruction and selection criteria described in Section 5.3.2.

5.4.1 Simulation of Neutron Attenuation by Shielding

Similarly to the external γ flux analysis, attenuated neutron flux and spectrum have to be obtained. The study of shielding performance of different materials and thicknesses for ambient neutron attenuation was previously conducted and discussed by a member of SuperNEMO collaboration in work [116]. In this work, only fast LSM neutron flux was considered. For purposes of my work, the code and approach of work [116] was utilized, but the simulation was split for thermal and fast neutrons separately. The approach of the simulation consists of propagating neutrons from LSM spectrum through a simple wall of polyethylene (PE), borated polyethylene (PEB), water, borated water (waterB), and through a combination of these materials with 18 cm of iron. The incoming neutron spectrum was normalized to 10^{-6} n s^{-1}cm^{-2} so that the resulting spectrum could be easily normalized to any measured value of LSM flux. Results of this simulation are plotted in Figure 5.11. For the thermal neutron attenuation, only some thicknesses were simulated as for the maximum plotted thickness for a given material, overall good suppression of thermal neutrons has already been achieved. For example, behind the wall of 16 cm of polyethylene, the ratio of outcoming and incoming neutron flux is only 0.5 %, and this ratio is only 0.004 % for 40 cm of water.

From the point of view of background simulations, the fluxes that enter the iron shield are more important than the fluxes that reach the detector behind the iron shield, because the neutrons can capture here and subsequently produce gammas that can lead to background event production. These fluxes are given in Table 5.4. As it is also important to determine the energy spectrum of outcoming neutrons, not only fluxes but also energies of neutrons were stored. These results are plotted in Figure 5.12 for relevant thicknesses of materials considered now[3] for the shielding configuration used for the Demonstrator. Since the composition of PE and PE(B) is the same, except for the addition of boron, the attenuated spectrum of neutrons looks the same, but the same thickness of PE(B) performed better in terms of outcoming flux. The main difference can be seen in the thermal part of the spectrum, where the addition of boron plays important role in neutron absorption. Comparison of outcoming spectra of neutrons that were thermalized in these shielding materials is shown in Figure 5.13.

It is clear that borated polyethylene is the best performing shielding material. It has the ability to suppress incoming neutron flux and absorb thermalized neutrons. In suppression abilities, this material is followed by pure polyethylene. Water, however, is also performing well if sufficient thickness is used. However, one has to also consider the radiogenic neutron contributions of these materials. Table 4.5 showed measured activities and activity limits of contaminated Demonstrator components. Among these available materials, PE(B) bricks are the most contaminated. Since SuperNEMO places importance on the selection of radiopure materials this has to be taken into account. Especially, since pure

---

[3]In the time of writing this thesis. Borated water is no longer considered due to laboratory safety rules. Thicknesses of materials are based on laboratory size and material cost restrictions.

Chapter 5. Monte Carlo Simulation of External Background in the SuperNEMO Experiment Induced by High Energy Gamma Rays

90
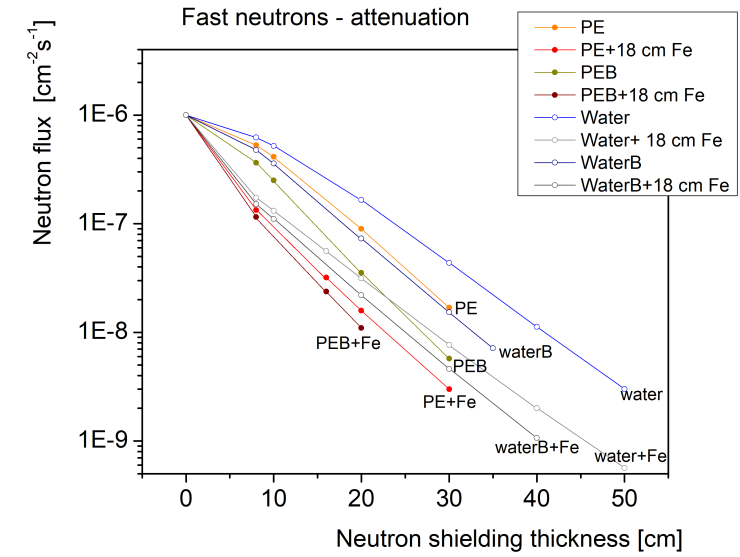
(A)
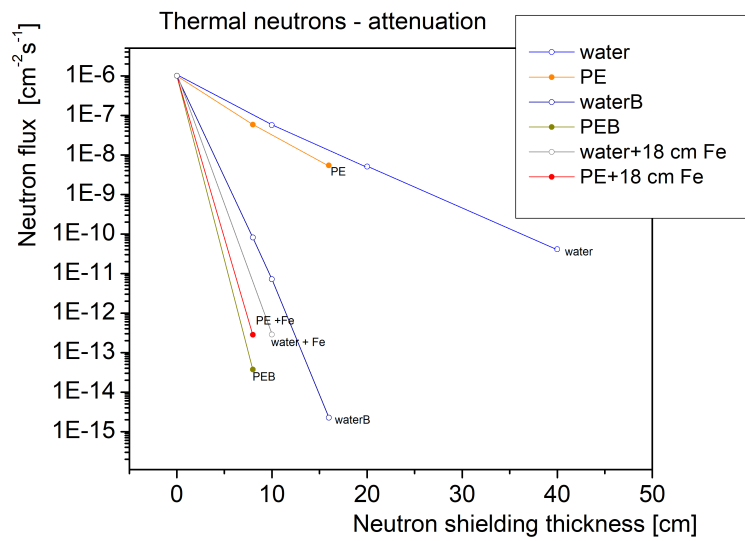
(B)

FIGURE 5.11: Attenuation of fast and thermal LSM neutron fluxes by different shielding

Chapter 5. Monte Carlo Simulation of External Background in the SuperNEMO Experiment Induced by High Energy Gamma Rays

91
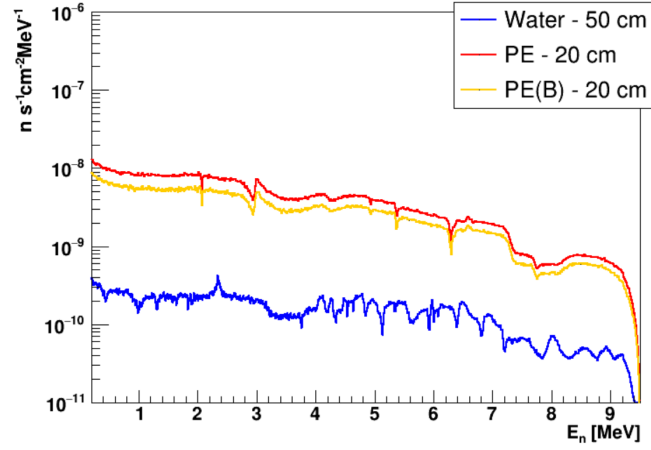
FIGURE 5.12: Spectrum of outcoming neutrons for 50 cm of water and 20 cm of polyethylene and borated polyethylene

TABLE 5.4: Total outcoming neutron fluxes after attenuation of environmental fast LSM neutron spectrum

Thickness [cm]	Total outcoming flux [$s^{-1}cm^{-2}$]		
	PE	PE(B)	Water
0	1.00×10^{-6}	1.00×10^{-6}	1.00×10^{-6}
8	5.28×10^{-7}	3.64×10^{-7}	6.21×10^{-7}
10	4.13×10^{-7}	2.50×10^{-7}	5.20×10^{-7}
20	8.94×10^{-8}	3.54×10^{-8}	1.66×10^{-7}
30	1.69×10^{-8}	5.72×10^{-9}	4.35×10^{-8}
40	-	-	1.12×10^{-8}
50	-	-	3.01×10^{-9}
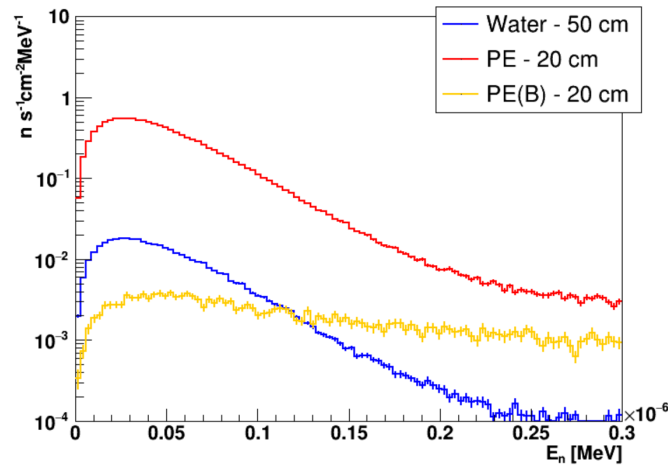
FIGURE 5.13: Spectra of outcoming thermalized neutrons for 50 cm of water and 20 cm of polyethylene and borated polyethylene

Chapter 5. Monte Carlo Simulation of External Background in the SuperNEMO Experiment Induced by High Energy Gamma Rays

92

polyethylene also shows good suppression abilities. The use of pure polyethylene could be justified by Monte Carlo simulations of neutron induced background considering this shielding configuration, provided that the results would show negligible contributions to the expected background. Radiogenic neutron production in pure polyethylene is also the lowest out of all sources.

5.4.2 Neutron Capture Positions and Fractions

The high energy γs of interest that can lead to external background event production arise from thermal neutron captures on iron and copper. Iron is used as a frame of the Demonstrator[4] and some copper parts of the detector are, for example, calibration source carrier frame, copper-beryllium feedthrough pins and vertical beam rods of the source foil frame. Neutrons can capture, of course, on other material present in the detector as well (e.g. H, Ni, Si, Co, Ca etc.), but their abundance and mass in the detector is overall small or γs from the de-excitations of these nuclei don't reach very high energies. The capture process of neutron depends on its primary position where it originates and on its energy. Fast neutrons first scatter in the detector and subsequently thermalize until they get captured. A large amount of neutrons scatters in the detector and leaves the detector volume altogether without eventually capturing. That is why it is also important to estimate the fraction of captured neutrons from each source on each isotope.

Each neutron in the simulated event was tracked until its track ended with a thermal nCapture process which lead to either ^{55}Fe, ^{57}Fe, ^{64}Cu or ^{66}Cu creation and the x, y and z position of this end of the track was stored. Figure 5.14 shows an example of thermal neutron capture positions on iron and copper isotopes in the Demonstrator from two different perspectives. The positions are the results of captures of ambient neutrons coming from the laboratory environment (the box model generator in case of this simulation).

If the primary neutrons are generated from PMTs or CuBe pins within the detector, the capture positions remain almost the same, as the Demonstrator geometry and materials are unchanged, however, they tend to be concentrated on a specific side of the detector. For example, since the CuBe alloy pins are positioned on top and bottom of the detector (see. Fig. 5.10), the capture positions are also denser on these sides, as can be seen in Figure 5.15 (A).

These capture positions (examples shown in Fig. 5.15 and 5.14) will then be used as event vertex generators of gamma cascades[5].

There is another important fact to take into account already mentioned in Section 5.4.1. The baseline design for shielding the detector against γs consists of 18 cm thick iron. This introduces a large amount of iron for the neutrons to capture on and thus, a passive shield designed to suppress radiation can turn itself into a source of background. Additionally, neutrons that would otherwise scatter in the detector and leave, can now scatter in the iron shield, return back to the detector and capture on copper and iron in the detector volume. This ultimately increases the number of captures on all isotopes. For this reason, the simulation to obtain capture positions and capture fractions was performed for geometry without the iron shield - to see background contribution of the unshielded detector, and for geometry with the iron shield included - to investigate and estimate the background for the

---

[4]Some iron is also present in the concrete floor of the LSM.

[5]In these example figures, only a small sample of vertices is shown. In actual simulation larger statistics of positions is used.

Chapter 5.   Monte Carlo Simulation of External Background in the SuperNEMO Experiment Induced by High Energy Gamma Rays

93

(A) Iron
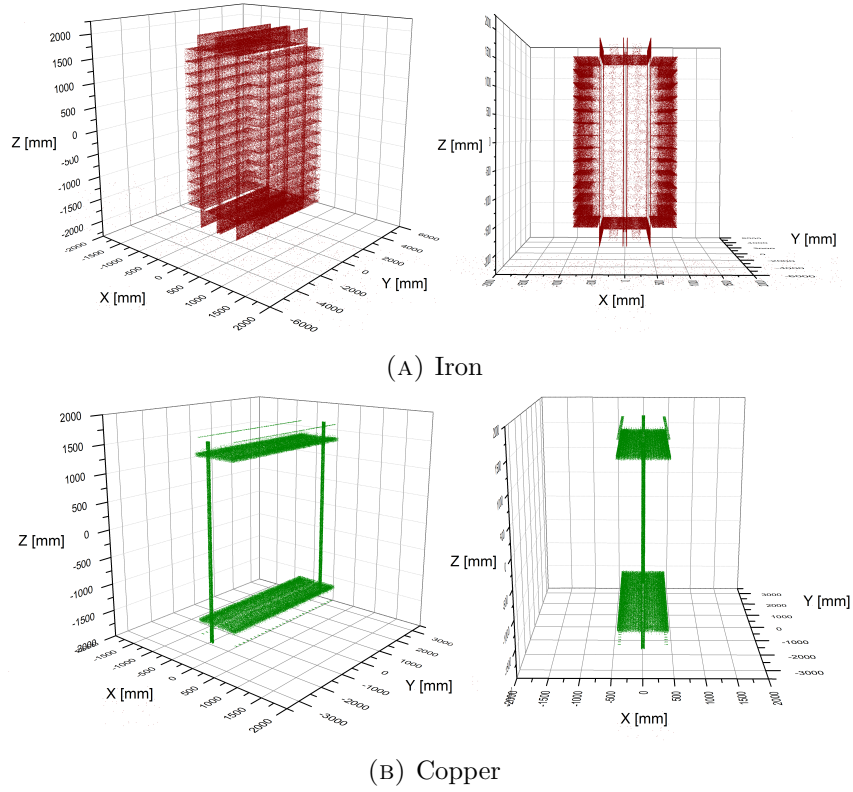
(B) Copper

FIGURE 5.14: Thermal neutron capture positions on iron and copper isotopes

(A) No shield
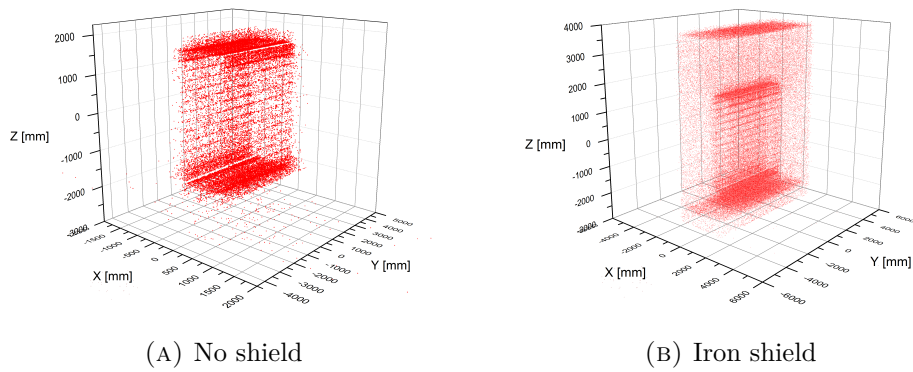
(B) Iron shield

FIGURE 5.15: Thermal neutron capture positions on iron from spontaneous fission of ^{238}U from CuBe pins for geometry with and without iron shield

Chapter 5. Monte Carlo Simulation of External Background in the SuperNEMO Experiment Induced by High Energy Gamma Rays

94

final design of the Demonstrator and to investigate the contributions to the background by introducing new materials [6]. Figure 5.15 (B) shows capture positions in iron for geometry with included iron shield.

Fractions of neutron captures, f_i, were similarly obtained for each isotope i in all simulations for each neutron source by counting the number of neutron captures out of all simulated neutrons. This way the abundance of each isotope is also taken into account. Stored fractions from simulations with and without the iron shield are summarized in Tables 5.5 and 5.6 respectively. The aforementioned point about the increase of the number of captures by introducing the iron shield is clear when comparing these tables. The difference in the number of captures between iron and copper can be explained by higher iron mass and abundance in the detector. And the difference in the number of captures between individual iron isotopes and individual copper isotopes can be explained by their natural abundances. This is more prominent in the case of ^{55}Fe and ^{57}Fe, where the difference between ^{54}Fe and ^{56}Fe abundances in ^{nat}Fe is more distinct.

TABLE 5.5: Fractions of neutron captures without iron shield

Neutron source		Fractions of neutron captures f_i [%]			
		^{55}Fe	^{57}Fe	^{64}Cu	^{66}Cu
Ambient neutrons	Thermal	0.61	10.94	0.16	0.034
	Fast	0.20	3.56	0.51	0.11
PMT glass	(α,n) ^{232}Th	0.63	11.05	0.90	0.19
	(α,n) ^{238}U	0.62	11.06	0.89	0.19
	SF ^{238}U	0.63	11.05	0.90	0.19
CuBe pins	(α,n) ^{238}U	0.32	5.59	1.98	0.43
	SF ^{238}U	0.33	5.94	2.18	0.48

TABLE 5.6: Fractions of neutron captures with iron shield included in the geometry

Neutron source		Fractions of neutron capture f_i [%]			
		^{55}Fe	^{57}Fe	^{64}Cu	^{66}Cu
PMT	(α,n) ^{232}Th	1.674	28.57	1.15	0.27
	(α,n) ^{238}U	1.70	28.80	1.15	0.25
	SF ^{238}U	1.70	28.77	1.11	0.24
CuBe	(α,n) ^{238}U	1.36	22.17	2.42	0.53
	SF ^{238}U	1.48	23.43	2.57	0.57
Iron shield – radiogenic	(α,n) ^{232}Th	0.97	14.12	0.34	0.07
	(α,n) ^{238}U	0.97	14.16	0.34	0.08
	SF ^{238}U	0.93	13.68	0.35	0.08

---

[6]For the purpose of this study, 18 cm thick iron shield was incorporated in the Demonstrator geometry in the Falaise software.

Chapter 5. Monte Carlo Simulation of External Background in the SuperNEMO Experiment Induced by High Energy Gamma Rays

95

Now we have to consider the shielded neutron flux. Particle energies were sampled according to attenuated neutron spectra for water and polyethylene shielding from Figure 5.12 and simulation was split separately for each side. Again, since the geometry of the Demonstrator is symmetrical the results remain the same (within statistical fluctuations) for opposite sides, and therefore the results are given in Table 5.7 for Top/Bottom, Left/Right and Front/Back sides.

TABLE 5.7: Fractions of neutron captures from shielded neutron flux with iron shield included in the geometry

Side	Isotope	Fractions of neutron captures f_i [%]	
		Shielded flux by water	Shielded flux by PE
Top / Bottom	^{55}**Fe**	1.10	1.13
	^{57}**Fe**	16.65	17.06
	^{64}**Cu**	1.04	1.03
	^{66}**Cu**	0.23	0.23
Left / Right	^{55}**Fe**	1.22	1.24
	^{57}**Fe**	18.31	18.82
	^{64}**Cu**	0.83	0.82
	^{66}**Cu**	0.19	0.18
Front / Back	^{55}**Fe**	1.46	1.49
	^{57}**Fe**	23.13	23.65
	^{64}**Cu**	0.85	0.80
	^{66}**Cu**	0.17	0.17

One can see, by comparing the neutron fractions in the presented tables, that fractions from individual radiogenic processes (SF, (α,n)) within neutron sources (PMT, iron, CuBe) are similar and they differ mostly in between the sources. This suggests that the position from which the neutrons are emitted, and the material in which these neutrons subsequently propagate, are more important. The fact that the radiogenic processes yield within each neutron source similar neutron capture fractions could be attributed to the fact, that the energy spectra of all processes are soft, with mean energies often centered around 2-3 MeV, and so the energy spectra from which the neutron energies were sampled do not differ significantly. This may justify and explain approaches used in some works, where the radiogenic neutrons are often generated uniformly in energy range of 0-10 MeV, for example, in [137].

The main advantage of this approach is that it uses cascades generated in a correlated way and it avoids the unreliable cascade production in the Geant4 package, where the results showed a violation of energy conservation in neutron capture events. This is very important for the task of estimation of neutron induced background. Splitting the simulation into several steps also allows to study the detector response to gammas from individual

Chapter 5. Monte Carlo Simulation of External Background in the SuperNEMO Experiment Induced by High Energy Gamma Rays

96

isotopes and to better understand contributions from individual background sources. It is important to mention that this approach doesn't take into considerations other modes of de-excitations after neutron capture, namely internal conversion and internal pair production. But as it was discussed in Section 4.4.3, γ emission dominates all de-excitation modes in all cases and contributions from IC and IPP can be considered negligible. Therefore, only gammas were generated. However, the branching ratios of γ emission were taken into account. Additionally, DICEBOX simulation doesn't treat consecutive decays of compound nuclei, such as beta decay of ^{66}Cu in this case. However, the Q_β value of ^{66}Cu is only 2642 keV [60] and so it doesn't reach the region of $Q_{\beta\beta}$ value of ^{82}Se. Moreover, given the lower abundance of ^{65}Cu isotope in ^{nat}Cu, it can be seen from the number of neutron capture fractions that the production of ^{66}Cu is the least dominant.

5.4.3 Neutron Capture γ-ray Induced Background Events - Results

In the *4th step* of this analysis, neutron capture gamma cascades were generated from obtained capture positions in Falaise. Again, simulation was performed for each isotope and each neutron source separately twice - with and without iron shield included in the geometry. All simulated data were then reconstructed using FLReconstruct. After simulation and reconstruction were complete, I looped through all events in ROOT to apply selection cuts to extract events in the desired topology.

To take into account the branching ratios of de-excitations of iron and copper nuclei via γ cascades and the fractions of captures, two normalization factors (NF) are used for the histograms based on whether neutron fluxes or yields were used:

$$NF_{for\ flux} = \frac{\Phi_n\,S\,t}{N}f_i, \tag{5.2}$$

where Φ_n is the neutron flux, S is the surface of neutron generator, t is time (=1 year), f_i is the fraction of neutron captures on isotope i ($i=^{54}$Fe, ^{56}Fe, ^{63}Cu or ^{65}Cu) and N is the number of simulated neutron capture reactions; or:

$$NF_{for\ yield} = \frac{Y_n\,A_j\,t}{N}f_i, \tag{5.3}$$

where Y_n is the neutron yield and A_j is the activity of radioisotope j ($j=^{238}$U or ^{232}Th).

Neutron fluxes were taken from experimental data, from Equations 3.11 and 3.9, for fast and thermal neutron fluxes in LSM respectively. Neutron yields were taken from the results of simulations a calculations in Chapter 4, from Tables 4.1 and 4.4 for spontaneous fission and (α,n) reactions respectively. Activities of ^{238}U and ^{232}Th were taken from measurements of material activities summarized in Table 4.5. The fractions of neutron captures corresponding to each process were taken from Tables 5.5, 5.6 and 5.7.

Firstly, we can investigate which element, copper or iron, contributes the most to the background rate in the 2e$^-$ channel. We can do this by not considering the capture fractions of generated neutrons. Figure 5.16 (left) shows contributions to background events from neutron captures on copper and iron isotopes normalized to counts per neutron capture obtained from Falaise simulation of gamma cascades.
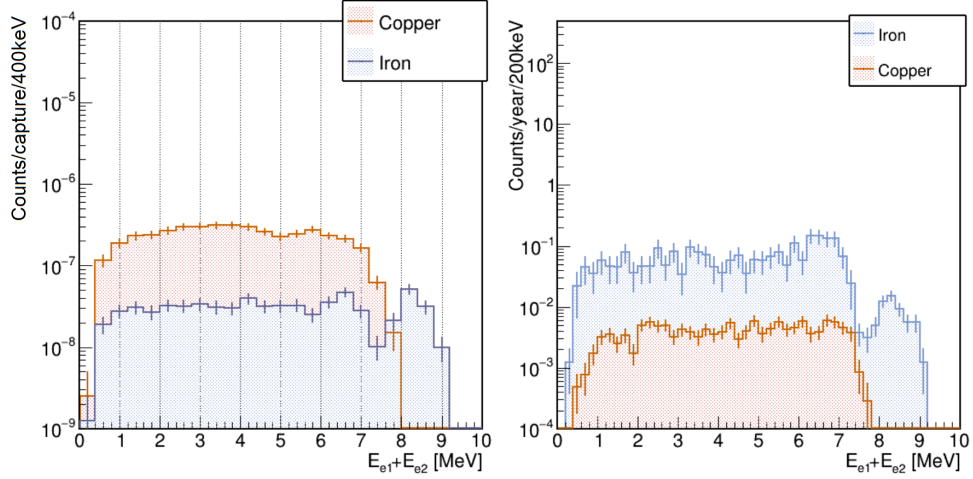
FIGURE 5.16: **Left:** Contributions to background events from neutron captures on copper and iron isotopes. **Right:** Background rate in the 2e$^-$ channel from ambient neutron fluxes.

This plot doesn't take into account the abundance of isotopes in ^{nat}Fe and ^{nat}Cu, but the dominant contribution from copper isotopes is visible. This can be attributed to the fact, that copper materials are closer to the source foil where they can interact without being flagged by the calorimeter first. Additionally, in comparison with iron, the thermal neutron capture cross-sections on copper isotopes are higher [138]. However, due to lower mass and abundance of copper in the detector, the capture fractions on copper isotopes are low enough to reduce the overall contribution below iron as can be seen in Figure 5.16 (right). This figure shows the background analysis of thermal and fast ambient neutron fluxes, separately for captures on copper and iron. The bump at the end of the iron spectrum comes from gamma cascades from ^{55}Fe, where the gammas extend up to ~ 9.3 MeV.

Besides unshielded flux, the background from contamination of several materials was analysed. The background contributions without shielding are as follows: ambient neutron flux, radiogenic neutrons from CuBe alloy pins, gammas from $(\alpha,n\gamma)$ reactions from CuBe alloy pins[7] and radiogenic neutrons from PMT glass. Their individual contributions can be seen in Figure 5.17 (left).

By far the most dominant source of background, in this case, is the ambient flux. It is followed by the γ production from the excited state of ^{12}C* from CuBe pins. It has a distinct feature with rapid drop above 4 MeV. This is due to the drop of yield for 9.6 MeV gamma from the 3rd excited state of ^{12}C by 2 orders of magnitude compared to the 4.4 MeV gamma yield (see Fig. 4.16).

The background contributions with passive shielding include: shielded ambient neutron flux, radiogenic neutrons from CuBe alloy pins, gammas from $(\alpha,n\gamma)$ reactions from CuBe alloy pins, radiogenic neutrons from PMT glass, and also radiogenic neutrons from the iron shield. Their individual contributions in this case can be seen in Figure 5.17 (right). The shielding geometry, in this case, is 50 cm of water on the lateral sides and 20 cm of polyethylene on the top and bottom. The iron shielding is creating a confinement effect on neutrons produced by sources which are internal to the detector (CuBe pins and PMT) and therefore leading to an increase of the number of background events for these

---

[7]γ production from excited state of $^{12}C^*$ after (α, n) on ^{9}Be.

Chapter 5. Monte Carlo Simulation of External Background in the SuperNEMO Experiment Induced by High Energy Gamma Rays

98
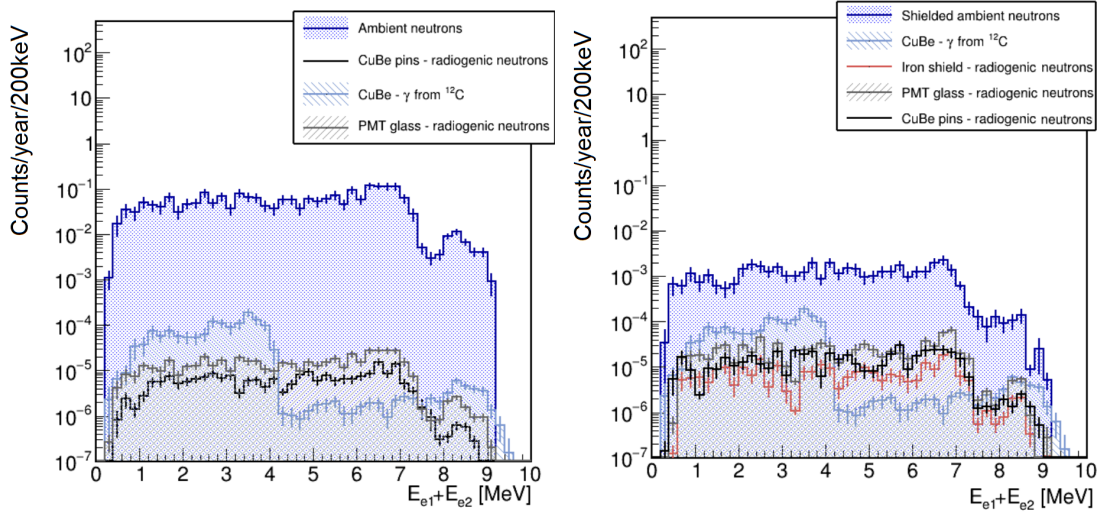
FIGURE 5.17: Background rate in the 2e$^-$ channel - neutron induced background from neutron captures on Fe and Cu without (left) and with (right) shield and γs from excited states of $^{12}C^*$

components. However, gammas from neutron captures in the iron shield do not contribute to the background rate significantly as they were simultaneously attenuated in the shield. The expected number of background events in ROI from individual sources are summarized in Table 5.8.

Overall, the contribution from radiogenic neutrons is negligible, compared to the ambient neutron flux, thanks to the selection of radioactively pure materials and strict activity limits. Figure 5.18 shows the total contribution to the background from all sources.
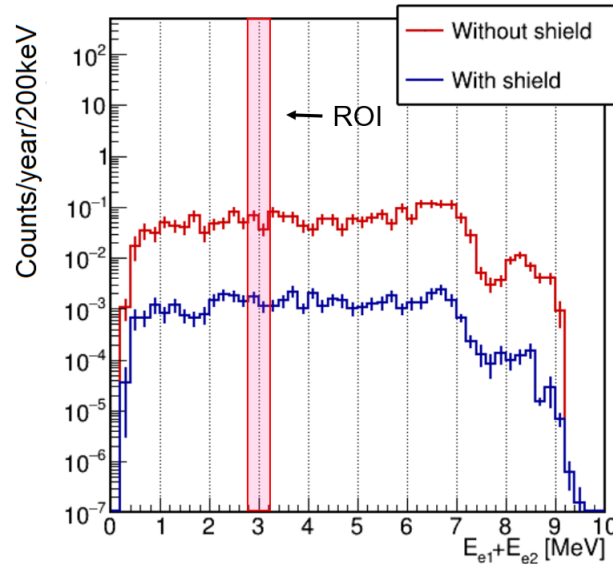
FIGURE 5.18: Background rate in the 2e$^-$ channel - total neutron induced background from neutron captures on Fe and Cu

The total background rate without the shield of 0.2 ± 0.03 (syst) ± 0.02 (stat) per year was reduced down to 0.0034 ± 0.0007 (syst) ± 0.0006 (stat) per year with the use of

Chapter 5. Monte Carlo Simulation of External Background in the SuperNEMO Experiment Induced by High Energy Gamma Rays

99

TABLE 5.8: Number of expected background events in ROI

	Background events /year	
Source	**Without shield**	**With shield**
Ambient	0.2	0.003
CuBe pins - radiogenic	0.00002	0.00004
CuBe pins - γs from $^{12}C^*$	0.00026	0.00026
PMT - radiogenic	0.00004	0.00005
Iron shield - radiogenic	-	0.00001
Total	0.2 ± 0.03	0.003 ± 0.001

passive shielding. Most of the incident fast neutrons were moderated to lower energies by the water or polyethylene and then captured in the iron shield. Gammas emitted in the neutron capture reactions were subsequently shielded from the detector by the iron shield.

Different Shielding Geometries

Due to possible laboratory constraints, there are several possibilities for the final design of the shielding. For simplicity, the naming convention of individual sides corresponds to the positioning of the detector inside the laboratory according to Figure 5.19.
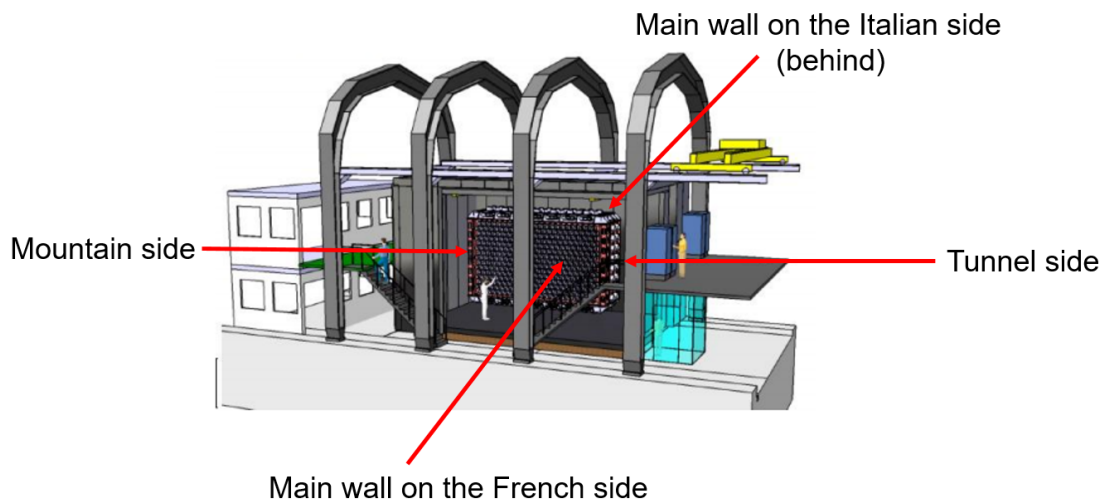
FIGURE 5.19: Position of the Demonstrator in LSM

Possible constraints due to lack of space concern the mountain side, where the electronics of the data acquisition system are placed, and the main wall on the French side of the laboratory, where the staircase leads to the main hall. The geometry discussed thus far corresponds to Geometry 1 in Table 5.9. The considered changes in the geometry are highlighted in bold font in the table.

Chapter 5. Monte Carlo Simulation of External Background in the SuperNEMO Experiment Induced by High Energy Gamma Rays

100

TABLE 5.9: Different neutron shielding geometries considered for the Demonstrator

Geometry 1	Geometry 2	Geometry 3	Geometry 4
Top: PE 20 cm	Top: PE 20 cm	Top: PE 20 cm	Top: PE 20 cm
Bottom: PE 20 cm	Bottom: PE 20 cm	Bottom: PE 20 cm	Bottom: PE 20 cm
Tunnel side: Water 50 cm	Tunnel side: Water 50 cm	Tunnel side: Water 50 cm	Tunnel side: Water 50 cm
Mountain side: Water 50 cm	Mountain side: Water 50 cm	**Mountain side: PE 20 cm**	**Mountain side: PE 20 cm**
IT main wall: Water 50 cm	IT main wall: Water 50 cm	IT main wall: Water 50 cm	IT main wall: Water 50 cm
FR main wall: Water 50 cm	**FR main wall: Water 40 cm**	FR main wall: Water 50 cm	**FR main wall: Water 40 cm**

The attenuated fluxes were already discussed in Section 5.4.1 and they were used for this analysis. The analysis method remains the same as in the previous section. Table 5.10 shows the number of expected background events from attenuated ambient neutron flux for different shielding configurations. The most affected side could be the mountain side where the water shielding would be replaced by 20 cm of PE, which attenuates the ambient flux less than 40 cm or 50 cm of water would. However, this side also has the smallest surface and therefore the number of neutrons that enter the detector from this side is also the smallest. While the background rate is increasing with smaller shielding thickness, all geometries are reaching the target of a negligible level of background.

TABLE 5.10: Background rate in the $2e^-$ channel from attenuated ambient neutron flux for different shielding configurations

Shielding configuration	Background events /year[*]
Geometry 1	0.0030
Geometry 2	0.0032
Geometry 3	0.0042
Geometry 4	0.0044

[*] $\sim \pm 20\%(\text{stat})$

The study included in this section and in Sections 5.4.1 and 5.3.1 was presented to the technical board of SuperNEMO, and was an important input to finalise the design of the shielding, with *geometry option 4* being the most probable.

5.5 Summary of the High Energy γ-Ray Induced External Background

In this chapter, the external background in the SuperNEMO experiment induced by high energy gamma rays was studied. The two main sources of these γ-rays under consideration were high energy gamma rays coming from the underground environment, and (n,γ) reactions from ambient neutrons and radiogenic neutrons produced in materials with the highest uranium and thorium contamination. Ambient radiation can be significantly suppressed by passive shielding. The best results are achieved for the shielding Geometry 1 (Table 5.10) - the iron shield of thickness of 18 cm, and 50 cm of water on lateral sides of the detector and 20 cm of polyethylene on top and bottom.

Chapter 5. Monte Carlo Simulation of External Background in the SuperNEMO Experiment Induced by High Energy Gamma Rays

101

The number of expected external background events after 2.5 years of exposure planned for the Demonstrator, from external and internal sources described in Subsection 2.3.2 and external sources investigated in this work, are summarized in Table 5.11. Background rates for the sources investigated in this work are from results of simulations with the use of shielding Geometry 1.

TABLE 5.11: Number of expected external background events in the energy ROI after 2.5 years of exposure

Source	Background rate
$2\nu\beta\beta^a$	0.03 ± 0.02 (stat)
^{208}Tl external^a	0.60 ± 0.42 (stat) ± 0.06 (syst)
^{214}Bi external^a	0.10 ± 0.01 (stat) ± 0.01 (syst)
Ambient γ-rays	0.02 ± 0.003 (stat) ± 0.005 (syst)
CuBe pins - γs from ^{12}C*	0.00065 ± 0.00013 (stat) ± 0.0001 (syst)
Ambient neutrons	0.0075 ± 0.0015 (stat) ± 0.0018 (syst)
Radiogenic neutrons	0.00025 ± 0.00005 (stat) ± 0.00003 (syst)
^{208}Tl internal^a	0.82 ± 0.02 (stat) ± 0.16 (syst)
^{214}Bi internal^a	1.41 ± 0.07 (stat) ± 0.01 (syst)

^{a}internal analysis of collaboration

We conclude, that background induced by high energy gamma rays is negligible compared to the background from ^{208}Tl and ^{214}Bi contamination of the source foils. The background events arising from ambient radiation are the dominant source investigated in this work. However, they were suppressed by passive shielding, which proved to be effective by reducing the number of expected background events by several orders of magnitude. The least contributing source of background are radiogenic neutrons. However, background rate at this level may become a problem for next generation experiments aiming for better sensitivity. It should be evaluated and possibly improved by continuing efforts on ultra-low background requirements needed in rare event searches.

Chapter 6

Comparison of Monte Carlo Simulations with Experimental Data

Measured experimental data can be used to validate the Monte Carlo based method used throughout Chapter 5 to estimate the external background in the SuperNEMO experiment induced by ambient gamma rays and neutrons. The complete design, construction and installation of the calorimeter was finished during the duration of this thesis project with an extensive commissioning campaign underway. Without an operating tracker yet, and therefore without any track reconstruction and particle identification, the commissioning data collected in calorimeter-only configuration could be used to probe MC vs DATA agreement.

Two measurements have been preformed in order to compare results of suggested Monte Carlo model with experimental data. Firstly, a measurement with a weak neutron (americium-beryllium) source was performed in order to study detector's response to radiative neutron capture and to investigate the validity of model proposed in Section 5.4 to evaluate neutron induced background.

Second measurement aimed to obtain data with sufficient statistics in the high energy region to compare input ambient gamma and neutron fluxes measured in the LSM from Tables 3.5 and 3.6 which were used in Sections 5.3 and 5.4 for further investigations of the background.

6.1 Americium-Beryllium (AmBe) Neutron Source

A measurement with a weak neutron AmBe source was performed during a data taking stage with the SuperNEMO calorimeter. Unfortunately, only the source strength was known and no information about its energy spectrum, composition or density was provided. To study and validate the model of radiative neutron capture in the detector (see Section 6.1.2), we use the method described previously in Section 4.2 to first determine the spectrum and rate of neutrons of such AmBe source, as well as the gamma component. This can later be used for validation between Monte Carlo simulation and real experimental data.

6.1.1 Simulation of Neutron and Gamma Energy Spectra of AmBe Source

AmBe Source

A representative alpha-beryllium neutron source, that combines an α emitter with a stable low-Z isotope ^{9}Be, is ^{241}Am^{9}Be source. AmBe is a source of fast neutrons widely employed as a calibration source for a variety of instrumentation [139] and it is also one of the ISO[1] recommended calibration standards for neutron radiation [140]. Currently available commercial neutron sources are usually prepared by blending the powders of the two materials in form of pure ^{9}Be metal mixed with ^{241}AmO$_2$. An efficient AmBe neutron source can be fabricated as a monolith of small crystals of AmBe$_{13}$ dispersed in excess Be metal with a byproduct of BeO according to reaction 6.1 with larger excess of Be required to obtain overall physical properties similar to bulk Be metal, with Be/Am atomic ratios typically varying between 15 and 21 [141] or 80% Be and 20% AmO$_2$ by weight [142]. The mixture is then often compressed into a cylindrical capsule with a density of about 1.3 g cm^{-3} [143].

$$AmO_2 + nBe \rightarrow AmBe_{13} + 2BeO + Excess\ Be\ (n-15) \tag{6.1}$$
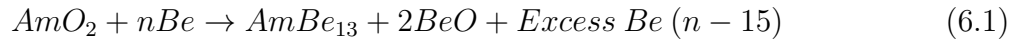
In many cases, the exact composition of neutron source and its mixing, assembly and fabrication is not provided by source manufacturers and only activity or neutron rate are given, which poses a difficulty for simulations.

^{241}Am has a half-life of 432.2 years and decays via α decay mode to ^{237}Np, with the most prominent different α energies averaging $\sim$ 5.4 MeV. The dominant energy of the resulting gamma-rays from the decay of the intermediate excited states of decay product ^{237}Np is 59.5 keV [144].

TABLE 6.1: $^{241}_{95}$Am nuclear data [60]

Half-life	432.2 y	
Most prominent alphas	**E$_\alpha$ [keV]**	**Intensity [%]**
α_1	5485.56	84.5
α_2	5442.8	13
α_3	5388.23	1.6
α_4	5544.5	0.34
α_5	5511.47	0.22
Most prominent gammas	**E$_\gamma$ [keV]**	**Intensity [%]**
γ_1	59.54	35.9
γ_2	26.34	2.40
γ_3	33.20	0.126
γ_4	43.42	0.073
γ_5	98.97	0.0203

The ^{9}Be(α,n)^{12}C and ^{17,18}O(α,n)^{20,21}Ne reactions

The most important reactions in the AmBe neutron source are:

$$^{241}_{95}Am \rightarrow^{237}_{93} Np + \alpha \tag{6.2}$$

---

[1]International Organization for Standardization

$$^{9}Be + \alpha \to\, ^{12}C^{(*)} + n \tag{6.3}$$

where the α particle is captured by ^{9}Be which then becomes ^{12}C in either its ground or excited state. The kinematics and the reaction cross-section determine the state of the residual ^{12}C nucleus produced in the reaction [144]. The de-excitation of the 1st excited state of ^{12}C produces characteristic γ-rays of 4.438 MeV with the 4.438 MeV γ-ray to total neutron ratio $S_\gamma/S_n = 0.575$ according to measurement in [139] and ~ 0.15 for the second excited state of energy 7.65 MeV [144]. This means that ~ 60 % of the neutrons emitted by an AmBe source are accompanied by prompt γ rays.

Since the mixture of materials in AmBe source contains some form of oxide of Am and Be, the second reaction that takes place is (α,n) reaction on oxygen isotopes:

$$^{17}O + \alpha \to\, ^{20}Ne^{(*)} + n \tag{6.4}$$

$$^{18}O + \alpha \to\, ^{21}Ne^{(*)} + n \tag{6.5}$$

Given the elemental abundance of ^{17}O and ^{18}O in O$_{nat}$ (0.038 and 0.205 % respectively), these reactions are not very common, but they still have an influence on AmBe neutron and prompt gamma energy spectra.

The cross-sections for (α,n) reactions for leaving the residual nucleus (^{12}C, $^{20/21}$Ne) in excited state can be seen in Figure 6.1 and corresponding excited states of ^{12}C and ^{21}Ne are shown in Figure 6.2.

AmBe (α,n) Neutron and Gamma Energy Spectra and Rates

The strength of any AmBe source depends on the activity of ^{241}Am. In general, a conversion factor between neutron rate and alpha activity of AmBe adapted from literature is [142]:

$$Y_{n,AmBe} = 2.2 \times 10^{6}\ ns^{-1}Ci^{-1}\ ^{2} \tag{6.6}$$

which corresponds to $\sim 59.5{\times}10^{-6}$ n/α. True yield always depends, however, on geometry and preparation of the source, measured values in available references are found to be up to 80 neutrons per 10^{6} alphas [142, 145].

To obtain the neutron and gamma energy spectrum simulation using Geant4 (and SOURCES-4C for cross-checking) has been performed. Defined composition of AmBe source in Geant4 simulation is given in Table 6.2, homogeneous mixture is assumed. Alpha particles are generated according to Table 6.1 (Fig. 6.3). JENDL/AN-2005 (α,n) data library was used, where the different reaction channels for ^{9}Be are given explicitly and so it is possible to obtain events with neutrons and gammas in coincidence.

TABLE 6.2: Composition of AmBe source used in simulation

Material	Density [g cm^{-3}]	Element	wt %	wt % in AmBe source
AmO$_2$	11.68	Am	88.28	20
		O	11.72	
pure Be	1.85	Be	100	80

$^{2}1Ci = 3.7 \times 10^{10}Bq$
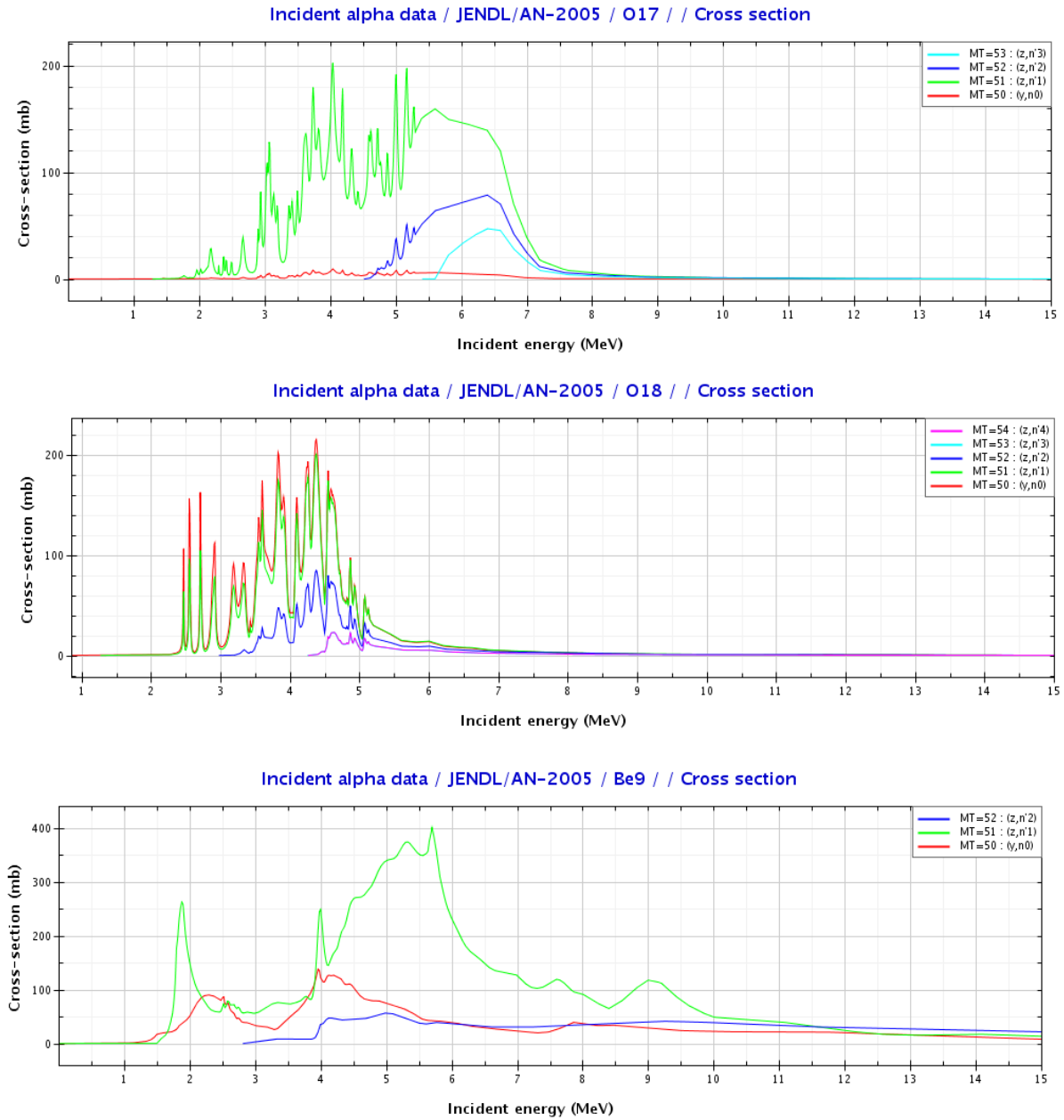
FIGURE 6.1: cross-sections for (α,n) reactions for oxygen isotopes and ^{9}Be, (z/y,n0-4) - production of a neutron, leaving the residual nucleus in the ground state, 1st, 2nd, 3rd and 4th excited state [92]
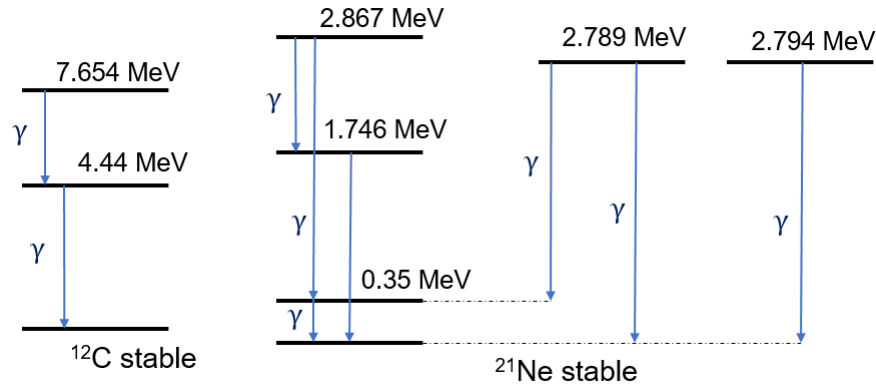
FIGURE 6.2: Excited states of residual nuclei ^{12}C and ^{21}Ne from AmBe source
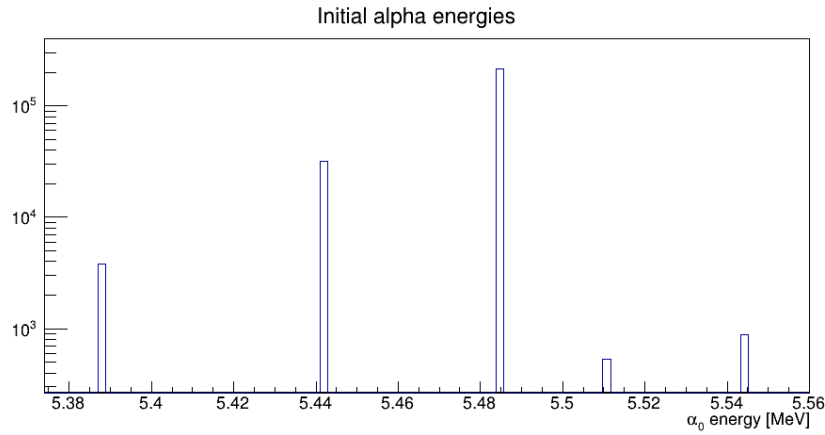
FIGURE 6.3: Energies of generated alpha particles from ^{241}Am decay in Geant4 simulation

Simulated neutron and gamma energy spectra are in Figure 6.4. The lowest part in the neutron energy spectrum (< 2 MeV) corresponds to reaction leaving ^{12}C in 2nd (7.65 MeV) excited state, following prominent peak from reaction leaving ^{12}C in 1st excited state and the highest energy part corresponds to the ground state of ^{12}C. In gamma spectrum, characteristic gamma transitions shown in Figure 6.2 can be observed. The resulting yields obtained from simulation are 72 $\frac{n}{10^6\alpha}$, corresponding well to values obtained from measurements and calculations given in aforementioned references, and 58 $\frac{\gamma}{10^6\alpha}$. The 4.4 MeV γ-ray to total neutron yield ratio is $S_\gamma/S_n = 0.73$, which is slightly overestimated compared to the measurements. Overall good agreement for neutron energy spectra has been also found with SOURCES-4C simulation (Fig. 6.5). This simulation was performed with the same source composition as defined in Table 6.2. In comparison with the Geant4 simulation, the SOURCES-4C spectrum predicts higher contribution to the highest neutron energy part, corresponding to the ground state of ^{12}C, and lower contributions to the 1st and 2nd excited states. This would also lead to lower gamma yield prediction[3].

Secondary processes that can change the shape of spectra are multibody break-up reaction ^{9}Be(α,αn)^{8}Be, elastic scattering of neutrons on ^{9}Be, oxygen, ^{241}Am, fission of

---

[3]The current state of the SOURCES-4C code does not calculate gamma production from (α,nγ) reactions.
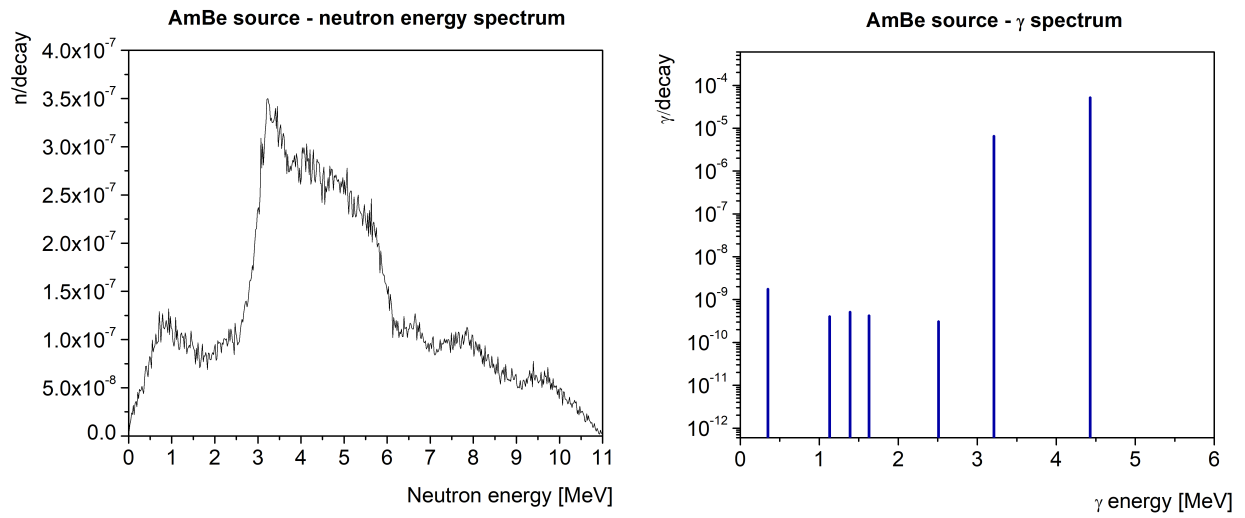
FIGURE 6.4: **Left:** Neutron energy spectrum of AmBe source from Geant4 simulation. **Right:** Gamma energy spectrum of AmBe source from Geant4 simulation.
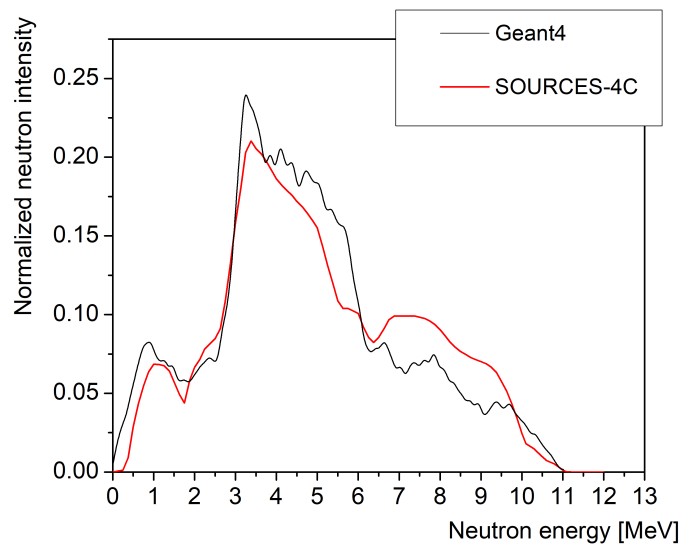
FIGURE 6.5:   Comparison of neutron energy spectra simulated in SOURCES-4C and Geant4.
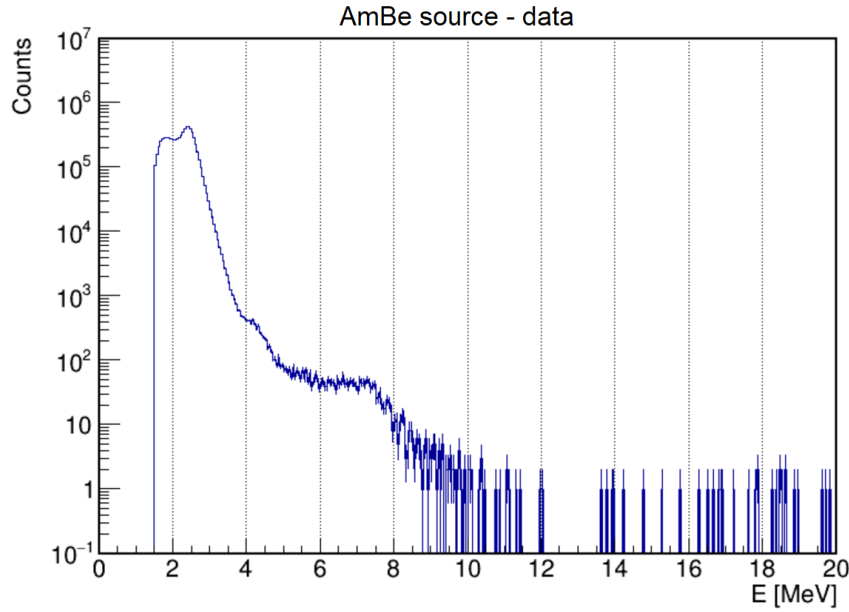
FIGURE 6.6: Energy spectrum of AmBe neutron source measured by the main walls of SuperNEMO calorimeter

^{241}Am, and (n,2n) events in ^{9}Be [146], which become prominent with large source strengths and were neglected in this work.

6.1.2 Comparison of AmBe Neutron Source Data and Simulation

During the time of writing this thesis, only the Demonstrator calorimeter without tracker was commissioned. It was therefore impossible to obtain information from data analysis about different event topologies. Nevertheless, the total deposited energy could be measured and this proved to be useful for calibration purposes and for some validation between Monte Carlo simulations and real data.

During calorimeter commissioning runs, a measurement with a weak AmBe neutron source was performed. The source strength was given as approximately *20 n s^{-1}* and its position was ~75 cm away from the main calorimeter wall, centered in the middle of the wall. The total time of this measurement was ~ 3.3 h. Analyzed and calibrated energy spectrum of this source measured by the main walls of SuperNEMO calorimeter is shown in Figure 6.6 (with a threshold at 1.5 MeV). Several features of the spectrum can be seen and analysed. Bellow 4 MeV the signal is flooded by the environmental ^{208}Tl gamma peak at 2.6 MeV and its Compton edge, and other sources of natural radioactivity. Just above 4 MeV there is a visible bump in the spectrum corresponding to 4.4 MeV gamma from the excited state of ^{12}C* after ^{9}Be(α,n)^{12}C reaction (see subsection 6.1.1). Above this energy is the region where gammas from (n, γ) reactions on metals are expected. And the highest energy region may also correspond to some muon interactions or gammas from bremsstrahlung of residual muon flux.

There is overall energy spectrum distortion which is expected due to the non-linearity of the scintillator light yield for electrons caused by effects like scintillation light quenching according to Birks' attenuation law[4] and additional light from Cherenkov radiation and the

---

[4]Because of quenching, the visible energy is smaller than the true electron energy.
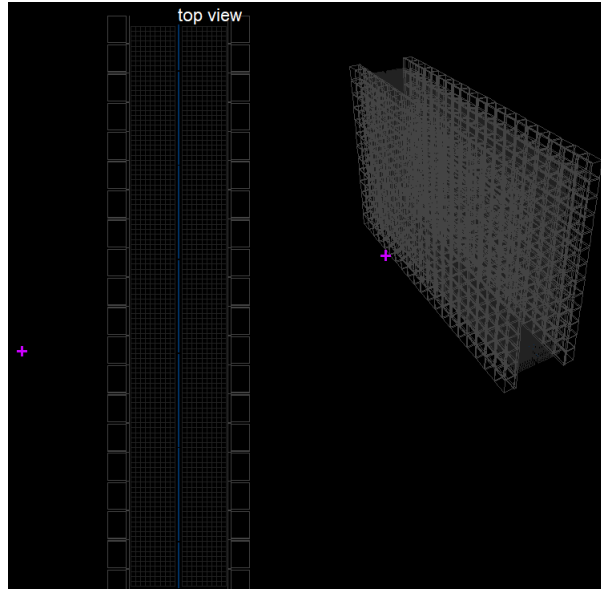
FIGURE 6.7: Visualization of the source position in Falaise

non-uniformity of energy response of the scintillator[5]. This has been taken into account for the reconstruction of simulated data.

The simulation in Falaise was done following the same method as in the previous section - according to the first 4 steps described in Section 5.4. The input spectrum for Falaise simulation from *step 1* was generated according to Figure 6.4 (**left**) (simulation performed in Section 6.1). To get to get a more realistic representation of the real AmBe spectrum neutrons were generated in coincidence with gammas from the source as well (Fig. 6.4 **right**). In Falaise, for the vertex generator, a point-like source position was added, at the same location as in the data set (see Fig. 6.7). From now on this simulation will be referred to as *AmBe-source simulation*[6].

From the *AmBe-source simulation* output, capture positions and capture fractions were extracted the same way as in Section 5.4.2 and these values are given in Table 6.3. Capture positions were used as vertex generators of gamma cascades from Fe and Cu isotopes obtained from the DICEBOX simulation. These gammas extend up to ~ 9.3 MeV with prominent gamma energies in the region from 6 to 8 MeV, but also in the lower part of the energy spectrum (Fig. 4.25). Capture fractions (along with the run time and source strength) were used for normalizing the histograms. Let's name this simulation *AmBe-cascades simulation*[7]. When calibrating the simulation according to calibration of real data from measurements and after application of energy corrections mentioned before, these gammas spread over a wide range of energies as it can be seen in the results of the *AmBe-cascades simulation* in Figure 6.8.

---

[5]A same energy deposit in the scintillator will give a different signal strength depending if it happens far or close to the PMT photocathode (see [147])

[6]AmBe spectrum due to neutrons and gammas from the source

[7]AmBe spectrum only due to neutron captures on Fe and Cu when using DICEBOX cascades as input events

TABLE 6.3: Fractions of neutron captures

| Neutron source | Fractions of neutron capture f_i [%] | | | |
	^{55}Fe	^{57}Fe	^{64}Cu	^{66}Cu
AmBe	1.6	24.9	0.94	0.2
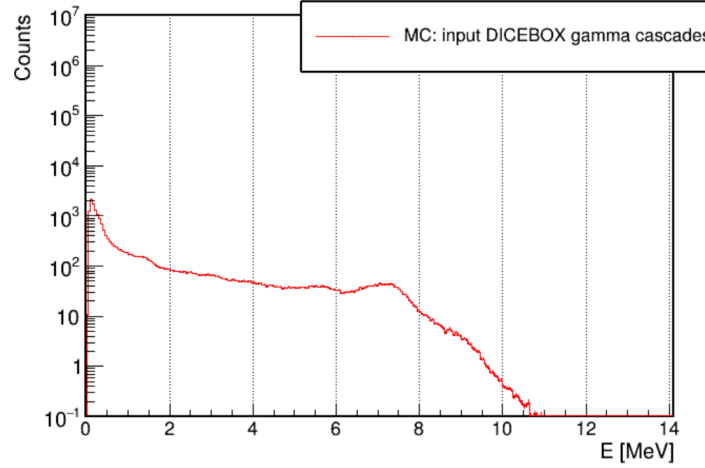
FIGURE 6.8: AmBe spectrum due to neutron captures on Fe and Cu from
AmBe-cascades simulation

In general, the signal from the AmBe source can be prompt or delayed. The prompt signal comes from proton recoils in the detector from fast neutron interactions and from gammas emitted from the source. The delayed signal is registered after a few *μs* and comes from gammas from (n,γ) reaction after fast neutrons are thermalized and captured. The delayed capture signal is expected to be similar to what we expect from background neutrons and is of bigger importance for the purposes of this work. This timing difference can be used in simulated data to remove unwanted events from neutron captures in *AmBe-source simulation* and replace them with results of simulation of gamma cascades from DICEBOX from the *AmBe-cascades simulation*. Such time distribution of calorimeter hits of one of the simulated files can be seen in Figure 6.9. As expected, there is a distinct peak of delayed hits after several *μs*. The timing of the prompt hits has 2 peak-like features - early and late. The earliest prompt hits come from the prompt gamma rays of the AmBe source (with various delay due to time of flight between the source and the optical module of the calorimeter), and the late prompt hits correspond to neutron scattering events.
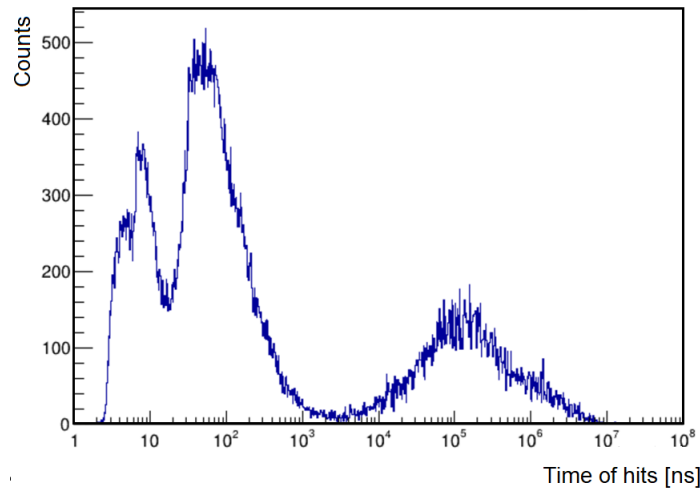
FIGURE 6.9: Prompt and delayed hit time distribution of *AmBe-source simulation*

By removing all delayed hits and replacing them with cascade events of Fe and Cu isotopes, we lose information about other capture events, for example, the 2.2 MeV gamma from capture on hydrogen. But in the relevant high energy part of the spectra (4 - 10 MeV, dominated by the AmBe source) the simulation and data can be compared. This comparison is plotted in Figure 6.10[8].
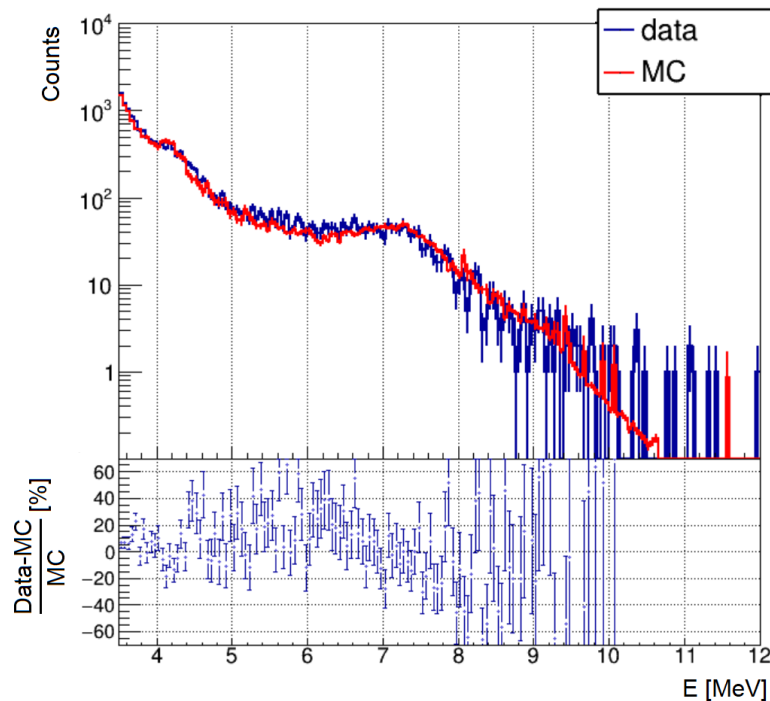
FIGURE 6.10: Comparison of experimental data and simulation of the AmBe source

___

[8]MC spectrum has also been combined with a background run without AmBe source to take into account natural radioactivity tail, especially ^{208}Tl edge that may extend up to 4 MeV

Overall, a good agreement between data and simulation has been achieved with a good match of the shape of both spectra. In terms of the number of counts, there are certain regions where the signal is overestimated or underestimated. There are several sources of ambiguities that may lead to these effects. Firstly, the source strength of 20 neutrons per second was given only approximately, without providing any measurement uncertainty. The neutron energy spectrum of the source was not provided, and so a simulation has been performed. The composition and density of the AmBe source used in the simulation were only roughly estimated and defined according to commercial neutron sources found in the available literature. It is clear that the overall physical and chemical properties of the source influence the resulting neutron yield and neutron energies. Additionally, the geometry of the source and how these neutrons propagate through the material have a big influence on the neutron energies. This was neglected in the final simulation as the source spectrum was generated from a point-like vertex generator. These small inaccuracies in the simulation may also influence number of detected neutrons and gammas. The overall γ-ray to neutron yield ratio was also found to be slightly overestimated, compared to ratios found in available references, in the performed Geant4 simulation. This is also found in this comparison, where the number of counts in the MC spectrum is in a slight disagreement with the data in the prompt signal region from the 4.4 MeV gammas from excited states of $^{12}C^*$ after $^9Be(\alpha,n)^{12}C$ reaction.

Considering these conditions and assumptions, we find both spectra in good agreement within the relative error. The fact that the measured spectrum compares well with the MC spectrum due to neutron captures on Fe and Cu in the energy region of 6 - 8 MeV supports the assumption that it is primarily iron and copper contributing to the (n,γ) reactions in the Demonstrator. It also demonstrates the possibility of using the proposed method of neutron capture cascades simulation to obtain a reasonable match with the data. Thus, we conclude that this approach can be used for an accurate prediction of the neutron induced background in the SuperNEMO experiment.

6.2 High Energy Spectrum Measured in the LSM with the SuperNEMO Demonstrator

Fluxes of ambient radiation in the LSM from available measurements were summarized in Section 3.3. As it was previously discussed, measured values of these fluxes do not represent ideal unaffected ambient fluxes, as they are highly dependant on the location of the detector in the laboratory, radioactive contamination of the detectors themselves and materials nearby. Therefore, several background runs of data taking with an accumulated live time of about 6.5 days was dedicated to obtain energy spectrum with sufficient statistics in the energy region > 4 MeV in order to compare simulated deposited energy from ambient neutron and gamma sources with measurement.

First, a brief summary of the measured LSM fluxes should be given with a more detailed discussion of fluxes in given energy regions. In the simulation, measured gamma fluxes from [65][9] were used. These fluxes were extracted from the energy spectrum measured by NaI scintillator shown in Figure 6.11. There were altogether three measurements with no shielding, with 3.5 % borated polyethylene shielding, and with 5 cm copper and 10 cm lead shielding.

---

[9]Measured by the NEMO-3 collaboration in 2001.
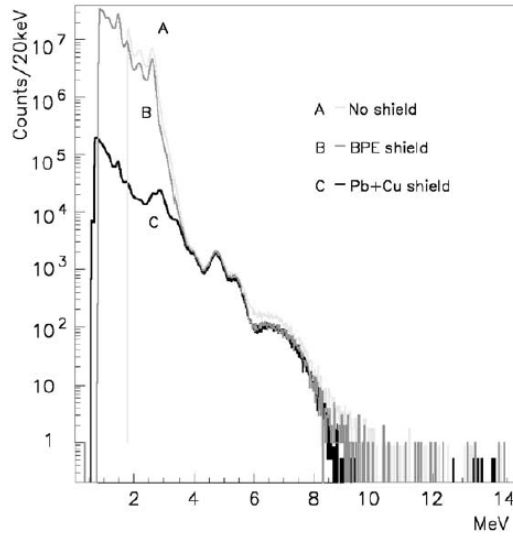
FIGURE 6.11: NaI energy spectra measured in LSM [65]

The ambient γ fluxes in individual energy intervals correspond to values presented in Table 6.4.

TABLE 6.4: The ambient γ fluxes measured in LSM [65]

Energy interval	Flux [cm^{-2}s^{-1}]
(4 - 6) MeV	3.8×10^{-6}
(6 - 7) MeV	1.5×10^{-6}
(7 - 8) MeV	1.6×10^{-6}
(8 - 9) MeV	0.07×10^{-6}
(9 - 10) MeV	0.05×10^{-6}

Measurement error is given as approximately 30 %. In the simulation, γ-ray energies were sampled from a flat distribution in each energy interval. The shape and counting rates of the measured spectra in [65] are explained for energy intervals bellow 10 MeV as follows:

- Below 4 MeV with γ-rays due to natural radioactivity of surrounding materials - this was neglected in this study.

- Between 4 and 6 MeV due to internal U and Th contamination of the NaI crystal, with pile-up events of summed energies between β and α decays of ^{212}Bi and ^{212}Po.

- From 6 to 10 MeV due to neutron induced γ-rays from neutron captures in the surrounding materials and in the iodine of the NaI crystal.

Neutron fluxes were taken from [61], which represents a quite old measurement of fast neutron flux, and [69], in which the ambient thermal neutron flux at different locations at LSM was monitored. The fast neutron flux was taken as $\Phi_{n,fast} = (4.0 \pm 1.0) \times 10^{-6}$ neutrons s^{-1}cm^{-2} corresponding to energies between 2 - 6 MeV. This value was found to be 4 times higher than simulated neutron flux above 1 MeV in the same study. Simulated

spectrum of these neutrons were used in our Monte Carlo model. Thermal neutron flux used in this study is $\Phi_{n,thermal} = (2.9 \pm 0.4) \times 10^{-6}$ neutrons s^{-1}cm^{-2}, which was measured in the main experimental hall of LSM, however, the value of measured fluxes varied by up to a factor of three from one location to another. In our Monte Carlo model, the energies of thermal neutrons were sampled from Maxwell-Boltzmann distribution.

6.2.1 Comparison of Measured High Energy Spectrum and Simulation

Measured energy spectrum above 4 MeV in the LSM with the unshielded calorimeter of the SuperNEMO Demonstrator is shown in Figure 6.12 (left). We can also divide the measured spectrum into several energy regions. Just above 4 MeV, there is still a contribution from the natural radioactivity, especially Compton edge events of 2.6 MeV γs from decays of ^{208}Tl. Above this tail and up to 10 MeV, we expect mainly ambient γ-rays and neutron induced events. The neutron effect, predominantly in the energy region between 6 and 10 MeV, can be confirmed by the similarity of the shapes of measured background spectrum and spectrum measured with a weak AmBe source from Figure 6.6. This is plotted in Figure 6.12 (right). Note that the spectra are not normalized in time and the scales have been adjusted for better comparison. The most energetic events above 10 MeV should correspond to residual weak muon flux and γ-rays induced by muon bremsstrahlung. Without passive shielding, it is, however, impossible to distinguish between events due to ambient fluxes and internal events. For example, γ-ray emissions from neutron captures come both from neutron captures on Cu and Fe in the detector and from neutron captures on nuclei in the surrounding materials (neutron binding energies of several metals used in construction materials, such as Pb, Cu or Fe, extend up to 10 MeV). Such effort will be made with future measurements after successful completion and installation of passive shielding.
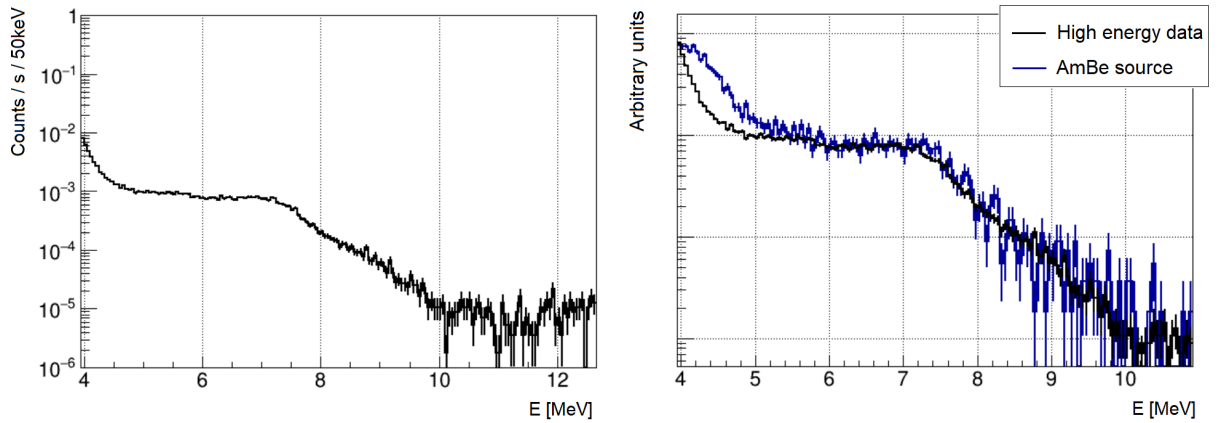
FIGURE 6.12: **Left:** Energy spectrum measured in the LSM with the SuperNEMO calorimeter. **Right:** Comparison of the high energy spectrum and AmBe source run with adjusted scales.

Figure 6.13 (left) shows a comparison of each simulated component of ambient radiation with measured deposited energy. In Figure 6.13 (right), all ambient gamma components are combined into single spectrum. Monte Carlo of neutron simulation includes the contributions from both thermal and fast neutron fluxes and was simulated using the same method described in Section 5.4. It is clear, that the total MC overestimates the expected
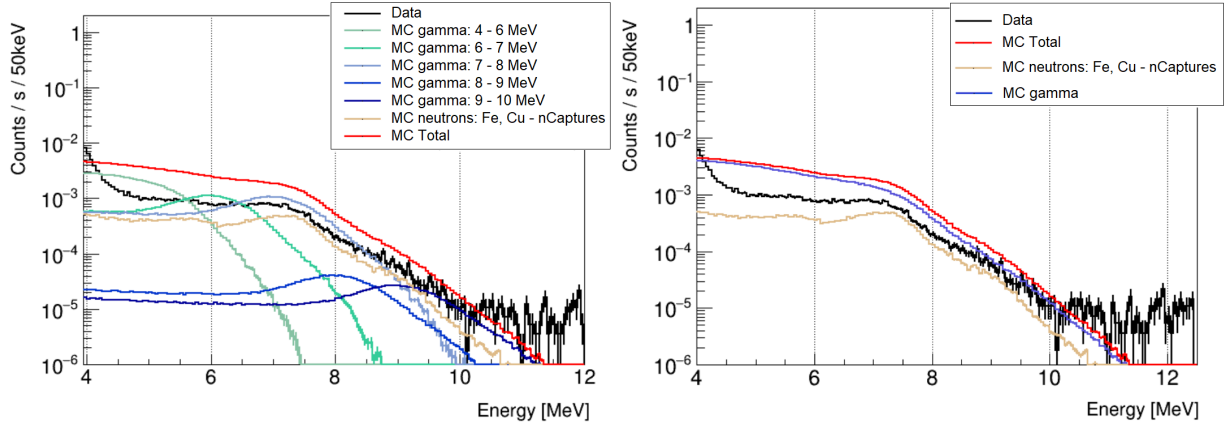
FIGURE 6.13: Comparison of experimental data and simulation of deposited energy from ambient gamma and neutron sources

number of counts. Table 6.5 gives the counting rates extracted from the total MC and measured data for each energy interval along with statistical uncertainties. The systematic uncertainty of the total counting rate in MC is estimated from errors of measured neutron and gamma fluxes. The counting rate in each interval is overestimated by the factor of 2.3 on average.

TABLE 6.5: Counting rates obtained from data and simulation in individual energy regions and ratios of $\frac{MC}{Data}$. Quoted errors are statistical only, unless stated otherwise.

| | Counting rates [counts/hour] | | |
Energy interval	MC	Data	MC/Data ratio
Total 4-10 MeV	790.89 ± 0.77 (stat) ± 199.35 (syst)	321.69 ± 1.44	2.46
(4 - 6) MeV	517.55 ± 0.67	215.44 ± 1.18	2.40
(6 - 7) MeV	159.87 ± 0.29	58.53 ± 0.61	2.73
(7 - 8) MeV	90.89 ± 0.22	36.96 ± 0.49	2.46
(8 - 9) MeV	18.78 ± 0.09	8.58 ± 0.23	2.19
(9 - 10) MeV	3.80 ± 0.03	2.18 ± 0.12	1.75

Let's first discuss possible sources of this overestimation. The biggest contribution to the overestimation is expected to come from the intrinsic radioactivity of components of detectors measuring these fluxes which cannot be fully accounted for even when using different shields. Especially, when also the activities of shielding materials are not known or not taken into account, and no comprehensive Monte Carlo model was performed. Moreover, as it can be seen from summarized measurements of LSM fluxes in Section 3.3, the fluxes vary between different locations in the laboratory. See, for example, Table 3.5, where measured gamma fluxes from natural radionuclides vary by factors of 1.5 - 3.0 at two different locations. Moreover, [69] reports that thermal neutron flux varies by a factor of three from measurements at eight different locations. Ambient fluxes therefore always depend on other materials present in the laboratory, their U and Th content, and in the case of neutron fluxes, also on their water and hydrogen content as well. In the case of the NaI crystal, possible bias in the >4 MeV flux measurement could come from alpha contamination and

pile-up events with summed energies between β and α decays[10]. Additionally, in [65], only the γ-ray fluxes between 6 and 10 MeV were assumed to be due to neutron effect and were extracted from the measurement with the detector inside the borated polyethylene shield. A large contribution to these fluxes may come from the capture reactions on ^{127}I whose neutron separation energy S_n equals to 9.14 MeV [60]. However, the γ transitions with the highest intensities during the de-excitation process extend from 4.5 - 6.7 MeV, with the strongest transition being $E_\gamma = 5.6$ MeV [148]. If this was neglected in their analysis it could lead to some overestimation of extracted ambient γ fluxes. Another potential source of disagreement comes from approximations made in the MC simulations described previously.

To further test the validity of the model, we can have a look if the overall shape of the spectrum can be explained by our model. Although the shape of the MC neutron spectrum matches the measured spectrum, where neutron effect is expected, the predicted counting rate is higher when combined with the ambient gamma component. It is, however, difficult to say, whether the values of neutron fluxes or the ambient gamma component in this energy region or both, were too high. The best match is obtained in the energy region of 9 - 10 MeV. In fact, the wrong counting rates, affected by high values of fluxes, disrupts the overall comparison of the spectral shapes. The worst fit can be observed in the lower energy region, where the measured spectrum starts to rise below 4.5 MeV. This effect is due to natural radioactivity which has not been included in the MC model. Above 10 MeV, muons and their interaction in the laboratory and materials can affect the spectrum, which has not been taken into account in the simulation as well. It is, therefore, better to compare the shapes in the energy region of 4.5 - 10 MeV.

It is clear, that the counting rate of the MC spectrum depends on the values of the ambient neutron and gamma fluxes used to normalize the model. For a better comparison, and to see if considered capture reactions and gamma fluxes in the model can explain observed data, we can try to match the counting rates. The total Monte Carlo model is composed of six histograms all together - neutron induced background[11] and five ambient gamma components in individual energy intervals. Each component can explain the shape of a different region of the energy spectrum, but the total counting rate is given by the sum of all components in this region. For example, as it was mentioned above, the MC neutron spectrum matches the measured spectrum, where neutron effect is expected, especially the dip in the spectrum around 8 MeV, and together with 7-8, 8-9 and 9-10 MeV gamma components, it can explain the slope and tail of the spectrum. The combined counting rate is, however, too high. Each of these MC components can be re-scaled individually to obtain identical counting rates in a given energy interval which gives a rise to a lot of degrees of freedom. The individual MC components were re-scaled until the condition

$$N_{Total\,MC}\left(E_{min}, E_{max}\right) = N_{Data}\left(E_{min}, E_{max}\right) \tag{6.7}$$

was fulfilled, where $N_{Total\,MC}$[12] and N_{Data} are the counting rates and (E_{min}, E_{max}) is the corresponding energy interval region $(4.5, 6), (6, 7), (7, 8), (8, 9)$ or $(9, 10)$ MeV. In the gamma component of 4 - 6 MeV, the counting rate of 4.5 - 6 MeV region was considered instead.

---

[10]Which is possible due to the slow scintillation time constants of NaI crystal.

[11]Which itself is composed of thermal and fast neutron components that are combined into one.

[12]$N_{Total\,MC}(E_{min},E_{max})=N_{MC,\,neutrons}(E_{min},E_{max})+N_{MC,\,\gamma:\,4-6}(E_{min},E_{max})+N_{MC,\,\gamma:\,6-7}(E_{min},E_{max})$
$+N_{MC,\,\gamma:\,7-8}(E_{min},E_{max})+N_{MC,\,\gamma:\,8-9}(E_{min},E_{max})+N_{MC,\,\gamma:\,9-10}(E_{min},E_{max})$

TABLE 6.6: Re-scaling factors of simulation components with corresponding fluxes obtained from MC where the counting rate matches the experimental data

MC component	Scaling factor	Corresponding flux $[\text{cm}^{-2}\text{s}^{-1}]$
γ: (4 - 6) MeV	0.21	$\Phi_{\gamma,4-6} = 7.95 \times 10^{-7}$
γ: (6 - 7) MeV	0.27	$\Phi_{\gamma,6-7} = 4.12 \times 10^{-7}$
γ: (7 - 8) MeV	0.34	$\Phi_{\gamma,7-8} = 5.40 \times 10^{-7}$
γ: (8 - 9) MeV	0.40	$\Phi_{\gamma,8-9} = 2.82 \times 10^{-8}$
γ: (9 - 10) MeV	0.73	$\Phi_{\gamma,9-10} = 3.66 \times 10^{-8}$
Fe, Cu - nCaptures	0.61	$\Phi_{n,th} + \Phi_{n,fast} = 4.21 \times 10^{-6}$

The result of this re-scaling is shown in Figure 6.14. It can be seen, that our model explains well the experimental spectrum in the 4.5 -10 MeV energy region, and therefore we can conclude that it is mostly the original counting rates, affected by input gamma and neutron fluxes, that do not correspond to observed data.

The constants by which each MC component has been re-scaled are presented in Table 6.6. We can use these constants to extract the expected fluxes corresponding to the MC spectrum in Figure 6.14. It is, however, difficult to determine with confidence the true values of these fluxes, as the overall spectrum in each energy region is given by a sum of gamma and neutron components, and the overall counting rate can be kept the same with decreasing one component while increasing the other. It is also impossible to differentiate between contributions from thermal and fast neutrons. Nevertheless, the fluxes given in Table 6.6 keep each MC component balanced enough to explain the slight dips around 6 and 8 MeV, and the slope and tail above 7 MeV observed in the measured spectrum. Therefore, they may represent indicative estimates of γ-ray fluxes incident on the Demonstrator.
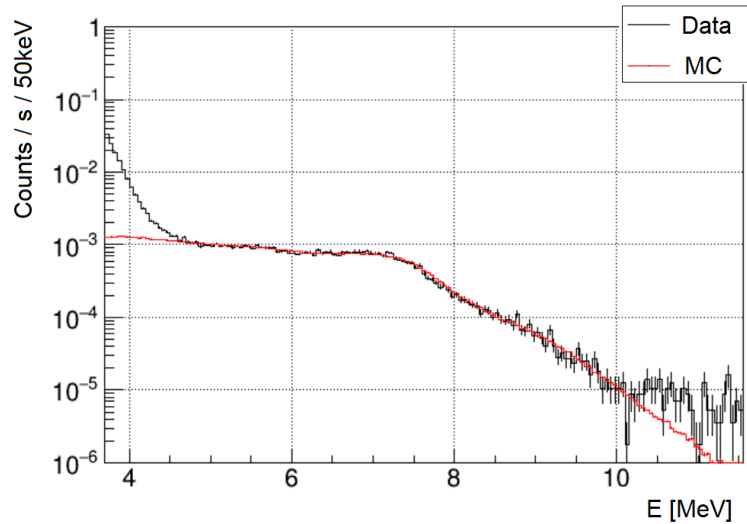
FIGURE 6.14:   Comparison of measured data and MC simulation with matching counting rates

With this single measurement, it is difficult to estimate the actual flux in the laboratory and to properly separate the neutron and gamma fluxes incident on the detector. With

more measurements including both neutron or/and gamma shielding, it will be easier to separate ambient fluxes and internal contamination. With higher statistics, it will also be possible to study the muon induced part of the spectrum and estimate a muon flux in the laboratory.

Nevertheless, from this comparison of MC simulation and experimental data, the total incident flux was found to be lower than the flux used in the analysis of external background in Chapter 5. This has implications on the estimated number of expected background events from ambient neutron and gamma radiation. The values of the background rate from ambient γ-rays and ambient neutrons given in Table 5.11 in the summary of the last chapter, therefore, represent the upper bound on the background rate. We can conclude, that we are on the side of overestimating the background in the model rather than underestimating it, which, as discussed previously, is often more prudent from the point of view of the experiment's sensitivity.

6.3 Summary

In this Chapter, two data set of the SuperNEMO demonstrator calorimeter have been used in order to compare the results of proposed Monte Carlo models with experimental data.

With the first measurement using a weak neutron AmBe source, the validity of the model of radiative neutron capture in the detector, to evaluate neutron induced background, was studied. Firstly, neutron and gamma energy spectra of the AmBe source were simulated using the Geant4 toolkit. This provided input data for the Falaise software to study the Demonstrator's response. This simulation was performed following the same method as used in the analysis of neutron capture γ-ray induced background.

The neutron AmBe source had a strength of 20 neutrons per second and the total measurement time was 3.3 hours. The total deposited energy in the calorimeter was found to be in good agreement with the MC model.

In the next Section 6.2, a background energy spectrum of the Demonstrator in the high energy region was compared with the Monte Carlo model of deposited energy from ambient LSM gamma and neutron fluxes. The measured spectrum corresponded to 6.5 days of measurement time with sufficient statistics in the energy region above 4 MeV. Monte Carlo model consisted of five ambient gamma components with energies ranging from 4 to 10 MeV, and of gammas from neutron captures on iron and copper in the detector. From the comparison of counting rates between MC and data in individual energy intervals, the counting rate in each interval was overestimated by the factor of 2.3 on average. Given the point-to-point variance of measured fluxes from available literature and other ambiguities discussed in this section, such overestimation is not unexpected.

To see if considered capture reactions and gamma fluxes can explain observed data, the MC counting rates were matched to the experimental data by re-scaling each MC component. The MC model explained well the shape of the experimental spectrum in the energy region of 4.5 - 10 MeV, which demonstrates that the proposed approach can be used to study the Demonstrator's response to ambient LSM radiation after adjusting the values of input ambient fluxes. The final background rate will depend on the values of incident ambient gamma and neutron fluxes in the time of operation of the finalized detector. New extracted values of these fluxes from Table 6.6 represent a preliminary analysis, which is yet to be confirmed by more measurements including also both neutron and gamma shields.

Chapter 7

Conclusions

Neutrinoless double beta decay is a hypothesized, but as of yet unobserved, process. It violates lepton number conservation and is forbidden in the Standard Model of particle physics. It represents a possible experimental tool capable of providing relevant information on the nature of neutrino - Majorana or Dirac - and it might be a key to answering the neutrino mass hierarchy problem, and the matter-antimatter asymmetry problem as well. One of the experiments searching for this rare process, of which I am a member, is the SuperNEMO experiment. SuperNEMO builds on the success of its predecessor - the NEMO-3 experiment - using the same tracker-calorimeter technology. Currently, the first module of the experiment, called the Demonstrator, aims to take the first data in the Modane underground laboratory.

It is a goal of every $0\nu\beta\beta$ experiment to reach the lowest possible background and to have a comprehensive Monte Carlo model for expected background rate estimation and for sensitivity studies. Presented dissertation thesis contributed to such efforts by various results.

The aim of this work was to estimate the background contributions from high energy gamma rays originating from de-excitations of radionuclides in natural decay chains of uranium and thorium present in the underground environment, residual cosmic ray cascades, and from neutron capture reactions. For this purpose, there is a need for understanding individual background sources and evaluation of each component. Where measurements are available these data on fluxes and energy spectra were used, otherwise, evaluation of different sources of the background was performed by exploiting various software. Throughout this research I became acquainted with many software packages, such as Geant4, Geant based SaG4n and Falaise, NeuCBOT, SOURCES-4C, and DICEBOX, which represent state-of-art of simulation packages for the interaction and transport of particles and nuclei in matter used in a variety of applications in nuclear physics.

In Chapter 4, I presented obtained results from such simulations and calculations of neutron yields from spontaneous fission and from (α,n) reactions in materials, used for construction of the Demonstrator, that are contaminated with radionuclides from ^{238}U and ^{232}Th decay chains. They represent an important input used for Monte Carlo simulation of the background induced by high energy gamma rays in the SuperNEMO software.

A problem with simulation of gamma cascades emitted after thermal neutron capture in this software had to be addressed and it was solved by a separate simulation of gamma de-excitations using a dedicated gamma decay software. These results represent an important input for accurate simulation of the detector response to (n,γ) reactions.

External background events induced by high energy γ-rays were studied in detail in Chapter 5. Here, I have estimated the expected background rate through a Monte Carlo simulation. The background reduction technique that is based on the rejection method

by reconstructing the topology of events, and on background suppression by selecting radiopure materials used in detector construction and passive shielding, was demonstrated. It proved to be effective by reducing the number of expected background events from these sources by several orders of magnitude.

Dedicated simulations of attenuation of radiation passing through different shielding configurations and geometries were also performed. This ultimately helps to optimize the final design of passive shielding used for the Demonstrator module.

Lastly, the method of the simulation of radiative neutron capture in the detector, for evaluation of neutron induced background, was validated by simulation of neutron and gamma energy spectra of AmBe source and their comparison with experimental data. Data and Monte Carlo simulation were found to be in good agreement. The Monte Carlo model of deposited energy from ambient LSM gamma and neutron fluxes was validated by the high energy spectrum measured in the LSM with the SuperNEMO Demonstrator.

I also contributed to the assembly and construction process of the Demonstrator during the calorimeter commissioning phase.

Many fundamental questions remain to be answered in future neutrino experiments, and these can have very important implications for our understanding of the Standard Model and our Universe. With a rich experimental program in future neutrino experiments lying ahead, where fundamental physics discoveries are very likely, SuperNEMO could bring more insight into some processes.

Bibliography

[1] P. Povinec et al. "New isotope technologies in environmental physics". In: *Acta Physica Slovaca* 58 (Jan. 2008), pp. 1–154. DOI: 10.2478/v10155-010-0088-6 (cit. on pp. xvii, 32, 38).

[2] *Scheme of the Standard Model of particle physics*. URL: http://www.yorku.ca/menary/oldhep/oldhep.html (cit. on p. 1).

[3] C.L. Cowan et al. "Detection of the free neutrino: A Confirmation". In: *Science* 124 (1956), pp. 103–104. DOI: 10.1126/science.124.3212.103 (cit. on p. 3).

[4] G. Danby et al. "Observation of High-Energy Neutrino Reactions and the Existence of Two Kinds of Neutrinos". In: *Phys. Rev. Lett.* 9 (1 July 1962), pp. 36–44. DOI: 10.1103/PhysRevLett.9.36 (cit. on p. 4).

[5] K. Kodama et al. "Observation of tau neutrino interactions". In: *Physics Letters B* 504.3 (2001), pp. 218–224. ISSN: 0370-2693. DOI: https://doi.org/10.1016/S0370-2693(01)00307-0 (cit. on p. 4).

[6] A. Balantekin and B. Kayser. *On the Properties of Neutrinos*. 2018. arXiv: 1805.00922 [hep-ph] (cit. on pp. 4, 7, 8).

[7] P. Lipari. "Introduction to neutrino physics". In: *1st CERN-CLAF School of High-Energy Physics*. May 2001, pp. 115–199 (cit. on pp. 4, 5).

[8] B. Pontecorvo. "Neutrino Experiments and the Problem of Conservation of Leptonic Charge". In: *Sov. Phys. JETP* 26 (1968), pp. 984–988 (cit. on p. 5).

[9] Y. Fukuda et al. "Measurement of the Flux and Zenith-Angle Distribution of Upward Throughgoing Muons by Super-Kamiokande". In: *Phys. Rev. Lett.* 82 (13 Mar. 1999), pp. 2644–2648. DOI: 10.1103/PhysRevLett.82.2644. URL: https://link.aps.org/doi/10.1103/PhysRevLett.82.2644 (cit. on p. 5).

[10] Q. R. Ahmad et al. "Direct Evidence for Neutrino Flavor Transformation from Neutral-Current Interactions in the Sudbury Neutrino Observatory". In: *Phys. Rev. Lett.* 89 (1 June 2002), p. 011301. DOI: 10.1103/PhysRevLett.89.011301. URL: https://link.aps.org/doi/10.1103/PhysRevLett.89.011301 (cit. on p. 5).

[11] K. Eguchi et al. "First Results from KamLAND: Evidence for Reactor Antineutrino Disappearance". In: *Phys. Rev. Lett.* 90 (2 Jan. 2003), p. 021802. DOI: 10.1103/PhysRevLett.90.021802. URL: https://link.aps.org/doi/10.1103/PhysRevLett.90.021802 (cit. on p. 5).

[12] B. Kayser. "Neutrino Mass, Mixing, and Flavor Change". In: (Nov. 2002), pp. 1–24. arXiv: hep-ph/0211134 (cit. on pp. 6, 7).

[13] P.A. Zyla et al. "Review of Particle Physics". In: *PTEP* 2020.8 (2020), p. 083C01. DOI: 10.1093/ptep/ptaa104 (cit. on pp. 7–9).

[14] M. Aker et al. "Improved Upper Limit on the Neutrino Mass from a Direct Kinematic Method by KATRIN". In: *Physical Review Letters* 123.22 (Nov. 2019). ISSN: 1079-7114. DOI: 10.1103/physrevlett.123.221802. URL: http://dx.doi.org/10.1103/PhysRevLett.123.221802 (cit. on p. 8).

[15] A. Loureiro et al. "Upper Bound of Neutrino Masses from Combined Cosmological Observations and Particle Physics Experiments". In: *Physical Review Letters* 123.8 (Aug. 2019). ISSN: 1079-7114. DOI: 10.1103/physrevlett.123.081301. URL: http://dx.doi.org/10.1103/PhysRevLett.123.081301 (cit. on p. 8).

[16] N. Aghanim et al. "Planck 2018 results". In: *Astronomy Astrophysics* 641 (Sept. 2020), A6. ISSN: 1432-0746. DOI: 10.1051/0004-6361/201833910. URL: http://dx.doi.org/10.1051/0004-6361/201833910 (cit. on p. 8).

[17] M. Tanabashi et al. "Review of Particle Physics". In: *Phys. Rev. D* 98 (3 Aug. 2018), p. 030001. DOI: 10.1103/PhysRevD.98.030001 (cit. on p. 9).

[18] M. Goeppert-Mayer. "Double Beta-Disintegration". In: *Physical Review* 48 (1935), pp. 512–516. DOI: 10.1103/PhysRev.48.512 (cit. on p. 10).

[19] K. Zuber et al. "Double beta decay". In: *Contemporary Physics* 45.6 (2004), pp. 491–502. DOI: 10.1080/00107510412331283540. URL: https://doi.org/10.1080/00107510412331283540 (cit. on pp. 10, 11).

[20] A. Barabash et al. "Precise half-life values for two neutrino double beta decay". In: *Physical Review C* 81 (2010). DOI: 10.1103/PhysRevC.81.035501. eprint: arXiv:1003.1005 (cit. on pp. 10, 11).

[21] S. Dell'Oro et al. "Neutrinoless Double Beta Decay: 2015 Review". In: *Advances in High Energy Physics* 2016 (2016), pp. 1–37. ISSN: 1687-7365. DOI: 10.1155/2016/2162659. URL: http://dx.doi.org/10.1155/2016/2162659 (cit. on pp. 12, 13).

[22] M. J. Dolinski, A. Poon, and W. Rodejohann. "Neutrinoless Double-Beta Decay: Status and Prospects". In: *Annual Review of Nuclear and Particle Science* 69.1 (2019), pp. 219–251. DOI: 10.1146/annurev-nucl-101918-023407 (cit. on pp. 13–16).

[23] A. Barabash et al. "SuperNEMO double beta decay experiment". In: *Journal of Physics: Conference Series* 375 (Dec. 2011). DOI: 10.1088/1742-6596/375/1/042012 (cit. on p. 13).

[24] S. Umehara et al. "Neutrino-less double-β decay of ^{48}Ca studied by CaF$_2$(Eu) scintillators". In: *Phys. Rev. C* 78 (5 Nov. 2008), p. 058501. DOI: 10.1103/PhysRevC.78.058501. URL: https://link.aps.org/doi/10.1103/PhysRevC.78.058501 (cit. on p. 14).

[25] C. E. Aalseth et al. "Search for Neutrinoless Double-β Decay in ^{76}Ge with the Majorana Demonstrator". In: *Phys. Rev. Lett.* 120 (13 Mar. 2018), p. 132502. DOI: 10.1103/PhysRevLett.120.132502. URL: https://link.aps.org/doi/10.1103/PhysRevLett.120.132502 (cit. on p. 14).

[26] M. Agostini et al. "Final Results of GERDA on the Search for Neutrinoless Double-β Decay". In: *Phys. Rev. Lett.* 125 (25 Dec. 2020), p. 252502. DOI: 10.1103/PhysRevLett.125.252502. URL: https://link.aps.org/doi/10.1103/PhysRevLett.125.252502 (cit. on p. 14).

[27] R. Arnold et al. "Final results on ^{82}Se double beta decay to the ground state of ^{82}Kr from the NEMO-3 experiment". In: *Eur. Phys. J. C* 78.10 (2018), p. 821. DOI: 10.1140/epjc/s10052-018-6295-x. arXiv: 1806.05553 [hep-ex] (cit. on p. 14).

[28] O. Azzolini et al. "First Result on the Neutrinoless Double-β Decay of ^{82}Se with CUPID-0". In: *Phys. Rev. Lett.* 120 (23 June 2018), p. 232502. DOI: 10.1103/PhysRevLett.120.232502. URL: https://link.aps.org/doi/10.1103/PhysRevLett.120.232502 (cit. on p. 14).

[29] S. Blot, J. Mott, and C. Vilela. "Latest results of NEMO-3: New limit on the $0\nu\beta\beta$ decay half-life for 100Mo". In: *Journal of Physics: Conference Series* 598 (Apr. 2015), p. 012015. DOI: 10.1088/1742-6596/598/1/012015 (cit. on p. 14).

[30] A. S. Barabash et al. "Final results of the Aurora experiment to study 2β decay of ^{116}Cd with enriched ^{116}CdWO$_4$ crystal scintillators". In: *Phys. Rev. D* 98 (9 Nov. 2018), p. 092007. DOI: 10.1103/PhysRevD.98.092007. URL: https://link.aps.org/doi/10.1103/PhysRevD.98.092007 (cit. on p. 14).

[31] D. Q. Adams et al. "Improved Limit on Neutrinoless Double-Beta Decay in ^{130}Te with CUORE". In: *Phys. Rev. Lett.* 124 (12 Mar. 2020), p. 122501. DOI: 10.1103/PhysRevLett.124.122501. URL: https://link.aps.org/doi/10.1103/PhysRevLett.124.122501 (cit. on p. 14).

[32] K. Ni et al. "Searching for neutrino-less double beta decay of 136Xe with PandaX-II liquid xenon detector". In: *Chinese Physics C* 43.11 (2019), p. 113001. ISSN: 2058-6132. DOI: 10.1088/1674-1137/43/11/113001. URL: http://dx.doi.org/10.1088/1674-1137/43/11/113001 (cit. on p. 14).

[33] J. B. Albert et al. "Search for Neutrinoless Double-Beta Decay with the Upgraded EXO-200 Detector". In: *Phys. Rev. Lett.* 120 (7 Feb. 2018), p. 072701. DOI: 10.1103/PhysRevLett.120.072701. URL: https://link.aps.org/doi/10.1103/PhysRevLett.120.072701 (cit. on p. 14).

[34] Y. Gando. "Neutrinoless double beta decay search with KamLAND-Zen". In: *PoS* NOW2018 (2018), p. 068. DOI: 10.22323/1.337.0068 (cit. on p. 14).

[35] R. Arnold et al. "Measurement of the $2\nu\beta\beta$ decay half-life of ^{150}Nd and a search for $0\nu\beta\beta$ decay processes with the full exposure from the NEMO-3 detector". In: *Phys. Rev. D* 94 (7 Oct. 2016), p. 072003. DOI: 10.1103/PhysRevD.94.072003. URL: https://link.aps.org/doi/10.1103/PhysRevD.94.072003 (cit. on p. 14).

[36] N. Abgrall. "The Large Enriched Germanium Experiment for Neutrinoless Double Beta Decay (LEGEND)". In: *Proceedings of the MEDEX'17 meeting, Prague, May 29 - June 2, 2017*. 2017. DOI: 10.1063/1.5007652 (cit. on p. 14).

[37] V. Lozza. "The SNO+ Experiment for Neutrinoless Double-Beta Decay". In: *Nuclear and Particle Physics Proceedings* 273-275 (2016). 37th International Conference on High Energy Physics (ICHEP), pp. 1836–1841. ISSN: 2405-6014. DOI: https://doi.org/10.1016/j.nuclphysbps.2015.09.296 (cit. on p. 15).

[38] Juan Jose Gomez-Cadenas. *The NEXT experiment*. 2014. arXiv: 1411.2433 [physics.ins-det] (cit. on p. 15).

[39] E. Akhmedov. *Majorana neutrinos and other Majorana particles:Theory and experiment*. 2014. arXiv: 1412.3320 [hep-ph] (cit. on p. 16).

[40] R. Arnold et al. "Technical design and performance of the NEMO3 detector". In: *Nuclear Instruments and Methods in Physics Research Section A* 536 (Feb. 2004). DOI: 10.1016/j.nima.2004.07.194 (cit. on p. 18).

[41] M. Cascella et al. "Construction and commissioning of the SuperNEMO detector tracker". In: *Nuclear Instruments and Methods in Physics Research A* 824 (2016), pp. 507–509. ISSN: 0168-9002. DOI: 10.1016/j.nima.2015.11.083. URL: http://dx.doi.org/10.1016/j.nima.2015.11.083 (cit. on p. 18).

[42] A.S. Barabash et al. "Calorimeter development for the SuperNEMO double beta decay experiment". In: *Nuclear Instruments and Methods in Physics Research Section A: Accelerators, Spectrometers, Detectors and Associated Equipment* 868 (2017), pp. 98–108. ISSN: 0168-9002. DOI: https://doi.org/10.1016/j.nima.2017.06.044. URL: https://www.sciencedirect.com/science/article/pii/S0168900217306976 (cit. on pp. 19, 20).

[43] Ch. Marquet. "The SuperNEMO calorimeter". In: *Journal of Physics: Conference Series* 888 (Sept. 2017), p. 012227. DOI: 10.1088/1742-6596/888/1/012227. URL: https://doi.org/10.1088/1742-6596/888/1/012227 (cit. on p. 20).

[44] T. Noblet. "Background studies and design optimisation of the SuperNEMO demonstrator module: search for $2\nu\beta\beta$ and $0\nu\beta\beta$ decays of 116Cd into the excited states of 116Sn with NEMO-3". PhD thesis. Sept. 2017 (cit. on p. 24).

[45] R. Arnold et al. "Probing new physics models of neutrinoless double beta decay with SuperNEMO". In: *The European Physical Journal C* 70.4 (Nov. 2010), pp. 927–943. ISSN: 1434-6052. DOI: 10.1140/epjc/s10052-010-1481-5. URL: http://dx.doi.org/10.1140/epjc/s10052-010-1481-5 (cit. on p. 25).

[46] G Heusser. "Low-Radioactivity Background Techniques". In: *Annual Review of Nuclear and Particle Science* 45 (Nov. 2003), pp. 543–590. DOI: 10.1146/annurev.ns.45.120195.002551 (cit. on pp. 32, 33, 38, 39).

[47] V. Kudryavtsev, Luciano Pandola, and V. Tomasello. "Neutron- and muon-induced background in underground physics experiments". In: *The European Physical Journal A* 36 (Feb. 2008). DOI: 10.1140/epja/i2007-10539-6 (cit. on pp. 33, 35, 36).

[48] T. K. Gaisser. *Cosmic rays and particle physics.* 1990 (cit. on p. 33).

[49] Dongming Mei and A. Hime. "Muon-Induced Background Study for Underground Laboratories". In: *Physical Review D* 73 (Dec. 2005). DOI: 10.1103/PhysRevD.73.053004 (cit. on pp. 33, 35–37).

[50] W. Y. Cheng et al. "Measurement of Cosmic Ray Flux in China JinPing underground Laboratory". In: *Chinese Physics C* 37.8 (2013), p. 086001. DOI: 10.1088/1674-1137/37/8/086001. eprint: 1305.0899 (cit. on p. 34).

[51] A. S. Malgin. "Phenomenology of muon-induced neutron yield". In: *Phys. Rev. C* 96 (1 July 2017), p. 014605. DOI: 10.1103/PhysRevC.96.014605. URL: https://link.aps.org/doi/10.1103/PhysRevC.96.014605 (cit. on pp. 34, 35, 67, 68).

[52] H. Kluck. "Measurement of the Cosmic-Induced Neutron Yield at the Modane Underground Laboratory". PhD thesis. KIT, Karlsruhe, 2013. DOI: 10.1007/978-3-319-18527-9. URL: http://nbn-resolving.org/urn:nbn:de:swb:90-398379 (cit. on pp. 36, 67, 68).

[53] G. V. Gorshkov and V. A. Zyabkin. "Production of neutrons in Pb, Cd, Fe, and Al under the influence of cosmic-ray muons at a depth of 150 m water equivalent". In: *Sov. J. Nucl. Phys.* 7 (1968), pp. 470–474 (cit. on p. 36).

[54] L. Reichhart et al. "Measurement and simulation of the muon-induced neutron yield in lead". In: *Astroparticle Physics* 47 (2013), pp. 67–76. ISSN: 0927-6505. DOI: https://doi.org/10.1016/j.astropartphys.2013.06.002 (cit. on p. 36).

[55] N. Yu. Agafonova and A. S. Malgin. "Universal formula for the muon-induced neutron yield". In: *Physical Review D* 87 (11 June 2013), p. 113013. DOI: 10.1103/PhysRevD.87.113013 (cit. on p. 36).

[56] Y.-F. Wang et al. "Predicting neutron production from cosmic-ray muons". In: *Physical Review D* 64 (1 June 2001), p. 013012. DOI: 10.1103/PhysRevD.64.013012 (cit. on p. 35).

[57] J. Monroe. "Neutrino backgrounds to dark matter searches and directionality". In: *Journal of Physics: Conference Series* 136 (2008). DOI: 10.1088/1742-6596/136/2/022037 (cit. on p. 37).

[58] S. Cebrián. "Cosmogenic activation of materials". In: *International Journal of Modern Physics A* 32.30 (2017), p. 1743006. DOI: 10.1142/S0217751X17430060 (cit. on p. 39).

[59] J. Masarik and J. Beer. "Simulation of particle fluxes and cosmogenic nuclide production in the Earth's atmosphere". In: *Journal of Geophysical Research: Atmospheres* 104.D10 (1999), pp. 12099–12111. DOI: https://doi.org/10.1029/1998JD200091 (cit. on p. 40).

[60] S.Y.F. Chu, L. P. Ekström, and R. B. Firestone. *The Lund/LBNL Nuclear Data Search.* URL: http://nucleardata.nuclear.lu.se/toi/ (cit. on pp. 40, 41, 96, 103, 116).

[61] V. Chazal et al. "Neutron background measurements in the Underground Laboratory of Modane". In: *Astroparticle Physics* 9.2 (1998), pp. 163–172. ISSN: 0927-6505. DOI: https://doi.org/10.1016/S0927-6505(98)00012-7 (cit. on pp. 42–46, 67, 113).

[62] D. Malczewski, J. Kisiel, and J. Dorda. "Gamma background measurements in the Laboratoire Souterrain de Modane". In: *Journal of Radioanalytical and Nuclear Chemistry* 292 (May 2012), pp. 751–756. DOI: 10.1007/s10967-011-1497-9 (cit. on pp. 42–44).

[63] Ch. Berger et al. "Experimental study of muon bundles observed in the Fréjus detector". In: *Phys. Rev. D* 40 (7 Oct. 1989), pp. 2163–2171. DOI: 10.1103/PhysRevD.40.2163 (cit. on p. 43).

[64] W. Rhode et al. "Limits on the flux of very high energy neutrinos with the Fréjus detector". In: *Astroparticle Physics* 4.3 (1996), pp. 217–225. ISSN: 0927-6505. DOI: https://doi.org/10.1016/0927-6505(95)00038-0 (cit. on p. 43).

[65] H. Ohsumi et al. "Gamma-ray flux in the Fréjus underground laboratory measured with NaI detector". In: *Nuclear Instruments and Methods in Physics Research Section A: Accelerators, Spectrometers, Detectors and Associated Equipment* 482.3 (2002), pp. 832–839. ISSN: 0168-9002. DOI: https://doi.org/10.1016/S0168-9002(01)01866-6 (cit. on pp. 43, 44, 112, 113, 116).

[66] E. Armengaud et al. "Background studies for the EDELWEISS dark matter experiment". In: *Astroparticle Physics* 47 (2013), pp. 1–9. ISSN: 0927-6505. DOI: https://doi.org/10.1016/j.astropartphys.2013.05.004 (cit. on p. 43).

[67] S. Fiorucci et al. "Identification of backgrounds in the EDELWEISS-I dark matter search experiment". In: *Astroparticle Physics* 28.1 (2007), pp. 143–153. ISSN: 0927-6505. DOI: https://doi.org/10.1016/j.astropartphys.2007.05.003 (cit. on p. 43).

[68] I. Štekl et al. "Low Radon Cleanroom for Underground Laboratories". In: *Frontiers in Public Health* 8 (Feb. 2021). DOI: 10.3389/fpubh.2020.589891 (cit. on p. 43).

[69] S. Rozov et al. *Monitoring of the thermal neutron flux in the LSM underground laboratory.* 2010. arXiv: 1001.4383 [astro-ph.IM] (cit. on pp. 44, 46, 113, 115).

[70] Joseph A. Formaggio and C.J. Martoff. "Backgrounds to sensitive experiments underground". In: *Annual Review of Nuclear and Particle Science* 54.1 (2004), pp. 361–412. DOI: 10.1146/annurev.nucl.54.070103.181248 (cit. on p. 47).

[71] G. Royer. "Generalized liquid drop model and fission, fusion, alpha and cluster radioactivity and superheavy nuclei". In: *4th International Conference on Current Problems in Nuclear Physics and Atomic Energy, NPAE 2012 - Proceedings* (Sept. 2012) (cit. on p. 47).

[72] K. S. Krane. *Introductory nuclear physics.* New York, NY: Wiley, 1988 (cit. on pp. 47, 48, 52, 54).

[73] N. Ensslin. "The Origin of Neutron Radiation". In: *Passive Nondestructive Assay Manual (PANDA).* 1991. ISBN: 0160327245 (cit. on pp. 48, 50, 52–54).

[74] S. Simakov, M. Verpelli, and N. Otsuka. *Update of the nuclear data for the neutron emissions for actinides of interest in safeguards, Nuclear Data Section, IAEA.* 2015. URL: https://www-nds.iaea.org/sgnucdat/ (cit. on p. 48).

[75] J. M. Verbeke, Ch. Hagmann, and D. Wright. *Simulation of neutron and gamma ray emission from fission and photofission. LLNL Fission Library 2.0.2.* Tech. rep. 2016 (cit. on pp. 48, 49).

[76] G. Vlaskin and Y. Khomiakov. "Calculation of Neutron Production Rates and Spectra from Compounds of Actinides and Light Elements". In: *EPJ Web of Conferences* 153 (Jan. 2017), p. 07033. DOI: 10.1051/epjconf/201715307033 (cit. on pp. 48, 49, 54, 55).

[77] E. F. Shores. *Data Updates for the SOURCES-4A Computer Code, LA-UR-00-5016.* 2000 (cit. on p. 48).

[78] D. G. Madland et al. *SOURCES 4A: A Code for Calculating (alpha,n), Spontaneous Fission, and Delayed Neutron Sources and Spectra.* Tech. rep. United States, 1999, pp. 1–159. URL: http://inis.iaea.org/search/search.aspx?orig_q=RN:32027512 (cit. on pp. 49, 50, 53–55).

[79] V.A. Kudryavtsev, P. Zakhary, and B. Easeman. "Neutron production in (α,n) reactions". In: *Nuclear Instruments and Methods in Physics Research Section A: Accelerators, Spectrometers, Detectors and Associated Equipment* 972 (2020), p. 164095. ISSN: 0168-9002. DOI: https://doi.org/10.1016/j.nima.2020.164095. URL: http://www.sciencedirect.com/science/article/pii/S0168900220305088 (cit. on pp. 49, 50, 52–54).

[80]   *MCNP - A General Monte Carlo N-Particle Transport Code, Version 5, LA-UR-03-1987* (cit. on p. 49).

[81]   *Evaluated Nuclear Data Library, ENDL.* URL: https://www.oecd-nea.org/dbdata/data/nds_eval_libs.htm (cit. on p. 49).

[82]   J. Lestone. *Watt parameters for the Los Alamos Model : Subroutine getab.* Sept. 2014 (cit. on p. 49).

[83]   B. Broadhead and J. Wagschal. "The Fission Spectrum Uncertainty. United States: American Nuclear Society - ANS". In: (Jan. 2004) (cit. on p. 49).

[84]   M. M. Islam and H. H. Knitter. "The Energy Spectrum of Prompt Neutrons from the Fission of Uranium-235 by 0.40-MeV Neutrons". In: *Nuclear Science and Engineering* 50.2 (1973), pp. 108–114. DOI: 10.13182/NSE73-A23234 (cit. on p. 49).

[85]   M. Kocak, H. Ahmadov, and G. Dere. "On prompt fission neutron spectrum in spontaneous fission of 252Cf". In: *Annals of Nuclear Energy* 70 (Aug. 2014), pp. 82–86. DOI: 10.1016/j.anucene.2014.03.006 (cit. on p. 49).

[86]   T. E. Valentine. "Evaluation of prompt fission gamma rays for use in simulating nuclear safeguard measurements". In: *Annals of Nuclear Energy* 28.3 (2001), pp. 191–201. ISSN: 0306-4549. DOI: https://doi.org/10.1016/S0306-4549(00)00039-6 (cit. on p. 50).

[87]   H. Shengnian, C. Jinggui, and H. Honguin. *Neutron multiplicity of U-238 spontaneous fission, INDC(NDS)–220.* 1989 (cit. on pp. 50, 51).

[88]   J. P. Lestone. *A comparison between two evaluations of neutron multiplicity distributions, LA-UR-08-1084.* 2008 (cit. on p. 50).

[89]   S. Cristallo et al. "The Importance of the 13C(α,n)16O Reaction in Asymptotic Giant Branch Stars". In: *The Astrophysical Journal* 859.2 (May 2018), p. 105. DOI: 10.3847/1538-4357/aac177 (cit. on p. 53).

[90]   M. La Cognata et al. "On the Measurement of the 13C(α, n)16O S-factor at Negative Energies and its Influence on the s-process". In: *The Astrophysical Journal* 777 (Nov. 2013), p. 143. DOI: 10.1088/0004-637X/777/2/143 (cit. on p. 53).

[91]   J.P. Mason. "A 6130 keV gamma-ray source using the 13C(α, n)16O reaction". In: *Nuclear Instruments and Methods in Physics Research Section A: Accelerators, Spectrometers, Detectors and Associated Equipment* 241.1 (1985), pp. 207–209. ISSN: 0168-9002. DOI: https://doi.org/10.1016/0168-9002(85)90534-0. URL: http://www.sciencedirect.com/science/article/pii/0168900285905340 (cit. on p. 53).

[92]   *JANIS: Java-based Nuclear Data Information Software.* URL: http://www.oecd-nea.org/janisweb/ (cit. on pp. 53, 57, 61, 105, 135).

[93]   G.W. Kerr, J.M. Morris, and J.R. Risser. "Energy levels of 17O from 13C(α,α0)13C and 13C(α,n)16O". In: *Nuclear Physics A* 110.3 (1968), pp. 637–656. ISSN: 0375-9474. DOI: https://doi.org/10.1016/0375-9474(68)90378-3. URL: http://www.sciencedirect.com/science/article/pii/0375947468903783 (cit. on p. 53).

[94] S. Westerdale and P.D. Meyers. "Radiogenic neutron yield calculations for low-background experiments". In: *Elsevier Nuclear Instruments and Methods in Physics Research Section A: Accelerators, Spectrometers, Detectors and Associated Equipment* 875 (2017), pp. 57–64. DOI: 10.1016/j.nima.2017.09.007 (cit. on pp. 53, 54, 56).

[95] D. M. Mei, C. Zhang, and A. Hime. "Evaluation of (α, n) Induced Neutrons as a Background for Dark Matter Experiments". In: *Nuclear Instruments and Methods in Physics Research Section A: Accelerators, Spectrometers, Detectors and Associated Equipment* 606 (July 2009), pp. 651–660. DOI: 10.1016/j.nima.2009.04.032 (cit. on pp. 53, 54).

[96] R. Heaton et al. "Neutron production from thick-target (α, n) reactions". In: *Nuclear Instruments and Methods in Physics Research Section A: Accelerators, Spectrometers, Detectors and Associated Equipment* 276.3 (Apr. 1989), pp. 529–538. ISSN: 0168-9002. DOI: https://doi.org/10.1016/0168-9002(89)90579-2. URL: http://www.sciencedirect.com/science/article/pii/0168900289905792 (cit. on p. 54).

[97] R. Babut, E. Fort, and E. Dupont. "Modeling of (α, n) Reactions on Light Nuclei". In: *Journal of Nuclear Science and Technology* 39.sup2 (2002), pp. 180–183. DOI: 10.1080/00223131.2002.10875070. URL: https://doi.org/10.1080/00223131.2002.10875070 (cit. on p. 54).

[98] M.T. Pigni, I.C. Gauld, and S. Croft. "(α,n) reactions in oxide compounds calculated from the R-matrix theory". In: *Progress in Nuclear Energy* 118 (2020), p. 103130. ISSN: 0149-1970. DOI: https://doi.org/10.1016/j.pnucene.2019.103130. URL: http://www.sciencedirect.com/science/article/pii/S0149197019302392 (cit. on pp. 54, 55).

[99] E. Mendoza et al. "Neutron production induced by α-decay with Geant4". In: *Nuclear Instruments and Methods in Physics Research Section A: Accelerators, Spectrometers, Detectors and Associated Equipment* 960 (2020), p. 163659. ISSN: 0168-9002. DOI: https://doi.org/10.1016/j.nima.2020.163659. URL: http://www.sciencedirect.com/science/article/pii/S0168900220302333 (cit. on pp. 54–56).

[100] S. Westerdale. *NeuCBOT*. URL: https://github.com/shawest/neucbot (cit. on p. 54).

[101] S. Agostinelli et al. "Geant4—a simulation toolkit". In: *Nuclear Instruments and Methods in Physics Research Section A: Accelerators, Spectrometers, Detectors and Associated Equipment* 506.3 (July 2003), pp. 250–303. ISSN: 0168-9002. DOI: https://doi.org/10.1016/S0168-9002(03)01368-8. URL: http://www.sciencedirect.com/science/article/pii/S0168900203013688 (cit. on p. 54).

[102] V. Ramkumar et al. *Nuclear Data – Benchmarking 19F(alpha,n) Yield Data for Nuclear Safeguards. ORNL Report.* 2019 (cit. on p. 54).

[103] W. N. Hess. *Neutrons from ([alpha], n) sources.* UCRL 3839. Berkeley, CA: University of California Radiation Laboratory, 1957. URL: http://hdl.handle.net/2027/mdp.39015077592767 (cit. on p. 55).

[104] A.J. Koning and D. Rochman. "Modern Nuclear Data Evaluation with the TALYS Code System". In: *Nuclear Data Sheets* 113.12 (2012). Special Issue on Nuclear Reaction Data, pp. 2841–2934. ISSN: 0090-3752. DOI: https://doi.org/10.1016/j.nds.2012.11.002. URL: http://www.sciencedirect.com/science/article/pii/S0090375212000889 (cit. on p. 55).

[105] M. Herman et al. "EMPIRE: Nuclear Reaction Model Code System for Data Evaluation". In: *Nuclear Data Sheets* 108.12 (2007). Special Issue on Evaluations of Neutron Cross Sections, pp. 2655–2715. ISSN: 0090-3752. DOI: https://doi.org/10.1016/j.nds.2007.11.003. URL: http://www.sciencedirect.com/science/article/pii/S0090375207000981 (cit. on p. 55).

[106] T. Murata, H. Matsunobu, and K. Shibata. *Evaluation of the (α, xn) reaction data for JENDL/AN-2005 (JAEA-Research–2006-052)*. Tech. rep. 2006 (cit. on pp. 55, 56).

[107] A.J. Koning et al. "TENDL: Complete Nuclear Data Library for Innovative Nuclear Science and Technology". In: *Nuclear Data Sheets* 155 (2019). Special Issue on Nuclear Reaction Data, pp. 1–55. ISSN: 0090-3752. DOI: https://doi.org/10.1016/j.nds.2019.01.002. URL: http://www.sciencedirect.com/science/article/pii/S009037521930002X (cit. on pp. 55, 56).

[108] *ASTAR program*. URL: https://physics.nist.gov/PhysRefData/Star/Text/ASTAR.html (cit. on p. 55).

[109] J. F. Ziegler, M.D. Ziegler, and J.P. Biersack. "SRIM – The stopping and range of ions in matter (2010)". In: *Nuclear Instruments and Methods in Physics Research Section B: Beam Interactions with Materials and Atoms* 268.11 (2010). 19th International Conference on Ion Beam Analysis, pp. 1818–1823. ISSN: 0168-583X. DOI: https://doi.org/10.1016/j.nimb.2010.02.091. URL: http://www.sciencedirect.com/science/article/pii/S0168583X10001862 (cit. on p. 55).

[110] V. Pesudo et al. "SaG4n: Calculation of (α,n) yields for low background experiments using Geant4". In: *Journal of Physics: Conference Series* 1468 (Feb. 2020), p. 012059. DOI: 10.1088/1742-6596/1468/1/012059 (cit. on p. 56).

[111] *TALYS-based evaluated nuclear data library, TENDL-2017*. URL: https://tendl.web.psi.ch/tendl_2017/tendl2017.html (cit. on p. 56).

[112] K. Paaren and H. K. Lee. "Simulation study of alpha-neutron reactions from AmBe directional source using MCNP 6.1.1 with TENDL 2012, 2014, and 2017 libraries". In: *Applied Radiation and Isotopes* 146 (2019), pp. 104–114. ISSN: 0969-8043. DOI: https://doi.org/10.1016/j.apradiso.2019.01.011 (cit. on p. 56).

[113] *TALYS: A tool to go from theoretical modeling of nuclear reactions to evaluations*. 2014. URL: https://ejc2014.sciencesconf.org/resource/page/id/53.html (cit. on p. 56).

[114] Zakalek, P. et al. "Energy and target material dependence of the neutron yield induced by proton and deuteron bombardment". In: *EPJ Web Conf.* 231 (2020), p. 03006. DOI: 10.1051/epjconf/202023103006. URL: https://doi.org/10.1051/epjconf/202023103006 (cit. on p. 56).

[115] E. Mendoza et al. "NuDEX: A new nuclear -ray cascades generator". In: *EPJ Web of Conferences* 239 (Jan. 2020), p. 17006. DOI: `10.1051/epjconf/202023917006` (cit. on p. 69).

[116] M. Macko. "SuperNEMO Experiment: Study of Systematic Uncertainties of Track Reconstruction and Energy Calibration. Evaluation of Sensitivity to $0\nu\beta\beta$ with Emission of Majoron for ^{82}Se." PhD thesis. Dec. 2018 (cit. on pp. 69, 89).

[117] P. Žugec et al. "GEANT4 simulation of the neutron background of the C6D6 set-up for capture studies at n$_T$OF". In: *Nuclear Instruments and Methods in Physics Research Section A: Accelerators, Spectrometers, Detectors and Associated Equipment* 760 (2014), pp. 57–67. ISSN: 0168-9002. DOI: `https://doi.org/10.1016/j.nima.2014.05.048` (cit. on p. 69).

[118] F. Bečvář. "DICEBOX. Simulation of γ cascades in complex nuclei with emphasis on assessment of uncertainties of cascade-related quantities". In: *Nuclear Instruments and Methods in Physics Research Section A: Accelerators, Spectrometers, Detectors and Associated Equipment* 417.2 (1998), pp. 434–449. ISSN: 0168-9002. DOI: `https://doi.org/10.1016/S0168-9002(98)00787-6`. URL: `https://www-nds.iaea.org/dicebox/` (cit. on p. 69).

[119] *Scheme of the radiative neutron capture (also called as (n,γ) reaction)*. URL: `https://www.bnc.hu/?q=radiative_neutron_capture` (cit. on p. 69).

[120] F. Bečvář. "Simulation of γ cascades in complex nuclei with emphasis on assessment of uncertainties of cascade-related quantities". In: *Nuclear Instruments and Methods in Physics Research Section A: Accelerators, Spectrometers, Detectors and Associated Equipment* 417.2 (1998), pp. 434–449. ISSN: 0168-9002. DOI: `https://doi.org/10.1016/S0168-9002(98)00787-6`. URL: `http://www.sciencedirect.com/science/article/pii/S0168900298007876` (cit. on pp. 69, 70).

[121] A. Hurst et al. "Investigation of the tungsten isotopes via thermal neutron capture". In: *Physical Review C* 89 (Nov. 2014). DOI: `10.1103/PhysRevC.89.014606` (cit. on p. 70).

[122] B. Sleaford et al. "Neutron Capture Gamma-Ray Libraries for Nuclear Applications". In: *AIP Conference Proceedings* 1342 (June 2011). DOI: `10.1063/1.3583170` (cit. on p. 70).

[123] M. Krticka. "Photon Strength Functions in Rare-Earth Nuclei Studied from Slow Neutron Capture". PhD thesis. Charles University in Prague, 2002 (cit. on p. 71).

[124] D. M. Brink. *Ph.D. thesis, Oxford University*. 1955 (cit. on p. 71).

[125] P. Axel. "Electric Dipole Ground-State Transition Width Strength Function and 7-Mev Photon Interactions". In: *Phys. Rev.* 126 (2 Apr. 1962), pp. 671–683. DOI: `10.1103/PhysRev.126.671`. URL: `https://link.aps.org/doi/10.1103/PhysRev.126.671` (cit. on p. 71).

[126] J. Isaak et al. "The concept of nuclear photon strength functions: A model-independent approach via $(\gamma \rightarrow \gamma', \gamma'')$ reactions". In: *Physics Letters B* 788 (2019), pp. 225–230. ISSN: 0370-2693. DOI: `https://doi.org/10.1016/j.physletb.2018.11.038` (cit. on p. 71).

[127] *Evaluated Nuclear Structure Data File (ENSDF), an electronic database of evaluated experimental nuclear structure data maintained by the National Nuclear Data Center, Brookhaven National laboratory.* URL: https://www.nndc.bnl.gov/ensdf/ (cit. on p. 72).

[128] M. R. Bhat. "Evaluated Nuclear Structure Data File (ENSDF)". In: *Nuclear Data for Science and Technology.* Ed. by Syed M. Qaim. Berlin, Heidelberg: Springer Berlin Heidelberg, 1992, pp. 817–821. ISBN: 978-3-642-58113-7 (cit. on p. 72).

[129] R. Firestone et al. "Thermal neutron capture cross section for Fe 56 (n , γ)". In: *Physical Review C* 95 (Jan. 2017). DOI: 10.1103/PhysRevC.95.014328 (cit. on pp. 72, 76).

[130] C. J. Prokop et al. "Measurement of the ^{65}Cu(n, γ) cross section using the Detector for Advanced Neutron Capture Experiments at LANL". In: *Phys. Rev. C* 99 (5 May 2019), p. 055809. DOI: 10.1103/PhysRevC.99.055809 (cit. on p. 72).

[131] T. Kibédi et al. "Evaluation of theoretical conversion coefficients using BrIcc". In: *Nuclear Instruments and Methods in Physics Research Section A: Accelerators, Spectrometers, Detectors and Associated Equipment* 589.2 (2008), pp. 202–229. ISSN: 0168-9002. DOI: https://doi.org/10.1016/j.nima.2008.02.051 (cit. on p. 72).

[132] R. Capote et al. "RIPL – Reference Input Parameter Library for Calculation of Nuclear Reactions and Nuclear Data Evaluations". In: *Nuclear Data Sheets* 110.12 (2009). Special Issue on Nuclear Reaction Data, pp. 3107–3214. ISSN: 0090-3752. DOI: https://doi.org/10.1016/j.nds.2009.10.004. URL: https://www-nds.iaea.org/RIPL-3/ (cit. on p. 72).

[133] M. F. L'Annunziata. "1 - NUCLEAR RADIATION, ITS INTERACTION WITH MATTER AND RADIOISOTOPE DECAY". In: *Handbook of Radioactivity Analysis (Second Edition).* Ed. by Michael F. L'Annunziata. Second Edition. San Diego: Academic Press, 2003, pp. 1–121. ISBN: 978-0-12-436603-9. DOI: https://doi.org/10.1016/B978-012436603-9/50006-5 (cit. on p. 76).

[134] *Falaise simulation software web page.* URL: http://supernemo.org/Falaise (cit. on p. 80).

[135] R. Brun et al. "ROOT - An Object Oriented Data Analysis Framework, Proceedings AIHENP'96 Workshop, Lausanne". In: *Nuclear Instruments and Methods in Physics Research Section A* 389 (1996), pp. 81–86 (cit. on p. 80).

[136] Ch. Patrick. *Sensitivity Module.* URL: https://github.com/SuperNEMO-DBD/SensitivityModule (cit. on p. 80).

[137] S. Westerdale. "A Study of Nuclear Recoil Backgrounds in Dark Matter Detectors". PhD thesis. Princeton University, 2016. URL: https://dataspace.princeton.edu/handle/88435/dsp01hx11xh73n (cit. on p. 95).

[138] S. F. Mughabghab. *Thermal neutron capture cross sections resonance integrals and g-factors, (INDC(NDS)–440), IAEA.* 2003 (cit. on p. 97).

[139] Z. Liu et al. "The 4.438MeV gamma to neutron ratio for the Am–Be neutron source". In: *Applied Radiation and Isotopes* 65 (Jan. 2007), pp. 1318–1321. DOI: 10.1016/j.apradiso.2007.04.007 (cit. on pp. 103, 104).

[140] Switzerland International Organization for Standardization Geneva. *ISO 8529-1:2001: Reference neutron radiations. Part 1: Characteristics and methods of production.* URL: http://www.iso.org/iso/%20catalogue_detail.htm?csnumber=25666 (cit. on p. 103).

[141] U. Benedict et al. "Preparation and X-ray diffraction study of PaBe13, AmBe13, and CmBe13". In: *Journal of the Less Common Metals* 42.3 (1975), pp. 345–354. ISSN: 0022-5088. DOI: https://doi.org/10.1016/0022-5088(75)90054-5. URL: http://www.sciencedirect.com/science/article/pii/0022508875900545 (cit. on p. 103).

[142] L. D. Schulte. *Actinide Beryllium Neutron Source with Reduced Dispersion Characteristics. Background Information on AmBe Source Fabrication. Patent S-116,232. LA-UR-11-01808.* 2011 (cit. on pp. 103, 104).

[143] A. Didi et al. "Neutron activation analysis: Modelling studies to improve the neutron flux of Americium–Beryllium source". In: *Nuclear Engineering and Technology* 49.4 (2017), pp. 787–791. ISSN: 1738-5733. DOI: https://doi.org/10.1016/j.net.2017.02.002 (cit. on p. 103).

[144] J. Scherzinger et al. "Tagging fast neutrons from an 241Am/9Be source". In: *Applied Radiation and Isotopes* 98 (2015), pp. 74–79. ISSN: 0969-8043. DOI: https://doi.org/10.1016/j.apradiso.2015.01.003. URL: http://www.sciencedirect.com/science/article/pii/S0969804315000044 (cit. on pp. 103, 104).

[145] K. W. Geiger and L. Van Der Zwan. "Radioactive neutron source spectra from 9Be(α, n) cross section data". In: *Nuclear Instruments and Methods* 131.2 (1975), pp. 315–321. ISSN: 0029-554X. DOI: https://doi.org/10.1016/0029-554X(75)90336-5 (cit. on p. 104).

[146] A.D. Vijaya and A. Kumar. "The neutron spectrum of Am-Be neutron sources". In: *Nuclear Instruments and Methods* 111.3 (1973), pp. 435–440. ISSN: 0029-554X. DOI: https://doi.org/10.1016/0029-554X(73)90199-7 (cit. on p. 108).

[147] A. Pin. "Recherche de la nature du neutrino via la décroissance double bêta sans émission de neutrinos : Caractérisation et optimisation du calorimètre SuperNEMO et impact sur la recherche de la décroissance du 82Se : Développement du premier prototype LiquidO". PhD thesis. Université de Bordeaux, 2020. URL: http://www.theses.fr/2020BORD0277 (cit. on p. 109).

[148] International Atomic Energy Agency - Nuclear Data Section. *Thermal Neutron Capture γ's (CapGam).* URL: https://www-nds.iaea.org/capgam/index.htmlx (cit. on p. 116).

Appendix A

(α,n) Reactions

Isotopic abundances of elements used in elemental definition of materials, along with the α particle energies of ^{238}U and ^{232}Th decay chains, and reaction cross-sections used in the Geant4 simulation are found in this appendix.

TABLE A.1: Isotope abundances used in simulation

Element	Isotope	Abundance [%]
H	^{1}H	99.989
	^{2}H	0.011
C	^{12}C	98.93
	^{13}C	1.07
O	^{16}O	99.757
	^{17}O	0.038
	^{18}O	0.205
B	^{10}B	19.9
	^{11}B	80.1
Fe	^{54}Fe	5.845
	^{56}Fe	91.754
	^{57}Fe	2.119
	^{58}Fe	0.282
Si	^{28}Si	92.93
	^{29}Si	4.683
	^{30}Si	3.087
Na	^{23}Na	100
K	^{39}K	93.258
	^{40}K	0.012
	^{41}K	6.73
Al	^{27}Al	100
Be	^{9}Be	100
Cu	^{63}Cu	69.17
	^{65}Cu	30.83

TABLE A.2: ^{238}U decay chain α particle energies used in SaG4n simulation

Nuclide	α energy [MeV]	Intensity
$^{238}_{92}U$	4.198	79
	4.151	20.9
	4.038	0.078
$^{234}_{92}U$	4.7746	71.38
	4.7224	28.42
	4.6035	0.2
	4.2773	4.00×10^{-5}
	4.1506	2.60×10^{-5}
	4.1086	7.00×10^{-6}
$^{230}_{90}Th$	4.687	76.3
	4.6205	23.4
	4.4798	0.12
	4.4384	0.03
	4.3718	0.00097
	4.2783	8.00×10^{-6}
	4.2485	1.03×10^{-5}
	3.8778	3.40×10^{-6}
	3.8294	1.40×10^{-6}
$^{226}_{88}Ra$	4.78434	93.84
	4.601	6.16
	4.34	0.0065
	4.191	0.001
	4.16	0.00027
$^{222}_{86}Rn$	5.48948	99.92
	4.986	0.078
	4.826	0.0005
$^{218}_{84}Po$	6.00235	99.9789002
	5.181	0.00109978
	6.756	0.00071928
	6.693	0.017982
$^{218}_{85}At$	6.653	0.00127872
$^{218}_{86}Rn$	7.1292	2.00×10^{-5}
	6.5311	2.54×10^{-8}
$^{214}_{83}Bi$	5.516	0.009408
	5.452	0.012936
	5.273	0.001392
	5.184	0.0001464
	5.023	5.04×10^{-5}
	4.941	6.00×10^{-5}
$^{214}_{84}Po$	7.68682	99.9655025
	6.9022	0.0103975
	6.6098	6.00×10^{-5}
$^{210}_{82}Pb$	3.72	1.90×10^{-6}
$^{210}_{83}Bi$	4.694	5.20×10^{-5}
	4.656	7.80×10^{-5}
$^{210}_{84}Po$	5.30433	99.99987
	4.51658	0.00104

TABLE A.3: ^{232}Th decay chain α particle energies used in SaG4n simulation

Nuclide	α energy [MeV]	Intensity
$^{232}_{90}Th$	4.0123	78.2
	3.9472	21.7
	3.8111	0.069
	5.42315	73.4
$^{228}_{90}Th$	5.34036	26
	5.211	0.408
	5.173	0.218
	5.138	0.036
$^{224}_{88}Ra$	5.68537	94.92
	5.4486	5.06
	5.161	0.0071
	5.051	0.0076
	5.034	0.003
$^{220}_{86}Rn$	6.28808	99.886
	5.747	0.114
$^{216}_{84}Po$	6.7783	99.9981
	5.985	0.0019
$^{212}_{83}Bi$	6.08988	9.746928
	6.05078	25.125654
	5.768	0.61098
	5.626	0.0564258
	5.607	0.406122
	5.481	0.0046722
	5.345	0.0003594
	5.302	3.95×10^{-5}
$^{212}_{84}Po$	8.78486	64.06
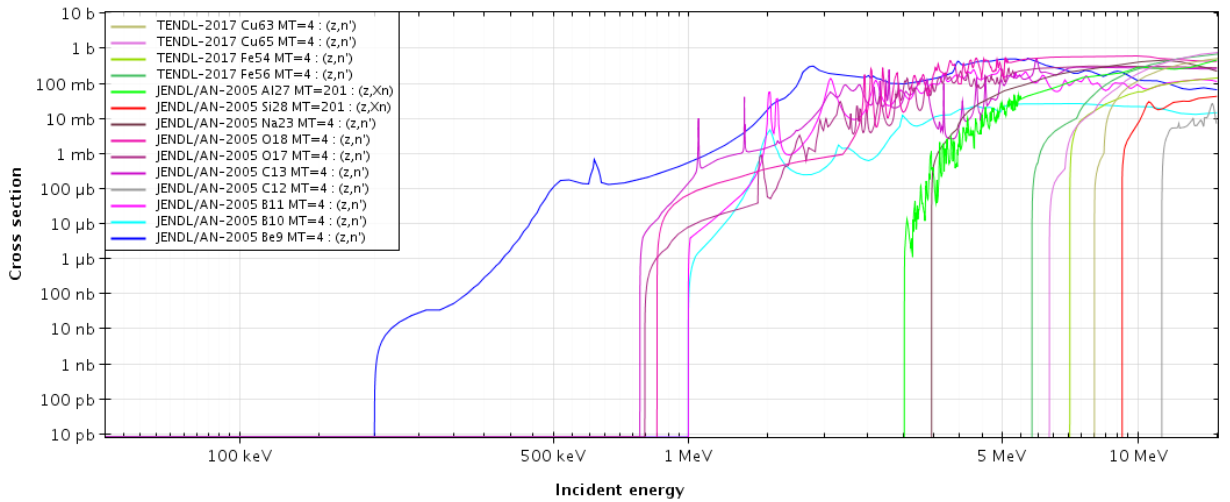
FIGURE A.1: Cross-sections for (α,Xn) reactions [92] (z - incident particle (α), (z,n) - production of neutron in the exit channel)
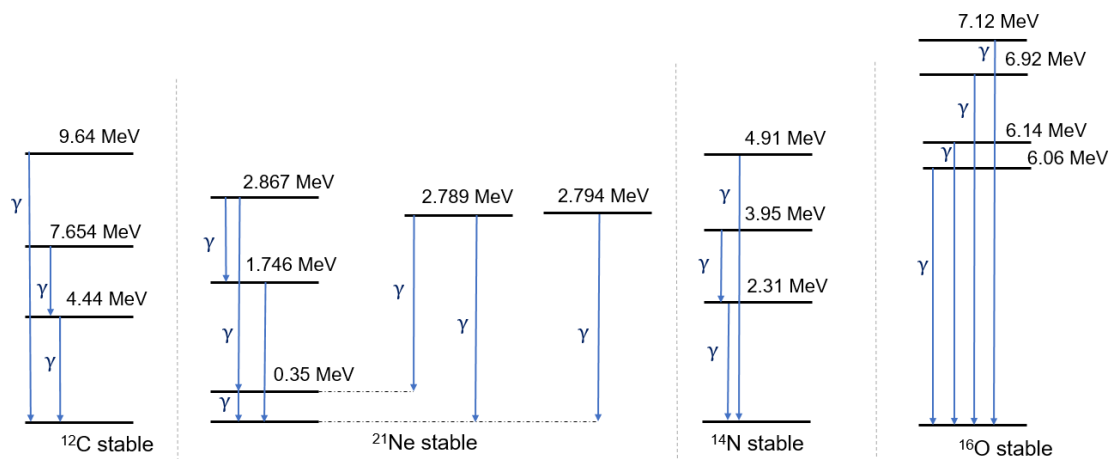
FIGURE A.2: Energy level diagrams showing the excited states observed in (α,n) reactions of some light compound nuclei

Appendix B

Conference Contributions and Publications

List of publications:

- V. Palušová on behalf of the SuperNEMO collaboration. "Monte Carlo simulation of external background in the SuperNEMO experiment". Abstract Contribution in Poster Session in: *The 28th International Workshop on Weak Interactions and Neutrinos* (2021)

- V. Palušová et al. "Natural radionuclides as background sources in the Modane underground laboratory". In: *Journal of Environmental Radioactivity* 216 (2020),p. 106185. issn: 0265-931X. DOI:https://doi.org/10.1016/j.jenvrad.2020.106185.

- V. Palušová, R. Breier, and P. P. Povinec. "Monte Carlo simulatio nof environmental background sources of a HPGe detector operating in underground laboratory". In: *Journal of Radioanalytical and Nuclear Chemistry* 318.3 (2018), pp. 2329–2334. DOI:10.1007/s10967-018-6235-0

- V. Palušová et al. "Monte Carlo simulations of detectorsbackground and development of AMS methodsfor radiopurity measurements". *Proceedings of the VII International Pontecorvo Neutrino Physics School August 20 – September 1*, (2017), pp. 135-141.

Co-authored and collaboration publications:

- R. Arnold et al. "Measurement of the distribution of ^{207}Bi depositions on calibration sources for SuperNEMO". In: *Journal of Instrumentation* 16 (2021), pp. T07012, DOI:10.1088/1748-0221/16/07/t07012

- R. Breier et al. "Monte-Carlo calculation of production rates of cosmogenic radionuclides in a HPGe detector operating in the Modane underground laboratory". In: *Nuclear Instruments and Methods in Physics Research Section A: Accelerators, Spectrometers, Detectors and Associated Equipment* 978 (2020), pp. 164355. issn:0168-9002. DOI:https://doi.org/10.1016/j.nima.2020.164355.

- R. Arnold et al. "Search for the double-beta decay of ^{82}Se to the excited states of ^{82}Kr with NEMO-3". In: *Nuclear Physics A* 996 (2020), pp. 121701. DOI:https://doi.org/10.1016/j.nuclphysa.2020.121701.

- A. V. Rakhimov et al. "Development of methods for the preparation of radiopure ^{82}Se sources for the SuperNEMO neutrinoless double-beta decay experiment". In: *Radiochimica Acta* 108.2 (2020), pp. 87–97. DOI:doi:10.1515/ract-2019-3129.

Monte Carlo simulation of external background in the SuperNEMO experiment

Investigation of neutrino properties is one of the most essential interests for particle physics and for better understanding the evolution of our Universe. Crucial missing information could be provided by the observation of neutrinoless double beta-decay ($0\nu\beta\beta$), a rare decay that violates total lepton number by two units which makes it forbidden in the Standard Model of particle physics. If observed, it would prove neutrinos are their own antiparticles - Majorana particles - and they could be the key to the matter-antimatter asymmetry problem.

SuperNEMO is a one-of-a-kind experiment searching for neutrinoless double beta decay in the Modane Underground Laboratory (LSM). It utilizes a tracking approach by separating the source isotope from the detector, while combining tracker and calorimetry techniques to detect emitted electrons independently. This approach provides the means to discriminate different underlying mechanisms for the $0\nu\beta\beta$ decay by measuring the decay half-life and the electron angular and energy distributions.

The modular design of SuperNEMO consists of modules containing approximately 5-7 kg of enriched and purified $\beta\beta$ emitting isotope in the form of a thin layer deposited on a foil placed between 2 tracker detectors and 2 plastic scintillator blocks with photo-multiplier tubes. The baseline isotope currently used in the first module, the Demonstrator, is ^{82}Se. This unique approach offers extremely good background rejection based on reconstructing the topology of measured events.

Backgrounds to SuperNEMO's double beta-decay measurements arise from events that mimic the topology of two electrons emitted from a common vertex in the source foil at energies up to the $Q_{\beta\beta}$ value of ^{82}Se, 2995 keV. In order to design a system with the lowest possible background, there is a need for understanding individual background sources and estimation of each component.
High energy γ-rays originating from de-excitations of radionuclides in ^{238}U and ^{232}Th decay chains and from neutron capture reactions can mimic $2e^-$ events through their interaction in the source foil.
The aim of this work is to estimate the background contributions from high energy gamma rays coming from the underground environment and (n,γ) reactions that constitute a major source of background to almost all underground experiments.

Primary author: PALUŠOVÁ, Veronika (Comenius University/ Université de Bordeaux)

Presenter: PALUŠOVÁ, Veronika (Comenius University/ Université de Bordeaux)

Session Classification: Neutrino Physics Session 2

Track Classification: Neutrino Physics
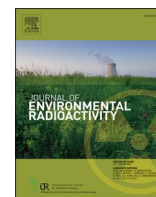
Natural radionuclides as background sources in the Modane underground laboratory

V. Palušová [a,b,*], R. Breier [a], E. Chauveau [b], F. Piquemal [b], P.P. Povinec [a]

[a] *Comenius University, Faculty of Mathematics, Physics and Informatics, SK-84248, Bratislava, Slovakia*
[b] *Université de Bordeaux, CNRS/IN2P3, CENBG, F-33170, Gradignan, France*

ABSTRACT

The Modane underground laboratory (LSM) is the deepest operating underground laboratory in Europe. It is located under the Fréjus peak in Savoie Alps in France, with average overburden of 4800 m w. e. (water equivalent), providing low-background environment for experiments in nuclear and particle physics, astrophysics and environmental physics. It is crucial to understand individual sources of background such as residual cosmic-ray flux of high-energy muons, muon-induced neutrons and contributions from radionuclides present in the environment. The identified dominant sources of background are radioactive contamination of construction materials of detectors and laboratory walls, radon contamination of the laboratory air, and neutrons produced in the laboratory. The largest neutron contribution has been identified from (α, n) reactions in low Z materials (10^{-7}-10^{-4} n s^{-1} Bq^{-1}) and from spontaneous fission of ^{238}U (1.1×10^{-6} n s^{-1} Bq^{-1}).

1. Introduction

Deep underground laboratories are presently the main framework for sensitive experiments as they provide the crucial ultra-low radiation background to search for very rare nuclear processes and decays that happen at extremely low rates. They also represent a significant breakthrough for radiometric and mass spectrometry technologies, mostly based on low-level gamma-spectrometry, Inductively Coupled Plasma Mass Spectrometry (ICPMS) and Accelerator Mass Spectrometry (AMS) (Povinec et al., 2008; Povinec, 2018, 2019). The overburden rock coverage in underground laboratories considerably reduces the cosmic-ray flux and cosmic-ray induced spallation products to a point, that it becomes almost negligible (Heusser, 1995; Povinec et al., 2008; Breier et al., 2017). The main attempt to advance in underground physics is the reduction and control of the background sources that may produce events mimicking searched signals. Despite the fact that underground experiments have different physics objectives and detection methods, there are several common background components present in the underground environment, mainly radioactive contamination and residual cosmic-ray background.

As cosmic-ray protons have low intensity compared to neutrons, and further they are converted to neutrons in nuclear reactions, mainly muons and neutrons play important part in detector's background in shallow as well as in deep underground laboratories (Ludwig et al., 2019; Povinec et al., 2008). Residual high-energy muon flux comes from interactions of high-energy cosmic rays in the upper atmosphere, while cosmogenic neutrons are produced in muon reactions with rock nuclei and experimental setup components.

Contributions of radioactive contamination to the background come from primordial, cosmogenic and anthropogenic radionuclides present in detectors and surrounding materials. The dominant sources are:

- Contributions from radioactive contamination of construction materials of detectors and the surrounding environment (concrete, shielding, electronics, etc.).
- Radon contamination of the laboratory air.
- In the absence of muons, neutrons produced in spontaneous fission processes and in (α, n) reactions of uranium and thorium and their decay products.
- Cosmogenic radionuclides produced by interactions of cosmic-ray particles in construction materials exposed on the earth surface (e. g., ^{26}Al).
- Anthropogenic radionuclides present in construction materials (e. g., ^{60}Co, ^{137}Cs).

Recently frequently studied problem is the production of cosmogenic

Table 1
Concentrations of elements in rock and concrete samples collected in LSM.

Compound	Rock[a]	Concrete[a]	Element	Rock[b]	Concrete[b]
	(%)			(%)	
SiO_2	14.9	5.8	O	49.4	49.7
Al_2O_3	5.0	1.1	Ca	30.6	36.8
FeO_3	2.8	0.74	C	5.94	7.78
MnO	0.038	0.008	Si	6.93	2.69
MgO	1.4	1.3	H	1.00	1.09
CaO	42.8	51.5	Mg	0.84	0.78
TiO_2	0.12	0.17	Fe	1.90	0.52
K_2O	0.25	0.02	Al	2.58	0.48
Na_2O	0.6	0.02	Ti	0.07	0.09
P_2O_5	0.15	0.15	P	0.06	0.07
			K	0.21	0.02
			Na	0.44	0.01
			Mn	0.03	0.01

[a] Chazal et al.(1998).
[b] Kluck, (2015).

radionuclides in construction materials during their transportation in air, storage or manufacture, by the hadronic component of cosmic rays. The resulting contamination can reach even higher radionuclide levels than the residual contamination from primordial radionuclides (Cebrián, 2017). Cosmic-ray activation can be minimized by storing materials underground and avoiding their flight transport. In many low-background experiments even short-living radionuclides are important for the detector's background. A lot of research has been dedicated for studying the production of [22]Na, [26]Al, [49]V, [54]Mn, [55]Fe, [57]Co, [58]Co, ^{60}Co, [65]Zn, [68]Ge in construction materials of germanium detectors, [32]Si in silicon medium in cryogenic detectors, iodine and tellurium radionuclides in NaI(Tl) crystals, xenon radionuclides in xenon-based detectors, argon radionuclides in liquid argon, cobalt radionuclides in copper and stainless steel, etc. (Heusser, 1995; Zhang et al., 2016; Cebrián, 2017).

The aim of the present work has been to review, analyze and discuss background contributions in the LSM coming mainly from radioactive contamination of construction materials and the laboratory walls, radon contamination of the laboratory air, and neutrons produced in spontaneous fission and in (α, n) reactions of uranium and thorium and their decay products in rocks and construction materials. The radiogenic contributions to the LSM background will be compared with cosmogenic ones induced by interactions of cosmic-ray muons with construction materials and surrounding rocks.

2. Modane underground laboratory

The Modane underground laboratory (Laboratoire Souterrain de Modane, LSM) is located in the middle of the Fréjus road tunnel under Savoie Alps that is connecting Modane in France to Bardonecchia in Italy (Fig.1). It sits below the Fréjus Peak with rock overburden of approximately 1700 m, which corresponds to 4800 m w.e. (water equivalent). It has been in operation since 1982 and is currently the deepest underground laboratory in Europe. The LSM serves as an interdisciplinary platform providing low-background environment for several experiments in nuclear and particle physics, astrophysics and environmental

physics. Presently the laboratory houses, e. g., the SuperNEMO experiment searching for neutrinoless double beta-decay, the EDELWEISS dark matter search experiment, germanium hall for low background gamma-spectrometry, radon trapping facility, etc.

The geological composition of rock surrounding the LSM is generally considered to be homogenous. Geologically the site is constituted of metamorphic rocks, called schists, that are characterized by several mineral constituents (Chazal et al., 1998; Malczewski et al., 2012). In the past, LSM rock and concrete samples from the main experimental hall were collected and analyzed by spectrometry methods to determine the chemical composition. Table 1 summarizes the elemental composition of the Fréjus rock and LSM concrete. The uranium and thorium content of the rock and concrete samples is given in Table 2.

3. Background radiation in LSM

3.1. Gamma-ray background

Background from environmental radioactivity sources present in the LSM laboratory imposes severe constraints on the sensitivity of the installed detectors. To overall gamma-ray background contribute mainly radionuclides present in construction and surrounding materials, that are mostly represented by decay products of the [238]U, [235]U and [232]Th day series, and by primordial [40]K. Decays and de-excitations of these radionuclides produce both low-energy (<1 MeV) and high-energy (>1 MeV) photons, but also electrons or alpha particles, that constitute serious background problems for all low-level counting experiments (Formaggio and Martoff, 2004). Of particular interest and concern are these radionuclides: [214]Pb, [214]Bi, [212]Pb and [208]Tl. The [214]Pb emits low energy gamma-rays, the most abundant are with energy of 0.352 MeV (37.6%). The [214]Bi gamma-line of highest yield is at 0.609 MeV (46.1%), then at 1.12 MeV (15.1%) and at 1.765 MeV (15.4%). The others have individual yields lower than 5%, for example, [214]Bi emits gamma-rays of 2.204 MeV and 2.447 MeV with emission probability of 4.99% and of 1.55%, respectively. [208]Tl is a product of alpha-decay of [212]Bi in [232]Th series and decays by β[−]-emission to [208]Pb with main gamma lines of 0.583 MeV and 2.614 MeV with emission probability of 84.5% and 99%, respectively. [212]Pb is also important radionuclide from the [232]Th decay chain with gamma-ray energy of 0.238 MeV. [40]K is a main source of the background gamma-radiation, as 10.7% of the time the isotope undergoes electron capture to form [40]Ar and emits 1.46 MeV gamma-rays. Other sources of high-energy gamma rays include gammas from neutron captures in materials surrounding the detectors or even muon bremsstrahlung from weak residual muon flux in the laboratory. For example, in water and polyethylene (often used for neutron shields), the slow neutron capture by H is responsible for production of gamma-rays with energy of 2.223 MeV. Higher gamma-ray energies may come from neutron capture in iron (e.g. 7.6 MeV from neutron capture in [56]Fe), titanium, nickel, zinc, etc. Other mechanisms of background induction by neutrons are nuclear excitations by inelastic neutron scattering on the detector and shielding materials that lead to saw-tooth shaped peaks with sharp edges (for example Pb (n, n'γ) and Cu (n, n'γ) reactions).

Malczewski et al. (2012) measured the gamma-radiation background in the LSM at two locations by using a coaxial HPGe detector. Ohsumi et al. (2002) studied gamma-ray fluxes using a NaI detector. Results of

Table 2
Activity of primordial radionuclides in rock and concrete samples collected in LSM.

Samples	[238]U				[232]Th				[40]K	
	(Chazal et al., 1998)		(Malczewski et al., 2012)		(Chazal et al., 1998)		(Malczewski et al., 2012)		(Chazal et al., 1998)	Malczewski (2012)
	[ppm]	[Bq kg^{-1}]	[ppm]	[Bq kg^{-1}]	[ppm]	[Bq kg^{-1}]	[ppm]	[Bq kg^{-1}]	[Bq kg^{-1}]	[Bq kg^{-1}]
Rock	0.84	10.4[a]	0.95	11.8	2.45	9.9[a]	2.48	10.2	213	182
Concrete	1.9	23.5[a]	1.83	22.8	1.4	5.7[a]	1.63	6.7	77	91

[a] Calculated using conversion factors.

Table 3
The main gamma-ray fluxes measured in LSM.

Energy [MeV]	Gamma ray flux [$cm^{-2}s^{-1}$]
0.352 (^{214}Pb)	6.04×10^{-3} [a]
	2.10×10^{-3} [a]
0.609 (^{214}Bi)	5.26×10^{-3} [a]
	1.78×10^{-3} [a]
0.911 (^{228}Ac)	1.31×10^{-3} [a]
	6.10×10^{-4} [a]
1.46 (^{40}K)	0.1 [a]
	3.55×10^{-3} [a]
	2.40×10^{-3} [a]
2.204 (^{214}Bi)	4.53×10^{-4} [a]
	2.02×10^{-4} [a]
2.614 (^{208}Tl)	4.0×10^{-2} [a]
	1.0×10^{-3} [a]
	4.78×10^{-4} [a]
4–6	3.8×10^{-6} [b]
6–7	1.5×10^{-6} [b]
7–8	1.6×10^{-6} [b]
8–9	7.0×10^{-8} [b]
9–10	5.0×10^{-8} [b]
>10	1.0×10^{-8} [b]

[a] Malczewski et al. (2012).
[b] Ohsumi et al. (2002).

both investigations are presented in Table 3. It is important to note, that these fluxes are highly dependent on the materials placed near the detectors, and on the contamination of the detectors themselves. Therefore, they do not represent an unaffected ambient gamma-ray flux. Such a bias is unavoidable and should be considered when using these values for further studies of background of experiments.

3.2. Radon

Radon and its decay products form by far the strongest source of airborne radioactivity in many low-background experiments. All of radon isotopes emanate naturally from the rocks, soil and building materials wherever traces of uranium and thorium can be found. Usually the beta-decaying radioisotopes within the uranium and thorium decay chains are the crucial contributors to the background. As the alpha-decaying radioisotopes emit mono-energetic alpha-rays with energies of a few MeV, they can be easily identified in analysis (Rupp, 2017). The measured ^{222}Rn activity in the LSM main hall is 5–20 Bq m^{-3} (Armengaud et al., 2013; Loaiza, 2005) with the mean value of 10 Bq m^{-3} (Fiorucci et al., 2007). Such a low radon level is kept thanks to a ventilation system that is renewing the entire laboratory air. Further reductions in the radon concentration down to a fewmBq m^{-3} has been achieved using a radon trapping facility (Loaiza, 2005). From the standpoint of gamma-background, radon (^{222}Rn) and its progenies (^{214}Pb and ^{214}Bi) are more important than thoron (^{220}Rn) and its progenies (^{212}Pb and ^{208}Tl) because of thoron's short half-life (55.6 s) (Povinec et al., 2008).

3.3. Cosmic-ray muon flux

As mentioned before, in deep underground laboratories, the cosmic-ray background component should be negligible and only residual high-energy muon flux remains. Muons originate in the upper layers of

Table 4
Summary of measured and simulated neutron fluxes in LSM.

Neutron flux [10^{-6} n cm^{-2}s^{-1}]	Neutron energy	Technique	Reference
4.0 ± 1.0	fast, 2–6 MeV	Slowing down neutrons and $n_{th}+^6Li\rightarrow\alpha+^3H$ reaction	Chazal et al. (1998)
1.6 ± 0.1	thermal	^{3}He detectors, $n+^3He\rightarrow T+p$ reaction	Chazal et al. (1998)
(2.0 ± 0.2)-(6.2 ± 0.6)	thermal	^{3}He proportional counter $n+^3He\rightarrow T+p$ reaction	Rozov et al. (2010)
9.6	total ambient flux	^{3}He proportional counter $n+^3He\rightarrow T+p$ reaction	Eitel (2012)
1.06	>1 MeV	Simulation (SOURCES, MCNPX)	Fiorucci et al. (2007)

atmosphere and subsequently travel and propagate through the air and rocks. The LSM overburden attenuates the muon flux, $\Phi_\mu \sim 5$ μ m^{-2}d^{-1} (Kluck, 2015; Loaiza, 2005; Fiorucci et al., 2007). More precise values of the LSM muon flux were measured by Berger et al. (1989) ($\Phi_\mu = 4.73$ μ m^{-2}d^{-1}), and by the EDELWEISS dark matter collaboration ($\Phi_\mu = 5.4 \pm 0.2$ μ m^{-2}d^{-1}; Schmidt et al., 2013). For comparison, the total flux of the muon component of cosmic rays at sea level is $\sim$190 μm^{-2}s^{-1} (Povinec et al., 2008).

In addition to the total muon flux at a given site, the energy spectrum of muons is important information in order to evaluate muon-induced reactions and to optimize the suppression and rejection tools, in order to improve the experimental sensitivity. Unfortunately, there is only limited information on muon energy spectra in LSM from measurements, and one has to rely, therefore, on Monte Carlo simulations, taking as an input the muon energy spectrum observed at surface. The average muon energy increases with the site depth, for the LSM the average muon energy was estimated as $E_{\mu, LSM} = 255.0(45)$ GeV (Kluck, 2015; Berger et al., 1989).

Muons by themselves, when interacting directly with detectors, do not contribute significantly to the background of underground experiments. They are either vetoed or easily identified. However, there is a muon-induced background, caused by spallation products created by high-energy muons. Especially dangerous are secondary neutrons produced either in the detector itself or in construction and surrounding materials, such as overburden rock, shielding, etc.

3.4. Neutron flux

The total flux of the nucleonic component of cosmic rays at sea level is around 60 particles m^{-2} s^{-1} (Povinec et al., 2008). Structures absorb secondary neutrons far better than muons, thus the relative composition of nucleonic component is dramatically changing with the depth (Hensel et al., 2019).

The ambient neutron flux in the LSM originates mainly from radionuclides present in rock and construction materials. Neutrons in the rock are produced by cosmic muons, plus neutrons induced by spontaneous fission and (α, n) reactions due to U and Th present in the rock. Several neutron flux measurements were carried out in the past in the LSM (Table 4). Chazal et al. (1998) estimated the flux of neutrons in the energy range of 2–6 MeV and of thermal neutrons to be $\Phi_n = (4.0 \pm 1.0) \times 10^{-6}$ n cm^{-2}s^{-1} and $\Phi_{n, thermal} = (1.6 \pm 0.1) \times 10^{-6}$ n cm^{-2}s^{-1}, respectively. More recent neutron measurements in various places in the LSM were carried out by Rozov et al. (2010) and Eitel (2012) using proportional counters filled with ^{3}He. The total ambient flux of neutrons, $\Phi_{n, ambient} = 9.6 \times 10^{-6}$ n cm^{-2}s^{-1} was mostly due to thermal neutrons. As can be seen from Table 4, the thermal neutron flux at LSM may vary by up to a factor of three from one location to another. Near the experimental set-up of EDELWEISS and NEMO3

Table 5
Chemical composition of materials used in neutron yield calculation.

Material	Composition	% mass
Polyethylene $(CH_2)_n$	C	85.7
	H	14.3
Borated polyethylene (5%)	C	61.2
	H	11.6
	O	22.2
	B	5
Lithium-Polyethylene	C	57.9
	O	26.4
	Li	7.5
	H	7.8
Steel	Fe	94
	Mn	1.6
	Co	1
	Cr	1
	Ni	1
	Cu	0.6
	Si	0.6
	C	0.2
Aluminium oxide Al_2O_3	Al	52.9
	O	47.1
PTFE C_2F_4	F	76
	C	24
Water	H	11.1
	O	88.9
Borosilicate glass	O	53.9
	Si	37.7
	Na	2.82
	Al	1.16
	B	0.40
	K	0.33

Table 6
Neutron yields from (α, n) reactions in given materials.

Material	^{232}Th [n s^{-1} Bq^{-1}]	^{238}U [n s^{-1} Bq^{-1}]
Polyethylene $(CH_2)_n$	1.49×10^{-06}	1.34×10^{-06}
Borated polyethylene (5%)	1.22×10^{-05}	1.17×10^{-05}
Lithium-Polyethylene	1.46×10^{-05}	1.02×10^{-05}
Steel	1.65×10^{-06}	4.19×10^{-07}
Aluminum oxide Al_2O_3	2.20×10^{-05}	1.43×10^{-05}
PTFE C_2F_4	1.27×10^{-04}	1.00×10^{-04}
Water	4.42×10^{-07}	3.74×10^{-07}
Borosilicate glass	5.60×10^{-06}	4.17×10^{-06}
B	2.73×10^{-04}	2.64×10^{-04}
C	2.18×10^{-06}	1.97×10^{-06}
O	6.09×10^{-07}	5.16×10^{-07}
Al	4.53×10^{-05}	2.93×10^{-05}
Si	3.45×10^{-06}	2.19×10^{-06}
Ar	2.64×10^{-05}	1.41×10^{-05}
Ti	7.34×10^{-06}	2.82×10^{-06}
Fe	1.62×10^{-06}	3.93×10^{-07}
Cu	3.86×10^{-07}	3.17×10^{-08}
Xe	6.15×10^{-12}	1.25×10^{-13}

produced alone in the reaction with no accompanying signal that could help to tag them in analysis (Westerdale and Meyers, 2017).

The detector shielding in deep underground laboratories is usually optimized against gamma-rays as they are the main background contributors. This is achieved with a substance that has a high density of electrons (which correlates with a high mass density) and also a high Z. Radiopure iron and steel are usually considered as the best choice. Another widely used shielding material is lead, however, it should be usually accompanied with an iron construction, and its radiopurity is worse. On the other hand, there is no neutron yield from (α, n) reactions in lead due to its high Coulomb barrier.

Neutron shielding materials are typically constructed from low atomic number elements (hydrogen, carbon, and oxygen) with high scattering cross sections that can effectively moderate or thermalize incident neutrons. Water, pure polyethylene, 3–5% borated polyethylene and 7.5% lithium polyethylene have been widely used. Whereas borated polyethylene effectively attenuates the neutron flux, neutron capture reactions on boron result in 0.42 MeV gamma-rays, which may contribute to the gamma-background, while lithium polyethylene produces no gamma-rays from neutron capture reactions. However, lithium has a lower cross section for capturing thermal neutrons in comparison with boron.

Borosilicate glass is the most commonly used window material in photomultiplier (PMT) tubes. Another PMT window material is sapphire, made of Al_2O_3 crystal. Xenon and argon are commonly used in underground experiments as scintillators due to their high scintillation light yields and possibility to achieve large detector masses. Another considered materials include PTFE (Teflon), copper, titanium, silicon, carbon and aluminum (having usually the lowest radiopurity) that often compose internal detector components. Chemical composition of these materials is defined in Table 5.

There are several toolkits for calculation of (α, n) induced neutrons, including SOURCES-4A and the USD webtool, or recently even GEANT4, each package being suited for this type of simulation, although further improvements are desirable in all cases. We have used the NeuCBOT (Neutron Calculator Based on TALYS) software (available for general use at https://github.com/shawest/neucbot). The advantage of using NeuCBOT is in its availability and validation (Westerdale and Meyers, 2017). NeuCBOT uses the ENSDF database for decay-data of alpha-emitters, SRIM-generated stopping power database and nuclear reaction database generated by TALYS (Westerdale, 2019). Secular equilibrium in ^{232}Th and ^{238}U decay chains was considered.

Table 6 shows results of neutron yields in given target elements and materials (assuming a homogeneous composition) that are contaminated with alpha-emitting radionuclides from ^{232}Th and ^{238}U decay series. Table 7 shows contributions to total neutron yield from each

(a predecessor of the SuperNEMO) experiments in the main hall, the fluxes were similar, $\Phi_{n, thermal} = (3.52 \pm 0.06) \times 10^{-6}$ n cm^{-2}s^{-1} and $\Phi_{n, thermal} = (2.9 \pm 0.4) \times 10^{-6}$ n cm^{-2}s^{-1}, respectively. These experimental results may be compared with simulations carried out by Fiorucci et al. (2007) using SOURCES package for simulations of neutron production rates from ^{238}U and ^{232}Th traces in the rock, and using MCNPX software for neutron propagation. The obtained neutron flux for energies above 1 MeV, $\Phi_{n, >1MeV} = 1.06 \pm 0.10$ (stat.) ± 0.59 (syst.) $\times 10^{-6}$ n cm^{-2}s^{-1}, is smaller than the experimental result of Chazal et al. (1998) (Table 4).

4. Radiogenic neutron production

4.1. Production of neutrons in (α, n) reactions

We have seen that radiogenic neutrons (together with high-energy gamma-rays) play dominant role in background of detectors operating deep underground. Radiogenic neutrons result from nuclear interactions with nuclei present in construction and shielding materials of detectors. They are predominantly produced by (α, n) reactions of alpha-particles from alpha-decaying radionuclides in ^{235}U, ^{238}U and ^{232}Th day chains with light (low to mid Z) nuclei. The neutron yield is thus mainly affected by alpha-decay energy spectra, the Coulomb barrier (which describes the energy of alpha-particles needed to overcome repulsion between alpha-particles and nuclei), stopping power of alpha-particles in particular materials and reaction cross sections. Calculations of radiogenic neutron production and their energy spectra are important for simulation of neutron background to many underground experiments, as the total neutron yield indicates the number of neutrons that enter or are produced in the target, and the neutron energy spectrum determines the total background events in the region of interest (Mei et al., 2009). They constitute a problematic background as they are often

Table 7
Neutron yields from each isotope in target elements.

Isotope	Abundance %	^{232}Th [n s^{-1}Bq^{-1}]	^{238}U [n s^{-1}Bq^{-1}]
^{10}B	19.9	4.96×10^{-05}	4.47×10^{-05}
^{11}B	80.1	2.24×10^{-04}	2.19×10^{-04}
^{13}C	1.1	2.18×10^{-06}	1.97×10^{-06}
^{17}O	0.038	6.53×10^{-08}	5.52×10^{-08}
^{18}O	0.2	5.43×10^{-07}	4.61×10^{-07}
^{27}Al	100	4.53×10^{-05}	2.93×10^{-05}
^{29}Si	4.67	2.04×10^{-06}	1.32×10^{-06}
^{30}Si	3.1	1.41×10^{-06}	8.70×10^{-07}
^{38}Ar	0.063	7.34×10^{-09}	3.12×10^{-09}
^{40}Ar	99.6	2.64×10^{-05}	1.41×10^{-05}
^{46}Ti	8	5.05×10^{-07}	1.81×10^{-07}
^{47}Ti	7.3	5.44×10^{-07}	2.09×10^{-07}
^{48}Ti	73.8	5.40×10^{-06}	2.08×10^{-06}
^{49}Ti	5.5	4.41×10^{-07}	1.73×10^{-07}
^{50}Ti	5.4	4.44×10^{-07}	1.76×10^{-07}
^{54}Fe	5.8	7.25×10^{-08}	1.60×10^{-08}
^{56}Fe	91.72	1.50×10^{-06}	3.65×10^{-07}
^{57}Fe	2.2	4.12×10^{-08}	1.03×10^{-08}
^{58}Fe	0.28	5.45×10^{-09}	1.37×10^{-09}
^{63}Cu	69.17	2.06×10^{-07}	0
^{65}Cu	30.83	1.80×10^{-07}	3.17×10^{-08}
^{129}Xe	26.4	1.6×10^{-12}	5.6×10^{-14}
^{130}Xe	4.1	1.7×10^{-13}	0
^{131}Xe	21.2	1.3×10^{-12}	1.6×10^{-14}
^{132}Xe	26.9	1.7×10^{-12}	3.8×10^{-14}
^{134}Xe	10.4	7.1×10^{-13}	8.2×10^{-15}
^{136}Xe	8.9	6.3×10^{-13}	7.5×10^{-15}

isotope in target elements. Uncertainties of these calculations are usually below 10% (depending on the precision of input data). Neutron energy spectra from ^{238}U and ^{232}Th induced (α, n) reactions in target elements of Ar, Al, Xe, Ti, C, O, Cu, Si, Fe, and B are shown in Fig. 2. They represent unmoderated spectra which can be used for propagation of neutrons through materials of interest where they further thermalize and interact with target nuclei.

4.2. Neutrons from spontaneous fission of ^{238}U and ^{232}Th

There are over 100 radionuclides known to decay by spontaneous fission with the emission of neutrons. The probability of spontaneous fission strongly depends on the atomic number of the heavy element. The underground fission neutron flux is mostly due to spontaneous fission of ^{238}U that is present in the environment. The fission rate for thorium and uranium is low compared to the rate of decay by alpha-particle emission, which dominates the total half-life. This process is also a source of high energy gamma-rays. When a nucleus undergoes fission and the excitation energy falls behind the neutron binding energy, prompt gamma-rays take over and carry away the remaining energy. If we assume the neutron yields per fission given by Ensslin (1991) for ^{238}U and ^{232}Th (1.36×10^{-2} n s^{-1} g^{-1} and about 6×10^{-8} n s^{-1} g^{-1}, respectively), we can obtain neutron yields in n s^{-1} Bq^{-1} for the total activity of ^{238}U and ^{232}Th, and for radionuclides undergoing

spontaneous fission in the ^{238}U chain with decay products in secular equilibrium (Table 8). The average energy of emitted neutrons is approximately 2 MeV (Westerdale and Meyers, 2017). These values are in good agreement with values of Westerdale and Meyers (2017) calculated using SOURCES-4C software (1.1×10^{-6} n s^{-1} Bq^{-1} for ^{238}U and 3.85×10^{-11} n s^{-1} Bq^{-1} for ^{232}Th.

As the natural abundance of ^{235}U is relatively low, the neutron yield from spontaneous fission of ^{235}U is only about 5% of the total neutron yields from uranium and thorium decays (Mei et al., 2009). The spontaneous fission rates and neutron yields of these isotopes are very low (Table 8), therefore, these processes contribute to neutron background only in materials with high contamination levels.

5. Muon-induced neutrons

Cosmogenic neutrons are mainly produced in hadronic and electromagnetic showers in the matter by incident cosmic-ray muons. These neutrons can be identified via associated muons or electromagnetic cascades, however, as they spread away from the incident muon track, large detectors are needed to study them with necessary accuracy (Araújo et al., 2005). Although most of the neutrons in deep underground laboratories come from spontaneous fission and (α, n) reactions, and muon induced neutrons contribute less than 1% to the neutron flux, they are still of interest as a potential source of background in underground low-background experiments (Kluck, 2015; Malgin, 2017; Araújo et al., 2005; Eitel, 2010). Moreover, an increased gamma-ray flux is also expected from neutron activation of materials (Araújo et al., 2005).

The main characteristics associated with muon induced neutrons are the muon energy, the reaction cross section, the target material and the neutron yield, Y_n, given in number of neutrons produced by a muon per unit path length [n μ^{-1} (g cm^{-2})$^{-1}$]. Generally, the neutron production rate increases with the average atomic weight of the material. The FLUKA (Böhlen et al., 2014; Ferrari et al., 2005) and GEANT4 simulation tools are well established and widely used for neutron yields calculations.

Very little data is available from measurements and simulations on muon induced neutron yields in LSM. We already mentioned that the measured muon flux in the LSM was about 5 μ m^{-2}d^{-1} (Berger et al., 1989), and the neutron flux at the EDELWEISS detector was about 0.5 n m^{-2} d^{-1} in Gd-loaded scintillator (Eitel, 2010). Results of measurements from different underground laboratories and experiments were discussed by Kluck (2015) and Malgin (2017). The dependence of the averaged muon-induced neutron yields in different targets and at different averaged muon energies presented in Fig. 3 was discussed by several authors (Kluck, 2015; Gorshkov et al., 1968, 1971, 1974; Annis et al., 1954; Agafonova and Malgin, 2013; Bergamasco et al., 1973; Reichhart et al., 2013). Reichhart et al. (2013) estimated the muon induced neutron yield in pure lead for a mean muon energy of 260 GeV (which approximately corresponds to the mean muon energy in LSM) to be $(5.78^{+0.21}_{-0.28} \times 10^{-3})$ n μ^{-1} (g cm^{-2})$^{-1}$. For example, in 30 cm lead
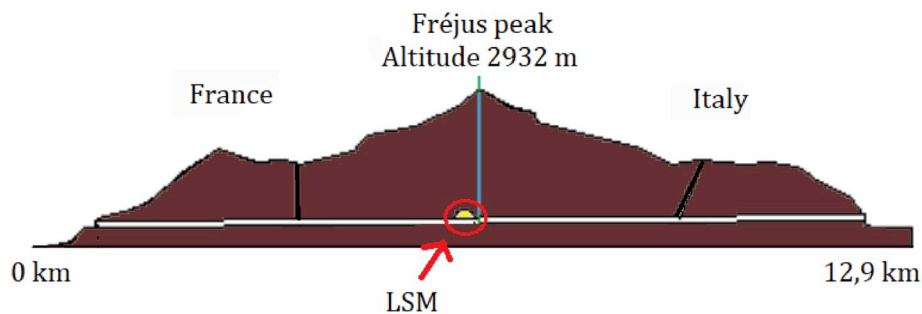
Fig. 1. Location of the LSM.
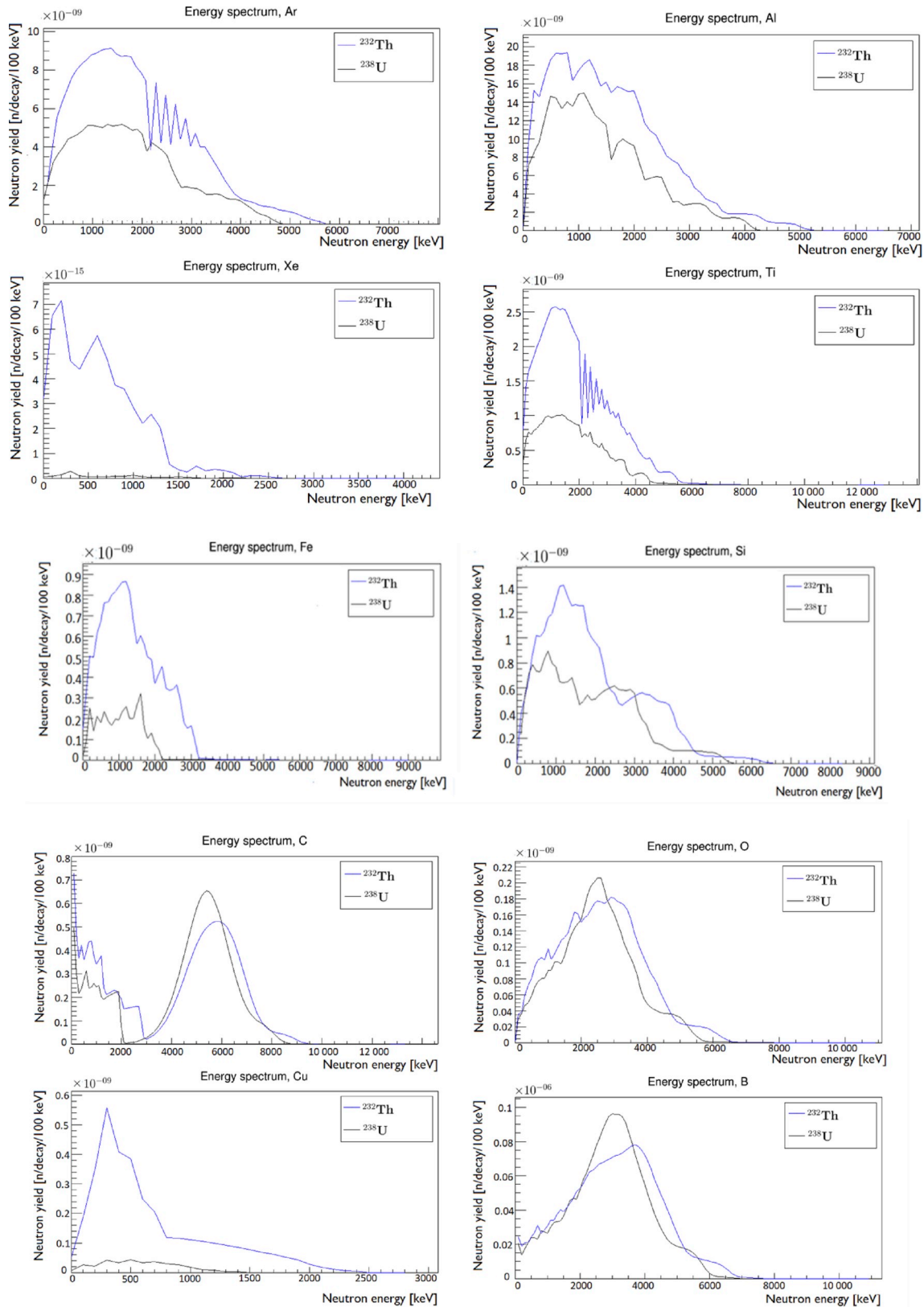
Fig. 2. Neutron energy spectra from ^{238}U and ^{232}Th induced (α, n) reactions in selected target elements.

shielding, which corresponds to 340.2 g cm^{-2} of interaction length (assuming the lead density of 11.34 g cm^{-3}), a muon of energy 260 GeV produces 1.97 neutrons per muon. This assumption corresponds well with result obtained by Araújo et al. (2005), i.e., 2 neutrons per muon

for 30 cm lead shielding for the mean muon energy of 280 GeV (Table 9). With the given LSM muon flux, these values can be scaled to number of events per unit area and time. However, to get accurate results on the neutron yields and the energy distribution of neutrons, more

Table 8
Neutron yields from spontaneous fission of ^{238}U, ^{234}U, ^{230}Th and ^{232}Th.

Isotope	Half-life [y]	Half-life of spontaneous fission [y]	Neutron yield [n s^{-1}Bq^{-1}]
^{238}U	4.47×10^9	8.2×10^{15}	1.1×10^{-6}
^{232}Th	1.41×10^{10}	$>1 \times 10^{21}$	1.5×10^{-11}
^{234}U	2.46×10^5	1.5×10^{16}	2.9×10^{-11}
^{230}Th	7.5×10^4	$>2 \times 10^{18}$	1.1×10^{-12}
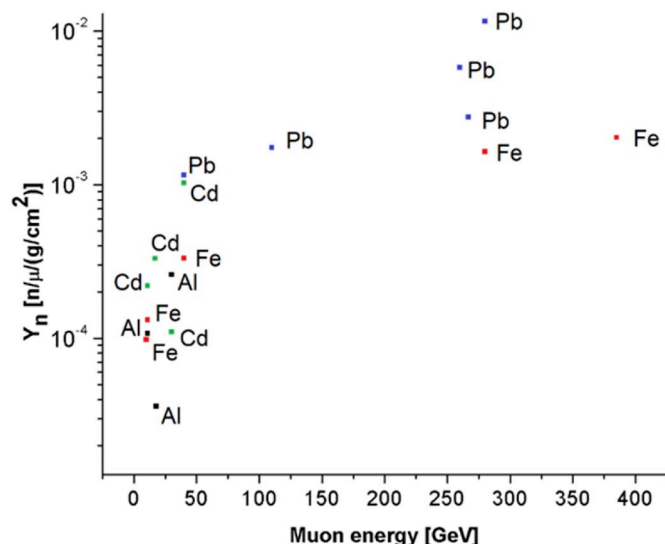
Fig. 3. Dependence of neutron yield on the muon energy in target materials (data from Kluck (2015), Gorshkov et al. (1974), Gorshkov and Zyabkin (1971), Gorshkov and Zyabkin (1968), Annis et al. (1954), Agafonova and Malgin (2013), Bergamasco et al. (1973), Reichhart et al. (2013)).

Table 9
Muon induced neutron fluxes in LSM for Fe and Pb shielding materials.

Material	Thickness [cm]	Flux	
		[n μ^{-1}]	[n cm^{-2} s^{-1}]
Iron	20	0.32	1.8×10^{-9}
Lead	30	1.97	1.2×10^{-8}

Table 10
Summary of neutron fluxes in LSM.

Background source	Flux [n s^{-1} Bq^{-1}]
Neutrons from spontaneous fission of ^{238}U	1.1×10^{-6}
Neutrons from spontaneous fission of ^{232}Th	1.5×10^{-11}
Neutrons from (α, n) reactions in low Z materials* *depending on target nuclei	10^{-7}-10^{-4}

measurements and simulations are needed.

6. Summary on neutron fluxes

Experiments searching for rare events in underground laboratories need to reach as low background as possible. Natural radioactive contamination in the detector construction and laboratory environment, that is mostly represented by decay products in the ^{238}U, ^{235}U and ^{232}Th day series, and by primordial ^{40}K, leads to alpha, beta and gamma-background, as well as production of neutrons in (α, n) reactions and in spontaneous fission. The selection of very radiopure materials therefore plays a key role in background reduction. Radiogenic neutron

sources summarized in Table 10 indicate that the dominant contributions are from (α, n) reactions in low Z materials and from spontaneous fission of ^{238}U.

Assuming production rates of muon-induced neutrons in the LSM (for the mean muon energy of 260 GeV and the Fe and Pb targets) of $2 \times 10^{-3} n$ μ^{-1} (g cm^{-2})$^{-1}$ and 5.78×10^{-3} n μ^{-1} (g cm^{-2})$^{-1}$, respectively, the muon-induced neutron fluxes of 1.8×10^{-9} n cm^{-2} s^{-1} and 1.2×10^{-8} n cm^{-2} s^{-1} were calculated.

7. Conclusions

The main background sources in the LSM Modane underground laboratory were discussed. Results of several measurements of environmental radioactivity in LSM were summarized, including measurements of ambient muon (Φ_μ ~5 μ m^{-2}d^{-1}) and neutron fluxes ($\Phi_{n, ambient} = 9.6 \times 10^{-6}$ ncm^{-2}s^{-1}). Neutrons coming from the (α, n) reactions and spontaneous fission have been identified as the dominant neutron background sources. The neutron yields and neutron energy spectra from (α, n) reactions in several elements and materials used in detector components or in shielding were calculated using the NeuCBOT software. The neutron production rates were determined for radionuclides naturally present in the underground environment which undergo spontaneous fission. The largest neutron contribution to underground experiments carried out in the LSM laboratory has been identified from (α, n) reactions in low Z materials (10^{-7}-10^{-4} n s^{-1} Bq^{-1}) and from spontaneous fission of ^{238}U (1.1×10^{-6} n s^{-1} Bq^{-1}).

Assuming production rates of muon induced neutrons in the LSM (for the mean muon energy of 260 GeV and the Fe and Pb targets) of $2 \times 10^{-3} n$ μ^{-1} (g cm^{-2})$^{-1}$ and 5.78×10^{-3} n μ^{-1} (g cm^{-2})$^{-1}$, respectively, the muon-induced neutron fluxes of 1.8×10^{-9} n cm^{-2} s^{-1} in Fe and 1.2×10^{-8} n cm^{-2} s^{-1} in Pb were calculated.

The obtained results can be further used for Monte Carlo simulations and prediction of background events in underground experiments.

Declaration of competing interest

The authors declare that they have no known competing financial interests or personal relationships that could have appeared to influence the work reported in this paper.

References

Agafonova, N.Y., Malgin, A.S., 2013. Universal formula for the muon-induced neutron yield. Phys. Rev. D 87, 113013. https://doi.org/10.1103/PhysRevD.87.113013.

Annis, M., Wilkins, H.C., Miller, J.D., 1954. Nuclear interaction of fast μ-mesons. Phys. Rev. 94, 1038–1045. https://doi.org/10.1103/Phys. Rev.94.1038.

Araújo, H.M., Kudryavtsev, V.A., Spooner, N.J.C., Sumner, T.J., 2005. Muon-induced neutron production and detection with GEANT4 and FLUKA. Nucl. Instrum. Methods Phys. Res. A 545, 398–411. https://doi.org/10.1016/j.nima.2005.02.004.

Armengaud, E., Augier, C., Benoît, A., Bergé, L., Bergmann, T., Blümer, J., Broniatowski, A., Brudanin, V., Censier, B., 2013. Background studies for the EDELWEISS dark matter experiment. Astropart. Phys. 47, 1–9. https://doi.org/10.1016/j.astropartphys.2013.05.004.

Bergamasco, L., Costa, S., Pic, P., 1973. Experimental results on neutron production by muons at 4300 m w.e. Nuovo Cimento A 13, 403–412. https://doi.org/10.1007/BF02827344.

Berger, Ch, Fröhlich, M., Mönch, H., Nisius, R., Raupach, F., Schleper, P., Benadjal, Y., Blum, D., Bourdarious, C., Dudelzak, B., Eschstruth, P., Jullian, S., Lalanne, D., Laplanche, F., Longuemare, C., Paulot, C., Perdereau, O., Roy, Ph, Szklarz, G., Behr, L., Degrange, B., Minet, Y., Nguyen-Khac, U., Serri, P., Tisserant, S., Tripp, R.

D., Arpesella, C., Bareyre, P., Barloutaud, R., Borg, A., Chardin, G., Ernwein, J., Glicenstein, J.F., Mosca, L., Moscoso, L., Becker, J., Becker, K.H., Daum, H.J., Demski, S., Jacobi, B., Kuznik, B., Mayer, R., Meyer, H., Möller, R., Schubnell, M., Seyffert, B., Wei, Y., Wintgen, P., 1989. Experimental study of muon bundles observed in the Fréjus detector. Phys. Rev. D 40, 2163–2171. https://doi.org/10.1103/physrevd.40.2163.

Böhlen, T.T., Cerutti, F., Chin, M.P.W., Fassò, A., Ferrari, A., Ortega, P.G., Mairani, A., Sala, P.R., Smirnov, G., Vlachoudis, V., 2014. The FLUKA code: developments and challenges for high energy and medical applications. Nucl. Data Sheets 120, 211–214.

Breier, R., Laubenstein, M., Povinec, P.P., 2017. Monte Carlo simulation of background characteristics of a HPGe detector operating underground in the Gran Sasso National Laboratory. Appl. Radiat. Isot. 126, 188–190. https://doi.org/10.1016/j.apradiso.2016.12.039 issn: 18729800.

Cebrián, S., 2017. Cosmogenic activation of materials. Int. J. Mod. Phys. A. https://doi.org/10.1142/S0217751X17430060.

Chazal, V., Chambon, B., Jesus, M. De, Drain, D., Pastor, C., Vagneron, L., Brissot, R., Cavaignac, J.F., Stutz, A., Giraud-Heraud, Y., 1998. Neutron background measurements in the underground laboratory of Modane. Astropart. Phys. 9, 163–172. https://doi.org/10.1016/S0927-6505(98)00012-7.

Eitel, K., 2012. Measurements of neutron fluxes in the LSM underground laboratory. J. Phys. Conf. Ser. 375 https://doi.org/10.1088/1742-6596/375/1/012016.

Eitel, K., 2010. Investigation of ambient and μ-induced neutron background in LSM. J. Phys. Conf. Ser. 203, 012027 https://doi.org/10.1088/1742-6596/203/1/012027.

Ensslin, N., 1991. In: Kreiner, S. (Ed.), The Origin of Neutron Radiation. Passive Nondestructive Assay Manual (PANDA) (NUREG/CR–5550, s (United State).

Ferrari, A., Sala, P., Fassò, A., Ranft, J., 2005. FLUKA: A Multi-Particle Transport Code. https://doi.org/10.2172/877507. CERN 2005-10, INFN/TC 05/11, SLAC-R 773.

Fiorucci, S., Benoit, A., Berge, L., Blümer, J., Broniatowski, A., Censier, B., Chantelauze, A., Chapellier, M., Chardin, G., Collin, S., Defay, X., De Jesus, M., Deschamps, H., Stefano, P., Dolgorouky, Y., Dumoulin, L., Eitel, K., Fesquet, M., Gascon, J., Yakushev, E., 2007. Identification of backgrounds in the EDELWEISS-I dark matter search experiment. Astropart. Phys. 28, 143–153. https://doi.org/10.1016/j.astropartphys.2007.05.005.

Formaggio, J., Martoff, C.J., 2004. Backgrounds to sensitive experiments underground. Annu. Rev. Nucl. Part Sci. 54 (1), 361–412. https://doi.org/10.1146/annurev.nucl.54.070103.181248.

Gorshkov, G.V., Zyabkin, V.A., Yakovlev, R.M., 1974. Production of neutrons in Pb, Cd, Fe, and Al by high energy muons. Sov. J. Nucl. Phys. 18, 57–61.

Gorshkov, G.V., Zyabkin, V.A., 1968. Production of neutrons in Pb, Cd, Fe, and Al under the influence of cosmic-ray muons at a depth of 150 in water equivalent. Sov. J. Nucl. Phys. 7, 470–474.

Gorshkov, G.V., Zyabkin, V.A., 1971. Production of neutrons in Pb, Cd, Fe, and Al and fission of Pb nuclei by cosmic rays in the depth range 0-1000 m water equiv. Sov. J. Nucl. Phys. 13, 450–452.

Hensel, T., Grieger, M., Agramunt, J., Tain, J.L., Bemmerer, D., Muller, S.E., Szucs, T., Degering, D., Dillmann, I., Fraile, L.M., Koester, U., Marta, M., Zuber, K., 2019. Ambient neutron background in the shallow-underground laboratory Felsenkeller. In: 5th International Solar Neutrino Conference. Dresden, Germany, pp. 477–484. https://doi.org/10.1142/9789811204296_0031.

Heusser, G., 1995. Low-radioactivity background techniques. Annu. Rev. Nucl. Part Sci. 45, 543–590. https://doi.org/10.1146/annurev.ns.45.120195.002551.

Kluck, H., 2015. Production Yield of Muon-Induced Neutrons in Lead: Measured at the Modane Underground Laboratory. Springer International Publishing AG, Cham, Switzerland. https://doi.org/10.1007/978-3-319-18527-9.

Loaiza, P., 2005. Low radioactivity at the Modane underground laboratory. AIP Conference Proceedings 785 (1), 100–103. https://doi.org/10.1063/1.2060459.

Ludwig, F., Wagner, L., Al-Abdullah, T., Barnafoldi, G.G., Bemmerer, D., Degering, D., Schmidt, K., Suranyi, G., Szucs, T., Zuber, K., 2019. The Muon Intensity in the Felsenkeller Shallow Underground Laboratory arXiv:1904.11501v1, physics.ins-det.

Malczewski, D., Kisiel, J., Dorda, J., 2012. Gamma background measurements in the laboratoire Souterrain de Modane. J. Radioanal. Nucl. Chem. 292, 751–756. https://doi.org/10.1007/s10967-011-1497-9.

Malgin, A.S., 2017. Phenomenology of muon-induced neutron yield. Phys. Rev. C 96, 1. https://doi.org/10.1103/physrevc.96.014605.Mei, D., Zhang, C., Hime, A., 2009. Evaluation of (α, n) induced neutrons as a background for dark matter experiments. Nucl. Instrum. Methods Phys. Res. A 606 (3), 651–660 doi: 0.1016/j.nima.2009.04.032. arXiv:0812.4307.

Ohsumi, H., 2002. Gamma-ray flux in the Fréjus underground laboratory measured with NaI detector. Nucl. Instrum. Methods Phys. Res. A 482, 832–839. https://doi.org/10.1016/S01689002(01)01866-6.

Povinec, P.P., 2018. New ultra-sensitive radioanalytical technologies for new science (Hevesy lecture). J. Radioanal. Nucl. Chem. 316, 893–931. https://doi.org/10.1007/s10967-018-5787-3.

Povinec, P.P., 2019. Ultra-sensitive radionuclide analyses: new frontiers in radioanalytics. J. Radioanal. Nucl. Chem. 322, 1247–1255. https://doi.org/10.1007/s10967-019-06707-2.

Povinec, P.P., Betti, M., Jull, A.J.T., Vojtyla, P., 2008. New isotope technologies in environmental physics. Acta Phys. Slovaca 58, 1–154. https://doi.org/10.2478/v10155-010-0088-6.

Reichhart, L., Lindote, A., Akimov, D.Yu, Araújo, H.M., Barnes, E.J., Belov, V.A., Bewick, A., Burenkov, A.A., Chepel, V., Currie, A., et al., 2013. Measurement and simulation of the muon-induced neutron yield in lead. Astropart. Phys. 47, 67–76. https://doi.org/10.1016/j.astropartphys.2013.06.002.

Rozov, S., Armengaud, E., Augier, C., Bergé, L., Benoit, A., Besida, O., Blümer, J., Broniatowski, A., Brudanin, V., Chantelauze, A., Chapellier, M., Chardin, G., Charlieux, F., Collin, S., Crauste, O., De Jesus, M., Defay, X., Di Stefano, P., Dolgorouki, Y., Domange, J., Dumoulin, L., Eitel, K., Filosofov, D., Gascon, J., Gerbier, G., Gros, M., Hannawald, M., Juillard, A., Kluck, H., Kozlov, V., Lemrani, R., Lubashevskiy, A., Marrach, C., Marnieros, S., Navick, X.-F., Nones, C., Olivieri, E., Pari, P., Paul, B., Sanglard, V., Scorza, S., Semikh, S., Verdier, M.-A., Vagneron, L., Yakushev, E., 2010. Monitoring of the thermal neutron flux in the LSM underground laboratory. Russ. Acad. Sci. Phys. 74, 464–466.

Rupp, N., 2017. Radon background in liquid xenon detectors. J. Instrum. 13 https://doi.org/10.1088/1748-0221/13/02/C02001. C02001-C02001.

Schmidt, B., Armengaud, E., Augier, C., Benoit, A., Bergé, L., Bergmann, T., Blümer, J., Bres, G., Broniatowski, A., Brudanin, V., et al., 2013. Muon-induced background in the EDELWEISS dark matter search. Astropart. Phys. 44, 28–39. https://doi.org/10.1016/j.astropartphys.2013.01.014.

Westerdale, S., Meyers, P.D., 2017. Radiogenic neutron yield calculations for low-background experiments. Nucl. Instrum. Methods Phys. Res. A 875, 57–64. https://doi.org/10.1016/j.nima.2017.09.007.

Westerdale, S., 2019. NeuCBOT. url. https://github.com/shawest/neucbot.

Zhang, Ch, Mei, D., Kudryavtsev, V.A., Fiorucci, S., 2016. Cosmogenic activation of materials used in rare event search experiments. Astropart. Phys. 84, 62–69. https://doi.org/10.1016/j.astropartphys.2016.08.008.

CrossMark

Monte Carlo simulation of environmental background sources of a HPGe detector operating in underground laboratory

Veronika Palušová[1] · Robert Breier[1] · Pavel P. Povinec[1]

Abstract

The overlying rock of underground laboratories provides excellent radiation shielding necessary for many experiments searching for extremely rare nuclear and astroparticle events. Monte Carlo simulations of HPGe detector background and attenuation of gamma-ray fluxes with different shielding configurations were carried out for an underground laboratory. It has been found that even a small radioactive contamination of the shielding material may increase gamma-ray fluxes in underground laboratory by several orders of magnitude.

Keywords Gamma-ray spectrometry · Background · Monte Carlo simulation · Underground laboratory

Introduction

Deep underground laboratories provide the necessary low radiation background to search for very rare nuclear phenomena that happen at extremely low rates, such as neutrinoless double beta-decay or detection of dark matter candidates [1]. While in surface laboratories the cosmic ray component plays an important part of the background, the overburden rock coverage in underground laboratories reduces considerably the cosmic-ray flux and cosmic-ray induced spallation products, therefore investigations of rare nuclear processes can be carried out [2]. The main challenge towards higher sensitivities and the main struggle to advance in underground physics is the reduction and control of the background. Once the cosmic-ray component has been reduced, other background sources become dominant [2]:

(a) High-energy muon flux induced by interactions of high energy cosmic rays in the upper atmosphere

(b) Neutrons produced in cosmic-ray muon spallation reactions with rock nuclei, in fission processes of uranium and thorium in the rocks, and in (α, n) reactions

(c) Contributions from radioactive contamination of the detector and its surroundings (concrete, shielding, electronics, etc.)

(d) Radon contamination of the laboratory air.

Therefore, detectors and supporting instruments must be made out of radio-pure materials, and all components must be thoroughly screened before construction and their installation underground [3, 4].

Large volume high-purity germanium (HPGe) detectors because of their high detection efficiency and good energy resolution have been extensively used in radio-purity measurements of construction materials [5]. Additionally, the ultra-sensitive HPGe γ-ray spectrometers operating underground have been used in wide range of other scientific applications, such as environmental radionuclide monitoring or development of new detector technologies [3].

The dominant part of background comes from radioactive contamination of construction materials of HPGe detectors (cryostat, detector holder, electronics, etc.), as well as their shielding (lead, iron, copper). Radioactive contamination of construction materials is mostly represented by decay products in the ^{238}U and ^{232}Th decay series, and by primordial ^{40}K [6, 7].

In order to understand origin of induced radioactive background, or to evaluate the background before the

✉ Veronika Palušová
veronika.palusova@fmph.uniba.sk

[1] Department of Nuclear Physics and Biophysics, Faculty of Mathematics, Physics and Informatics, Comenius University, 84248 Bratislava, Slovakia

detector construction, a simulated background spectrum can be obtained with Monte Carlo simulation. Decay events can be simulated for different parts of the detector separately, following various radionuclide contaminants. Under investigation are γ-rays from different sources, e.g. from ^{208}Tl (mainly of 583 and 2615 keV) in ^{232}Th decay chain, from ^{214}Bi (mainly 609, 1120 and 1764 keV) in ^{238}U decay chain, from ^{40}K, and from neutron capture and muon bremsstrahlung in rocks.

The main motivation for this work has been to study effects of external shielding on the background of the SuperNEMO detector which represents a new generation of ultra-low background physics experiment searching for neutrinoless double beta-decay in the Modane underground laboratory (LSM – Laboratoire Souterrain de Modane) [8]. This process, if observed, would indicate that neutrinos are Majorana (not Dirac) particles, meaning that neutrino and antineutrino are the same. It is expected, that background γ-rays could produce events in different topologies that could mimic the event topology of the searched neutrinoless double beta decay.

To reduce the background and to reach sensitivities capable of detecting this process, strict radiopurity requirements are imposed on the detector construction materials [9–11]. The detector must be surrounded by shielding to provide additional background reduction from external sources [12]. Since external gamma-rays have big impact on the detector background (that might influence the experiment), the task to define and investigate different shielding configurations (iron, copper, water) and their thickness becomes important.

The aim of the paper has been to develop a Monte Carlo model designed for background studies of simple HPGe spectrometers operating in underground laboratories (Modane and Gran Sasso) [5, 13–15]. A combination of iron and copper shielding (proposed for the SuperNEMO detector on the basis of cost efficiency and its availability) has also been studied for attenuation of the environmental gamma-ray in the Modane underground laboratory. The obtained results will later help to investigate suitability of the Monte Carlo simulation model for the assessment of the background of the large-scale SuperNEMO experiment [8]. The presented Monte Carlo model is based on the GEANT4 package developed at CERN [16].

The γ-ray fluxes in the Modane underground laboratory

The LSM is the deepest operating underground laboratory in Europe. It is located under the Fréjus mountain in France, with average overburden of 4800 m w.e, (water equivalent), providing low-background environment for

several experiments in nuclear and particle physics, astrophysics and environmental physics. The measured muon ((6.25 ± 0.01) 10^{-5} m^{-2} s^{-1} [17]), the fast neutron ((1.1 ± 0.1) 10^{-2} m^{-2} s^{-1} [18]) and the thermal neutron fluxes (1.9 10^{-2} m^{-2} s^{-1} [19]) are very low and thus suitable for investigation of rare nuclear processes. The γ-ray spectrum in the LSM underground laboratory measured using NaI(Tl) detector was divided into four energy intervals [20]:

(i) Bellow 4 MeV with γ-rays mainly produced by natural radionuclides in materials surrounding the detector

(ii) 4–6 MeV with γ-rays due to α and β-decays of uranium and thorium decay series present in construction parts of the detector

(iii) 6–10 MeV with γ-rays due to neutron capture reactions

(iv) Above 10 MeV with γ-rays produced by interactions of cosmic-ray muons with rocks.

The extracted environmental γ-ray fluxes measured in the LSM for each energy interval are shown in Table 1. The obtained values have been used for further background investigations of detectors operating in LSM.

Methods

HPGe detector "Obelix"

An ultra-low background large volume HPGe detector Obelix installed in LSM is a coaxial detector with diameter of 93.5 mm and height of 89.6 mm, which corresponds to useful volume of 600 cm^3. Its shielding is composed of an inner layer (12 cm) made out of low-activity Roman lead, and an external layer (20 cm) is made of low-activity lead. The experimental setup with construction materials used in Monte Carlo simulations is shown in Fig. 1. To eliminate background contribution from radon and its decay products, the air is pushed out from the sample chamber with

Table 1 The γ-ray fluxes in the LSM [16]

Energy interval (MeV)	γ-ray flux (10^{-6} cm^{-2} s^{-1})
4.0–6.0	3.8
6.0–7.0	1.5
7.0–8.0	1.6
8.0–9.0	0.07
9.0–10.0	0.05
> 10.0	0.01

Fig. 1 Visualization of the experimental setup of the investigated HPGe detector Obelix operating in the Modane underground laboratory
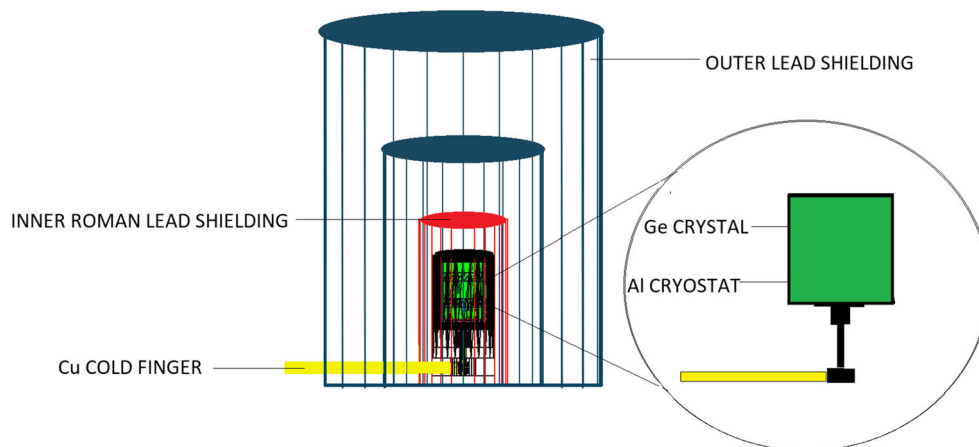
radon-depleted air from radon trapping facility, which is able to produce radon-free air (about 15 mBq/m^3) [21].

Monte-Carlo simulations

Monte-Carlo simulations have been widely applied in studying physical processes and interactions to explain measured background spectra or to predict detector background and to evaluate individual background contributions [5, 6, 15, 22, 23]. That makes them an excellent tool to optimize background characteristics for planned experiments and to study detector background before the system is built. They are also useful for prediction of shielding thickness necessary to reduce the background to desirable level.

GEANT4 has been used for the Monte-Carlo simulation of environmental background sources of the investigated HPGe detector operating in underground laboratories. GEANT4 is a simulation tool-kit developed at CERN for particle physics simulations, but it has also been used in low energy physics applications [5, 8, 15, 16]. The shielding physics list used in Monte Carlo simulations presented in this paper included except of muon ionization, muon bremsstrahlung, production of electron–positron pairs, and muon photonuclear reactions also fluorescence, Auger electron emission and Auger cascades, and particle induced X-ray emission. The γ-ray fluxes measured in LSM in each energy range were used to simulate the background response of the investigated Obelix detector, and to study flux attenuation by different shielding configurations.

An attenuation of the environmental gamma-ray flux in the LSM laboratory was also studied using Monte Carlo simulations. A shielding consisting of iron (3, 6, 9, 12, 15 and 18 cm) plus copper (0, 1 and 2 cm) was considered in this case. A scheme of shielding configurations is shown in Fig. 2. Environmental γ-rays measured in the LSM laboratory [20] bombarded the shield of the SuperNEMO
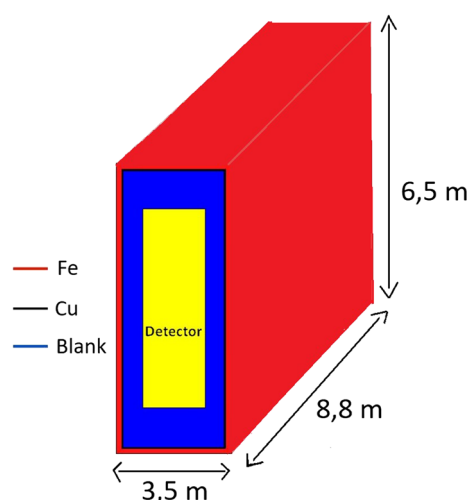
Fig. 2 GEANT4 geometry of iron and copper shielding of the SuperNEMO detector

detector, and the resulting attenuated γ-ray fluxes inside the detector were simulated by GEANT4.

An influence of radionuclide contamination of the iron shield of the SuperNEMO detector background was studied by artificially contaminating the iron with 1 Bq/kg of ^{208}Tl. The ^{208}Tl has been chosen as it is expected to be the main contributor to the SuperNEMO detector background during investigation of the neutrinoless double beta-decay of ^{82}Se (Q value of 2.99 MeV) because of its high Q value (5.1 MeV) and high energy of its γ-rays (2.615 MeV). A commercial iron, similarly as lead, has been found to be contaminated with ^{232}Th and ^{238}U decay products, namely by ^{208}Tl and ^{214}Bi, respectively. Even old iron is not entirely radio-pure as ^{232}Th activities of 8 mBq/kg were found [24]. ^{232}Th levels in modern stainless steel may be even higher, 1–20 Bq/kg [6].

Results and discussion

Simulation of the Obelix HPGe detector background in LSM

Monte Carlo simulated background γ-ray spectrum of the Obelix HPGe detector operating in the LSM laboratory in 32 cm thick lead shield shown in Fig. 3 is in reasonable agreement with the experimental spectrum. Both spectra have been strongly influenced by radioactive contamination of the lead shield, mainly by [214]Bi, [208]Tl and [40]K [22]. Simulated integrated background counts in the energy interval 40–3000 keV (144,370 counts/year) compare well with experimental counts (126,660 counts/year).

Figure 4 shows a predicted Monte Carlo background γ-ray spectrum in the energy interval 3–10 MeV calculated using the environmental γ-ray flux measured in the LSM laboratory. The drop in counting rates at 8 MeV has been caused by about two orders of magnitude lower environmental γ-ray flux measured in the LSM laboratory (Table 1).

Simulation of attenuation of γ-ray fluxes with shielding of the SuperNEMO detector in LSM

Monte Carlo simulations of the attenuation of environmental γ-ray flux observed in the underground hall hosting the SuperNEMO detector by iron and copper walls have
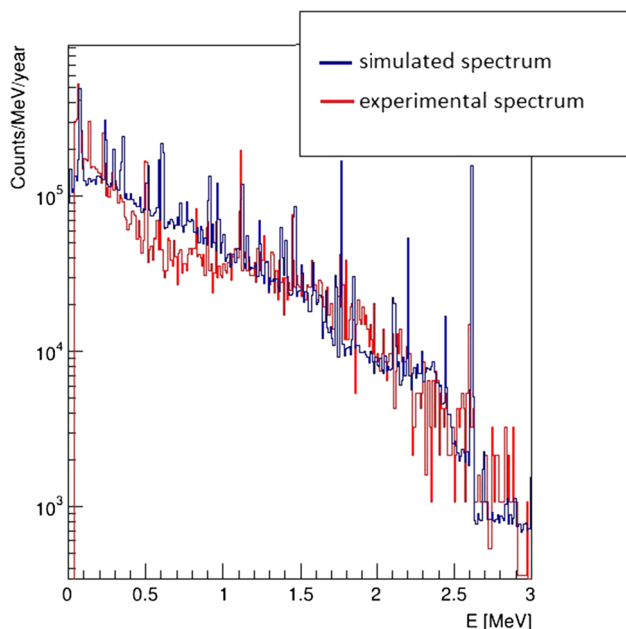
Fig. 4 Monte Carlo simulated background γ-ray spectrum of the Obelix HPGe detector in the LSM Modane underground laboratory

been carried out with the aim to estimate an impact of radioactive contamination of iron (supposed to be used for shielding of the SuperNEMO detector, Fig. 2) on the γ-ray flux behind the shielding wall. Copper has been used as an additional shielding to partially suppress [208]Tl contamination as copper has been found to have a better radiopurity than iron [9, 10]. Figure 5 shows that γ-ray flux in LSM decreases with thickness of the shielding material as expected. At 18 cm of iron, the influence of copper seems to be negligible as all fluxes have been asymptotically decreasing to the same value.

After introducing a [208]Tl contamination of the iron shield by 1 Bq/kg, the γ-ray flux has increased by about 4 orders of magnitude (Fig. 6). All fluxes seem to saturate at the iron thickness above 12 cm, which could be explained by self-shielding effects. Placing 2 cm of copper after the contaminated iron, the γ-ray flux has been reduced by about a factor of 3. Further work is in progress to estimate the impact of the [208]Tl contamination on the background of the SuperNEMO detector by simulating electron trajectories in the sensitive volume of the detector.

Conclusions

Monte-Carlo simulations were carried out with the aim to investigate background γ-ray sources in the Modane underground laboratory. First, the background γ-ray spectrum of the ultra-low level HPGe detector (Obelix) placed in the lead shield was simulated using γ-ray fluxes measured in the Modane underground laboratory. The

Fig. 3 Comparison of simulated and experimental background γ-ray spectra of the Obelix HPGe detector in the Modane underground laboratory

Fig. 5 Simulation of attenuation of gamma-ray fluxes in the LSM Modane underground laboratory after passing iron and copper wall shielding
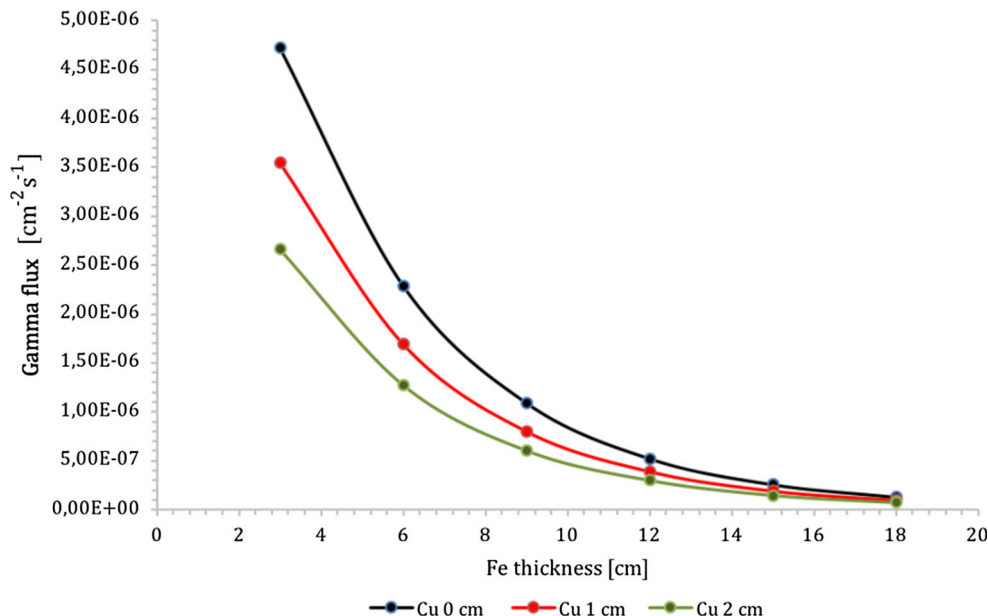
Fig. 6 Simulation of attenuation of gamma-ray fluxes in the LSM Modane underground laboratory after contamination of the iron shield with 1 Bq/kg of ^{208}Tl
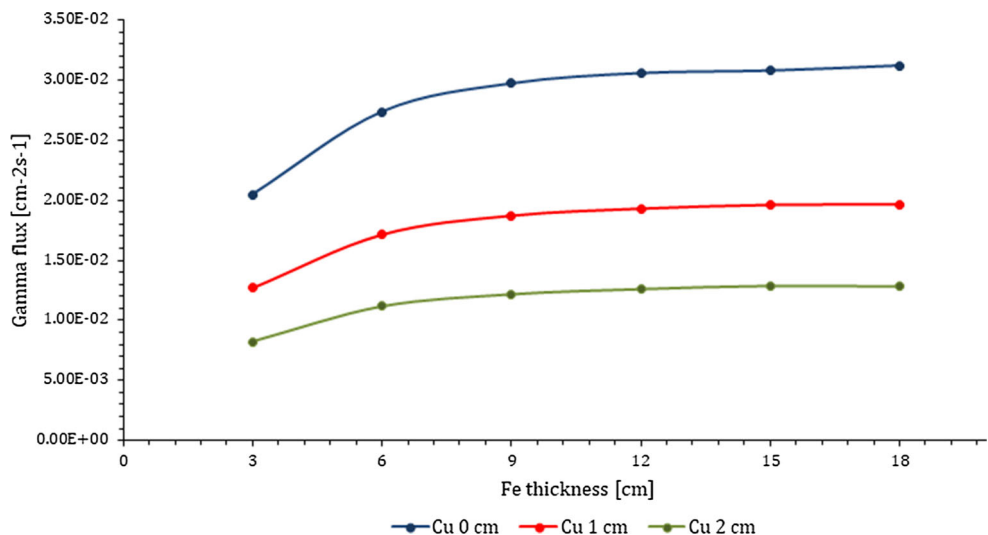
experimental background γ-ray spectrum of the Obelix detector measured in the energy interval 0–3 MeV was in reasonable agreement with the simulated spectrum. The experimental spectrum was strongly influenced by radioactive contamination of the lead shield, mainly by ^{214}Bi, ^{208}Tl and ^{40}K.

The second Monte Carlo simulation focused on the study of attenuation of γ-ray fluxes in the LSM laboratory by iron and copper shields, and on the estimation of the impact of artificially introduced radio-contamination of the iron shield. The γ-ray flux increased by about 4 orders of magnitude after placing 1 Bq/kg of ^{208}Tl in the iron shield. Further work is in progress to estimate an impact of ^{208}Tl contamination on the background of the SuperNEMO detector.

The developed Monte Carlo model could also be useful for studying and predicting background of a future large-volume HPGe γ-ray spectrometer, which is under construction in the Modane underground laboratory. Presented Monte Carlo simulations have confirmed that radiopurity of construction materials and methods of radionuclide analysis are of great importance for future nuclear and astroparticle physics underground experiments [11, 25].

References

1. Coccia E (2006) Underground laboratories in Europe. J Phys Conf Ser 39:497
2. Votano L. (2010) Underground Laboratories. In: Proceedings of 6th Patras workshop on Axions, WIMPs and WISPS https://doi.org/10.3204/desy-proc-2010-03/votano_lucia
3. Pandola L. (2011) Overview of the European Underground Facilities. In: AIP conference proceedings, vol 1338. https://doi.org/10.1063/1.3579554
4. Budjáš D et al (2009) Gamma-ray spectrometry of ultra low levels of radioactivity within the material screening program for the GERDA experiment. Appl Radiat Isot 67:755–758
5. Breier R et al (2017) Monte Carlo simulation of background characteristics of a HPGe detector operating underground in the Gran Sasso National Laboratory. Appl Radiat Isot 126:188–190
6. Povinec PP et al (2008) New isotope technologies in environmental physics. Acta Phys Slov 58:1–154
7. Heusser G (1995) Low-radioactivity background techniques. Ann Rev Nucl Part Sci 45:543–590
8. Arnold R et al (2010) Probing new physics models of neutrinoless double beta-decay with SuperNEMO. Eur Phys J C 70:927–943
9. Povinec PP (2017) Background constrains of the SuperNEMO experiment for neu- trinoless double beta-decay searches. Nucl Instrum Meth Phys Res A 845:398–403
10. Povinec PP (2017) Analysis of radionuclides at ultra-low levels: A comparison of low and high- energy mass spectrometry with gamma-spectrometry for radiopurity measurements. Appl Rad Isot 126:26–30
11. Povinec PP (2018) New ultra-sensitive radioanalytical technologies for new science. J. Radioanal. Nucl. Chem. https://doi.org/10.1007/s10967-018-5787-3
12. Liu R. X. (2015) UK low-background infrastructure for delivering SuperNEMO. arXiv:1504.08335 [physics.ins-det]
13. Loaiza P et al (2015) Obelix, a new low-background HPGe at Modane underground laboratory. AIP Conf Proc 1672(1):130002
14. Brudanin VB et al (2017) Development of the ultra-low background Ge spectrometer OBELIX at Modane underground laboratory. JINST 12:P02004
15. Vojtyla P, Povinec PP (2000) A Monte Carlo simulation of background characteristics of low-level HPGe detectors. Appl Radiat Isot 53(1–2):185–190
16. Agostinelli S et al (2003) Geant4 - a simulation toolkit. Nucl Instrum Methods Phys Res A 506:250–303
17. Schmidt B et al (2013) Muon-induced background in the EDELWEISS dark matter search. Astropart Phys 44:28–39
18. Lemrani R et al (2006) Update of neutron studies in EDEL-WEISS. J Phys. https://doi.org/10.1088/1742-6596/39/1/033
19. Savvidis I et al (2010) Underground low flux neutron background measurements in LSM using a large volume (1 m^3) spherical proportional counter. J Phys Conf Ser 203:012030
20. Ohsumi H et al (2002) Gamma-ray flux in the Fréjus underground laboratory measured with NaI detector. Nucl Instrum Methods Phys Res A 482:832–839
21. Brudanin VB et al (2017) The low-background HPGe gamma-spectrometer OBELIX for the investigation of the double beta decay to excited states. J Appl Phys. https://doi.org/10.9790/4861-0901012229
22. Breier R et al (2018) Environmental radionuclides as contaminants of HPGe gamma-ray spectrometers: Monte Carlo simulations for Modane underground laboratory. J Environ Radioact 190–191:134–140
23. Tenzer C. (2008) Monte-Carlo background simulations of present and future detectors in x-ray astronomy Proc. SPIE 7011, Space Telescopes and Instrumentation 2008: Ultraviolet to Gamma Ray, 70112G https://doi.org/10.1117/12.789685
24. Theodorsson P (1996) Measurement of weak radioactivity. World Scientific, Singapore, p 126
25. Povinec PP et al (2018) Ultra-sensitive Radioanalytical technologies for underground physics experiments. J Radioanal Nucl Chem. 25:96. https://doi.org/10.1007/s10967-018-6105-9

Monte Carlo simulations of detectors background and development of AMS methods for radiopurity measurements

V. Palušová[1], R. Breier[1], M. Ješkovský[1], J. Kaizer[1], I. Kontuľ[1], P. Loaiza[2], F. Piquemal[3], P. P. Povinec[1]

[1] *Department of Nuclear Physics and Biophysics, Comenius University, Bratislava, Slovakia*
[2] *LAL, Orsay, France*
[3] *Centre Etudes Nucleaires de Bordeaux, Gradignan, France*

Abstract. Natural radioactivity of construction materials of high-purity germanium detectors has been identified as the main component of detector background. A Monte-Carlo code was developed to evaluate the background of HPGe detector operating in the Modane underground laboratory (Laboratoire Souterrain de Modane, 4800 m w.e.). The measured background was by about 3 orders of magnitude higher than the simulated one when accounting only for its cosmic-ray components. Very low-radioactivity methods using AMS are under development at the CENTA facility in Bratislava. Prelimianary studies of uranium analysis in electrolytic copper are presented.

Keywords: Monte Carlo simulation, HPGe detectors, background, radiopurity, AMS
PACS: 29.20.-c,29.40.Wk

1. INTRODUCTION

Low-radioactivity measurement techniques have been widely applied in nuclear physics experiments searching for rare nuclear events. The detectors used in these experiments should operate in deep underground laboratories where very low background is important pre-requisite. While long-lived radionuclides have been mostly analyzed by accelerator mass spectrometry (AMS) or inductively coupled plasma mass spectrometry (ICPMS) [1], analyses of short-lived radionuclides have been mainly carried out by gamma-ray spectrometry [2]. Large volume high-purity germanium (HPGe) detectors have been widely used in such measurements because of their high efficiency and good energy resolution. A background of these detectors is due to a radioactive contamination of its construction parts and of cosmic-ray component. At sea level three components of secondary cosmic-rays are observable: a hard component consisting of muons, a soft component consisting of electrons, positrons and photons, and a nucleonic component. The flux of hard component muons can be partially eliminated by using an anticosmic shield [3]. If detectors operate in deep underground laboratories, the cosmic-ray component should be negligible [4, 5, 6, 7, 8, 9], as all components of cosmic-ray induced background are substantially decreased by surrounding rock. The dominant part of the background is therefore a radioactive contamination of construction materials which is mostly represented by decay products in the ^{238}U and ^{232}Th decay series, and by ^{40}K [1, 5]. Radiopurity measurements of construction materials of underground detectors

have mostly been carried out by non-destructive gamma-ray spectrometry. Before construction of the Ge gamma-spectrometers, Monte Carlo simulations of their background should be carried out. A new generation of underground experiments (e.g. SuperNEMO experiment that searches for neutrinoless double beta-decay) require substantial improvements of their detection limits, therefore radiopurity of construction materials is a limiting factor.

2. MATERIALS AND METHODS

2.1 HPGe detectors and Monte Carlo simulations

The Ge detector under investigation was the Obelix (volume of 600 cm^3), which is operating in LSM. The passive shielding of the Obelix has an inner layer made of Roman lead of 12 cm thickness and an outer layer made of low-activity lead of 20 cm thickness [10]. The Ge crystal was placed in an aluminum cryostat.

GEANT4 and MuonSImulationCode (MUSIC) were used in Monte Carlo (MC) simulations [11]. GEANT4 was developed at CERN and is widely used for interaction simulations in nuclear physics [12]. MUSIC is a Fortran subroutine that simulates 3D transport of muons through a standard rock. The MC code for simulation of cosmic-rays has three parts: a muon generator, part describing transport of muons in surrounding rock, and simulation of the interaction of muons with the detector. Interaction model described in GEANT4 includes four mechanisms: muon ionization, muon bremsstrahlung, production of electron-positron pairs and muon photonuclear reactions. In investigation of different radionuclide contaminants, decay events should be simulated for different parts of the detector separately. Several million events per each radionuclide from the U and Th decay series and from ^{40}K were simulated. As a result we were able to compute background gamma-ray spectra.

2.2 SuperNEMO experiment

Similiar MC simulations can be performed for the SuperNEMO experiment searching for neutrinoless double beta decay in LSM using ^{82}Se as source. The basic detection strategy of the detector remains the same as it was for its predecessor, the NEMO-3 detector, but several improvements for detection components were accomplished [13, 14]. The detector technology offers a powerful tool for background rejection and combines tracking and calorimetry techniques. Background of the SuperNEMO detector consists of external (including cosmic-rays, contamination of the laboratory air and of construction materials) and internal (contamination of the internal construction parts and radon inside the tracker) sources. The most important are events that may imitate neutrinoless double beta decay [14].

Currently under investigation are gamma-rays from different origins: radioactivity of laboratory and surrounding rocks, and neutron capture and muon bremsstrahlung in rocks. It is expected, that these gamma rays have wide spectrum and will produce events in different topologies (2e$^-$, 1e$^-$1e$^+$, crossing e$^-$, 1e$^-$ 1gamma external) that

2
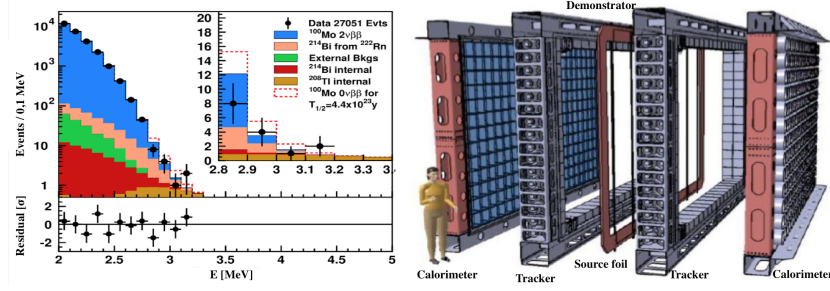
FIGURE 1. Sources of background in the NEMO-3 experiment (Arnold, 2015) and the block design of the SuperNEMO experiment

could imitate double beta-decay and neutrinoless double beta-decay. MC simulations of this external background will be done using the Falaise software (based on GEANT4), developed by the SuperNEMO collaboration.

2.3 Accelerator Mass Spectrometry (AMS)

Radiopurity of construction materials is important for reduction of background of detectors, therefore measurements of concentrations of radionuclides are of great importance for experiments that require very low background. Problem with gamma spectrometry is that analyzed radionuclides are also found in the background of the spectrometer. Alternative methods for these analyses have been under development, one of which is AMS. AMS is a technique for measuring long-lived natural and anthropogenic radionuclides that occur in the environment. It represents a change in the philosophy of counting - a direct atom counting is applied instead of waiting for decay products. A Centre for Nuclear and Accelerator Technologies (CENTA) has recently been established at the Comenius University in Bratislava. One of the goals of the CENTA laboratory is the development of the AMS technique for radiopurity measurements at levels below 1 nBq/g [15].

Very low-radioactivity measurements can be carried out mainly by AMS (Table 1), preferably without any chemical treatment of samples, as this process could add radioactive contamination from chemicals used during sample processing [16]. Tests were carried out in the CENTA laboratory using various uranium targets in the MC-SNICS ion source (multi cathode source of negative ions by caesium sputtering) and a double focusing injection magnet. Tests with analysis of uranium in wire targets made of electrolytic copper were carried out as well. The ^{238}U concentration in the wire was 10nBq/g [17].

TABLE 1. Comparison of detection limits (μBq)

Nuclide	Alpha-spec.	Gamma-spec.	BiPo-3	ICPMS	AMS	NAA
^{232}Th	100	2400	1.4	0.003	0.0002	0.08
^{238}U	100	2000	1.6	0.01	0.0001	0.2
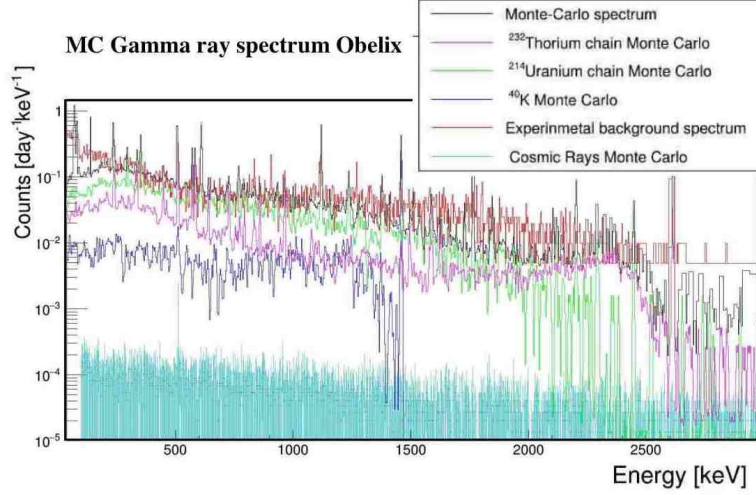
FIGURE 2. Monte Carlo simulations of background and contamination gamma-ray spectra for a HPGe detector operating in the Modane underground laboratory (4800 m w.e.)

3. RESULTS AND DISCUSSION

3.1 Gamma-ray spectra

The MC simulated background gamma-ray spectrum for the Obelix detector operating in LSM (4800 m w.e.) shows that the experimental spectrum is up to 3-orders of magnitude higher than the simulated cosmic-ray background. The difference is due to natural radioactivity in the construction parts surrounding the Ge crystal. Contributions to the Obelix detector background from environmental radionuclides (^{238}U and ^{232}Th decay products in respective chains and ^{40}K) found in various construction parts of the spectrometer were investigated. Background contributions from ^{40}K and from the ^{232}Th chain were lower than from the ^{238}U chain background continuum, except for the energies above 2000 keV, where ^{208}Tl from the ^{232}Th chain is dominant.

3.2 MC simulation of the external background of the SuperNEMO detector without shielding

Background contributions from gamma-rays of ^{214}Bi, ^{208}Tl and ^{40}K were simulated inside all internal surfaces of the experimental hall of the SuperNEMO experiment. Fig. 3 presents preliminary simulated energy deposition in the calorimeter of the Demonstrator module (the first SuperNEMO module presented in Fig. 1) of the SuperNEMO detector.
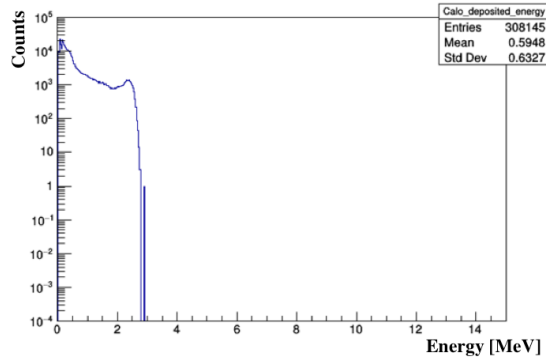
FIGURE 3. Deposited energy in the calorimeter of the SuperNEMO detector

Spectrum does not yet include neutron capture and muon bremsstrahlung in rocks, which will be covered later.

3.3 Investigations of uranium targets for AMS measurements

We did preliminary investigations with analysis of uranium in copper wire targets made of OFHC. Uranium and thorium ions extracted from the copper produce in the ion source negative ions either as uranium/thorium oxides, or as uranium/thorium compounds with copper. The ion clusters of ^{63}Cu and ^{65}Cu (^{63}Cu$_3^{65}$Cu, etc.) with masses of 254 (256), 319 (325) and 374 (388) were observed after the injection magnet, however, the UO and ThO$_2$ ions with masses of 254 and 264, respectively, should be expected in the first mass peak as well. This has been expected as U and Th oxides are the most frequently observed compounds of these two elements in the environment, and therefore they will make the most influential background contributions during AMS measurements. A more favourable case should be therefore a formation of negative molecules of UCu$^-$ or ThCu$^-$ which would fall into the mass windows of 301 and 295, respectively, where they would be free of copper cluster interferences (Fig. 4). Further investigations are going on with optimization of ion production/acceleration and post-acceleration ion analyses. A work is in progress as well to separate radiochemically ^{238}U and ^{232}Th from the enriched ^{82}Se source which will be used in the SuperNEMO experiment for investigation of its neutrinoless double beta-decay.
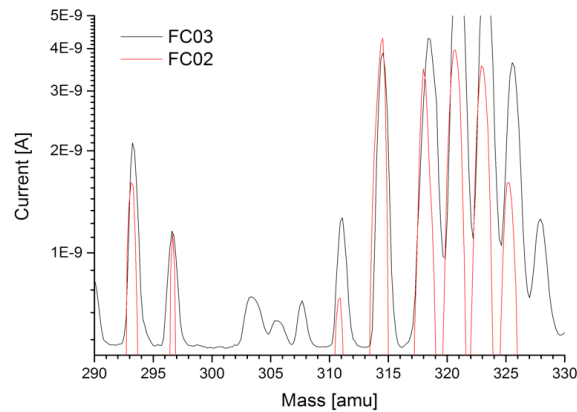
FIGURE 4. Uranium ions extracted from the copper were either as uranium oxides, or as uranium compounds with copper

4. CONCLUSIONS

MC simulation of background of the Obelix HPGe detector operating in LSM (4800 m w.e.) was carried out. When accounting only for cosmic-ray induced background the measured experimental spectrum was by about 3 orders of magnitude higher than the simulated one. The difference is due to radioactive contamination of the construction and surrounding materials placed around the Ge detector. This underlines the importance of using radiopure materials for construction of detectors used in experiments that require ultra low background. Briefly mentioned was the development of AMS technique for radiopurity measurements at CENTA in Bratislava.

ACKNOWLEDGMENTS

REFERENCES

1. Povinec, P.P., et al., Acta Phys. Slov., 58, 1-154 (2008).
2. Povinec, P.P., Radioactivity in the Environment, 6, 237-294 (2003).
3. Povinec P.P., et al., Appl. Radiat. Isot. 61:85-9310 (2004).
4. Arnold et al., Phys. Rev. D, 92, 072011 (2015).
5. Heusser, G., Ann. Rev. Nucl. Part. Sci. 45, 543-590 (1995).
6. Laubenstein, M., et al., Appl. Radiat. Isot. 61, 167-172 (2004).
7. Heusser, G., et al., Eur. Phys. J. C75, 531-539 (2015).
8. Hult, M., et al., Phys. Rev. C 74, 054311 (2006).
9. Budjas, D., et al., Appl. Radiat. Isot. 67, 755-758 (2009).

10. Brudanin, V.B. et al.,JINST, 12 (2017).
11. Kudryavtsev, V.A., Comp. Phys. Comm., 180, 339-346 (2009).
12. Agostinelli, S. et. al., Nucl. Instrum. Methods Phys. Res. A,506, 250-303 (2003).
13. Arnold, R., et al. Nucl. Instrum. Methods Phys. Res. A, 536 , p. 79 (2005).
14. Povinec, P.P., Nucl. Instrum. Methods A , 845, 398-403 (2017).
15. Povinec, P.P., et al., Appl. Radiat. Isot. 126, 26-30 (2017).
16. Povinec, P.P., et al., Nucl. Instrum. Methods Phys. Res. B, 361, pp. 87-94 (2015).
17. Povinec, P.P., et al. , Nucl. Instrum. Methods Phys. Res. B, 342, 321-326 (2015).

TECHNICAL REPORT

Measurement of the distribution of ^{207}Bi depositions on calibration sources for SuperNEMO

SuperNEMO Collaboration

R. Arnold,[a] C. Augier,[b] A.S. Barabash,[c] A. Basharina-Freshville,[d] E. Birdsall,[e] S. Blondel,[b] M. Bongrand,[b] D. Boursette,[b] R. Breier,[f] V. Brudanin,[g,h,1] J. Busto,[i] S. Calvez,[b] C. Cerna,[j] J.P. Cesar,[k] M. Ceschia,[d] A. Chapon,[l] E. Chauveau,[j] A. Chopra,[d] L. Dawson,[d] S. De Capua,[e] D. Duchesneau,[m] D. Durand,[l] G. Eurin,[b,d] J.J. Evans,[e] D. Filosofov,[g] R. Flack,[d] P. Franchini,[n] C. Girard-Carillo,[b] H. Gómez,[b] B. Guillon,[l] P. Guzowski,[e] M. Hoballah,[b] R. Hodák,[o] M.H. Hussain,[d] A. Jeremie,[m] S. Jullian,[b] J. Kaizer,[f] A. Klimenko,[g] O. Kochetov,[g] S.I. Konovalov,[c] V. Kovalenko,[g] D. Lalanne,[b] K. Lang,[k] Y. Lemière,[l] T. Le Noblet,[m] Z. Liptak,[l] X.R. Liu,[d] P. Loaiza,[b] M. Macko,[o,*] C. Macolino,[b] C. Marquet,[j] F. Mauger,[l] A. Minotti,[m] Y. Mora,[o] B. Morgan,[p] J. Mott,[d] I. Nemchenok,[g] M. Nomachi,[q] F. Nova,[k] F. Nowacki,[a] H. Ohsumi,[r] G. Oliviéro,[l] R.B. Pahlka,[k] V. Palušová,[f,j] C. Patrick,[d] F. Perrot,[j] A. Pin,[j] F. Piquemal,[j] P. Povinec,[f] M. Proga,[k] W.S. Quinn,[d] Y.A. Ramachers,[p] A. Remoto,[m] J.L. Reyss,[s] R. Saakyan,[d] A. Salamatin,[g] R. Salazar,[k] X. Sarazin,[b] J. Sedgbeer,[n] Yu. Shitov,[g,n] L. Simard,[b,t] F. Šimkovic,[f] A. Smolnikov,[g] S. Söldner-Rembold,[e] I. Štekl,[o] J. Suhonen,[u] C.S. Sutton,[v,1] G. Szklarz,[b] H. Tedjditi,[i] J. Thomas,[d] V. Timkin,[g] S. Torre,[d] Vl.I. Tretyak,[w] V.I. Tretyak,[g] V.I. Umatov,[c] C. Vilela,[d] V. Vorobel,[x] D. Waters,[d] F. Xie[d] and J. Žemlička[o]

^{a}*IPHC, ULP, CNRS/IN2P3, F-67037 Strasbourg, France*

^{b}*Université Paris-Saclay, CNRS/IN2P3, IJCLab, 91405 Orsay, France*

^{c}*NRC "Kurchatov Institute", ITEP, 117218 Moscow, Russia*

^{d}*UCL, London WC1E 6BT, United Kingdom*

^{e}*University of Manchester, Manchester M13 9PL, United Kingdom*

^{f}*FMFI, Comenius University, SK-842 48 Bratislava, Slovakia*

^{g}*JINR, 141980 Dubna, Russia*

^{h}*National Research Nuclear University MEPhI, 115409 Moscow, Russia*

^{i}*Aix Marseille Université, CNRS, CPPM, F-13288 Marseille, France*

^{j}*Univ. Bordeaux, CNRS, CENBG, UMR 5797, F-33170 Gradignan, France*

^{1}Deceased.

*Corresponding author.

^{k} *University of Texas at Austin, Austin, TX 78712, U.S.A.*

^{l} *LPC Caen, ENSICAEN, Université de Caen, CNRS/IN2P3, F-14050 Caen, France*

^{m} *Univ. Savoie Mont Blanc, CNRS, LAPP - IN2P3, 74000 Annecy, France*

^{n} *Imperial College London, London SW7 2AZ, United Kingdom*

^{o} *IEAP, Czech Technical University in Prague, CZ-11000 Prague, Czech Republic*

^{p} *University of Warwick, Coventry CV4 7AL, United Kingdom*

^{q} *Osaka University, 1-1 Machikaneyama Toyonaka, Osaka 560-0043, Japan*

^{r} *Saga University, Saga 840-8502, Japan*

^{s} *LSCE, CNRS, F-91190 Gif-sur-Yvette, France*

^{t} *Institut Universitaire de France, F-75005 Paris, France*

^{u} *Jyväskylä University, FIN-40351 Jyväskylä, Finland*

^{v} *MHC, South Hadley, Massachusetts 01075, U.S.A.*

^{w} *Institute for Nuclear Research, 03028, Kyiv, Ukraine*

^{x} *Charles University, Faculty of Mathematics and Physics, CZ-12116 Prague, Czech Republic*

E-mail: miroslav.macko@utef.cvut.cz

ABSTRACT: The SuperNEMO experiment will search for neutrinoless double-beta decay ($0\nu\beta\beta$), and study the Standard-Model double-beta decay process ($2\nu\beta\beta$). The SuperNEMO technology can measure the energy of each of the electrons produced in a double-beta ($\beta\beta$) decay, and can reconstruct the topology of their individual tracks. The study of the double-beta decay spectrum requires very accurate energy calibration to be carried out periodically. The SuperNEMO Demonstrator Module will be calibrated using 42 calibration sources, each consisting of a droplet of ^{207}Bi within a frame assembly.

The quality of these sources, which depends upon the entire ^{207}Bi droplet being contained within the frame, is key for correctly calibrating SuperNEMO's energy response. In this paper, we present a novel method for precisely measuring the exact geometry of the deposition of ^{207}Bi droplets within the frames, using Timepix pixel detectors. We studied 49 different sources and selected 42 high-quality sources with the most central source positioning.

Contents

1 Introduction

1.1 The SuperNEMO experiment

SuperNEMO [1, 2] is a double-beta ($\beta\beta$) decay experiment, designed to look for the hypothesized lepton-number-violating process of neutrinoless double-beta decay ($0\nu\beta\beta$). SuperNEMO's tracker-calorimeter design, based on the NEMO-3 technology, is also well suited for precision studies of the Standard Model double-beta decay process ($2\nu\beta\beta$) which is present in all $0\nu\beta\beta$ candidate isotopes. Both types of $\beta\beta$ decay produce two electrons around the MeV energy scale, which SuperNEMO can individually track; the processes can be distinguished by studying the energies of these electrons.

The majority of $0\nu\beta\beta$ detectors are homogeneous, meaning that the $\beta\beta$ source also serves as the detection material (for example ^{76}Ge semiconductor detectors, or bolometers of $\beta\beta$ isotope-enriched crystals). In SuperNEMO, however, the source is independent of the detector. The basic unit of a SuperNEMO-style detector is a module, as shown in figure 1. The modular design allows the detector size to be increased by adding identical modules to the detector. After the construction of each module, it is possible to verify whether the expected specifications (e.g. energy resolution, background level, etc.) have been met. An initial module, known as the SuperNEMO Demonstrator, is currently undergoing the final stages of installation and commissioning at LSM (the Modane Underground Laboratory, France).

A SuperNEMO module consists of a $\beta\beta$-decay source in the form of thin, solid foils enriched in a $\beta\beta$-decaying isotope, sandwiched between two identical detector halves. This opens up the
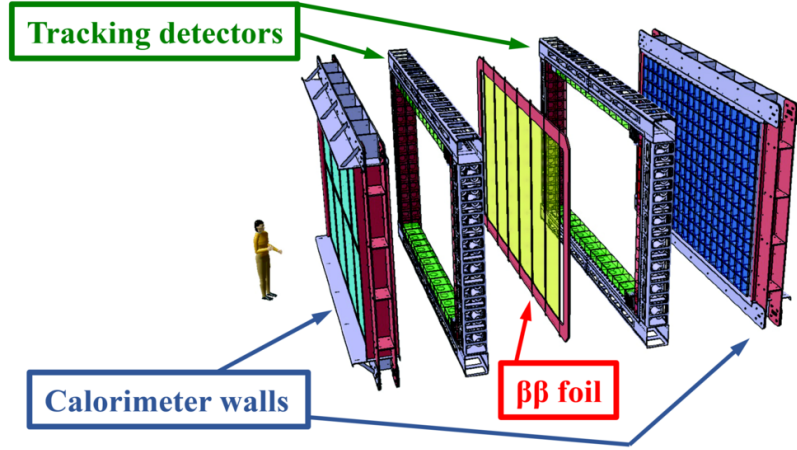
Figure 1. Overview of the SuperNEMO Demonstrator Module. Figure by C. Bourgeois [3].

possibility of studying any $\beta\beta$-decaying candidate isotope that can be produced in the form of thin foils. The SuperNEMO Demonstrator Module has 34 source foils amounting to a total of 6.25 kg of selenium, of which 6.11 kg is the $\beta\beta$ isotope ^{82}Se, with an average thickness of 0.286 mm and an average surface density of 50 mg of selenium per cm^2 [4, 5]. The feasibility of using other isotopes (such as ^{150}Nd) is also under investigation.

The two electrons emitted in $\beta\beta$ decays are detected in the SuperNEMO Demonstrator Module by its particle tracker and calorimeter. The source foils are sandwiched between two tracking detectors, which together consist of 2034 drift cells operating in Geiger mode, in a vertical magnetic field [6]. The tracker reconstructs charged-particle trajectories, allowing significant background suppression, as well as extracting the angular distribution of the $\beta\beta$ electrons. The energy of the individual decay electrons is measured by a segmented calorimeter, consisting of plastic scintillator blocks coupled to photomultiplier tubes surrounding the detector on all six sides. Calorimeter modules in the main walls of the detector have an average energy resolution of 7.5% FWHM at 1 MeV. The ability of the calorimeter to distinguish a $0\nu\beta\beta$ signal from $2\nu\beta\beta$, and to study $2\nu\beta\beta$ decay mechanisms that affect the energy spectrum, depends on the correct calibration of its energy response [3].

1.2 SuperNEMO calibration system

In order to perform energy calibrations of the SuperNEMO Demonstrator Module, ^{207}Bi sources are used. K-shell electrons from internal-conversion decays of ^{207}Bi provide three relevant calibration lines at 482 keV, 976 keV and 1682 keV; lower-intensity lines from L- and M-shell conversions are also included to achieve a good fit of the ^{207}Bi spectrum. The sources, which were previously used in the NEMO-3 detector [7], were produced at IPHC Strasbourg. For each source, a very thin droplet of ^{207}Bi solution was deposited on a Mylar foil (12 μm thick) and then covered with another identical foil. Over time, the solvent has dried out, but the droplets of ^{207}Bi remain stable. Both Mylar foils were sealed by a rectangular frame made of radiopure copper, with internal dimensions 8 mm × 13 mm (figures 2a and 2b). The dimensions of the sources were chosen for compatibility with NEMO-3's calibration tubes, and have been incorporated into the SuperNEMO design.
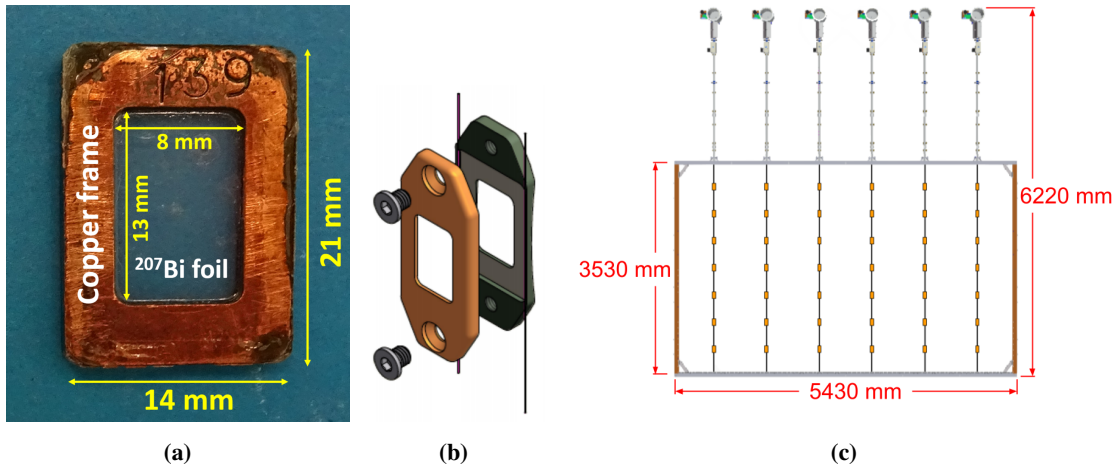
Figure 2. a) Photograph of ^{207}Bi source number 139. b) Diagram of the envelope which fixes the source within the deployment system. c) Simplified diagram of the ^{207}Bi deployment system. Orange rectangles represent source envelopes (not to scale). Six columns, each comprising seven ^{207}Bi sources, are vertically deployed into gaps between the ^{82}Se $\beta\beta$ source foils by an automatic system above the SuperNEMO Demonstrator Module.

The 42 calibration sources used in the SuperNEMO Demonstrator Module are inserted and guided into gaps between the ^{82}Se $\beta\beta$ source foils, using six identical mechanisms (figure 2c). The insertion and removal of the sources will be controlled by an automatic source deployment system developed by the University of Texas at Austin [8]. The calibration procedure will be performed at regular intervals during the data taking; the necessary calibration frequency will be determined experimentally, and is expected to be on the order of one run every few days or weeks. Information about the position of the sources relative to the rest of the detector is used when reconstructing the emitted electron trajectories and the associated energy losses. The deployment system lowers the source envelopes to their predefined locations as shown in figure 2c, with a precision of 60 µm. However, the deposition distribution of the ^{207}Bi droplet within the copper frame is unknown (figure 2a). Most importantly, one needs to verify that the ^{207}Bi droplet did not spill in between the copper frame parts during the sealing process. This could cause emitted electrons to lose additional energy, which would result in a distortion of the reconstructed energy lines, and spoil the energy calibration of the SuperNEMO Demonstrator Module.

The goal of this work was to establish an experimental method to describe the deposition distribution of ^{207}Bi droplets within the calibration sources for the SuperNEMO Demonstrator Module. ^{207}Bi is a complex emitter; along with electrons, it emits both X-rays and gammas. For this analysis, instead of observing the electrons used to calibrate the SuperNEMO Demonstrator Module, the ^{207}Bi deposition within each source was studied by detecting low-energy X-rays from the ^{207}Bi source, which produce single-pixel depositions in a silicon pixel detector, allowing us to take advantage of the detector's peak sensitivity, and providing better localization of signals. As a result, we established a ranking of the measured SuperNEMO calibration sources based on how closely the ^{207}Bi droplet had been deposited relative to the center of the copper frame. The best 42 sources were chosen to be installed in the calibration setup for the SuperNEMO Demonstrator Module.

2 Measurement and data analysis

2.1 Timepix detectors and calibrations

The droplet positioning measurements were performed using three Timepix silicon pixel detectors provided by IEAP, CTU in Prague (figure 3). Two of the detectors (H04-W0163 and H11-W0163) are 0.3 mm thick, while the third (L05-W0163) is 1 mm thick. Timepix detectors have the ability to measure the energy deposited by an incident particle, and its time of arrival. They were developed by the Medipix collaboration [9]. The sensitive chip is a square with sides 14.08 mm long, divided into 256×256 pixels (size of each pixel: $0.055\,\text{mm} \times 0.055\,\text{mm}$).

For the Timepix detectors to be used to measure the distribution of the ^{207}Bi source droplets, the detectors required a precise spatial calibration, and an approximate energy calibration. Both were carried out at IEAP, CTU in Prague. The energy response of each of the 65536 pixels in each detector was calibrated individually. This calibration consisted of relatively long measurements (several hours) in order to collect enough statistics in each pixel. The calibration was performed using fluorescent foils exposed to X-rays. Three fluorescent foils — Fe (6.398 keV), Cu (8.04 keV) and Cd (23.106 keV) — each provided one energy calibration point. The calibration function has four parameters; the fourth parameter is the result of threshold equalization of the detector. [10]. This energy calibration allowed the energy-weighted distribution of spatial data from the ^{207}Bi sources to be generated, and enabled a basic energy cut to select the particles of interest for our ^{207}Bi measurement. By using low-energy X-rays, we were able to select single-pixel depositions, which give us the best position localization. Higher-energy depositions, like those from β-decay electrons, activate several pixels, which reduces the ability to identify the spatial coordinates of the decay.

When a Timepix detector is used to monitor the ^{207}Bi source, the ^{207}Bi droplet position is only represented in the detector chip coordinates. However, the purpose of the measurement is to represent the position of the ^{207}Bi droplet with respect to its copper frame. In order to make such spatial calibration possible, we defined a Reference Alignment Point (RAP, figure 3b) for all measurements.

An additional measurement was taken in which a thin metallic square, perforated by holes distributed equidistantly in a grid (figure 4a) laser-cut to few-µm precision, was placed on top of the detector, so that the yellow dot in figure 4a matched the RAP. The distance between the centers of adjacent holes, in both the vertical and horizontal directions, was equal to 1 mm. We irradiated this setup with X-rays. The result of this measurement can be seen in figure 4b. Thanks to this measurement, we were able to extract the position of each pixel in the sensitive area of the detector relative to the RAP. The position of the RAP and the 1-mm spacing of the metal grid were used to convert from the coordinate system of the detector (in pixels) to that of the source frame (in mm).

2.2 Measurement protocol

The duration of a measurement sufficient to collect enough data for an individual ^{207}Bi source was typically around 2–3 hours, due to the relatively low source activity (120-145 Bq) and selection efficiency (approximately 6% for the thinner detectors, and 9% for the thicker, for the data of interest to this study: while the detector's efficiency is close to 100% for X-rays produced by ^{207}Bi, these values refer to the efficiency of the single-pixel and energy-range cuts imposed to ensure that the position of the droplet corresponds to the activated pixel). This led to an event rate in our region of interest (ROI), as explained in section 2.4, of around 8–10 events per second. To accumulate
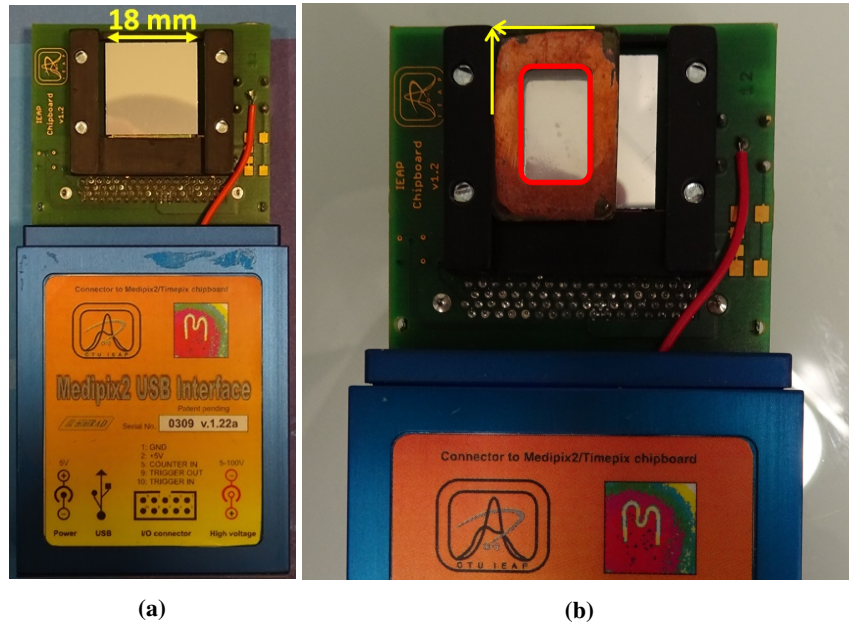
Figure 3. a) Photograph of one of the Timepix pixel detectors used in this work, H04-W0163, which has a 0.3 mm-thick silicon sensor. b) Photograph of the source position during each measurement. The two yellow arrows point to the Reference Alignment Point (RAP).
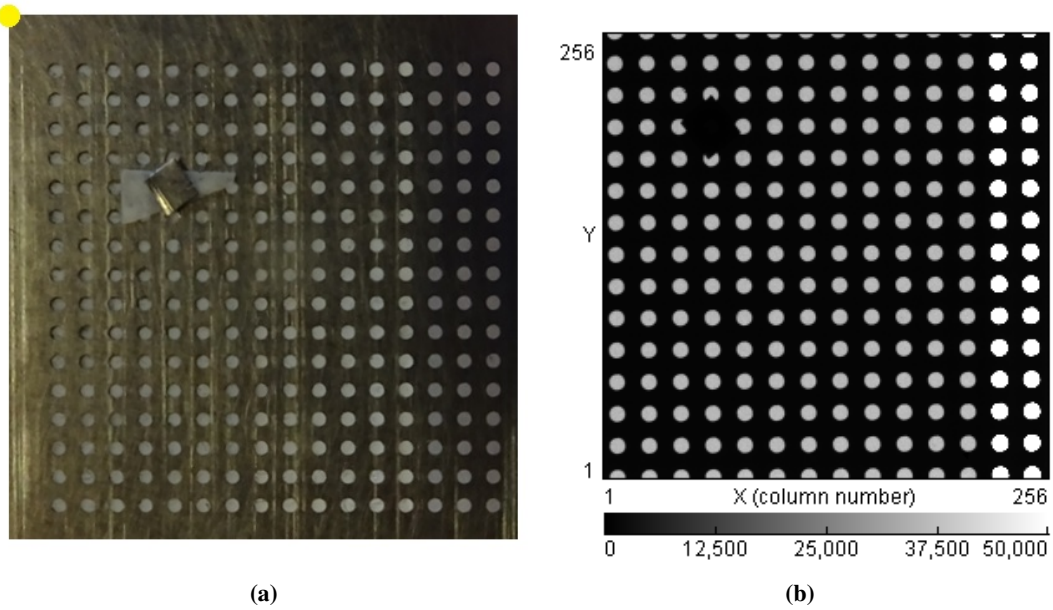
Figure 4. a) Photograph of the calibration grid. The yellow circle denotes the corner corresponding to the RAP during the spatial calibration measurements. b) The grid as seen in the detector after the exposure to X-rays. Neither the first two rows nor the first column are visible in the dataset; nor is the yellow reference point shown in the left-hand figure, as these lie outside the sensitive area of the detector. In order to identify individual holes in the dataset, we covered one of the holes with a piece of metal.
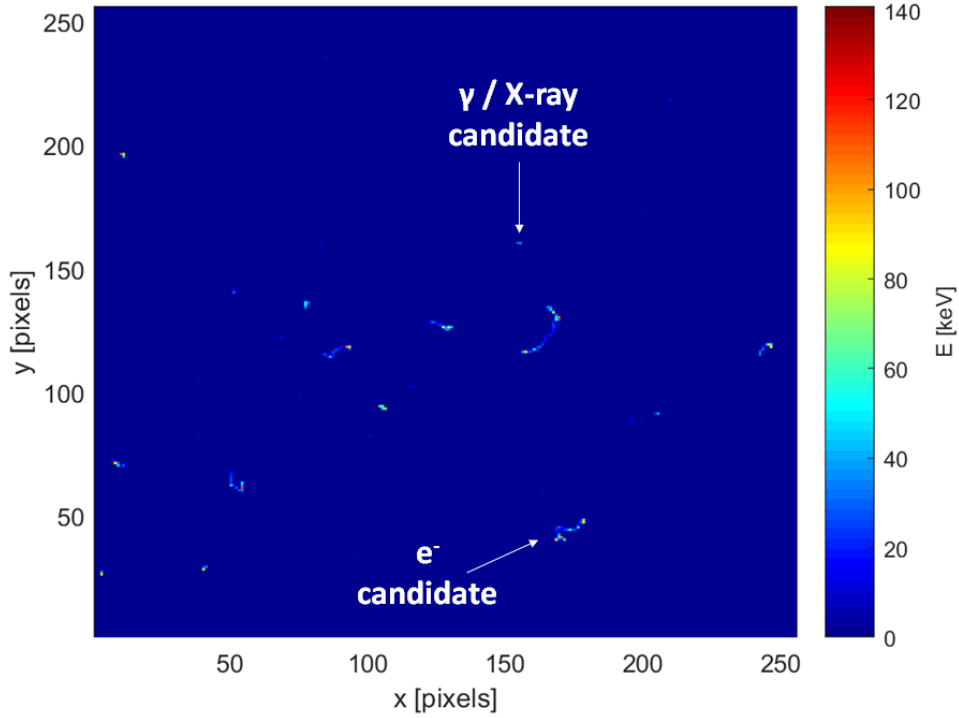
Figure 5. Visualization of the data collected from a sample ^{207}Bi source in a one-second time slice. A typical photon and electron candidate are marked.

sufficient statistics to precisely measure the droplet position, we aimed for around 50000 events in the ROI for each source. Due to scheduling constraints, less data was collected for sources 93, 94, and 95; nevertheless, it was sufficient to evaluate these sources. Repeated and extended measurements were taken for a subset of sources, taking advantage of the laboratory schedule to collect larger samples with millions of events and confirm consistency with the lower-statistics measurements. All three pixel detectors were used in parallel, and were connected to one computer. Measurements for the 49 available ^{207}Bi sources were taken over a period of almost 12 full days, which included short interruptions to exchange the samples.

2.3 Structure of measured data

As mentioned above, each of the Timepix pixel detectors used in the study has a square chip with a size of 14.08 mm × 14.08 mm divided into 256 × 256 pixels. Raw data obtained from a detector has a simple format of three columns, storing the x and y coordinates of each pixel and the energy deposited in the pixel, respectively. Each file contains information about the total energy per individual pixel over a specified time period known as a "time slice". The dead time between two time slices is typically around 200 ms, regardless of the length of the time slice. A time slice of 1 second was chosen, as this allowed individual particles to be isolated, while minimizing the relative fraction of dead time. In figure 5, data recorded in a single 1-second time slice is visualized as an example.

The software used, Pixelman [11] (developed at IEAP, CTU in Prague), provides a user interface for the Timepix detectors. While the software can be used to extract the previously-described raw data, Pixelman also provides a pre-analyzed 'clustered output' [12] format, which enables the identification and energy measurement of individual particles. The algorithm that transforms the raw data into clustered output first groups the triggered pixels from one time slice into clusters, based on their spatial adjacency. It then extracts the energy of each cluster (representing one particle, which might have triggered several pixels) and its position. The sum of the energy deposited in all the individual pixels of a cluster represents the energy deposited by the particle in the detector. The cluster position is defined as the average position of the individual pixels in the cluster, weighted by the energy deposited in each pixel. The clustered output also reports a 'cluster size', corresponding to the number of pixels in each cluster, which is related to the particle type: single-pixel isolated energy deposits are typically produced by photons and Auger electrons, while high-energy electrons generate multi-pixel clusters. The analysis described in the following sections was performed on this clustered output.

2.4 Data analysis method

The main goal of this study was to develop an experimental method that could evaluate the quality of a source based on the position of ^{207}Bi within its source frame assembly. In practice, this can prevent the use of any sources with unwanted contamination caused by ^{207}Bi droplet leakage into the region of the copper source frame. The study also has the potential to reduce systematic uncertainties related to the calibration source positions within the SuperNEMO Demonstrator Module. Precise knowledge of source positions can enable us to evaluate our tracker's vertex resolution capabilities, and to ensure that electron track lengths are correctly reconstructed.

The positions of the clusters measured for a single source (integrated over all the time slices) can be represented by a two-dimensional histogram. Each cluster is weighted by its energy in order to obtain an energy distribution. This histogram shows a wide peak corresponding to the region of the source frame where the ^{207}Bi has been deposited (figure 6). The x and y directions are aligned with the 8-mm and 13-mm axes of the source frame, respectively.

High-energy electrons activate several pixels; the location of the earliest hit, likely to correspond to the electron's source position in the ^{207}Bi droplet, is unknown. The best source localization of the ^{207}Bi droplet was therefore achieved by selecting only the clusters corresponding to a single pixel, and with a reconstructed energy between 3 keV and 30 keV, reducing the uncertainty on the measurement of the cluster position (figure 6b). This energy region consists of X-rays and Auger electrons from electron capture on ^{207}Bi, and contains the majority of these single-pixel events (figure 7). This selection made a negligible difference to the best-fitted position coordinates of the droplets' centers, with an average difference between the pre-cut and post-cut position of 0.054 mm, comparable to the size of a single detector pixel. This energy range and single-pixel cut will henceforth define our region of interest (ROI). It should be noted that, during measurement, there is a small gap (1.5–3 mm, depending on the individual source) between the ^{207}Bi source and the Timepix detector. As particles are emitted from the source at varying angles, even when a single pixel is triggered, the corresponding particle may not have been emitted immediately above that pixel.

The comparison of energy distributions with and without these cuts is shown in figure 6. After applying the cuts (figure 6b), the radius of the half-width-at-half-maximum (HWHM) contour is reduced by approximately 20% with respect to the full sample (figure 6a). A plot similar to figure 6b
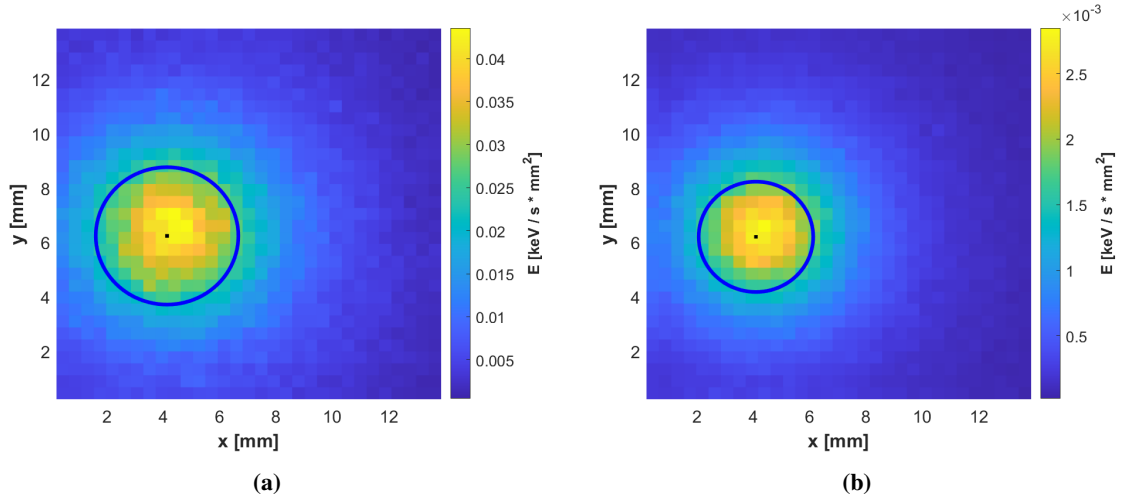
Figure 6. Energy distributions measured for source number 133, with different selections applied. The black points represent the position of the calculated weighted center (x_0, y_0). The blue circles represent the contour lines where the fitting function reaches half of the maximal value (thus, the radius of the circle is the half width at half maximum, HWHM). a) Energy distribution for all clusters with an energy in the range 3–1300 keV (no cluster size cut). The distribution includes all types of particle produced in ^{207}Bi decays (X-rays, gammas and electrons). b) Energy distribution for single-pixel clusters with an energy in the range 3–30 keV, corresponding to Auger electrons and X-rays. Note differing scale on color axis.
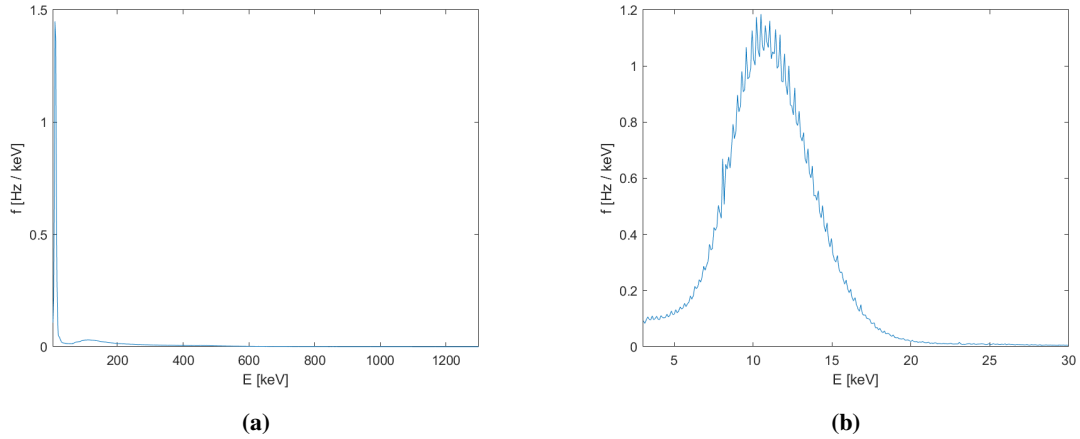
Figure 7. Measured energy spectrum for source number 126, including a) all clusters in the energy range 3–1300 keV (no cluster size cut) and b) single-pixel clusters in the range 3–30 keV.

was obtained for each measured source and fitted with a two-dimensional function.

$$ f(x, y) = \frac{A}{(x - x_0)^2 + (y - y_0)^2 + \gamma} \, . \tag{2.1} $$

Here, the x_0 and y_0 coordinates represent the measured center of the source (in pixels), γ is proportional to the square of the width of the peak, and A is a scale factor. A visual representation of the quantities extracted from the fit can be found in figure 8. The blue circles in figures 6 and 8 represent the border where the fitting function drops to half of its peak value (i.e. $A/2\gamma$). The

radius of the blue circle represents a two-dimensional equivalent of the HWHM of the distribution. For the purpose of this study, we considered this contour as a measured effective size of the ^{207}Bi droplet. The fitting function was chosen for its simple form that contains all necessary degrees of freedom. All of the droplets were confirmed visually to be circular in shape, apart from two; both sources with non-circular drops also failed subsequent selection criteria, and were not installed in the SuperNEMO Demonstrator Module.
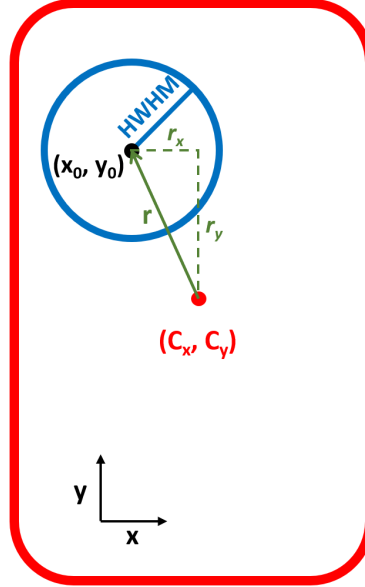
Figure 8. Graphical representation of quantities extracted from the fit to equation (2.1): the blue circle represents the HWHM contour; the black dot denotes the center of the ^{207}Bi deposition (x_0, y_0); the red dot, the center of the frame (C_x, C_y); and the green arrow, the vector $\vec{r}$ of the droplet's position with respect to the frame's center.

The position of the source extracted from the fit is given relative to the sensitive detector chip. Since the aim of the study was to extract the relative position of the source droplet with respect to the source frame, a spatial calibration, described in section 2.1, was used to provide the relative position of the center of the source frame (C_x, C_y) with respect to the chip. Information about the center of the frame allows us to define the position, $\vec{r}$, of the ^{207}Bi droplet relative to the center of the source frame. It can be calculated as follows:

$$\vec{r} = (r_x, r_y) = (x_0 - C_x, y_0 - C_y). \tag{2.2}$$

The vector $\vec{r}$ can be seen in figure 8.

3 Results

3.1 Categorization of sources based on droplet position

For this study, we collected data from 49 different source samples in 52 measurements. As explained previously, the standard acquisition time to collect sufficient statistics was 2–3 hours. Supplementary high-statistics measurements on sources 126, 132 and 139, for periods of up to a few days, aimed to

improve precision and better estimate systematic uncertainties, as explained in section 3.2. A sample of some of these measurements is shown in table 1; a complete list is in tables A1 and A2 of [13].

Table 1. Statistics of a sample set of measurements, including standard measurements of 2–3 hours and extended measurements of 2 days or more. The first column shows the ID number of the measured source, with an asterisk (*) denoting measurements repeated under the same experimental conditions. The second and third columns indicate the Timepix detector and its thickness (d_{DET}). The table also contains the active exposure time (not including dead time) (t_{live}), total statistics collected (N_{TOT}), number (N_{ROI}) and fraction of events in the ROI, and detection rate. The ROI included all single-pixel clusters in the energy range 3–30 keV. The full data set (TOT) contains all 3–1300 keV clusters of 1 to 100 pixels. Note the improved detection rate and fraction in the ROI for the thicker (1 mm) detector.

Source ID	Detector	d_{DET} [mm]	t_{live} [h]	N_{TOT} [cnts]	N_{ROI} [cnts]	$\frac{N_{\mathrm{ROI}}}{N_{\mathrm{TOT}}}$ [%]	$\frac{N_{\mathrm{ROI}}}{t_{\mathrm{live}}}$ [s^{-1}]
73	H04-W0163	0.3	1.7	1.1×10^5	5.0×10^4	43.3	8.3
74	H11-W0163	0.3	1.8	1.2×10^5	5.4×10^4	43.4	8.4
111	H11-W0163	0.3	3.8	2.9×10^5	1.3×10^5	43.3	9.1
120	L05-W0163	1.0	12.7	1.1×10^6	5.5×10^5	50.4	12.1
126	H04-W0163	0.3	55.5	3.4×10^6	1.5×10^6	43.0	7.4
126*	H04-W0163	0.3	46.2	3.0×10^6	1.3×10^6	42.5	7.8
132	H11-W0163	0.3	54.8	4.0×10^6	1.7×10^6	43.5	8.7
132*	H11-W0163	0.3	46.0	3.3×10^6	1.4×10^6	43.3	8.7
139	L05-W0163	1.0	54.8	4.7×10^6	2.3×10^6	49.6	11.9
139*	L05-W0163	1.0	46.0	4.0×10^6	2.0×10^6	49.5	11.9

As previously discussed, the aim of this study was to estimate the position of the ^{207}Bi droplet in each source relative to the center of its frame of (inner) dimensions 8 mm × 13 mm, where the x direction corresponds to the shorter axis of the frame. This droplet position is described by the length of the vector $r = |\vec{r}|$ defined in subsection 2.4. According to the magnitude of r we defined three source categories:

- very good sources ($r < 0.5$ mm), represented by green triangles;

- good sources (0.5 mm $\leq r < 1.0$ mm), represented by yellow circles;

- unacceptable sources ($r \geq 1.0$ mm), represented by red squares.

The computed values of $\vec{r}$, colored according to their category, are shown in table 2 for a subset of measurements, and in figure 9 for all measurements (the full list is also included in tables A3 and A4 of [13]). The positions of the 49 source droplets, and their radii, are summarized in figure 10.

We identified 5 sources where the center of the droplet had been deposited more than 1 mm away from the center of the source frame center (red squares), which were rejected. The centers of the remaining 44 droplets were within 1 mm of the centers of the frames (green triangles or yellow circles).

3.2 Estimation of the uncertainty on the droplet position

Before each of the measurements, the measured source was aligned to the RAP manually. In figure 3b one can notice that in the shorter, horizontal direction (x) the source touched the black
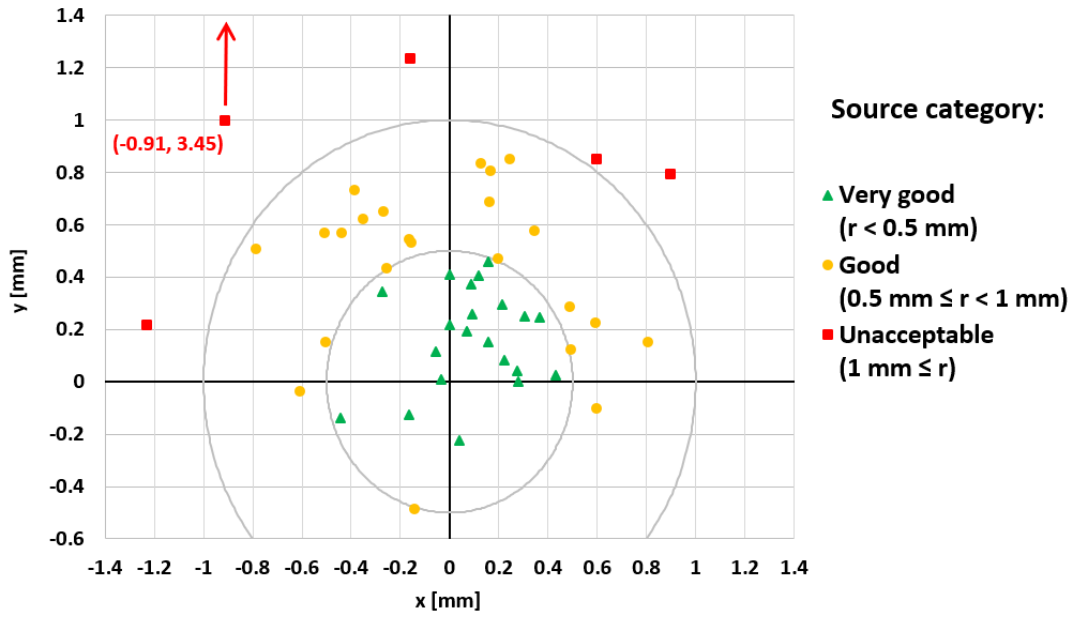
Figure 9. Position of the center of the ^{207}Bi droplet for each of the measured sources, relative to the center of the source frame. Source quality rankings of very good (green triangle), good (yellow circle) and unacceptable (red square), are explained in section 3.1. Uncertainties are not shown, for the purpose of clarity. Note that the position of one source fell outside the range of this plot.
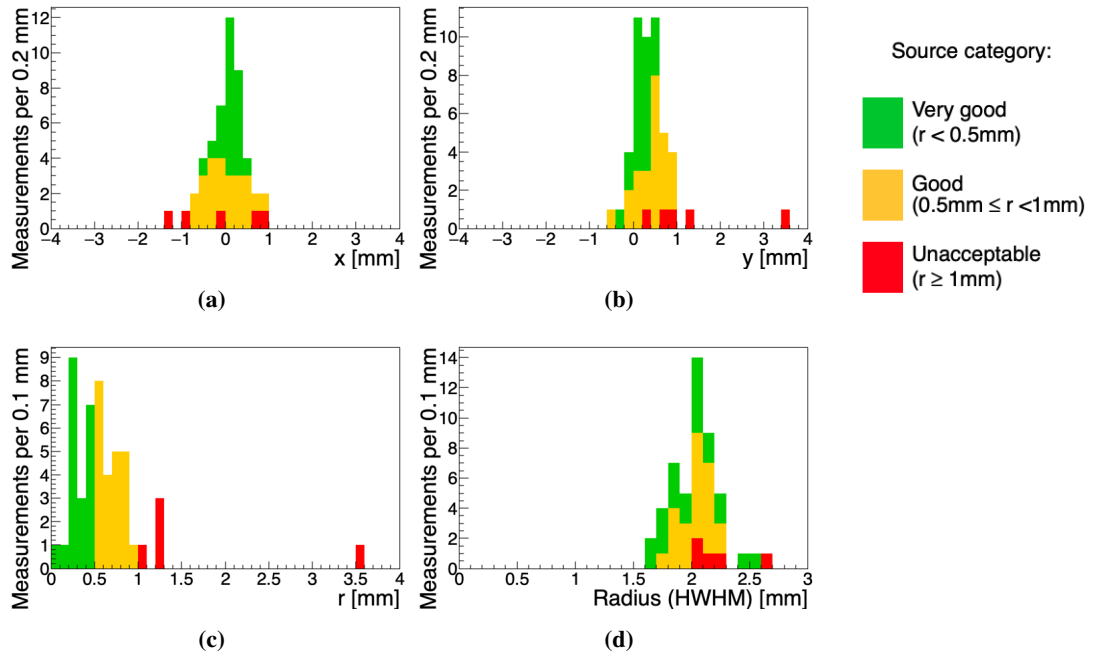
Figure 10. Summary histograms showing the positions of the droplets' centers, relative to the center of the source frame, for very good (green), good (yellow) and unacceptable (red) sources. Histograms a) and b) summarize the displacements along the short (x) and long (y) axes of the source frame respectively; c) shows the magnitudes of source droplet displacements; and d) shows the radii of the droplets. For sources where multiple measurements were taken, average values are plotted.

plastic chip holder; however, in the longer, vertical direction (y), the source could move freely and the human factor could introduce an extra source of uncertainty in this direction. An indication of this comes from the distribution of the measured droplet centers in 9, where it can be clearly seen that the measured y positions of the centers tend to be higher than the centers of their respected source frames, as calculated from the RAP of the calibration grid (as in 4). As there is no asymmetry to the frames, and because the foils were produced with the intention of placing droplets in the center of the frames, it is reasonable to assume that the mean position of the full set of droplets should be central with respect to the frame. The offset of this mean position from our measured central point should therefore provide an estimation of the uncertainty on the measured values of the droplet position $\vec{r}$. This mean position, indicated by the black cross in figure 11 has an offset of magnitude 0.02 mm in the x direction, and 0.39 mm in the y direction. It can be noted that, were this position to be taken as our central point, only two of our sources would be categorized as 'unacceptable', with a droplet position more than 1 mm from this new center (outside the yellow circle in figure 11). Both of these sources are already rejected by the original methodology.
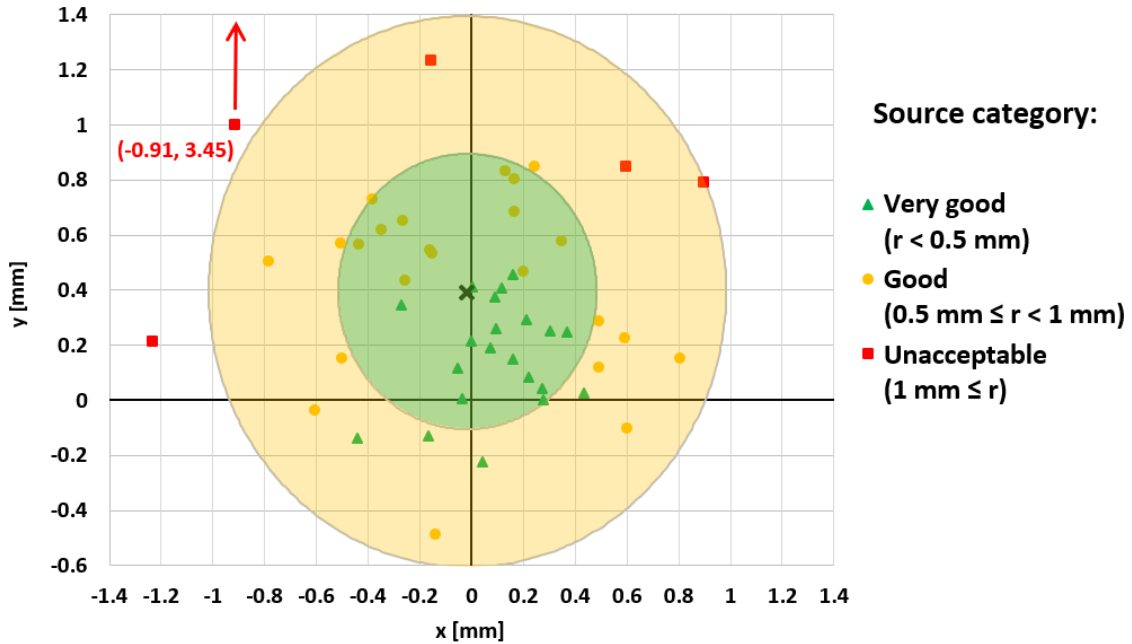
Figure 11. Position of the center of the ^{207}Bi droplet for each of the measured sources, relative to the center of the source frame, as in figure 9. Markers denote quality rankings as in the original figure. The black cross denotes the mean position of the droplet centers at (-0.02 mm, 0.39 mm). Green and yellow rings denote a 0.5 mm and 1.0 mm offset respectively from this mean position.

As an additional check of this method of estimating the uncertainty on the droplet position, we considered the higher-statistics repeated measurements of droplet position and radius for three sources (126, 132 and 139), as shown in table 2. Only clusters from the ROI (energy range 3–30 keV and cluster size of one pixel) were taken into account. By comparing the droplet position vector components, r_x and r_y, between two repeated measurements, we can (very roughly) estimate their uncertainty. The relative difference on the r_x component for two different measurements of source

Table 2. Summary of the quantities defined in figure 8, for repeated measurements on an unacceptable (red), good (yellow), and very good (green) source (see section 3.1). Asterisks denote a second measurement on a source, taken under the same conditions as the first.

Source	Droplet radius	Droplet displacement		
ID	HWHM	r_x	r_y	r
	[mm]	[mm]	[mm]	[mm]
126	2.44	−1.22	0.11	1.23
126*	2.14	−1.24	0.33	1.28
132	1.96	−0.25	0.57	0.62
132*	1.95	−0.29	0.74	0.79
139	1.61	−0.02	-0.07	0.07
139*	1.62	−0.05	0.08	0.10

132 is 0.04 mm. Since this value is smaller for sources 126 and 132, we considered 0.04 mm as the uncertainty in the r_x component, i.e. $\Delta x = 0.04$ mm. By applying the same logic for r_y, we obtain a value of $\Delta y = 0.22$ mm from the comparison of the two measurements for source 126.

In the x direction, where source positioning was constrained by the plastic holder, the repeated-measurement method yielded a larger variation in values than was indicated by the mean position offset (0.04 mm vs. 0.02 mm). Conversely, in the y direction, where manual alignment was required, the consideration of mean droplet position yielded a larger offset than the repeated measurements would indicate (0.39 mm vs. 0.22 mm). In order to be conservative, we consider that a source should be deemed unacceptable if the radius of the droplet comes within a distance $\Delta x = 0.04$ mm or $\Delta y = 0.39$ mm of the source frame. It should be noted that, in both cases, these uncertainty estimates are small relative to the typical effective radius of the ^{207}Bi droplet which, at around 2 mm (see section 3.1), can be understood as a very conservative estimate of the uncertainty on the source position.

3.3 Droplet containment within the source frames

As explained in section 2.4, one goal of this study was to ensure that sources selected for the SuperNEMO Demonstrator Module did not suffer leakage of the ^{207}Bi droplet into the region of the copper frame. To confirm this was the case for our selected sources, the profiles of each droplet in the x and y directions were plotted relative to the source frame (figure 12).

To produce the projected profiles in figure 12, each droplet is assumed to be circular, centered at its measured best-fit point, with a radius corresponding to the fitted HWHM. The projection of each droplet is shown relative to the position of the copper frame, at ±4 mm in the x direction, and ±6.5 mm in the y direction (the frame extends beyond the plot, but only its inner dimension is relevant). Gray bars inside the source frame represent the uncertainty on position measurements in each dimension ($\Delta x = 0.04$ mm and $\Delta y = 0.39$ mm) as estimated in section 3.2. Sources colored green were categorized as very good, yellow as good, and red as unacceptable, based on the positions of the droplets' centers, as explained in section 3.1. The mean HWHM value for all measurements, including the rejected sources and repeated measurements on individual sources, is 2.03 ± 0.21 mm. It can be seen that none of the selected (green and yellow) sources show any overlap between the droplet and the source frame, and furthermore, that the distance between the droplet and frame is
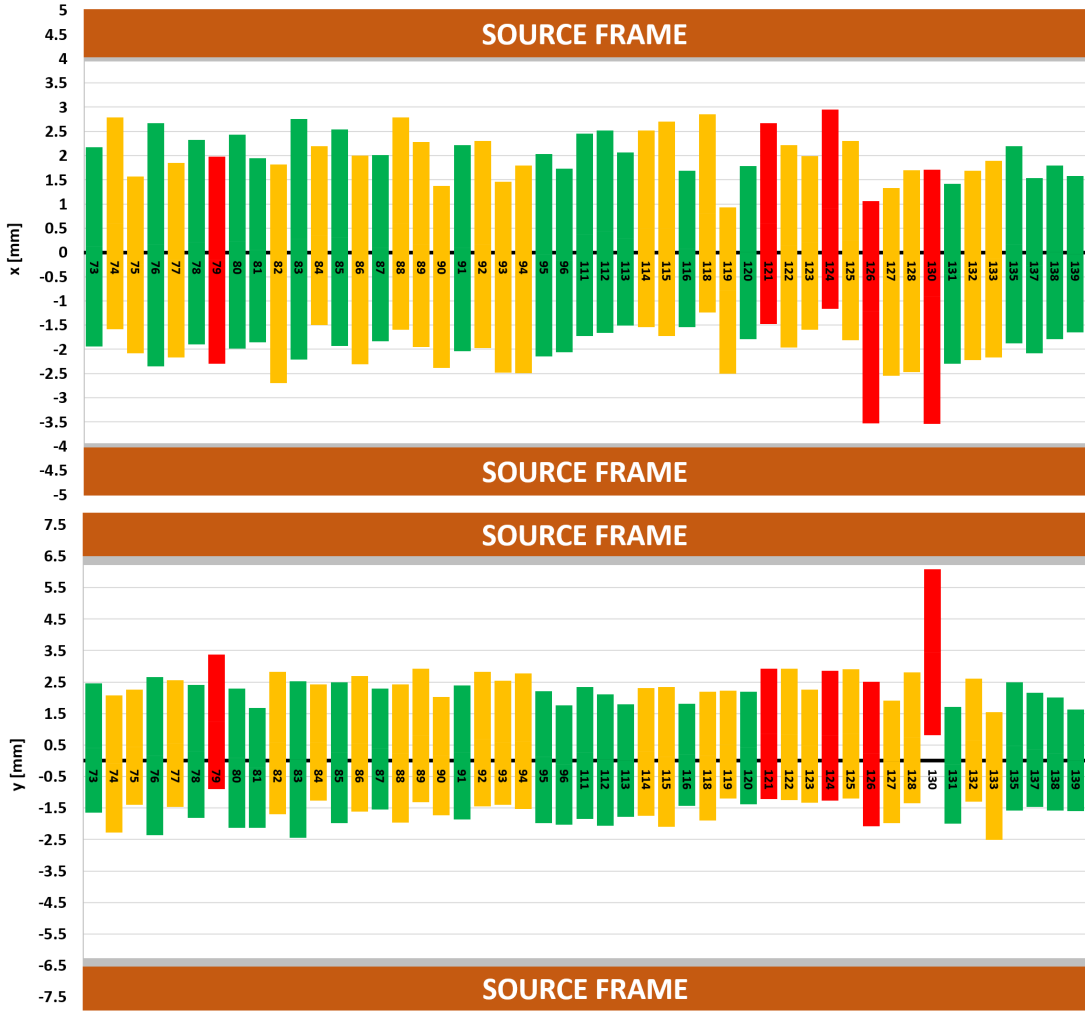
Figure 12. Projections of the x (top) and y (bottom) positions of the droplet in each source. The center of each bar indicates the fitted position of the droplet r_x or r_y; the bar height is twice the HWHM; and the label indicates source ID number. Colors indicate quality categories (see section 3.1). The brown horizontal bars indicate the position of the copper frame position; the adjoining gray bars show the uncertainty on position measurements.

greater than the uncertainty on the droplet's position. We therefore conclude that there is no danger of leakage under the copper frame from our selected sources. The selected sources have a mean HWHM of 2.01 ± 0.19 mm.

4 Conclusions

In this paper, we describe a method for measuring the position of ^{207}Bi droplets in the SuperNEMO calibration sources within their frames, using Timepix detectors. We successfully applied this method to 49 ^{207}Bi calibration sources developed for the SuperNEMO experiment, and evaluated their quality. All 49 sources of ^{207}Bi were proven to be eligible for calibration of the SuperNEMO Demonstrator Module, as none of them presented leaks towards the copper frame. The 42 sources

whose ^{207}Bi droplets were closest to the center of the copper source frames (out of 44 that passed our stricter quality criteria) were chosen and installed in the SuperNEMO Demonstrator Module. These measurements also allow better characterization of the source deposition distributions, ensuring that knowledge of the ^{207}Bi source positions does not limit the energy and vertex reconstruction of the SuperNEMO Demonstrator Module.

Acknowledgments

References

[1] SuperNEMO collaboration, *Probing New Physics Models of Neutrinoless Double Beta Decay with SuperNEMO*, *Eur. Phys. J. C* **70** (2010) 927 [`arXiv:1005.1241`].

[2] NEMO collaboration, *The SuperNEMO project*, *Phys. Atom. Nucl.* **69** (2006) 2096.

[3] A.S. Barabash et al., *Calorimeter development for the SuperNEMO double beta decay experiment*, *Nucl. Instrum. Meth. A* **868** (2017) 98 [`arXiv:1707.06823`].

[4] SuperNemo collaboration, *The SuperNemo ββ0ν enriched ^{82}Se source foils and their radiopurity measurement with the BiPo-3 detector*, *J. Phys. Conf. Ser.* **888** (2017) 012086.

[5] SuperNEMO collaboration, *The SuperNEMO ββ source production*, *PoS* **ICHEP2016** (2017) 1018.

[6] SuperNEMO collaboration, *Construction and commissioning of the SuperNEMO detector tracker*, *Nucl. Instrum. Meth. A* **824** (2016) 507.

[7] R. Arnold et al., *Technical design and performance of the NEMO 3 detector*, *Nucl. Instrum. Meth. A* **536** (2005) 79 [`physics/0402115`].

[8] SuperNEMO collaboration, *Radioactive source deployment system for the calibration of the SuperNEMO detector*, *PoS* **ICHEP2016** (2016) 808.

[9] X. Llopart, R. Ballabriga, M. Campbell, L. Tlustos and W. Wong, *Timepix, a 65k programmable pixel readout chip for arrival time, energy and/or photon counting measurements*, *Nucl. Instrum. Meth. A* **581** (2007) 485 [*Erratum ibid.* **585** (2008) 106]

[10] D. Turecek, J. Jakubek, M. Kroupa and P. Soukup, *Energy calibration of pixel detector working in time-over-threshold mode using test pulses*, *IEEE Nucl. Sci. Symp. Conf. Rec.* (2011) 1722.

[11] D. Tureček et al., *Pixelman: a multi-platform data acquisition and processing software package for medipix2, timepix and medipix3 detectors*, 2011 *JINST* **6** C01046.

[12] T. Holy, E. Heijne, J. Jakubek, S. Pospisil, J. Uher and Z. Vykydal, *Pattern recognition of tracks induced by individual quanta of ionizing radiation in Medipix2 silicon detector*, *Nucl. Instrum. Meth. A* **591** (2008) 287.

[13] M. Macko, *SuperNEMO Experiment: Study of Systematic Uncertainties of Track Reconstruction and Energy Calibration. Evaluation of Sensitivity to 0nbb with Emission of Majoron for Se-82.*, Ph.D. thesis, Université de Bordeaux, Univerzita Komenského, Bratislava (2018).

Monte-Carlo calculation of production rates of cosmogenic radionuclides in a HPGe detector operating in the Modane underground laboratory

Róbert Breier [*], Jozef Masarik, Veronika Palušová, Pavel P. Povinec

Department of Nuclear Physics and Biophysics, Faculty of Mathematics, Physics and Informatics, Comenius University, 84248 Bratislava, Slovakia

ARTICLE INFO

ABSTRACT

Monte Carlo models based on GEANT4, CONUS and ACTIVIA software packages were used for simulation of production rates of cosmogenic radionuclides in the Obelix HPGe detector operating in the Modane underground laboratory. Interactions of secondary cosmic-ray nucleons with Ge-crystal (production of ^{3}H, ^{54}Mn, ^{57}CO, ^{65}Zn and ^{68}Ge), with copper in the cold finger (production of ^{46}Sc, ^{54}Mn, ^{56}Co, ^{57}Co, ^{58}Co, ^{60}Co and ^{59}Fe), with Al in bauxite ore (production of ^{26}Al) and with Al-4%Si alloy in the cryostat (production of ^{22}Na) were included in the calculations. The contribution of cosmogenic radionuclides to the total detector background of the Obelix detector decreased from 39% (after 10 months of cooling down) to 14% (after three years of cooling down). The calculated production rates of cosmogenic radionuclides and simulated gamma-ray spectra were in reasonable agreement with experimental results.

Contents

1. Introduction

Low-level radioactivity measuring techniques have been frequently applied in underground nuclear physics experiments searching for rare nuclear events such as neutrinoless double beta-decay [1,2], and in searchers for dark matter (DM) candidate particles [3,4]. In both cases a radioactive contamination of underground detectors by primordial [5, 6] and cosmogenic [7–9] radionuclides produced during construction of detectors at the surface were important background sources influencing detection limits.

* Correspondence to: Department of Nuclear Physics and Biophysics, Faculty of Mathematics, Physics and Informatics, Comenius University, Mlynska Dolina F1, 84248 Bratislava, Slovakia.
  E-mail address: robert.breier@fmph.uniba.sk (R. Breier).

The neutrinoless double beta-decay energy scale is given by energy of beta-particles (<3 MeV), with expected half-life of this process over 10^{25} yr [2]. On the other hand, the search for DM has been focused on elastic scattering (nuclear recoil) of DM particles with nuclei in a detector. The energy scale of interest in this case is much lower (<100 keV), and less than 1 event per day is expected [4]. Therefore, to reach the proclaimed detection limits, contributions of all construction materials to the detector background should be minimized. Radiopurity of materials should be regularly checked, usually at levels down to 1 μBq kg^{-1} [10–12]. Such analyses could be carried out by HPGe detectors with large effective volumes and high detection efficiency, good resolution and low background.

The gamma-ray background of HPGe detectors operating in surface laboratories is induced by cosmic rays, by contamination of construction materials (detectors, shields, laboratory walls) with primordial (^{40}K, ^{232}Th, ^{238}U) and anthropogenic (^{60}Co, ^{137}Cs) radionuclides, and by radon in the air and its decay products [12]. Cosmic rays at sea level consist of a soft component (photons, electrons and positrons), a nucleonic component (neutrons and protons) and a hard component (muons). The elimination of the background induced by soft and nucleonic components is done by shields made from high Z material (lead, steel, copper). Low Z materials (polyethylene, paraffin) with addition of boron or lithium are used for slowing down and absorption of neutrons. A partial reduction of muon-induced background is possible by applying muon-veto detectors [12–14], however, the lowest background can be reached by placing HPGe detectors deep underground [10,12,15–19].

In the deep underground laboratory of Modane (Laboratoire Souterrain de Modane, LSM), which is the deepest underground laboratory in Europe (4800 m w. e., water equivalent), the muon flux is about six orders of magnitude lower than at sea level ($\Phi_\mu = 6.25 \times 10^{-9}$ muons cm^{-2} s^{-1}) [20]. The total ambient flux of neutrons measured in the LSM, $\Phi_n = 9.6 \times 10^{-6}$ neutrons cm^{-2}s^{-1}, is mostly due to thermal neutrons [21]. At such low muon and neutron fluxes, the background contributions from radionuclide contamination of detectors construction materials and the laboratory environment was about three orders of magnitude higher than the background induced by cosmic rays [18].

Although the main contribution to the background of HPGe detectors operating deep underground is expected from radioactive contamination of construction parts, it would be useful to quantify a contribution from cosmogenic radionuclides as well. The construction components of HPGe detectors are irradiated by cosmic rays during production and storage of materials, during the detector fabrication and its transport to an underground laboratory. The main contributors to the production of cosmogenic radionuclides at sea level are secondary cosmic-ray particles, mainly nucleons. As protons form <10% of the nucleonic component at sea level and taking into account their interaction with nuclei and absorption in shielding constructions (e.g. roofs), the neutrons are the dominant particles responsible for production of cosmogenic radionuclides at sea level [12].

An exception is ^{26}Al because of its very long half-life (T$_{1/2}$ = 0.717 Myr), its production in construction materials during storage, fabrication of required parts and even airplane transport would not be comparable with *in situ* production of ^{26}Al in bauxite, a sedimentary rock formed from several to tens of million years ago [22,23]).

The production of cosmogenic radionuclides is decreasing to negligible levels once the detector is installed in a deep underground laboratory where only cosmic-ray muons can penetrate. However, their contribution to production of cosmogenic radionuclides is negligible when compared to sea-level activation [12].

Most of cosmogenic radionuclides found in background gamma-spectra of HPGe detectors operating deep underground are short lived (^{46}Sc, ^{54}Mn, ^{59}Fe, ^{56}Co, ^{57}Co, ^{58}Co, ^{65}Zn), and we may assume that they reached a saturation activity during their production in construction materials at sea level. They contribute to the HPGe detector background mainly during the first year of its operation in an

underground laboratory. However, the medium-lived ^{22}Na and ^{60}Co could be observed in background spectra after several years, and especially the long-lived ^{26}Al will be present for the entire lifetime of the experiment [24,25].

Monte-Carlo simulations of HPGe detectors background were carried out in the past with the aim to determine the background components and to find ways how to decrease contributions from cosmic rays and radio-contamination of materials [16,18,26,27]. The developed Monte Carlo models usually did not include contributions to the detectors background from cosmogenic radionuclides produced by interactions of cosmic-ray particles with HPGe detector components and its shield during their exposure at the earth surface. As Monte Carlo simulations have shown that cosmic-ray induced background gamma-spectra of HPGe detectors operating in deep underground laboratories are by two-three orders of magnitude lower than the experimental gamma-spectra [16,18], the principal suspect is the production while handling and storage on surface, which requires a full investigation.

The aim of this work has been to quantify production rates of cosmogenic radionuclides in construction materials of HPGe detectors using Monte Carlo simulation toolkits, and calculate their contributions to the Obelix HPGe detector background operating in the Modane underground laboratory.

2. Monte-Carlo Models applied for simulation of production of cosmogenic radionuclides

Monte Carlo software packages were used in the present work to simulate the HPGe detector background. The GEANT4 (Geometry and Tracking) toolkit [28,29] was used to calculate the HPGe detector response to radiation, and the CONUS (COsmogenic NUclides Simulations) [30–32] toolkit was used to calculate production rates of cosmogenic radionuclides in the detector construction materials. The ACTIVIA C^{++} computer package [33] was used as an alternative method to compare production rates of cosmogenic radionuclides with the CONUS results.

2.1. HPGE detector geometry

The Monte Carlo simulations were carried out for the Obelix HPGe detector which is operating in the LSM underground laboratory in Modane at the depth of 4800 m w.e. [18,24,25]. It is p-type coaxial detector with diameter of 93.5 mm and length of 89.6 mm. The sensitive volume is 600 cm^3, the germanium mass is 3.19 kg, and the relative detector efficiency is 162%. The resolution of the detector is 1.12 keV at 122 keV, and 1.98 keV at 1332 keV. The HPGe crystal is mounted in a low background U-type cryostat of 115 mm in diameter and 196 mm long; the thickness of the entrance window is 1.6 mm. The cryostat and the detector holder are made from Al-4%Si alloy. The oxygen free high conductivity copper was used for production of the cold finger. The FET of the preamplifier is placed inside the cryostat and it is shielded by a ring (thickness of 10 mm) made of Roman lead with ^{210}Pb activity <60 mBq/kg. The inner shield (thickness of 12 cm) of the HPGe detector was made from Roman lead as well. The outer shield (thickness of 20 cm) was made from low activity lead [17,24,25]. The model of the HPGe detector used in Monte Carlo simulations is presented in Fig. 1.

2.2. GEANT4 simulations

The GEANT4 toolkit has been frequently used for simulation of particle transport in the matter [28,29], and for the simulation of the response of HPGe detectors to external radiation [12,16,18]. The LBE (Low Background Experiments) modular physics list, which is used for low background physics was applied in the model, and the Radioactive Decay Module (G4RadioactiveDecay) was used for description of radioactive decays of nuclei with emission of α, β^- or β^+ particles. The
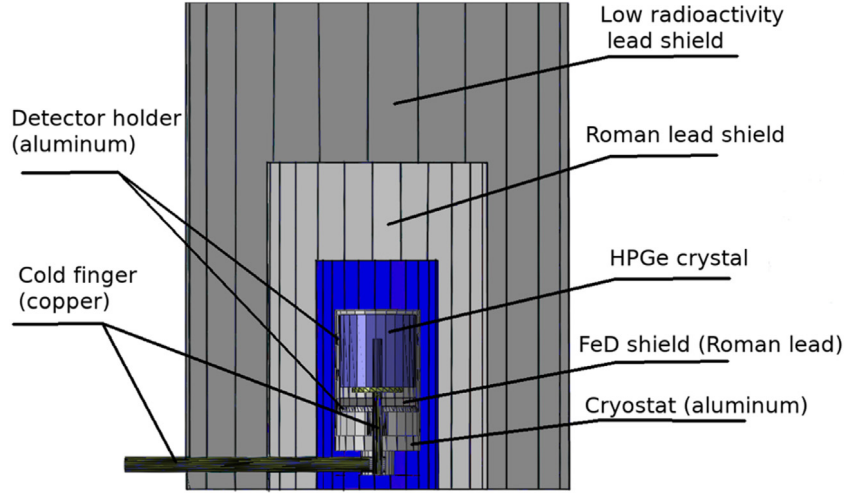
Fig. 1. Model of the Obelix HPGe detector used in GEANT4 simulations.

nuclear de-excitation of the excited daughter product was simulated using G4PhotoEvaporation class. The module is the empirical one using data from the Evaluated Nuclear Structure Data File (ENSDF) [34]. Radioactive decays were simulated in various components: The Ge detector itself, the aluminum cryostat, the detector holder, and the cold finger. More information on the GEANT4 simulations of HPGe detectors background can be found in our previous papers [16,18].

2.3. CONUS calculations

The CONUS toolkit was used to calculate production rates of cosmogenic radionuclides in detector materials. The code is based on the MCNPX (Monte Carlo N Particle eXtended) code combined with the LAHET code (high-energy particle transport of nucleons, pions, muons and light nuclei), and with the MCNP (Monte Carlo N-Particle) code for transport of neutrons, protons and electrons in matter. The CONUS code was developed by Masarik et al. [30–32] and used to calculate production rates of cosmogenic radionuclides in extra-terrestrial and terrestrial objects.

The production rate of the cosmogenic nuclide j at the Earth surface D is given as

$$P_{j(D,M,\Phi)} = \sum_i N_i \sum_k \int_0^\infty \sigma_{ijk}(E_k) \cdot J_k(E_k, D, M, \Phi) \, dE_k \qquad (1)$$

where N_i is the number of atoms in the target element i per kg of material, $\sigma_{ijk}(E_k)$ is the cross section for the production of the nuclide j from the target element i by particles of type k with energy E_k, and $J_k(E_k, D, M, \Phi)$ is the total flux of particles of type k with energy E_k at location D inside the atmosphere for the geomagnetic field M and the solar modulation function Φ. The incident particle fluxes $J_k(E_k, D, M, \Phi)$ were calculated using the GEANT4 [28,29] and MCNP [35] codes. A description of the interface between these two codes is given in [32].

The used cross sections $\sigma_{ijk}(E_k)$ were experimentally measured cross sections for involved nuclear reactions, which were taken from the European JEFF-3.1.1 [36] and the ENDF/B-VII.0 libraries [37]. As experimental data for nuclides studied in this paper are very sparse, some of the cross sections were calculated using the TALYS code [38], with input parameters based on the work [39]. The cross sections were tested on calculations of production rates of cosmogenic nuclides in extraterrestrial and terrestrial objects, as well as in irradiation experiments when available [30–32].

As the differences in the production of neutrons and protons in reactions of primary galactic cosmic-ray (GCR) protons and alpha-particles are small, an isotropic irradiation with primary GCR protons was used in calculations. The production rates were calculated for

the normalized omnidirectional flux of 1 proton cm^{-2} s^{-1} (used in our previous calculations for an easy comparison), which was then modified for the present case of 4.56 nucleons cm^{-2} s^{-1} (see below). To get good statistics in the Monte Carlo calculations, the number of events for each radionuclide calculation was $3 \cdot 10^6$ incident protons.

The solid Earth was considered as a sphere with a radius of 6378 km with a surface density of 2 g cm^{-2}, and an average chemical composition. The Earth's atmosphere was modeled as a spherical shell with a thickness of 100 km. The atmospheric density and temperature were approximated by the U.S. Standard Atmosphere (1976) model [40]. The primary cosmic-ray flux at the Earth's orbit has two components: GCR and solar cosmic rays (SCR). However, because of relatively low energies of SCR, their contribution to the production was not considered in the present simulations. The GCR particles are a mixture of ~87% of protons, ~12% of alpha-particles and ~1% of heavier nuclei with atomic numbers from 3 to ~90 [41]. The approximation for the primary GCR spectra introduced by Castagnoli and Lal [42] was used in the calculations. In the simulations within the Earth's magnetic field, alpha-particles have to be treated separately. This is due to the different geomagnetic effects on primary protons and alpha-particles. The effective flux of protons, including the contribution of alpha-particles with energies above 10 MeV at 1 AU, was determined (by fitting lunar experimental data [43]) to be 4.56 nucleons cm^{-2} s^{-1}.

The energy range of input particles in the CONUS model was from 0.001 eV to 20 GeV. Calculations were done for sea level and high latitudes, and both neutron and proton induced reactions were included in the model. Technical details on the codes, used cross sections and their applications to the cosmogenic radionuclide production rate calculations are given in [30–32], where uncertainties of these calculations are also discussed. Statistical uncertainties of the simulations were about 5%, while the systematic ones were of the order of 10%.

2.4. ACTIVIA Calculations

The ACTIVIA C^{++} computer package [33] was used as an alternative method to compare production rates of cosmogenic radionuclides in the HPGe detector materials with the CONUS results. ACTIVIA uses a combination of semi-empirical formulas and data-tables based on experimental results to calculate the cross-sections, production rates and yields of radionuclides during irradiation with cosmic-ray neutrons. The production rate is calculated as [33]

$$P_j = C \sum_i \frac{f_i}{A_{ti}} \int \frac{d\varphi}{dE} \sigma_{ij}(E) \, dE$$

where C is a normalization factor, f_i is the relative abundance fraction of the i-target, A_{ti} is the target mass number, $d\varphi/dE$ is the energy

spectrum of cosmic-ray neutrons, and $\sigma_{ij}(E)$ is the cross section for the production of the nuclide j from the target element i.

The program inputs are specified by ActAbsInput (abstract interface), which contains input-beams, products, targets, and decay-times. The default input-beam, defined in the ACTIVIA (version 1.3.0) package, based on the parametrized cosmic-ray spectrum (the same for neutrons and protons) was used in the calculations (also called the ACTIVIA1 approach). The beam was defined in the range of $10–10^4$ MeV, which is much narrower than that used in the CONUS code (0.001 eV– 20 GeV). The Experimental Nuclear Reaction Data (EXFOR) database (http://www-nds.iaea.org/exfor/), together with semi-empirical formulas were used for calculation of cross-sections of investigated nuclear reactions.

Calculations using the ACTIVIA package found in the literature were carried out for two different energy spectra of cosmic-ray neutrons and protons. While the ACTIVIA1 results ([9,33] and the present work) were obtained with the default input neutron spectrum, the ACTIVIA2 results were obtained with the GEANT4 input spectrum [9].

As discussed later, differences (generally within a factor of two) between the CONUS and ACTIVIA calculations of production rates were observed for some radionuclides. The ACTIVIA1 underproduction could be explained by different input cosmic-ray spectra used in the calculations, as well as by the fact that it does not simulate individual particles and their interactions with matter as it is done in Monte Carlo codes. As the energy threshold used in the CONUS code is lower than in ACTIVIA1, this can be also a reason for an underproduction due to the omission of neutrons with lower energies in the activation process. A much better agreement was obtained, however, between the CONUS and ACTIVIA2 results as the input cosmic-ray spectra were similar.

3. Results and discussion

3.1. Measured and simulated background gamma-spectra of the Obelix HPGe detector in the LSM laboratory

Background gamma-spectrum of the Obelix HPGe detector measured in the LSM laboratory ten months after its installation [17,24] is presented in Fig. 2. It can be seen that contributions of primordial (^{40}K) and radiogenic radionuclides (^{212}Pb, ^{208}Tl and ^{228}Ac from the ^{232}Th chain, and ^{214}Pb and ^{214}Bi from the ^{238}U chain) from the radio-contamination of construction parts of the HPGe detector and the shield to the total detector background are dominant.

Seven cosmogenic radionuclides (^{57}Co, ^{54}Mn, ^{68}Ge, ^{65}Zn, ^{22}Na, ^{60}Co and ^{26}Al) were identified in the experimental gamma-spectrum (Fig. 2, Table 1). The ^{60}Co peak can be seen only at 1332.5 keV, as the peak at 1173.2 keV is masked by the ^{65}Zn peak.

The Monte Carlo GEANT4 simulation of the radiogenic background gamma-spectrum of the Obelix detector has already been described in our previous work [18], therefore, it will not be discussed in detail in the present paper. A comparison of the measured and GEANT4 simulated gamma-spectra shows that there is a reasonable agreement in the low energy region of the spectra, except for the energies below 200 keV. This discrepancy has been observed in previous simulations as well [16,18], and it may be associated with underestimation of the Compton continuum, and production of Pb X-rays. The simulated high-energy part of the gamma-spectrum (1200–3000 keV), also shown in Fig. 2, follows the experimental spectrum very well.

A comparison of measured and calculated counting rates under the gamma-peaks of identified cosmogenic radionuclides shows that a reasonable agreement (within statistical uncertainties) has been found (Table 1). After about three years of cooling down of the Obelix detector underground, only ^{22}Na, ^{60}Co and ^{26}Al could be measured in the background gamma-spectrum [24]. In the long-term perspective only ^{26}Al will be identified in the Obelix background.

However, the contributions of cosmogenic radionuclides to the total background of HPGe detectors are smaller than from radiogenic

Table 1

Measured and Monte Carlo simulated counting rates under the gamma-peaks in the Obelix HPGe detector background gamma-ray spectra.

Radionuclide	Half-life	Gamma-ray energy [keV]	Counts[a]	
			Experiment [17,24]	GEANT4 (this paper)
^{57}Co	271.80 d	136.47	110 ± 12	145 ± 12
^{54}Mn	312.13 d	834.84	41 ± 9	45 ± 8
^{68}Ge+^{68}Ga	270.93 d	1077.40	8 ± 3	7 ± 3
^{65}Zn	243.93 d	1124.5	133 ± 13	168 ± 13
^{22}Na	2.60 yr	1274.5	34 ± 9	27 ± 5
^{60}Co	5.27 yr	1332.5	6 ± 3	4 ± 2
^{26}Al	0.717 Myr	1808.6	20 ± 8	12 ± 4

[a]Counting rates under the corresponding peaks 10 months after installation of the detector in the LSM Modane (counting time was 34 days) [17,24].

radionuclides (Fig. 2). When comparing the total background in the energy range of 40–3000 keV measured 10 months after the Obelix installation in LSM, we get for the experimental spectrum 109 ± 3 count per kg of Ge per day, and 111 ± 11 count kg^{-1} d^{-1} for the simulated spectrum. The simulated radiogenic contribution is 68 ± 7 count kg^{-1} d^{-1}, and 43 ± 4 count kg^{-1} d^{-1} we get for the simulated cosmogenic spectrum. Two years later, the simulated cosmogenic spectrum decreased to 11 ± 1 count kg^{-1} d^{-1}, and the total simulated spectrum to 79 ± 8 count kg^{-1} d^{-1}. The contribution of cosmogenic radionuclides to the total detector background of the Obelix detector decreased from 39% (after 10 months of cooling down) to 14% (after three years of cooling down). The estimated total background fits well with the general trend of total backgrounds of HPGe detectors operating in deep underground laboratories [12].

Further, in Section 3.2 we will calculate production rates of the identified cosmogenic radionuclides in various construction materials: germanium (HPGe detector), aluminum and silicon (Al-4%Si alloy, used in the cryostat and detector holder) and copper (used in the cold finger). Afterwards, we will compare the calculated production rates with experimental results, as well as with literature data.

3.2. Calculations of production rates of cosmogenic radionuclides in construction parts of the HPGe detector

The main target construction materials for production of cosmogenic radionuclides which are well visible in the experimental gamma-spectrum (Fig. 2) are Ge crystal (for production of ^{54}Mn, ^{57}Co, ^{65}Zn and ^{68}Ge), Al and Si in the cryostat and the detector holder (for production of ^{22}Na and ^{26}Al), and Cu in the cold finger (for production of ^{54}Mn, ^{57}Co and ^{60}Co).

3.2.1. Germanium crystal

Many experiments searching for rare nuclear events have used germanium crystals as the detectors, therefore the activation of natural and enriched germanium has been object of many studies [e.g., [44–49]. Calculated production rates of cosmogenic radionuclides (^{3}H, ^{54}Mn, ^{57}Co, ^{65}Zn, ^{68}Ge) after the germanium exposure to cosmic rays (Table 2) show a reasonable agreement with other published data [8,9,33,47], specifically for the CONUS model.

Large differences between the ACTIVIA1 and CONUS results were observed for ^{3}H, ^{65}Zn and ^{68}Ge, while better agreement was found between the ACTIVIA2 and CONUS results as they used similar cosmic-ray spectra. For other three radionuclides (^{54}Mn, ^{57}Co and ^{60}Co) the agreement between all results was very good. A reasonable agreement was also obtained between the ACTIVIA1 results in the present work when compared with ACTIVIA1 calculations in [33,47] (except for ^{68}Ge in [33]).

As already pointed out, there could be several reasons for observed disagreement, probably the most important are differences in cosmic-ray spectra used in the calculations.
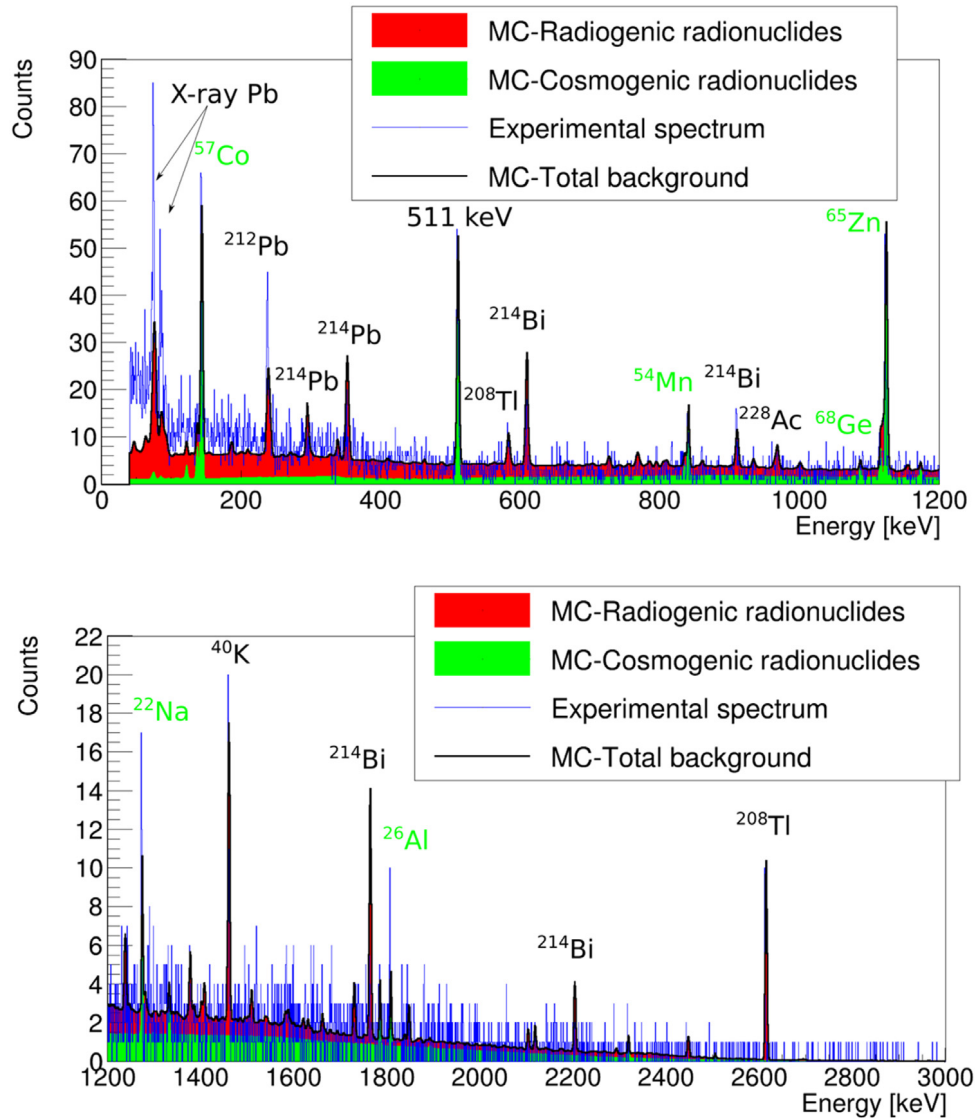
Fig. 2. Comparison of Monte Carlo measured and simulated background gamma-spectra ten months after installation of the Obelix HPGe detector in the Modane underground laboratory (counting time was 34 days).

Table 2
Production rates of cosmogenic radionuclides in germanium.

Radionuclide	Half-life	Gamma-ray energy [keV]	CONUS [atom kg^{-1} day^{-1}]	ACTIVIA1[a]	Other calculations[b]
^{3}H	12.3 yr	18.6[c]	50	30	48.3 [9]; 34.1/52.4 [47]
^{54}Mn	312.3 d	834.84	5	3	5.2 [8]; 2.7 [33]; 2.5/2.8 [47]
^{65}Zn	244.3 d	1124.5	60	20	63 [8]; 29 [33]; 19.5/44.2 [47]
^{57}Co	271.8 d	136.47	7	6	7.6 [8]; 6.7 [33]; 6.4/8.9 [47]
^{60}Co	5.27 yr	1332.5	4	3	3.9 [8]; 2.8 [33]; 2.6/4.1 [47]
^{68}Ge	270.93 d	1077.40	66	10	60 [8]; 45.8 [33]; 10.2/24.6 [47]

[a] ACTIVIA1 results obtained in the present work with the default input neutron spectrum.

[b] [8] MENDL+YIELDX package with neutrons only; [9] GEANT4; [33] ACTIVIA1; [47] ACTIVIA1/ACTIVIA2 (ACTIVIA2 results with GEANT4 input spectrum).

[c] Pure β^-- emitter with maximum energy of β-particles of 18.6 keV.

3.2.2. Al and Si in the cryostat and detector holder

Aluminum is frequently used for cryostats of HPGe detectors. Although its purity is usually very high (99.999% or better), its radiopurity sometimes is problematic because of presence of uranium and thorium decay products [12]. The production rates were calculated for two radionuclides of highest interest, ^{26}Al and ^{22}Na.

The main target material for the *in situ* production of ^{26}Al is aluminum present in raw bauxite (reaction ^{27}Al(n, 2n)^{26}Al). Bauxite mining is usually carried out in surface mines with negligible soil overburden, where bauxite layers are only a few meters thick [23]. Following detail discussions in [50], the average depth of bauxite where ^{26}Al was produced was taken as 2 m. As the bauxite deposits are at least several million years old, there was enough time for saturated production of ^{26}Al by cosmic rays. Aluminum is refined from bauxite, and after its

additional cleaning there are only tracers of other elements present in high-purity aluminum used in construction of HPGe detectors.

Although ^{22}Na was also produced in the bauxite, it is expected that during the refining process (and further aluminum cleaning) it was removed from aluminum. The main target material for ^{22}Na production is, therefore, the Al-4%Si alloy used in the cryostat and the detector holder. The total ^{22}Na production in the Al-4%Si alloy at sea level is then given as

$$^{22}\text{Na} = 62.4[\text{Al}] + 41.7[\text{Si}] = 169 \text{ atom/kg/day},$$

where the target-element concentrations are given in weight fractions.

A comparison of calculated production rates for ^{22}Na and ^{26}Al (Table 3) shows that a reasonable agreement with Majorovits et al. [50] GEANT4 calculations was obtained. Although the ACTIVIA1 predicts ^{22}Na and ^{26}Al production rates by about a factor of 3 smaller compared to CONUS and GEANT4 [50], it is closer to experimental data (unfortunately the uncertainties of measurements are too large).

As ^{22}Na and ^{26}Al activities of the Al+4%Si alloy used in the Obelix HPGe detector were measured [51], we may compare these results with calculations. The radionuclide activity in the material after its exposure to cosmic rays can be calculated as

$$A = P(1 - e^{-\lambda t}),$$

where P is the production rate, λ is the decay constant, and t is the activation time. Equilibrium between the production rate and decay of a radionuclide will be reached after several half-lives. This is a few million years in the case of ^{26}Al, and about ten years in the case of ^{22}Na. As the exposure time of bauxite to cosmic rays was at least for several million years, we can expect a saturated ^{26}Al activity in the Al+4%Si alloy. For the ^{22}Na activity because of lack of information about the history of the sample (e.g. production, air transport) it may happen that the activation time would be shorter than ten years.

The calculated ^{26}Al activity in aluminum (activation at the average depth of 2 m during several million years) and the measured one in the Al+4%Si alloy is in agreement within uncertainties (Table 3). In the case of the ^{22}Na production in the Al+4%Si alloy, and its comparison with the experiment, we see that the activation time was probably shorter than one half-life (2.6 yr).

3.2.3. Cu in cold finger

Copper is very often used for production of cold fingers of HPGe detectors, as well as an internal detector shielding. Several papers have already been dealing with calculation of production rates of cosmogenic radionuclides in copper [8,9,33,46,47,52]. Table 4 lists the most relevant cosmogenic radionuclides, ^{46}Sc, ^{54}Mn, ^{59}Fe, ^{56}Co, ^{57}Co, ^{58}Co and ^{60}Co, produced in copper. A reasonable agreement between the CONUS and ACTIVIA1 results was obtained, except for ^{60}Co, where the CONUS value is by about a factor of 3 higher, even by 30% higher than the ACTIVIA2 value. The saturation activities of investigated radionuclides calculated using the CONUS and ACTIVIA1 agree well with experimental values [53], except for the CONUS ^{60}Co value, which is again by about a factor of 3 higher.

3.2.4. Other target materials

Except twelve cosmogenic radionuclides produced in four target materials (Ge, Al, Si and Cu) discussed so far, several other radionuclides produced in detector construction and shielding materials could be of interest [52]. For HPGe spectrometers they are mostly found in their shields, such as iron (stainless steel), where dominant contributions are expected from ^{7}Be (a spallation product decaying by electron capture (EC) with half-life of 53.22 days and emission of gamma-rays with energy of 477.6 keV) with saturation activity of 4.6 mBq/kg), and from ^{54}Mn with saturation activity of 2.7 mBq/kg [54]. Production rates of cobalt radioisotopes were comparable with those calculated for copper.

In the case of lead shielding, two long-lived cosmogenic radionuclides were identified [55]:

– ^{202}Pb (EC-decay with $T_{1/2} = 52.5$ kyr to short-lived ^{202}Tl, which emits gamma-rays of 439.5 keV) with production rate of about 100 atom kg^{-1} day^{-1}, and
– ^{194}Hg (EC-decay with $T_{1/2} = 444$ yr to short-lived ^{194}Au, which emits gamma-rays of 328.5 keV) with production rate of about 10 atom kg^{-1} day^{-1}.

The expected saturation activities would be from 0.1 mBq/kg (for ^{194}Hg) to 1 mBq/kg (for ^{202}Pb), i.e. much lower than contributions from radio-contamination of lead by radiogenic radionuclides [18]. Even higher cosmogenic activities could be expected, e.g. about 3 mBq/kg of ^{125}I in NaI(Tl) used for dark matter searchers [56], or of ^{127}Xe in xenon detectors [9].

3.3. Monte Carlo simulation of the cosmogenic background gamma-spectrum

Production rates of cosmogenic radionuclides, calculated using the CONUS code (Tables 2–4), were used as inputs for the GEANT4 simulation of the cosmogenic background gamma-spectrum (Fig. 3). The main cosmogenic products from the germanium target (Table 2) are ^{68}Ge+^{68}Ga, ^{65}Zn and ^{3}H. Although the production rate of the ^{68}Ge+ ^{68}Ga pair is the highest, and the half-life is suitable (270.93 d), its decay contribution is mainly in the annihilation peak and the continuum (Fig. 3), as the intensity of the characteristic peak at 1077.40 keV is very low (3.3%). However, it can be identified in the experimental as well as in simulated gamma-spectra (Fig. 2). The ^{65}Zn is the main contributor to the background from the germanium target, comparable with the annihilation peak and the ^{57}Co peak (its main source is, however, copper). Although the tritium production is relatively high, its importance as a pure beta-ray emitter in gamma-spectrometry is low, except in Ge detectors looking for DM particles. Production of ^{54}Mn in germanium is low, its main target is copper.

There are only two important cosmogenic products from the Al+ 4%Si target, ^{26}Al and ^{22}Na (Table 3), with good visibility in the gamma-spectra (Figs. 2 and 3). The experimental and CONUS simulated ^{22}Na counting rates are in a reasonable agreement for the activation time of about two years. The ^{26}Al because of its long half-life (0.717 Myr) is the dominant long-term contributor to the detector background.

The calculated production rates of cosmogenic radionuclides in the copper target (^{46}Sc, ^{54}Mn, ^{59}Fe, ^{56}Co, ^{57}Co, ^{58}Co and ^{60}Co) are within experimental uncertainties with the measured ones (Table 3). Although the ^{58}Co production is high, its half-life (70.85 d) is too short to be visible in the simulated gamma-spectra. Similarly, ^{46}Sc, ^{59}Fe and ^{56}Co have too low production rates and short half-lives to be visible in the gamma-spectra (Fig. 2, 3). The ^{54}Mn peak is well visible due to its production both in copper and germanium. Therefore, the main contributor to the cosmogenic background from copper are cobalt radionuclides.

The obtained results have some implications on a choice of construction materials for deep underground experiments [57]. Generally, for all materials the cosmic-ray activation times should be minimized and the air transport should be avoided. For long-lived radionuclides, such as ^{26}Al, only aluminum refined from deep bauxite mining should be used in order to avoid *in situ* production by cosmic rays.

4. Conclusions

Production of cosmogenic radionuclides in construction parts of the Obelix HPGe detector was studied using Monte Carlo simulation packages GEANT4, CONUS and ACTIVIA. The simulation results were compared with experimental background measurements carried out in the LSM Modane underground laboratory. Production rates of several cosmogenic radionuclides induced by interactions of nucleons with germanium (^{3}H, ^{54}Mn, ^{57}Co, ^{65}Zn, ^{68}Ge, ^{60}Co), copper (^{46}Sc, ^{54}Mn, ^{59}Fe, ^{56}Co, ^{57}Co, ^{58}Co, ^{60}Co) and with aluminum and the Al+Si alloy

Table 3
Production rates of ^{22}Na (in Al+4%Si alloy) and ^{26}Al (in aluminum).

Radionuclide	Half-life (yr)	Gamma-ray energy [keV]	CONUS [atom kg^{-1} day^{-1}]	ACTIVIA1	GEANT4 [50]	Calculated activity [μBq kg^{-1}]	Measured activity [51]
^{22}Na	2.60	1274.5	170[a]	40[a]	150[a]	460[a] 230[b] (175[c]) 1970[a] 980[b] (750[c]) 1770[a] [50] 870[b] [50]	400 ± 200[d]
^{26}Al	7.17 · 10^5	1808.6	530[a] (80[e])	160[a]	390[a] (63[e])	300[e] 930[e] 730[e] [50]	380^{+190}_{-140}

[a] Saturation activity at sea level.
[b] At sea level, activation time 1 T$_{1/2}$ (2.6 yr).
[c] After 1 yr of cooling down.
[d] Estimated from the spectrum in Fig. 2.
[e] Saturation activity at an average bauxite depth of 2 m.

Table 4
Production of cosmogenic radionuclides in copper (ACTIVIA1 — present results; ACTIVIA1/ACTIVIA2 — results from [9]).

Radionuclide	Half-life	CONUS [atom kg^{-1} day^{-1}]	ACTIVIA1; ACTIVIA1/ ACTIVIA2 [9]	Saturation activity (CONUS/ACTIVIA1/ ACTIVIA2) [μBq kg^{-1}]	Measured activity [53]
^{46}Sc	83.787 d	3	3; 3.1/4.1	35/36.2/47.4	27^{+11}_{-9}
^{54}Mn	312.19 d	14	16; 14.3/30.0	160/166/347	154^{+35}_{-34}
^{59}Fe	44.494 d	5	2; 4.2/10.5	58/49.1/121	47^{+16}_{-14}
^{56}Co	77.236 d	10	9; 8.7/20.1	116/101/233	108^{+14}_{-16}
^{57}Co	271.82 d	50	34; 32.4/77.5	580/375/896	519^{+100}_{-95}
^{58}Co	70.85 d	76	60; 56.6/138.1	880/655/1598	798^{+62}_{-58}
^{60}Co	5.27 yr	92	29; 26.3/66.1	1060/296/744	340^{+82}_{-68}
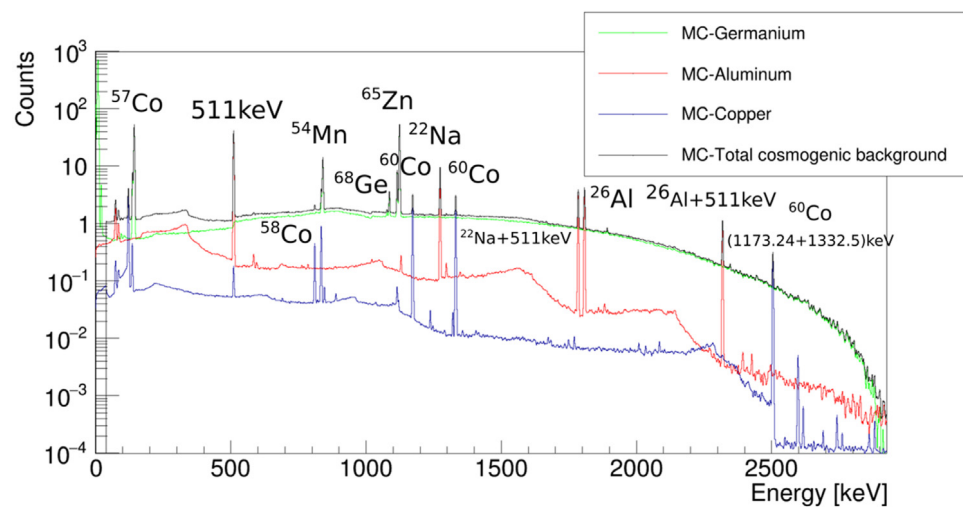
Fig. 3. GEANT4 simulation of background gamma-spectrum with cosmogenic radionuclide contributions.

(^{22}Na, ^{26}Al) were calculated. A reasonable agreement (within statistical uncertainties) was obtained between the calculated and measured results. The contribution of cosmogenic radionuclides to the total detector background of the Obelix detector decreased from 39% (after 10 months of cooling down) to 14% (after three years of cooling down).

While the short-lived cosmogenic radionuclides contributed to the detector background mainly during the first year of its operation in the underground laboratory, the long-lived ^{26}Al will be present in the detector background forever. Therefore, to minimize the detector background, cosmic-ray activation times of all construction materials should be minimized, and the air transport should be avoided. For long-lived ^{26}Al, only aluminum refined from deep bauxite mining should

be used for construction of ultra-low background detectors in order to avoid its production by cosmic rays.

Declaration of competing interest

detector operating in the Modane underground laboratory. This study was supported by the Slovak Research and Development Agency under the contracts APVV-15-0576 and APVV-15-0636, and by the Slovak Science Granting Agency under the contract VEGA 1/0891/17.

References

[1] R. Arnold, et al., Measurement of the double-beta decay half-life and search for the neutrinoless double-beta decay of 48Ca with the NEMO-3 detector, Phys. Rev. D 93 (2016) 112008.

[2] N. Abqrall, et al., The large enriched germanium experiment for neutrinoless double beta decay (LEGEND), AIP Conf. Proc. 1894 (2017) 020027, http://dx.doi.org/10.1063/1.5007652.

[3] G. Angloher, et al., Results on MeV-scale dark matter from a gram-scale cryogenic calorimeter operated above ground: CRESST Collaboration, Eur. Phys. J. C 77 (2017) 637.

[4] E. Armengaud, et al., Constraints on low-mass WIMPs from the EDELWEISS-III dark matter search, J. Cosmol. Astropart. Phys. 05 (2016) 19.

[5] G. Heusser, Low-radioactivity background techniques, Ann. Rev. Nucl. Part. Sci. 45 (1995) 543–590.

[6] P.P. Povinec, Background constrains of the SuperNEMO experiment for neutrinoless double beta-decay searches, Nucl. Instrum. Methods A 845 (2017) 398–403.

[7] V. Tomasello, M. Robinson, V.A. Kudryavtsev, Radioactive background in a cryogenic dark matter experiment, Astropart. Phys. 34 (2010) 70–79.

[8] S. Cebrián, et al., Cosmogenic activation in germanium and copper for rare event searches, Astropart. Phys. 33 (2010) 316–329.

[9] C. Zhang, et al., Cosmogenic activation of materials used in rare event search experiments, Astropart. Phys. 84 (2016) 62–69.

[10] G. Heusser, M. Laubenstein, H. Neder, Low-level germanium gamma-ray spectrometry at the μBq/kg level and future developments towards higher sensitivity, in: P.P. Povinec, J.A. Sanchez-Cabeza (Eds.), Radionuclides in the Environment, Elsevier, Amsterdam, 2006, pp. 495–510.

[11] P.P. Povinec, et al., Ultra-sensitive radioanalytical technologies for underground physics experiments, J. Radioanal. Nucl. Chem. 318 (2018) 677–684, http://dx.doi.org/10.1007/s10967-018-6105-9.

[12] P.P. Povinec, et al., New isotope technologies in environmental physics, Acta Phys. Slovaca 58 (2008) 1–154.

[13] P.P. Povinec, J.-F. Comanducci, I. Levy-Palomo, IAEA-MEL's underground counting laboratory in Monaco – background characteristics of HPGe detectors with anti- cosmic shielding, Appl. Radiat. Isot. 61 (2004) 85–93.

[14] P.P. Povinec, P. Vojtyla, J.F. Comanducci, Monte Carlo simulation of background characteristics of gamma-ray spectrometers: a comparison with experiment, Radioactiv. Environm 11 (2008) 163–208.

[15] M. Laubenstein, Screening of materials with high purity germanium detectors at the Laboratori Nazionali del Gran Sasso, Internat. J. Modern Phys. A 32 (2017) 1743002.

[16] R. Breier, M. Laubenstein, P.P. Povinec, Monte Carlo simulation of background characteristics of a HPGe detector operating underground in the Gran Sasso National Laboratory, Appl. Radiat. Isot. 126 (2017) 188–190.

[17] V. Brudanin, et al., Obelix, a new low-background HPGe at Modane Underground Laboratory, AIP Conf. Proc. 1672 (2015) 130002.

[18] R. Breier, et al., Environmental radionuclides as contaminants of HPGe gamma-ray spectrometers: Monte Carlo simulations for Modane underground laboratory, J. Environ. Radioact. 190–191 (2018) 134–140.

[19] A.H. Abdelhameed, et al., Geant4-based electromagnetic background model for the CRESST dark matter experiment, Eur. Phys. J. C 79 (2019) 881.

[20] B. Schmidt, et al., Muon-induced background in the EDELWEISS dark matter search, Astropart. Phys. 44 (2013) 28–39, http://dx.doi.org/10.1016/j.astropartphys.2013.01.014.

[21] K. Eitel, Measurements of neutron fluxes in the LSM underground laboratory, J. Phys. Conf. Ser. 375 (2012) http://dx.doi.org/10.1088/1742-6596/375/1/012016.

[22] G. Bárdossy, Karst Bauxites: Bauxite Deposits on Carbonate Rocks, Elsevier, Amsterdam, 1982, p. 441.

[23] G. Taylor, et al., Nature of the Weipa Bauxite deposit, northern Australia, Aust. J. Earth Sci. 55 (S1) (2008) S45–S70, http://dx.doi.org/10.1080/08120090802438241.

[24] V.B. Brudanin, et al., The low-background HPGe γ-spectrometer OBELIX for the investigation of the double beta decay to excited states, IOSR J. Appl. Phys. 9 (2017) 22–29.

[25] P. Loaiza, et al., Obelix, a new low-background HPGe at Modane underground laboratory, AIP Conf. Proc. 1672 (1) (2015) 130002–1.

[26] R. Breier, P.P. Povinec, Simulation of background characteristics of low-level gamma-ray spectrometers using Monte Carlo method, Appl. Radiat. Isot. 68 (2009) 1231–1235.

[27] R. Breier, Y. Hamajima, P.P. Povinec, Simulations of background characteristics of HPGe detectors operating in shallow underground using the Monte Carlo method, J. Radioan. Nucl. Chem. 307 (2016) 1957–1960.

[28] S. Agostinelli, et al., GEANT4 - A simulation toolkit, Nucl. Instrum. Methods Phys. Res. A 506 (2003) 250–303.

[29] J. Allison, et al., Recent developments in Geant4, Nucl. Instrum. Methods Phys. Res. A 835 (2016) 186–225.

[30] J. Masarik, R.C. Reedy, Effects of bulk composition on nuclide production processes in meteorites, Geochim. Cosmochim. Acta 58 (1994) 5307–5317.

[31] J. Masarik, R.C. Reedy, Terrestrial cosmogenic-nuclide production systematics calculated from numerical simulations, Earth Planet. Sci. Lett. 136 (1995) 381–395.

[32] J. Masarik, J. Beer, Simulation of particle fluxes and cosmogenic nuclide production in the Earth's atmosphere, J. Geophys. Res. 104 (D10) (1999) 12099.

[33] J.J. Back, A. Ramachers, ACTIVIA: Calculation of isotope production cross-sections and yields, Nucl. Instrum. Methods Phys. Res. A 586 (2008) 286–294.

[34] J. Tuli, Evaluated Nuclear Structure Data File, BNL-NCS-51655-Rev87, 1987.

[35] J.F. Briesmeister, MCNPTM – a General Monte Carlo N-Particle Transport Code, Los Alamos National Laboratory, 2000, p. 790.

[36] A. Santamarina, et al., The JEFF-3.1.1 Nuclear DataLibrary, OECD0NEA JEFF Report 22, 2009.

[37] M.B. Chadwick, et al., Nucl. Data Sheets 107 (2006) 2931.

[38] A.J. Koning, S. Hilaire, M.C. Duijvestijn, TALYS-1.0, in: Proc. Intern. Conf. Nuclear Data for Science and Technology, EDP Sciences, 2008, pp. 211–214.

[39] Rochman A. J. Koning, Evaluation and adjustment of the neutron-induced reactions of ^{63,65}Cu, Nucl. Sci. Eng. 170 (2012) 265–279.

[40] A.J. Kantor, K.S.W. Champion, A.E. Cole, Standard and reference atmosphere, in: Handbook of Geophysics and the Space Environment, Air Force Geophys. Lab. U.S. Air Force, 1985.

[41] J.A. Simpson, Elemental and isotopic composition of galactic cosmic rays, Ann. Rev. Nucl. Part S 33 (1983) 323–382.

[42] G. Castagnoli, D. Lal, Solar modulation effects in terrestrial production of carbon-14, Radiocarbon 22 (1980) 133–158.

[43] K. Nishiizumi, et al., Depth profile of ^{41}Ca in an Apollo 15 drill core and the low-energy neutron flux in the Moon, Earth Planet. Sci. Lett. 148 (1997) 545–552.

[44] M. Agostini, et al., The GERDA experiment for the search of $0\nu\beta\beta$ decay in ^{76}Ge, Eur. Phys. J. C 73 (2013) 2330.

[45] W. Xu, et al., The majorana demonstrator: A search for neutrinoless double-beta decay of $?^{76}$ge, J. Phys. Conf. Ser. 606 (2015) 012004.

[46] S. Cebrián, et al., Cosmogenic activation in germanium double beta decay experiments, J. Phys. Conf. Ser. 39 (2006) 344–346.

[47] W.Z. Wei, D.M. Mei, C. Zhang, Cosmogenic activation of germanium used for tonne-scale rare event search experiments, Astropart. Phys. 96 (2017) 24–31.

[48] J. Su, et al., A background simulation method for cosmogenic nuclides inside HPGe detectors for rare event experiments, Nucl. Instrum. Methods Phys. Res. A 763 (2014) 364–371.

[49] P. Loaiza, et al., Low background germanium planar detector for gamma-ray spectrometry, Nucl. Instrum. Methods Phys. Res. A 634 (2011) 64–70.

[50] B. Majorovits, et al., Aluminum as a source of background in low background experiments, Nucl. Instrum. Methods Phys. Res. A 647 (2011) 39–45.

[51] V.B. Brudanin, et al., Development of the ultra-low background HPGe spectrometer OBELIX at modane underground laboratory, J. Instrum. 12 (2017) P02004, http://dx.doi.org/10.1088/1748-0221/12/02/P02004.

[52] S. Cebrián, Cosmogenic activation of materials, AIP Conf. Proc. 1549 (2013) 136–141.

[53] L. Baudis, et al., Cosmogenic activation of xenon and copper, Eur. Phys. J. C 75 (2015) 10485, http://dx.doi.org/10.1140/epjc/s10052-015-3711-3.

[54] M. Laubenstein, G. Heusser, Cosmogenic radionuclides in metals as indicator for sea level exposure history, Appl. Radiat. Isot. 67 (2009) 750–754, http://dx.doi.org/10.1016/j.apradiso.2009.01.029.

[55] V.E. Giuseppe, et al., Fast-neutron activation of long-lived nuclides in natural Pb, Astropart. Phys. 64 (2015) 34–40.

[56] J. Amaré, et al., Cosmogenic radionuclide production in NaI(Tl) crystals, J. Cosmol. Astropart. Phys. 02 (2015) 046.

[57] M. Laubenstein, et al., Underground measurements of radioactivity, Appl. Radiat. Isot. 61 (2004) 167–172.

Search for the double-beta decay of ^{82}Se to the excited states of ^{82}Kr with NEMO-3

R. Arnold[a], C. Augier[b], A.S. Barabash[c], A. Basharina-Freshville[d], S. Blondel[b], S. Blot[e], M. Bongrand[b], D. Boursette[b], R. Breier[t], V. Brudanin[f,g], J. Busto[h], A.J. Caffrey[i], S. Calvez[b], M. Cascella[b], C. Cerna[j], J. P. Cesar[k], A. Chapon[l], E. Chauveau[j], A. Chopra[d], L. Dawson[d], D. Duchesneau[m], D. Durand[l], V. Egorov[f,1], G. Eurin[b,d], J.J. Evans[e], L. Fajt[n], D. Filosofov[f], R. Flack[d], X. Garrido[b], C. Girard-Carillo[b], H. Gómez[b], B. Guillon[l], P. Guzowski[e], R. Hodák[n], A. Huber[j], P. Hubert[j], C. Hugon[j], S. Jullian[b], A. Klimenko[f], O. Kochetov[f], S.I. Konovalov[c], V. Kovalenko[f], D. Lalanne[b], K. Lang[k], Y. Lemière[l], T. Le Noblet[m], Z. Liptak[k], X. R. Liu[d], P. Loaiza[b], G. Lutter[j], M. Macko[n], C. Macolino[b], F. Mamedov[n], C. Marquet[j], F. Mauger[l], A. Minotti[m], B. Morgan[o], J. Mott[d,p], I. Nemchenok[f], M. Nomachi[q], F. Nova[k], F. Nowacki[a], H. Ohsumi[r], G. Oliviéro[l], R.B. Pahlka[k], V. Palusova[j,t], C. Patrick[d], F. Perrot[j,*], A. Pin[j], F. Piquemal[j,s], P. Povinec[t], P. Přidal[n], Y.A. Ramachers[o], A. Remoto[m], J.L. Reyss[u], B. Richards[d], C.L. Riddle[i], E. Rukhadze[n], R. Saakyan[d], R. Salazar[k], X. Sarazin[b], J. Sedgbeer[v], Yu. Shitov[f], L. Simard[b,w], F. Šimkovic[t], A. Smetana[n], K. Smolek[n], A. Smolnikov[f], S. Söldner-Rembold[e], B. Soulé[j,*], I. Štekl[n], J. Suhonen[x], C.S. Sutton[y], G. Szklarz[b], H. Tedjditi[h], J. Thomas[d], V. Timkin[f], S. Torre[d], Vl.I. Tretyak[z], V.I. Tretyak[f], V.I. Umatov[c], I. Vanushin[c], C. Vilela[d], V. Vorobel[aa], D. Waters[d], F. Xie[d], A. Žukauskas[aa], The NEMO-3 collaboration

[a]IPHC, ULP, CNRS/IN2P3, F-67037 Strasbourg, France
[b]LAL, Univ Paris-Sud, CNRS/IN2P3, F-91405 Orsay, France
[c]NRC "Kurchatov Institute" - ITEP, 117218 Moscow, Russia
[d]UCL, London WC1E 6BT, United Kingdom
[e]University of Manchester, Manchester M13 9PL, United Kingdom
[f]JINR, 141980 Dubna, Russia
[g]National Research Nuclear University MEPhI, 115409 Moscow, Russia
[h]Aix Marseille Univ., CNRS,CPPM, Marseille, France
[i]Idaho National Laboratory, Idaho Falls, ID 83415, U.S.A.
[j]CENBG, Université de Bordeaux, CNRS/IN2P3, F-33175 Gradignan, France
[k]University of Texas at Austin, Austin, TX 78712, U.S.A.
[l]LPC Caen, ENSICAEN, Université de Caen, CNRS/IN2P3, F-14050 Caen, France
[m]LAPP, Université de Savoie, CNRS/IN2P3, F-74941 Annecy-le-Vieux, France
[n]Institute of Experimental and Applied Physics, Czech Technical University in Prague, CZ-11000 Prague, Czech Republic
[o]University of Warwick, Coventry CV4 7AL, United Kingdom
[p]Boston University, Boston, MA 02215, U.S.A.
[q]Osaka University, 1-1 Machikaney arna Toyonaka, Osaka 560-0043, Japan
[r]Saga University, Saga 840-8502, Japan
[s]Laboratoire Souterrain de Modane, F-73500 Modane, France
[t]FMFI, Comenius Univ., SK-842 48 Bratislava, Slovakia
[u]LSCE, CNRS, F-91190 Gif-sur-Yvette, France
[v]Imperial College London, London SW7 2AZ, United Kingdom
[w]Institut Universitaire de France, F-75005 Paris, France
[x]Jyväskylä University, FIN-40351 Jyväskylä, Finland
[y]MHC, South Hadley, Massachusetts 01075, U.S.A.
[z]Institute for Nuclear Research, 03028 Kyiv, Ukraine
[aa]Charles University in Prague, Faculty of Mathematics and Physics, CZ-12116 Prague, Czech Republic

1

Abstract

The double-beta decay of ^{82}Se to the 0^+_1 excited state of ^{82}Kr has been studied with the NEMO-3 detector using 0.93 kg of enriched ^{82}Se measured for 4.75 y, corresponding to an exposure of 4.42 kg·y. A dedicated analysis to reconstruct the γ-rays has been performed to search for events in the 2e2γ channel. No evidence of a $2\nu\beta\beta$ decay to the 0^+_1 state has been observed and a limit of $T^{2\nu}_{1/2}(^{82}\text{Se}, 0^+_{gs} \rightarrow 0^+_1) > 1.3 \times 10^{21}$ y at 90% CL has been set. Concerning the $0\nu\beta\beta$ decay to the 0^+_1 state, a limit for this decay has been obtained with $T^{0\nu}_{1/2}(^{82}\text{Se}, 0^+_{gs} \rightarrow 0^+_1) > 2.3 \times 10^{22}$ y at 90% CL, independently from the $2\nu\beta\beta$ decay process. These results are obtained for the first time with a tracko-calo detector, reconstructing every particle in the final state.

Keywords: Double beta decay; Neutrino; ^{82}Se; Excited State

1. Introduction

The search for the neutrinoless double-beta decay ($0\nu\beta\beta$) is of major importance in neutrino and particle physics. Its observation would prove the Majorana nature of the neutrino and would be the first evidence for lepton number violation. Up to now, no evidence of such a process has been found and the best half-life limits are in the 10^{24}-10^{26} y range [1–4]. ^{82}Se is one of the best isotopes to investigate $0\nu\beta\beta$ decay. In particular, its high $Q_{\beta\beta}$-value of 2997.9±0.3 keV [5] lies above the main backgrounds coming from natural radioactivity. There exist also well-known methods of Se isotopic enrichment through centrifugal separation. This is why ^{82}Se is the baseline isotope for past, current or future experiments such as LUCIFER [6], CUPID-0 [7] and SuperNEMO [8]. Several studies have been performed in the past to search for $0\nu\beta\beta$ decay of ^{82}Se to the ground state of ^{82}Kr and recently new limits on the half-life have been obtained with the NEMO-3 (2.5×10^{23} y [9]) and CUPID-0 experiments (3.5×10^{24} y [10]).

The double-beta decay with emission of two neutrinos ($2\nu\beta\beta$) is a second order electroweak process in the Standard Model. It allows the experimental determination of the Nuclear Matrix Elements (NME) for such processes and provides a robust test for the different nuclear models. It could constrain the quenching factor of the axial-vector coupling constant g_A and give the possibility to improve the quality of NME calculations for $0\nu\beta\beta$ decay [11–14]. This process has been observed for 11 double-beta isotopes with a range of measured half-lives between 10^{18}-10^{24} y [15, 16]. For ^{82}Se, several experiments have measured the $2\nu\beta\beta$ decay to the ground state with the most precise half-life value to date of $9.39 \pm 0.17(\text{stat}) \pm 0.58(\text{syst}) \times 10^{19}$ y measured with the NEMO-3 experiment [9].

The search for $\beta\beta$ decay to excited states is also an interesting way to study such processes. Indeed, these decays have a very clear-cut signature using the 2e1γ channel (to

---

*Corresponding authors

Email addresses: fperrot@cenbg.in2p3.fr (F. Perrot), soule@cenbg.in2p3.fr (B. Soulé)

[1]Deceased

the 2^+_1 state) or the $2e2\gamma$ channel (to the 0^+_1 or 2^+_2 state) which can dramatically reduce the number of background events. The disadvantages are a lower $Q_{\beta\beta}$ available energy for electrons which suppresses the probability of the decay and a lower detection efficiency for electrons and γ-rays. Nevertheless, the decay to excited states is of importance to test the nuclear matrix elements. A detailed analysis for $2\nu\beta\beta$ decay of ^{100}Mo and ^{150}Nd to the excited 0^+_1 state of ^{100}Ru and ^{150}Sm, respectively, showed that corresponding NME are only suppressed by $\sim 30\%$ when compared with the NME to ground state transition [17–23].

Up to now, the $2\nu\beta\beta$ decay to excited states has only been observed for two isotopes: ^{100}Mo and ^{150}Nd with typical half-lives of 10^{20}-10^{21} y [24]. It is important to note that this decay has been observed only to the 0^+_1 excited state (with the emission of two γ-rays) which is favoured compared to the decay to the 2^+_1 or 2^+_2 excited states. These measurements have been performed using both High Purity Germanium (HPGe) detectors by measuring only the γ-rays in the cascade [18, 21, 22, 25–29] and "tracker-calorimeter" detectors such as NEMO-3 able to measure the energies of both electrons and γ-rays [19, 30]. For ^{82}Se, there is up to now no evidence for such a decay. Stringent limits have been obtained by the LUCIFER collaboration for the $(2\nu+0\nu)\beta\beta$ decay to various excited states of ^{82}Kr using a HPGe detector [31]. Nevertheless, this technique using only γ-rays does not allow to distinguish between $2\nu\beta\beta$ and $0\nu\beta\beta$. More recently, more stringent limits have been set by the CUPID-0 collaboration for the $0\nu\beta\beta$ decay to various excited states of ^{82}Kr using ZnSe scintillating bolometers [32].

In this work, we will present a detailed study of the ^{82}Se $2\nu\beta\beta$ and $0\nu\beta\beta$ decays to the 0^+_1 excited state of ^{82}Kr, expected to be the most favoured [33, 34], with the full exposure of the NEMO-3 experiment. In this analysis, we have access to the full topology of the decay. It consists of the emission of two electrons sharing 1510.2 keV of energy and accompanied by two γ-rays with energies of 711.2 keV and 776.5 keV respectively, as illustrated in Figure 1. After a presentation of the NEMO-3 detector, the ^{82}Se source foils and the associated backgrounds, we will present a dedicated analysis tool called gamma tracking (GT) developed to reconstruct efficiently the γ-rays in such a decay. Finally, we will present the results of the $2\nu\beta\beta$ and $0\nu\beta\beta$ decays of ^{82}Se to the 0^+_1 excited state of ^{82}Kr with the full NEMO-3 exposure of 4.42 kg·y.

2. NEMO-3 detector, ^{82}Se source foils and associated backgrounds

2.1. NEMO-3 detector

NEMO-3 was a detector installed in the Modane Underground Laboratory (LSM) under 4800 m water-equivalent in order to be protected against cosmic muons. It took data from February 2003 to January 2011. It consisted of a hollow cylinder divided into 20 sectors hosting thin source foils from 7 different enriched isotopes with a typical thickness of approximately 50 mg/cm^2 (as shown in Figure 2). The main isotope to search for $0\nu\beta\beta$ decay was ^{100}Mo with a total mass of 6.914 kg. The second isotope of interest was ^{82}Se with a mass of 0.932 kg shared in 3 sectors. The five other isotopes studied were by decreasing order of mass: ^{130}Te (0.454 kg),^{116}Cd (0.405 kg), ^{150}Nd (36.55 g), ^{96}Zr (9.43 g), and ^{48}Ca (6.99 g) (see [1, 35] for more details).

The source foils were hung at the center of a wire chamber composed of 6180 cells operating in Geiger mode. The gas was a mixture composed of 94.85% helium, 4%

3
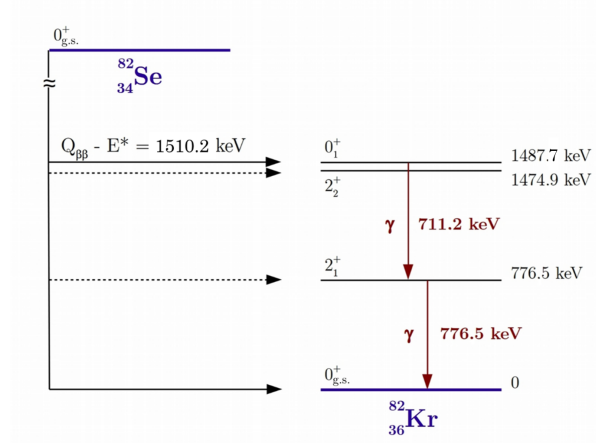
Figure 1: Decay scheme of the ^{82}Se $\beta\beta$ decay to the 0_1^+ excited state with the emission of two electrons sharing 1510.2 keV and two prompt γ-rays with energies of 711.2 and 776.5 keV [36].

ethanol, 1% argon and 0.15% of water vapour. These cells were placed inside a 25 G magnetic field produced by a solenoid surrounding the detector. Charged particles thus had a curved trajectory when crossing the tracking chamber, which allowed the identification of a negative curvature for 95% of electrons at 1 MeV. The minimal distance traveled by a particle crossing the tracker is $\sim$1.1 m, which corresponds to a typical minimal time of flight of 3 ns. The resolution of the tracker was 0.5 mm transverse to the wires and 8 mm in the vertical direction for 1 MeV electrons.

A calorimeter enclosed the wire chamber. It was made from 1940 plastic scintillator blocks, each one with a typical size of 20 x 20 x 10 cm^3 and coupled to a low background photomultiplier (PMT) through a light guide. The calorimeter measured the kinetic energy of the particles and the time difference between two distant hits could be recorded. The blocks had an energy resolution of $6 - 7\%/\sqrt{\text{E(MeV)}}$ and a time resolution of 250 ps (σ at 1 MeV).

NEMO-3 was a unique detector as it combined tracking and calorimetry techniques. A charged particle (e$^-$, e$^+$...) was identified when going across and ionizing the wire chamber gas. Its track was associated to an energy deposit in a calorimeter block neighbouring the last fired Geiger cell. γ-rays were identified when energy was deposited in a calorimeter block but no track was associated. Alpha particles were identified as straight, short tracks as they could not travel more than $\sim$ 40 cm in the tracker due to their high ionisation energy loss.

In order to run in low background conditions, the NEMO-3 detector had to be protected from natural radioactivity. To do so, a passive shielding of 19 cm iron was surrounding the detector in order to stop external γ-rays. In addition, borated water, paraffin and wood were also used to moderate and absorb the environmental neutrons. For a more detailed description of the NEMO-3 detector, see [35].

4
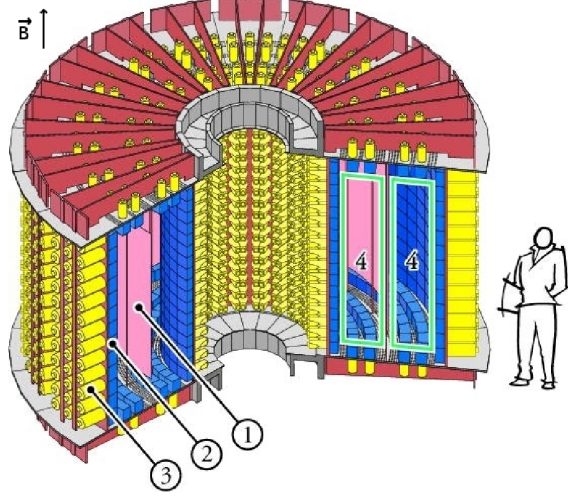
Figure 2: Cross-sectional view of the NEMO-3 detector. The detector consists of source foils (1), scintillators (2), photomultipliers (3) and a wire chamber (4).

2.2. ^{82}Se source

Two different batches of ^{82}Se source were used (referred to as ^{82}Se(I) and ^{82}Se(II)). Those batches had an enrichment factor of $97.02 \pm 0.05\%$ and $96.82 \pm 0.05\%$ respectively. To produce source foils, the enriched ^{82}Se powder was mixed with polyvinyl alcohol (PVA) glue and deposited between $\sim$23 μm thick Mylar foils, producing composite source foils. The total mass of the ^{82}Se isotope in NEMO-3 was 932.4 ± 5.0 g. An analysis of these ^{82}Se foils was conducted in order to search for $2\nu\beta\beta$ and $0\nu\beta\beta$ decays to ground state and is detailed in [9].

2.3. Backgrounds

With its powerful topology reconstruction ability, the NEMO-3 detector was able to identify $2e2\gamma$ events that were selected for $\beta\beta$ decay to excited states. However, some background isotopes could also produce this type of event. Among them, ^{214}Bi and ^{208}Tl decays were the main sources of background as the produced particles could carry similar energies as the β and γ particles from double beta decays to excited states. These two isotopes are β^- emitters from the ^{238}U and ^{232}Th radioactive decay chains, respectively, with Q-values of 3.27 and 4.99 MeV.

The main background contribution came from contamination in the source foils introduced during isotope production and residual contamination after isotope purification or during the foil production. This is described as *internal* contamination. In this case, those β emitting isotopes could produce two electrons coming from the same vertex via β-decay with internal conversion, β-decay followed by Møller scattering or β-decay to an excited state with a Compton scattering of the emitted photon. From these mechanisms, additional γ-rays could be produced by bremsstrahlung or from a decay to an excited state as presented in Figure 3. Prior to their installation, the activity of ^{82}Se foils in ^{214}Bi and ^{208}Tl had been measured by low background gamma spectrometry using HPGe

detectors. These small contaminations had been also measured and cross-checked by the NEMO-3 detector itself thanks to its capability to measure own background. In NEMO-3, the ^{214}Bi contamination of the foils could be studied by looking for the so called BiPo effect using ^{214}Bi and ^{214}Po sequential decay events. The β-decay of ^{214}Bi is followed by the α-decay of ^{214}Po with a half-life of 164.3 μs. The analysis channel used to study such events was the $1e1\alpha(n)\gamma$ channel. ^{208}Tl decays exclusively to excited states and emits mostly 2 or 3 γ-rays (99.9%). Its contamination was thus measured through the $1e2\gamma$ channel with a high γ-rays efficiency (about 50% at 1 MeV). Results and comparison of the ^{214}Bi and ^{208}Tl activities for ^{82}Se source foils using HPGe and NEMO-3 data are presented in Table 1 (including some other minor background isotopes [9]).

Finally, $2\nu\beta\beta$ decay to the ground state was also considered as a background source for $2\nu\beta\beta$ decay to excited states. When two electrons were produced, two extra γ-rays could be emitted via bremsstrahlung. A $2e2\gamma$ event was thus detected while excited states were not involved.

(a) Møller scattering   (b) Internal conversion   (c) Compton scattering
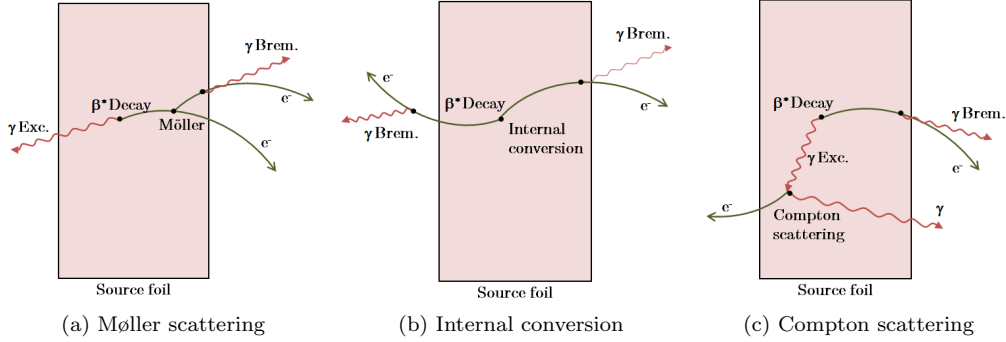
Figure 3: Mechanisms producing $2e2\gamma$ events from internal contamination of β emitters inside the source foils. β-decay to excited state followed by Møller scattering and bremsstrahlung (3(a)), β-decay to excited state with internal conversion and double bremsstrahlung (3(b)), β-decay to excited state followed by Compton scattering and bremsstrahlung (3(c)).

Isotope	NEMO-3 (mBq/kg)	HPGe (mBq/kg)
^{214}Bi	1.62 ± 0.05	1.2 ± 0.5
^{208}Tl	0.39 ± 0.01	0.40 ± 0.13
^{234m}Pa	16.7 ± 0.1	< 18
^{40}K	58.9 ± 0.2	55 ± 5

Table 1: Results of the contamination measured in the ^{82}Se source foils by using independently NEMO-3 and HPGe data. All uncertainties are of statistical origin only, given at the 1σ level. The limit shown is at the 2σ level. The activities of ^{214}Bi and ^{208}Tl are derived from this independent analysis and are consistent with the ones already published in [9].

In addition to the *internal* contamination of the source foils, radioactivity from other components of the detector can produce background events, leading to γ-rays. These γ-rays then interact with the source foil and two electrons coming from the same vertex

can then be reconstructed if there is either pair production with misreconstruction of the positron track, double Compton scattering or simple Compton scattering followed by Møller scattering of the produced electron. In the case of pair production, there can be annihilation of the positron which produces two photons. Considering that γ-ray interactions are involved in all those mechanisms, they have to be taken into account in the search of the $2\nu\beta\beta$ and $0\nu\beta\beta$ decay to the 0_1^+ excited state, with 2 γ-rays emitted in cascade. The different processes responsible for background production are described in Figure 4. The radioactivity of these external elements was first screened by low background γ-spectrometry. Also, when background isotopes produce a γ-ray, it can interact close to the surface of a calorimeter block and produce an electron. The latter crosses the whole wire chamber including the source foil. The initial γ-ray can also deposit energy in the calorimeter before interacting with the source and producing an electron. The contamination of external elements can thus be measured through two channels : crossing electron or (γ, e) external, i.e. Compton scattering in a scintillator block, producing a γ-ray energy deposit, followed by a Compton scattering in the source foil, emitting an electron detected in another scintillator block. An *external* background model was produced and can be found in [38].

(a) Double Compton scattering   (b) Pair production   (c) Møller diffusion
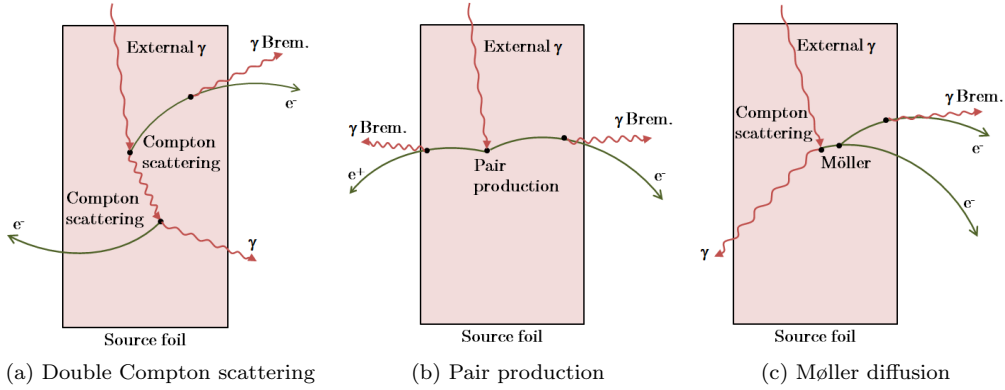
Figure 4: Mechanisms producing $2e2\gamma$ events from external contamination of the NEMO-3 detector emitting a γ-ray interacting inside the source foil. Double Compton scattering of the external γ-ray with bremsstrahlung in 4(a), pair production from the external γ-ray with double bremsstrahlung effects and poor reconstruction of the positron in 4(b), Compton scattering of the external γ-ray followed by a Møller scattering of the electron and a bremsstrahlung in 4(c).

A specific *external* background is the *radon* background. It comes from ^{222}Rn, a gaseous isotope in the ^{238}U chain. ^{222}Rn can be introduced via several mechanisms including emanation from detector materials, diffusion from laboratory air through detector seals or contamination of the wire chamber gas. This is only possible because of its long half-life of 3.82 days. Once inside the detector, mainly positive ions are produced from the radon decays. Because of their charge, they can drift and be deposited on the source foils or tracker wires. There, they decay into ^{214}Bi near the source material. This contamination can then be observed through the $1e1\alpha(n)\gamma$ channel.

For the first 18 months of data-taking, there was a relatively high level of ^{222}Rn inside the detector. To reduce it, an anti-radon tent was built around the detector reducing

the radon level inside the wire chamber volume by a factor ~ 6 [1]. The higher radon activity data-taking period is referred to as Phase 1 and the lower activity period that came after as Phase 2.

Both data and Monte Carlo simulations (MC) of signal and background are processed by the same reconstruction algorithm. The DECAY0 event generator [39] is used for generation of initial kinematics and particles are tracked through a detailed GEANT3 based detector simulation [40].

3. Gamma tracking technique

In most double-beta-decay experiments, a crucial aspect is to precisely measure the energy of the particles. Using the unique combination of tracking and calorimetry, NEMO-3 extracts other observables (angle between two electrons, track curvature, vertex position...) allowing a good discrimination of background and signal events. In addition, one of the most important features is the measurement of the time of flight of the particles inside the detector.

When looking for double-beta decays, selecting events with two electrons from the same vertex is not a strong enough criterion as seen in section 2.3. The time of flight measurement thus allows to reject external events by testing two hypothesis : the event has an *internal* or an *external* origin. This test is made possible in NEMO-3 by the knowledge of the particle track length, energy, time of flight and the energy and time resolution (σ_t) of the calorimeter. It can be conducted for charged particles for which tracks are reconstructed but also for γ-rays coming from the same vertex.

Time of flight for electrons is thus an essential parameter when looking for double-beta decay. The next section will describe its measurement in NEMO-3 before a new method for measuring γ-ray time of flight is presented. The latter is crucial since a more accurate description of events containing γ-rays and a higher sensitivity to these events will improve the efficiency and precision in the search for decays to excited states.

3.1. Time of flight calculation

In order to construct an hypothesis on the time ordering of an event, some energy must be deposited in at least two calorimeter blocks and one particle track or more must be reconstructed inside the wire chamber. This track also has to be associated to one of the calorimeter hits. The other calorimeter hit with no associated track is identified as a γ-ray. Figure 5 illustrates an event sketch in NEMO-3 with an electron (one reconstructed track with one calorimeter hit) and a γ-ray (only a calorimeter hit) coming from the same vertex.

Before making any time of flight calculation for an event, two hypotheses must be considered : *internal* or *external* origin. Theoretical times of flight between the vertex and the calorimeter hit (t^{th}) that should be measured by the calorimeter (for each block hit) are then calculated for both hypotheses. The sum (*external* origin) or difference (*internal* origin) of these theoretical times is compared to the difference between times actually measured by the calorimeter (t^{exp}). If the given hypothesis is favoured, then the difference noted $\triangle t_{hyp}$ must be close to zero, taking into account the time resolution of NEMO-3.

8
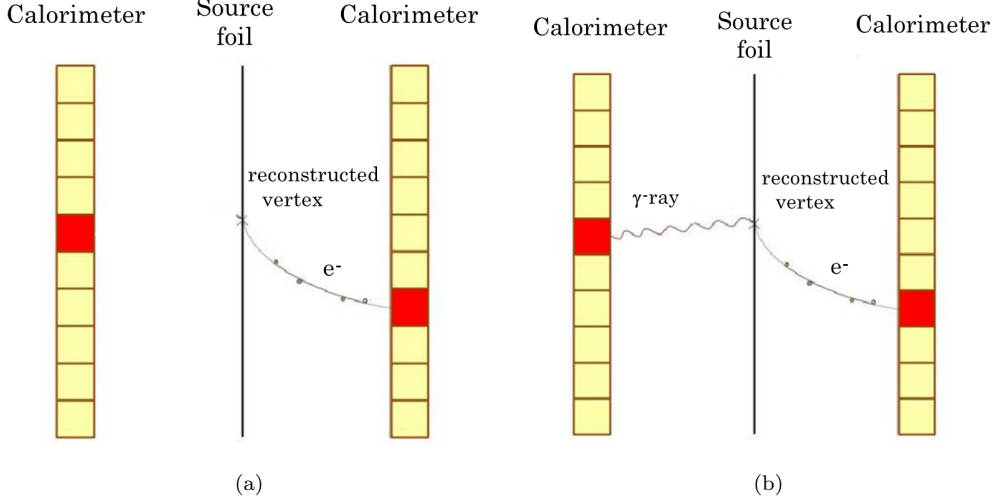
Figure 5: Event sketch with track reconstruction (5(a)) and scintillator association (5(b)). The reconstruction defines a γ-ray as energy deposit in a scintillator without any associated track. It can link it to the vertex in Figure 5(b).

Considering the example presented in Figure 5(b), these differences for both hypotheses are expressed by the following equations :

$$\triangle t_{int} = (t_e^{th} - t_\gamma^{th}) - (t_e^{exp} - t_\gamma^{exp}) \tag{1}$$

$$\triangle t_{ext} = (t_e^{th} + t_\gamma^{th}) - (t_e^{exp} - t_\gamma^{exp}) \tag{2}$$

Nevertheless, the calculation of $\triangle t_{hyp}$ is only a preliminary analysis. A more advanced study is based on the probability of time of flight and needs to take into account the uncertainties on theoretical and measured times. Thus the χ^2 method is used as described by :

$$\chi_{hyp}^2 = \frac{\triangle^2 t_{hyp}}{\sigma_{tot}^2}, \tag{3}$$

where σ_{tot}^2 is the quadratic sum of all uncertainties affecting time measurements or calculations. These are the uncertainties on track lengths (for charged particles), path lenghts (for γ-ray), measured energies (due to calorimeter energy resolution) and times (due to calorimeter time resolution).

When considering *external* or *internal* events, as in section 4, the selections will be based on the chi-squared probabilities for the respective hypotheses.

3.2. Gamma tracking

Another type of time of flight calculation is possible considering only the trajectory of photons. Because of the thickness of NEMO-3 scintillators, γ-rays do not always deposit

all their energy inside a single block. One photon can deposit part of its energy in a calorimeter block after Compton scattering, then hit another one and potentially more. Gamma tracking is an original and powerful analysis tool developed recently [41] in order to take this effect into account and reconstruct the complete trajectory of γ-rays inside the detector, with each step from one scintillator to the next.

When a single γ-ray is produced inside a source foil with one or more charged particles and hits several scintillators, a few PMTs measure energies without associating them to reconstructed tracks. Figure 6(a) describes the approach presented in the previous section, where every unassociated hit is considered as having a different origin. Here, the second unassociated block is neither *internal* nor *external* and the event is excluded when selecting events for the 2e1γ channel. Using gamma tracking, the same event can be properly reconstructed as shown in Figure 6(b) : the second unassociated hit is paired with the first one under the assumption of Compton scattering and the event satisfies the 2e1γ channel conditions.
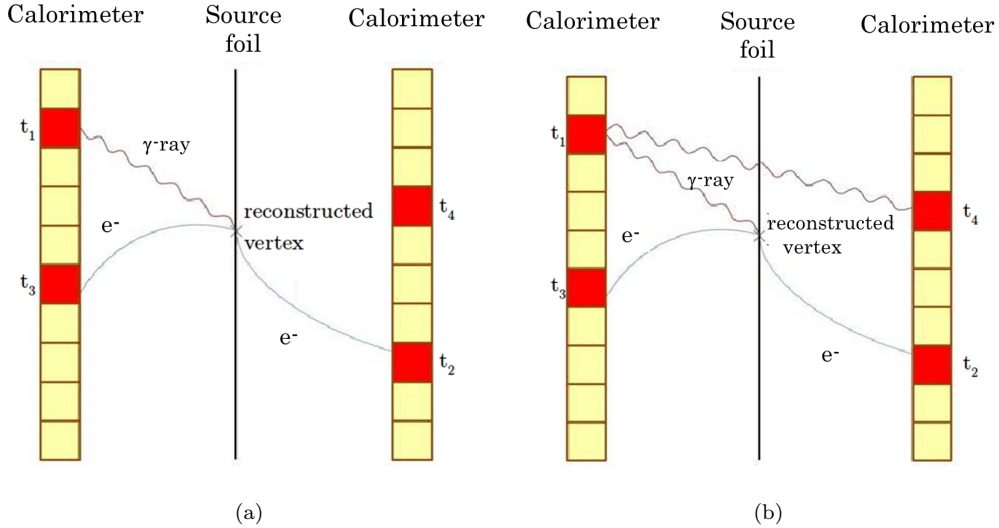
Figure 6: Example of an event reconstruction without using gamma tracking (6(a)). Only one of the two scintillators not associated to a track is consistent with the *internal* hypothesis, the other is neither *internal* nor *external*. The same event is reconstructed with gamma tracking (6(b)), the second scintillator can be associated to the first one under the assumption of Compton scattering.

In this example, the complete reconstruction of the photon can be done with only one time of flight probability calculation : between the two scintillators not associated to any track. However, when events include several unassociated calorimeter blocks, every combination has to be taken into account and evaluated. In that case, before making a complete calculation, the probability of time of flight is determined for each pair of blocks in the event, with once again the χ^2 method. All the pairs are then combined to extract all possible topologies, each associated to a combined time of flight probability,

10

using the equation :

$$\chi^2_{GT_{tot}} = \sum_{n=1}^{n=m} \chi^2_{GT}(Block_{n-1}Block_n), \qquad (4)$$

with m the total number of blocks involved in the chain of hit scintillator by a single γ-ray, $Block_{n-1}Block_n$ a pair of calorimeter blocks and $\chi^2_{GT}(Block_{n-1}Block_n)$ the χ^2 value calculated for each pair. The main drawback of this method is the computation time. To limit this effect, two additional conditions are applied : requiring an energy threshold of 150 keV for the energy deposit in each calorimeter block and only taking into account the probabilities greater than 0.1% for any combination.

Once all calculations have been performed, the topology with the highest probability is considered the most likely. This combination defines the number of photons in the event and their trajectories. The gamma tracking technique is thus key to the study of double-beta decays to excited states.

3.3. Validation of gamma tracking using calibration sources

During the data taking phase of NEMO-3, several calibration runs using three point-like ^{232}U radioactive sources, labelled 1, 2 and 3, were conducted. Their activities were measured through γ-spectrometry (HPGe detectors) and are given in Table 2, column 2. These sources are especially well suited for gamma tracking studies since they decay to the ^{228}Th nucleus which belongs to the natural ^{232}Th radioactive decay chain. At the end of the chain, it produces a ^{208}Tl nucleus which is a β^- emitter producing at least two γ-rays : e.g. 2.615 and 0.583 MeV.

We measured the activities of the ^{232}U sources using NEMO-3 analysis with and without gamma tracking. We can then compare the results with the activities measured by HPGe detectors. The main objectives are to confirm that the use of the gamma tracking method improves the signal efficiency and reduces the systematics. Several criteria are defined to only select events involving one electron and two γ-rays (1e2γ) since 99.8% of ^{208}Tl decays produce these three particles. Using Monte-Carlo simulations, the efficiency with gamma tracking is determined to be 1.16% for this topology (compared to 0.92% without gamma tracking) while 53082 data events are selected for source 3 with an acquisition time of 107.6 hours. The same analysis without gamma tracking, conducted on the same data sample, selected only 38956 events. About 27% more events were thus selected using gamma tracking, proving that part of the events involving Compton scattering are recovered, thus improving the efficiency. Figure 7 illustrates the number of scintillator blocks hit by a single γ-ray according to the path reconstruction calculated with the gamma tracking method. A reasonable agreement is obtained between data from the ^{232}U radioactive sources and Monte-Carlo simulations.

Futhermore, the ^{232}U sources activities obtained with gamma tracking are presented in Table 2 where they are compared to activities obtained without the use of gamma tracking and to the γ-spectrometry measurements. The interaction of γ-rays may induce low energy deposits in the bulk of the scintillator block. The energy response of the calorimeter does not take into account the interaction point in the scintillator block so the effect of the energy threshold may be difficult to simulate. However, the main observation is that activities measured using gamma tracking are more consistent with the γ-spectrometry results.

11
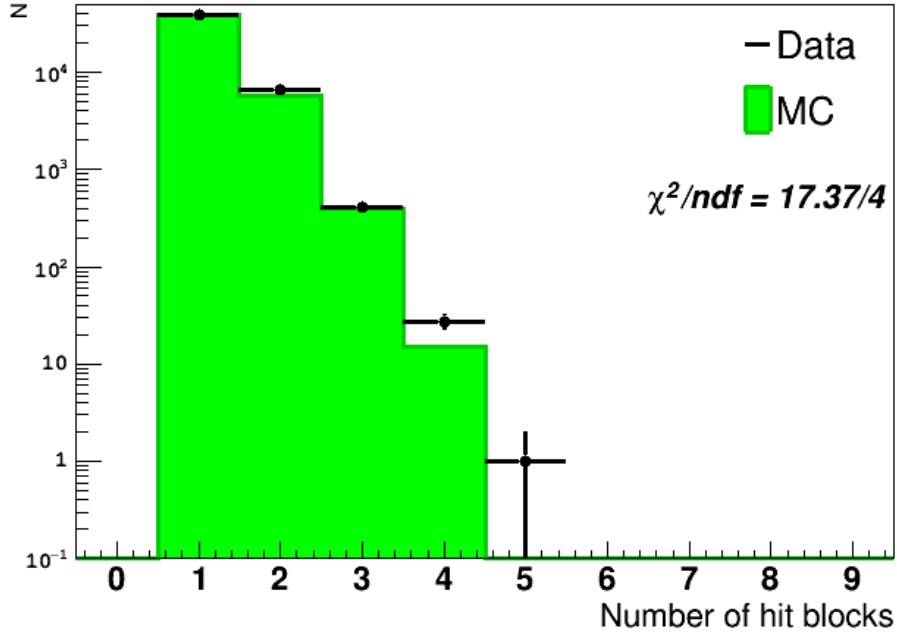
Figure 7: Number of scintillator blocks hit by a single γ-ray according to the path reconstruction calculated with the gamma tracking method, logarithmic scale. Data were acquired using γ-rays from the ^{232}U radioactive sources and are compared to Monte-Carlo simulations.

^{232}U	HPGe (Bq)	No GT act. (Bq)	Δ_{noGT} (%)	GT act. (Bq)	Δ_{GT} (%)
1	$7.79 \pm 0.04 \pm 0.21$	6.56 ± 0.08	15.8	6.98 ± 0.07	10.4
2	$15.91 \pm 0.09 \pm 0.43$	13.92 ± 0.13	12.5	14.88 ± 0.11	6.5
3	$32.76 \pm 0.17 \pm 0.89$	30.00 ± 0.17	8.4	32.11 ± 0.14	2.0

Table 2: Comparison of the ^{232}U sources activities measured by respectively γ-spectrometry (HPGe detector) and NEMO-3 analysis without and with the gamma tracking technique using the $1e2\gamma$ topology. Uncertainties in column 2 are respectively statistics and systematics. Columns 4 and 6 present the relative differences between HPGe and analysis activities (without and with gamma tracking).

However, activities measured through the analysis with gamma tracking are consistently lower than γ-spectrometry values. This difference is used as a way to estimate the systematic uncertainty induced by the use of the gamma tracking technique. The difference for sources 1, 2 and 3 are respectively 10.4%, 6.5% and 2.0% as reported in Table 2. As a conservative approach, the systematic uncertainty is considered to be 10%.

4. Double beta decay to the excited states

4.1. Two neutrino double-beta decay to 0_1^+ excited state

As mentioned in Section 1, $\beta\beta$ decays to the 0_1^+ excited state consist in the simultaneous emission (compared to the NEMO-3 time resolution) of two β and two γ particles. In order to select 2e2γ events, several criteria are applied to distinguish them from background events. The candidate events must contain two electron tracks, originating from the ^{82}Se source foil, each with an energy deposit greater than 150 keV. The distance between the tracks' intersections with the foil should fulfill Δ_{XY} less than 4 cm (perpendicular to the wires) and Δ_Z less than 8 cm (parallel to the wires) so they can be considered to have a common vertex. Two γ-rays must be reconstructed using the gamma tracking technique, each with a total energy greater than 150 keV. The timing of the calorimeter hits for electrons and γ-rays must be consistent with an *internal* event defined as those particles simultaneously emitted from their common vertex in the ^{82}Se foil. There should be no α-particle tracks and no extra reconstructed γ-rays in the event. 77 data events were selected from a total of 897,409,450 in the selenium sectors for the selected runs. Figure 8 shows that this number is compatible with the number of background events expected when using these criteria, as well as the energy distribution of both electrons for data events and background. Using these criteria, the efficiency for the expected signal is 0.078%.

(a) Phase 1　　　　　　　　　　(b) Phase 2
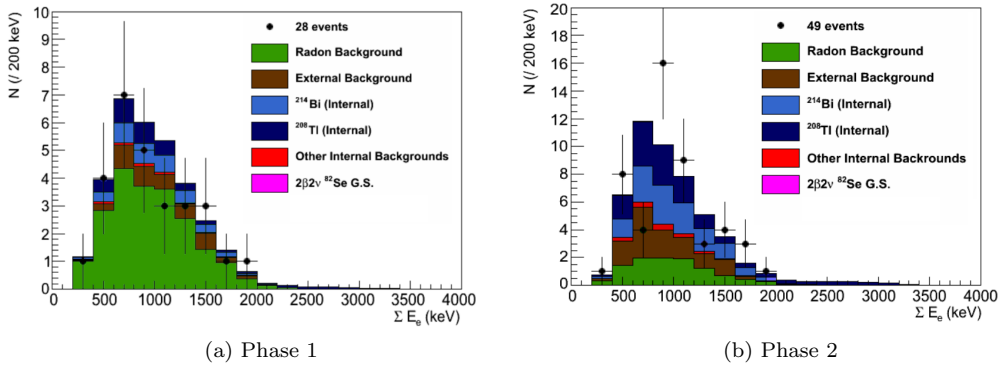
Figure 8: Sum of the electron energies distributions in the 2e2γ channel after the preselection criteria described in the text are applied, for Phase 1 in Figure 8(a) and Phase 2 in Figure 8(b). Data are compared to the MC prediction for the different backgrounds. The background coming from the $2\nu\beta\beta$ ^{82}Se decay to g.s. is completely negligible and thus not visible in the two plots.

These preselection criteria can be applied when looking for events including two internal electrons and γ-rays. In order to be more specific to the $2\nu\beta\beta(0_{gs}^+ \to 0_1^+)$ decay,

an optimisation is made considering the energies of the four particles for this decay. The first energies to be optimized are the individual energies of both electrons labelled $E_{e\ min}$ and $E_{e\ max}$. Both energies for each event are displayed using two-dimensional histograms for signal and total background, obtained from MC simulations as shown in Figures 9(a) and 9(b). For each bin of this two-dimensional histogram, the local statistical significance (noted N_σ^l) is calculated and displayed in Figure 9(c). This value is defined by the following equation :

$$N_\sigma^l = \frac{S^l}{\sqrt{S^l + B^l}}, \tag{5}$$

where S^l is the signal and B^l the background in each bin. The signal is given by the $2\nu\beta\beta$ to 0_1^+ state simulation with a half-life of 3×10^{20} years which is three times higher than the $2\nu\beta\beta$ decay to the ground state half-life.

The result of the optimization procedure was tested for several Monte Carlo samples, including $2\nu\beta\beta$ to the 0_1^+ state with various half-lives. If the half-life in the sample is different from 3×10^{20} y, the selection would not be optimal, thus the sensitivity to the $2\nu\beta\beta$ to the 0_1^+ excited state would be decreased. For samples with half-lives larger than 3×10^{20} y, the optimization procedure gives a too loose selection w.r.t optimum, increasing the background contribution. For samples with half-lives smaller than 3×10^{20} y, the optimization procedure results in a too strict selection, reducing the signal efficiency. Even if not optimal, the selection would not bias the half-life of the sample.

A selection criterion is defined on N_σ^l for the maximised total statistical significance N_σ as presented in Figure 9(d). N_σ is calculated over the total number of simulated signal events and expected background.

In Figure 9(a), simulations show that the signal is stronger when the energies of the two electrons $E_{e\ max}$ and $E_{e\ min}$ are in the range of [300-400] and [200-300] keV, respectively. This is due to their primary kinetic energies (with a total energy shared equal or lower than 1510.2 keV) slightly affected by the loss of energy in the source foil and in the tracking chamber. Concerning the background, the simulations in Figure 9(b) show that the energies of the two detected electrons can be much higher, up to 2.7 MeV, than those for the signal. This is due to the presence of ^{208}Tl isotope (Q-value of 4.99 MeV) which is one of the main backgrounds. Nevertheless, the optimization is able to remove all the events with high energy electrons, typically greater than 1.1-1.2 MeV as illustrated in Figure 9(c).

Other selections are then made on the total electron energy and total γ-rays energy and finally on the two γ-rays' individual energies as seen respectively in Figures 10 and 11. Figure 10 shows some of the features of Figure 9, whereby the total energy of γ-rays for background can be greater than 1500 keV due to higher energy γ-rays emitted in ^{208}Tl decays (usually 2.61 and 0.58 MeV). The signal simulation fits the $2\nu\beta\beta(0_{gs}^+ \to 0_1^+)$ transition with the two electrons sharing 1512.2 keV and two γ-rays with a total energy of 1487.7 keV. The optimisation process then only selects events with γ-rays sharing less than 1600 keV, taking into account the energy resolution of the detector. Figure 11 represents the third step of optimization and concerns individual γ-rays energies. By this stage, most of the ^{208}Tl induced events have been removed. Simulations indicate that most of the remaining background events contain two γ-rays of [300-400] and [200-300] keV. These can be related to ^{214}Bi, since its decay can produce a 609.3 keV γ-ray and

(a) Signal

(b) Background

(c) Local statistical significance

(d) Total statistical significance
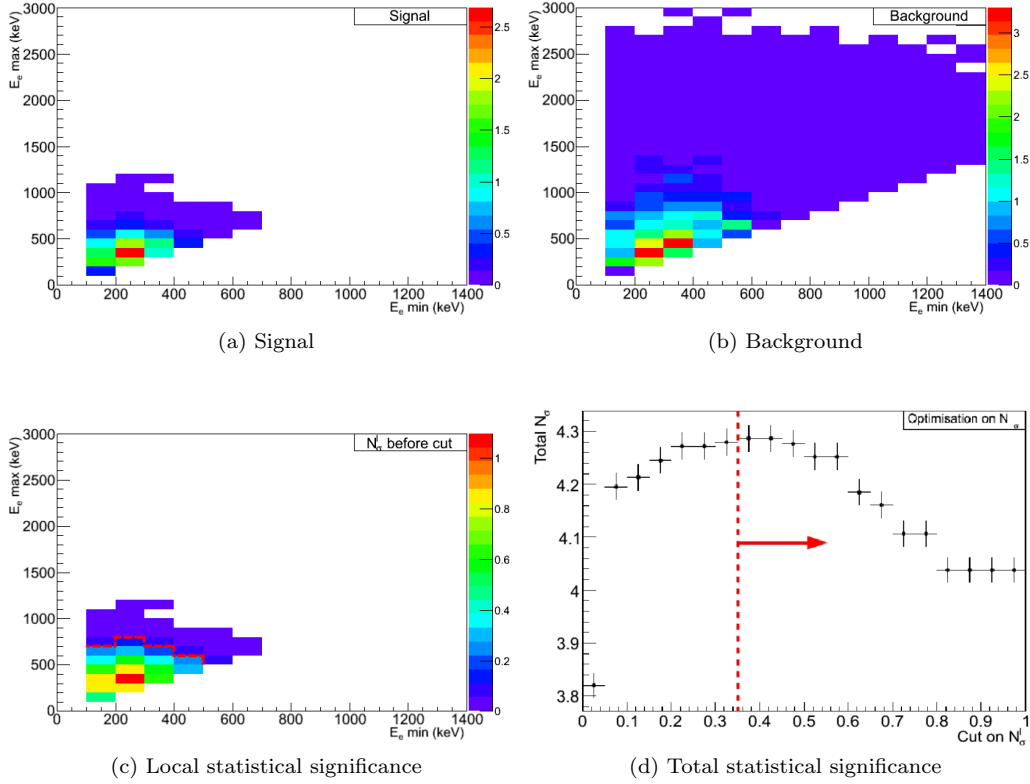
Figure 9: The distributions of signal $2\nu\beta\beta(0_{gs}^+ \to 0_1^+)$ and background events from MC simulation are represented in Figures 9(a) and 9(b) respectively, as a function of both electrons' individual energy. The local statistical significance N_σ^l distribution for the $2\nu\beta\beta(0_{gs}^+ \to 0_1^+)$ transition as a function of both electrons' individual energy is calculated for each bin of the 2-D histogram and represented in Figure 9(c). The total statistical significance N_σ as a function of a cut on the local significance in Figure 9(d) allows the optimization of this cut (dotted red line). Selected bins with high local statistical significance in Figure 9(c) are separated from the removed ones by the dotted red line.

15

a lower energy one through bremsstrahlung, shown in Figure 3(a). Finally, most signal events are expected to have two γ-rays of [400-500] and [500-600] keV, corresponding to the $2\nu\beta\beta(0_{gs}^+ \rightarrow 0_1^+)$ γ-rays of 711.2 and 776.5 keV.

After the complete optimization process described here, the selection efficiency for the $2\nu\beta\beta(0_{gs}^+ \rightarrow 0_1^+)$ signal calculated from MC is 0.069% with a total of 19 selected data events.

(a) Signal

(b) Background

(c) Local statistical significance

(d) Total statistical significance
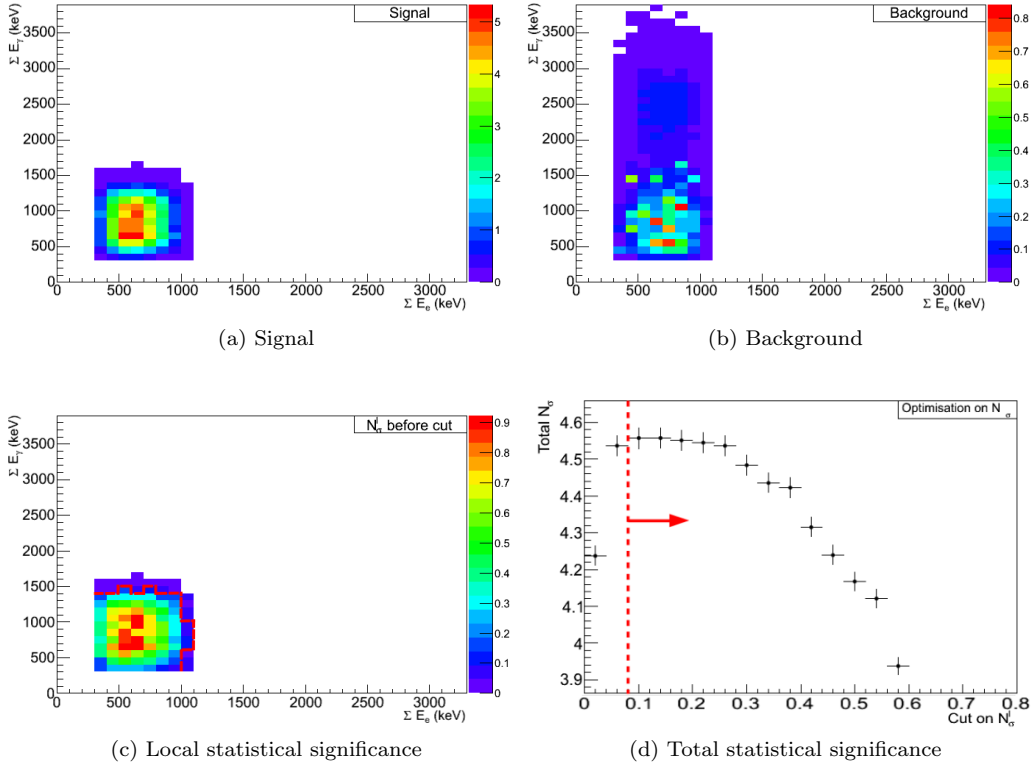
Figure 10: Total electron energy vs total γ-rays energy distributions for $2\nu\beta\beta(0_{gs}^+ \rightarrow 0_1^+)$ signal simulation (10(a)) and background (10(b)). Local statistical significance distributions for each bin of this histogram (10(c)) with optimisation cut (dotted red line) on total statistical significance N_σ presented in Figure 10(d).

The total electron energy distributions for Phase 1 and Phase 2 can be seen in Figure 12 while the total γ-rays energy distributions are shown in Figure 13. These figures also show the different background contributions that are detailed in Table 3. The largest contribution (52% in Phase 2) comes from internal contamination of the source foils and especially from ^{214}Bi. Radon is also responsible for 68% of background events during Phase 1 and was reduced to 28% in Phase 2. The external backgrounds account for 21% of the total expected background despite the strong criteria used to ensure that only internal events are selected.

It is also shown that there is a good compatibility with background and data events.

16

(a) Signal

(b) Background

(c) Local statistical significance

(d) Total statistical significance
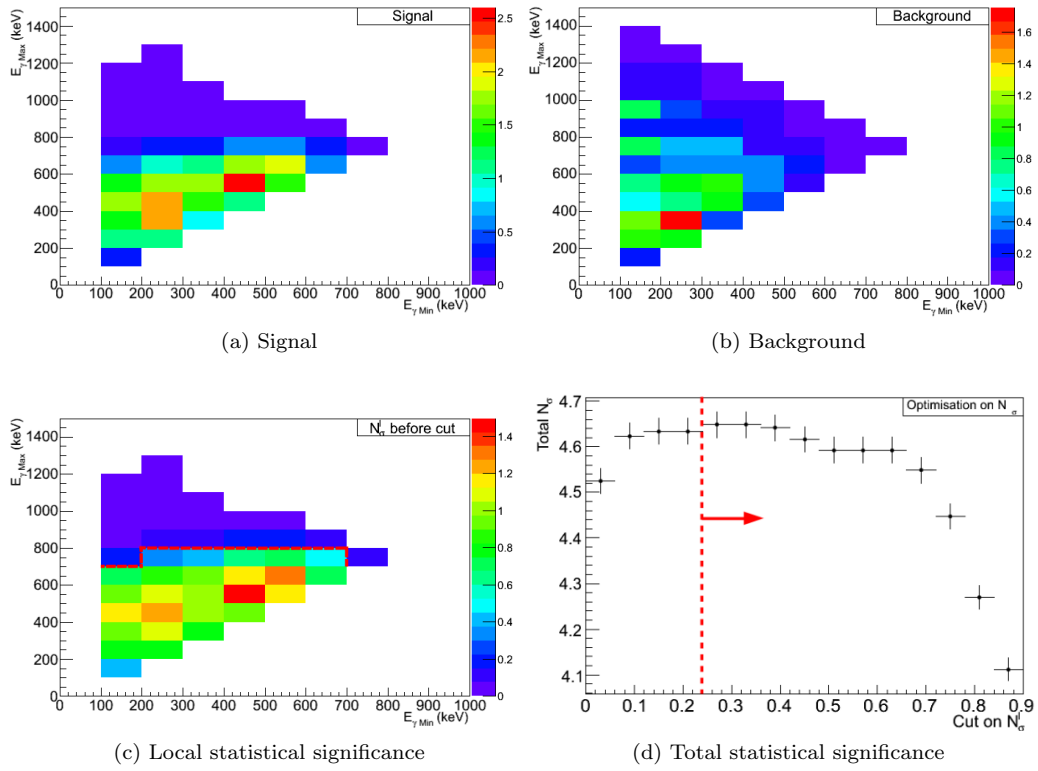
Figure 11: γ-ray 1 energy vs γ-ray 2 energy distributions for $2\nu\beta\beta$ $(0_{gs}^+ \rightarrow 0_1^+)$ signal simulation (11(a)) and background (11(b)). Local statistical significance distributions for each bin of this histogram (11(c)) with optimisation cut (dotted red line) on total statistical significance N_σ presented in Figure 11(d).
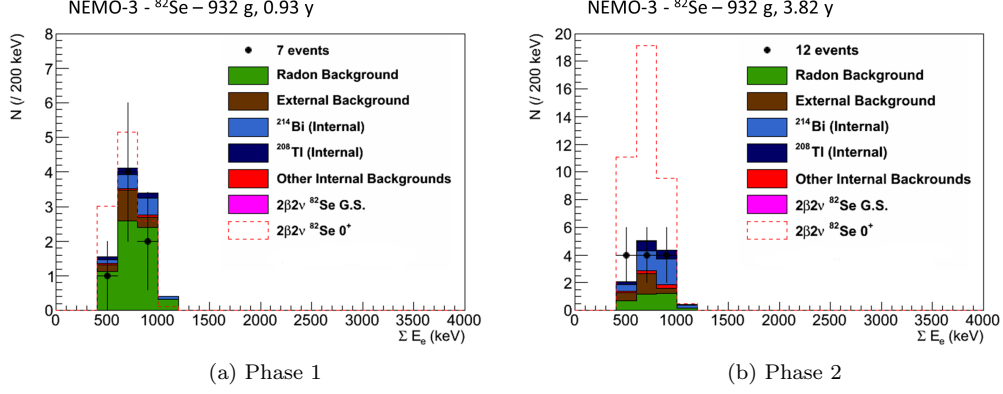
(a) Phase 1

(b) Phase 2

Figure 12: Total electron energy distributions after selection for the $2\nu\beta\beta(0_{gs}^{+} \to 0_{1}^{+})$ transition, for Phase 1 in Figure 12(a) and Phase 2 in Figure 12(b). Experimental data events are compared to the MC simulation for the different backgrounds. The dotted red line represents the simulated signal for a half-life of 3×10^{20} years.

(a) Phase 1

(b) Phase 2

Figure 13: Total γ-rays energy distributions after selection for the $2\nu\beta\beta(0_{gs}^{+} \to 0_{1}^{+})$ transition, for Phase 1 in Figure 13(a) and Phase 2 in Figure 13(b). Experimental data events are compared to the MC simulation for the different backgrounds. The dotted red line represents the simulated signal with a half-life of 3×10^{20} years.

18

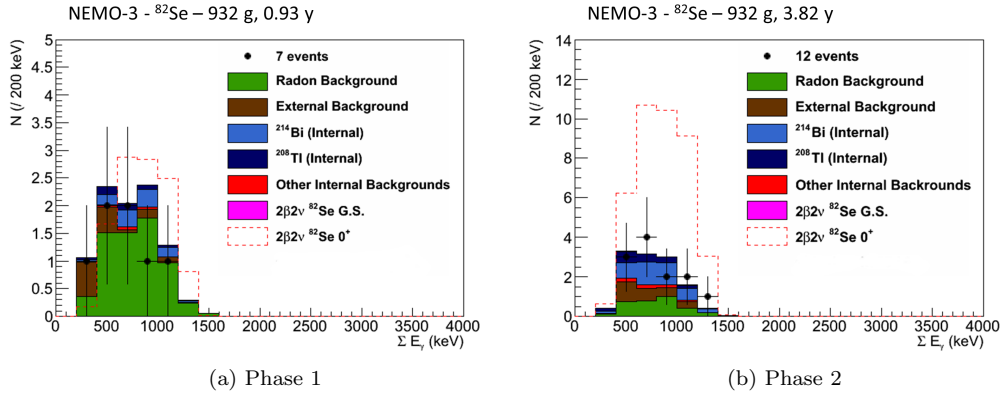|		Expected events		Contribution to total background (%)	
		Phase 1	Phase 2	Phase 1	Phase 2
Internal	^{214}Bi	$1.14 \pm 0.05 \pm 0.12$	$4.28 \pm 0.09 \pm 0.43$	12.1	36.1
	^{208}Tl	$0.43 \pm 0.02 \pm 0.07$	$1.58 \pm 0.04 \pm 0.23$	4.6	13.3
	Others	$0.06 \pm 0.03 \pm 0.01$	$0.29 \pm 0.14 \pm 0.02$	0.6	2.4
	Total	$1.64 \pm 0.07 \pm 0.20$	$6.15 \pm 0.49 \pm 0.68$	17.3	51.8
Radon		$6.44 \pm 0.63 \pm 0.65$	$3.26 \pm 0.31 \pm 0.33$	68.0	27.5
External	^{214}Bi	$0.38 \pm 0.19 \pm 0.04$	$1.49 \pm 0.75 \pm 0.15$	4.0	12.5
	^{208}Tl	$0.29 \pm 0.10 \pm 0.03$	$0.18 \pm 0.06 \pm 0.02$	2.9	1.6
	Others	$0.74 \pm 0.37 \pm 0.08$	$0.78 \pm 0.39 \pm 0.08$	7.8	6.6
	Total	$1.39 \pm 0.43 \pm 0.15$	$2.46 \pm 0.05 \pm 0.85$	14.7	20.7
Total background		$9.47 \pm 0.77 \pm 1.00$	$11.87 \pm 1.17 \pm 1.26$	100.0	100.0
Data events		7	12	–	–

Table 3: Numbers of expected background events from the main background sources in both Phases and their contribution to the total number of expected background events for the 2e2γ channel after optimisation for the study of $2\nu\beta\beta(0^+_{gs} \rightarrow 0^+_1)$ decay. 0.93 year of data taking are considered for Phase 1 and 3.82 years for Phase 2. The quoted uncertainties represent the statistical and systematic uncertainties, respectively. The number of selected data events for each phase is also presented.

In the absence of a significant excess of data versus background, a limit has been set. This can be performed using the following equation :

$$T_{1/2} > \epsilon \times N_{nuc} \times \ln(2) \times (t_{acq} - t_d) \times \frac{1}{N_{ex}}, \tag{6}$$

where ϵ is the detection efficiency, N_{nuc} the number of ^{82}Se nuclei, t_{acq} and t_d the acquisition and dead time respectively and N_{ex} the number of signal events that can be excluded. The method used here to obtain this last number is the CLs method [42], that takes into account the shape of the expected signal and backgrounds as well as the number of data events and several statistical and systematical uncertainties. The systematics are detailed in Table 4. Considering then the 4.42 kg.y exposure, the 0.069% efficiency, the 21.4 expected background events and 19 data events, the limit on the $2\nu\beta\beta$ $(0^+_{gs} \rightarrow 0^+_1)$ decay half-life for ^{82}Se is, at 90% CL :

$$T^{2\nu}_{1/2}(^{82}\text{Se}, 0^+_{gs} \rightarrow 0^+_1) > 1.3 \times 10^{21} \text{ y}. \tag{7}$$

This result is compatible with limit of 3×10^{21} y from Ref. [37] and lower than the value published by the LUCIFER collaboration, who determined a limit of 3.4×10^{22} y [31] for the $(2\nu+0\nu)\beta\beta$ processes. However, the NEMO-3 technique precisely identifies the event topology and could thus independently study $2\nu\beta\beta$ and $0\nu\beta\beta$ processes.

4.2. Neutrinoless double beta decay to 0^+_1 excited state

The search for $0\nu\beta\beta$ events is carried out similarly to what has been done for the $2\nu\beta\beta$ decay. The preselection criteria are the same as what is described in the first part of Section 4.1. However, in the $0\nu\beta\beta$ process through the $0^+_{gs} \rightarrow 0^+_1$ transition, the two

19

Systematic	Estimated uncertainty (%)	Method of estimate
Gamma tracking	10.4	^{232}U vs HPGe
Energy calibration	1	Neutron sources
$2\nu\beta\beta$ efficiency	5	^{207}Bi vs HPGe
^{82}Se mass	0.5	Uncertainty on mass and enrichment
Energy loss in foil	1	Neutron sources
bremsstrahlung	1	^{90}Y source analysis
Ext. BG activities	10	Variation from background model
Radon BG activities	10	1e1α vs 1e1γ
Int. BG activities (excl. ^{208}Tl & ^{214}Bi)	4	^{207}Bi 1eNγ vs 2e (^{40}K & ^{234m}Pa meas. in 1e)
Int. ^{214}Bi activity	10	1e1α vs. 1e1γ
Int. ^{208}Tl activity	15	NEMO-3 vs HPGe
$2\nu\beta\beta$ activity	1	Statistical uncertainty

Table 4: Values of the 1σ systematic uncertainties included in the calculation of the limits on $2\nu\beta\beta$ decay to excited states and their methods of estimate. The estimated uncertainties come from the comparison of the activity measurements of calibration sources between NEMO-3 and HPGe (^{232}U, ^{207}Bi, ^{90}Y), the uncertainties on background measurements and uncertainties specific to the detector or ^{82}Se sources.

electrons do not share energy with neutrinos contrary to the $2\nu\beta\beta$ decay. The signal efficiency using these criteria increases by a factor 10 compared to the $2\nu\beta\beta$ process. It reaches 0.71%, as higher energy electrons are expected. The selection has then been optimized with these energies, taking into account a simulated signal with a half-life of 3×10^{21} years and using the same method as the one described in Section 4.1. Applying those criteria, the final selection efficiency for this signal is 0.69% and 14 data events are selected.

The total electron energy distributions for Phase 1 and Phase 2 are shown in Figure 14. The background composition is similar to what was presented in Table 3 with a high radon contribution. The details are presented in Table 5. The total γ-rays energy distributions are shown in Figure 15.

As for the $2\nu\beta\beta(0_{gs}^+ \to 0_1^+)$ transition, data is consistent with background-only predictions so a limit has to be set on the half-life of the $0\nu\beta\beta(0_{gs}^+ \to 0_1^+)$ process. The method used to calculate such a limit remains the CLs method. With the 20.1 background events and the statistical and systematic uncertainties, the limit on the $0\nu\beta\beta$ $(0_{gs}^+ \to 0_1^+)$ decay half-life for ^{82}Se (at 90% CL) is :

$$T_{1/2}^{0\nu}(^{82}\text{Se}, 0_{gs}^+ \to 0_1^+) > 2.3 \times 10^{22} \text{ y}. \tag{8}$$

This result is given for the $0\nu\beta\beta(0_{gs}^+ \to 0_1^+)$ transition for ^{82}Se, separately from $2\nu\beta\beta(0_{gs}^+ \to 0_1^+)$. It is compatible with limit of 3.4×10^{22} y and 8.1×10^{22} y obtained in the LUCIFER experiment [31] for the $(2\nu + 0\nu)\beta\beta$ processes and CUPID-0 [32] experiment. According to the mass mechanism, a Majorana neutrino is exchanged during such a process and therefore a limit can also be set on the effective mass of the neutrino using

(a) Phase 1   (b) Phase 2

Figure 14: Total electron energy distributions after selection for the $0\nu\beta\beta$ ($0_{gs}^+ \to 0_1^+$) transition, for Phase 1 in Figure 14(a) and Phase 2 in Figure 14(b). Experimental data events are compared to the MC simulation for the different backgrounds. The dotted red line represents the simulated signal with a half-life of 3×10^{21} years.

(a) Phase 1   (b) Phase 2
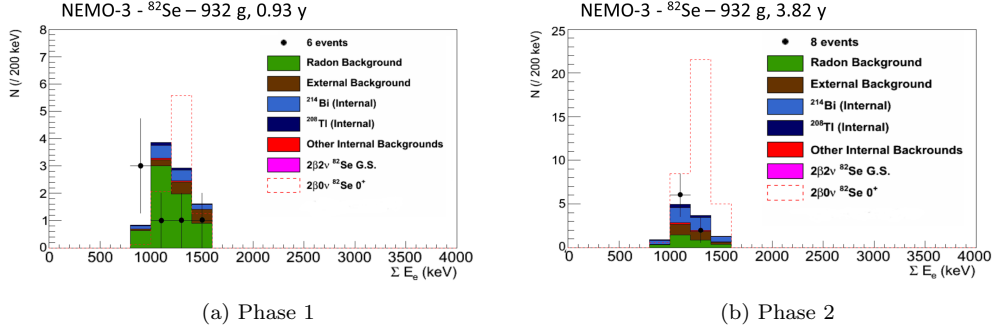
Figure 15: Total γ-rays energy distributions after selection for the $0\nu\beta\beta$ ($0_{gs}^+ \to 0_1^+$) transition, for Phase 1 in Figure 15(a) and Phase 2 in Figure 15(b). Experimental data events are compared to the MC simulation for the different backgrounds. The dotted red line represents the simulated signal with a half-life of 3×10^{21} years.
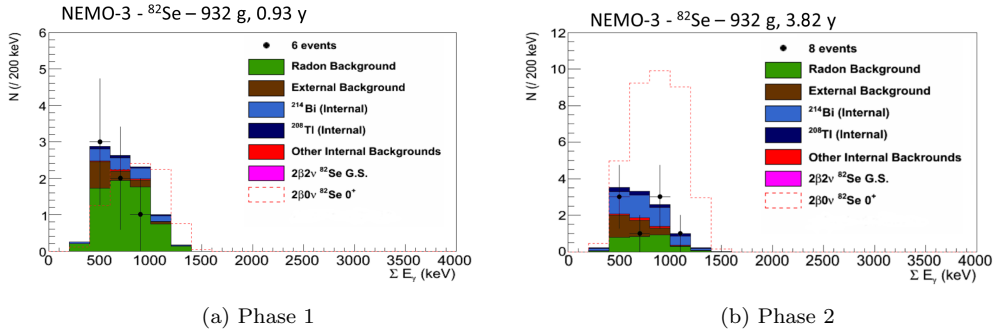
		Expected events		Contribution to total background (%)	
		Phase 1	Phase 2	Phase 1	Phase 2
⁸²Se foils	²¹⁴Bi	$1.25 \pm 0.05 \pm 0.13$	$4.57 \pm 0.10 \pm 0.46$	13.5	41.9
	²⁰⁸Tl	$0.24 \pm 0.01 \pm 0.03$	$0.82 \pm 0.02 \pm 0.12$	2.6	7.6
	Others	$0.02 \pm 0.01 \pm 0.01$	$0.07 \pm 0.03 \pm 0.01$	0.2	0.6
	Total	$1.50 \pm 0.06 \pm 0.17$	$5.46 \pm 0.11 \pm 0.59$	16.3	50.1
Radon		$6.50 \pm 0.64 \pm 0.65$	$2.97 \pm 0.27 \pm 0.30$	70.4	27.3
Detector	²¹⁴Bi	$0.45 \pm 0.22 \pm 0.05$	$1.33 \pm 0.62 \pm 0.14$	4.9	12.3
	²⁰⁸Tl	$0.79 \pm 0.09 \pm 0.08$	$1.13 \pm 0.14 \pm 0.12$	8.5	10.3
	Others	0	0	0	0
	Total	$1.24 \pm 0.24 \pm 0.13$	$2.46 \pm 0.62 \pm 0.26$	13.4	22.6
Total background		$9.24 \pm 0.69 \pm 0.95$	$10.89 \pm 0.69 \pm 1.15$	100.0	100.0
Data events		6	9	–	–

Table 5: Numbers of expected background events from the main background sources in both Phases and their contribution to the total number of expected background events for the 2e2γ channel after optimisation for the study of $0\nu\beta\beta(0_1^+ \rightarrow 0_2^+)$ decay. 0.93 years of data taking are considered for Phase 1 and 3.82 years for Phase 2. The quoted uncertainties represent the statistical and systematic uncertainties, respectively. The number of selected data events for each phase is also presented.

the following equation :

$$\frac{1}{\left(T_{1/2}^{0\nu}\right)_{MM}} = G^{0\nu}(Q_{\beta\beta}, Z)g_A^4 \left|M^{0\nu}\right|^2 \left|\frac{m_{\beta\beta}}{m_e}\right|^2, \tag{9}$$

where $G^{0\nu}(Q_{\beta\beta}, Z)$ is the phase space factor given in [43] for the transition, $g_A = 1.27$ and $M^{0\nu}$ the nuclear matrix element [12, 13, 44, 45]. The limit that can be set on the effective neutrino mass is $m_{\beta\beta} < [42 - 239]$ eV.

5. Summary and Conclusions

4 Using an innovative gamma tracking technique, the NEMO-3 data set was analysed to search for $\beta\beta$ decays of ⁸²Se to the excited states of ⁸²Kr with a 4.42 kg.y exposure. No evidence for the $2\nu\beta\beta$ process was found and thus an upper limit on the decay half-life was set at 90% CL : $T_{1/2}^{2\nu}(^{82}\mathrm{Se}, 0_{gs}^+ \rightarrow 0_1^+) > 1.3 \times 10^{21}$ y. This result can nevertheless help to constrain theoretical QRPA models presented in [33, 34, 46].

The analysis of the $0\nu\beta\beta$ decay to excited states was conducted in a similar fashion and, as once again no extra events were observed over the expected background, an upper limit was set at 90% CL : $T_{1/2}^{0\nu}(^{82}\mathrm{Se}, 0_{gs}^+ \rightarrow 0_1^+) > 2.3 \times 10^{22}$ y. These results are obtained for the first time with a detector which reconstructs each particle individually in the final state.

This analysis performed with ⁸²Se in NEMO-3 will also provide useful information for the next-generation SuperNEMO experiment which will host 100 kg of ⁸²Se, such as

optimisation of the selected events and identification of the main background contributions.

In parallel with its search for $0\nu\beta\beta$ decay to the ground state, SuperNEMO will also look for the $2\nu\beta\beta$ and $0\nu\beta\beta$ decays to excited states with major improvements. Using thicker scintillators, the sensitivity to γ-rays and efficiency to $2\nu\beta\beta$ and $0\nu\beta\beta(0_{gs}^+ \to 0_1^+)$ transitions will be enhanced. Backgrounds will also be reduced : more than a factor 30 for radon and a factor 100 for ^{214}Bi and ^{208}Tl. The expected sensitivities for SuperNEMO are respectively $\sim 10^{23}$ y and $\sim 10^{24}$ y for the $2\nu\beta\beta$ and $0\nu\beta\beta(0_{gs}^+ \to 0_1^+)$ half-lives. A first module, called Demonstrator, with 7 kg of ^{82}Se is undergoing commissioning and will start taking data in 2019. Its goal is to reach a sensitivity on the $0\nu\beta\beta$ half-life of 5×10^{24} y in 17.5 kg·y exposure with the demonstration of a "zero"-background experiment [47].

References

[1] R. Arnold et al. (NEMO-3 Collaboration) (NEMO-3 Collaboration), Phys. Rev. D **92** (2015) 072011. URL: `https://link.aps.org/doi/10.1103/PhysRevD.92.072011`. doi:`10.1103/PhysRevD.92.072011`.

[2] C. Alduino et al. (CUORE Collaboration) (CUORE Collaboration), Phys. Rev. Lett. **120** (2018) 132501. URL: `https://link.aps.org/doi/10.1103/PhysRevLett.120.132501`. doi:`10.1103/PhysRevLett.120.132501`.

[3] M. Agostini et al. (GERDA Collaboration) (GERDA Collaboration), Phys. Rev. Lett. **120** (2018) 132503. URL: `https://link.aps.org/doi/10.1103/PhysRevLett.120.132503`. doi:`10.1103/PhysRevLett.120.132503`.

[4] A. Gando et al. (KamLAND-Zen Collaboration) (KamLAND-Zen Collaboration), Phys. Rev. Lett. **117** (2016) 082503. URL: `https://link.aps.org/doi/10.1103/PhysRevLett.117.082503`. doi:`10.1103/PhysRevLett.117.082503`.

[5] D. L. Lincoln et al., Phys. Rev. Lett. **110** (2013) 012501.

[6] J. W. Beeman et al. (LUCIFER Collaboration), Adv. High Energy Phys. **2013** (2013) 237973.

[7] O. Azzolini, et al., Eur. Phys. J. C **78** (2018) 428

[8] R. Arnold et al., Eur. Phys. J. C **70** (2010) 927–943.

[9] R. Arnold, et al. (NEMO-3 Collaboration), Eur. Phys. J. C **78** (2018) 821.

[10] O. Azzolini, et al., Phys. Rev. Lett. **123** (2019) 032501 doi:10.3390/PhysRevLett.123.032501.

[11] J. Menéndez, A. Poves, E. Caurier, F. Nowacki, Nuclear Physics A **818** (2009) 139–151. URL: `http://www.sciencedirect.com/science/article/pii/S0375947408008233`. doi:`http://dx.doi.org/10.1016/j.nuclphysa.2008.12.005`.

[12] J. Barea, J. Kotila, F. Iachello, Phys. Rev. C **91** (2015) 034304. URL: `https://link.aps.org/doi/10.1103/PhysRevC.91.034304`. doi:`10.1103/PhysRevC.91.034304`.

[13] J. Hyvärinen, J. Suhonen, Phys. Rev. C **93** (2016) 064306. URL: `https://link.aps.org/doi/10.1103/PhysRevC.93.064306`. doi:`10.1103/PhysRevC.93.064306`.

[14] M. J. Dolinski et al, Annu. Rev. Nucl. Part. Sci. **69** (2019) 219-251. URL: `https://www.annualreviews.org/doi/10.1146/annurev-nucl-101918-023407`. doi:`10.1146/annurev-nucl-101918-023407`.

[15] A. S. Barabash, Nucl. Phys. A **393** (2015) 593. URL: `https://www.sciencedirect.com/science/article/pii/S037594741500010X?via%3Dihub`. doi:`10.1016/j.nuclphysa.2015.01.001`.

[16] A. S. Barabash, `arXiv:nucl-ex/190706887`.

[17] R. Arnold et al. (NEMO-3 Collaboration), Phys. Rev. Lett. **95** (2005) 182302. URL: `https://link.aps.org/doi/10.1103/PhysRevLett.120.132501`. doi:`10.1103/PhysRevLett.120.132501`.

[18] R. Arnold et al., Nucl. Phys. A **925** (2014) 25–36.

23

[19] R. Arnold et al., Nucl. Phys. A **781** (2007) 209–226.

[20] R. Arnold, et al. (NEMO-3 Collaboration), Phys. Rev. D **94** (2016) 072003. `https://link.aps.org/doi/10.1103/PhysRevD.94.072003`. doi:10.1103/PhysRevD.94.072003.

[21] A. S. Barabash, Ph. Hubert, A. Nachab and V. I. Umatov, Phys. Rev. C **79** (2009) 45501.

[22] M. F. Kidd, J. H. Esterline, S. W. Finch and W. Tornow, Phys. Rev. C **90** (2014) 055501.

[23] J. Kotila, F. Iachello, Phys. Rev. C **85** (2012) 034316.

[24] A. S. Barabash, AIP Conf. Proc. **1894** (2017) 020002.

[25] A. S. Barabash, Phys. Lett. B **345** (1995) 408–413.

[26] A. S. Barabash, Phys. At. Nucl. **62** (1999) 2039–2043.

[27] L. De Braeckeleer, M. Hornish, A. S. Barabash, V. Umatov, Phys. Rev. Lett. **86** (2001) 3510–3513.

[28] M. F. Kidd et al, Nucl. Phys. A **821** (2009) 251–261.

[29] P. Belli et al, Nucl. Phys. A **846** (2010) 143–156.

[30] S. Blondel, Optimisation du blindage contre les neutrons pour le démonstrateur de SuperNEMO et analyse de la double désintégration β du néodyme-150 vers les états excités du samarium-150 avec le détecteur NEMO 3, PhD thesis, Université Paris Sud, 2013.

[31] J. W. Beeman et al. (LUCIFER Collaboration), Eur. Phys. J. C **75** (2015) 591.

[32] O. Azzolini et al. (CUPID-0 Collaboration), Eur. Phys. J. C **78** (2018) 888.

[33] M. Aunola, J. Suhonen, Nucl. Phys. A **602** (1996) 133–166.

[34] J. Suhonen, O. Civitarese, Phys. Rep. **300** (1998) 123–214.

[35] R. Arnold, C. Augier, A. Bakalyarov, J. Baker, A. Barabash, et al., Nucl. Instrum. Meth. **A 536** (2005) 79–122. doi:10.1016/j.nima.2004.07.194. arXiv:physics/0402115.

[36] J. K. Tuli, E. Brown, Nucl. Data Sheets, **157**, 260, 2019.

[37] J. Suhonen, J. Toivanen, A. S. Barabash, I. A. Vanushin, V. I. Umatov, R. Gurriarán, F. Hubert, P. Hubert, Zeitschrift für Physik A Hadrons and Nuclei **358** (1997) 297–301. URL: `http://dx.doi.org/10.1007/s002180050333`. doi:10.1007/s002180050333.

[38] J. Argyriades, et al. (NEMO-3 Collaboration), Nucl. Instrum. Meth. **A 606** (2009) 449–465. doi:10.1016/j.nima.2009.04.011. arXiv:0903.2277.

[39] O. Ponkratenko, V. Tretyak, Y. Zdesenko, Phys. Atom. Nucl. **63** (2000) 1282.

[40] R. Brun, F. Bruyant, M.Maire, A.McPherson, P. Zanarini CERNDD- EE-84-1 (1987) .

[41] C. Hugon, Analyse des données de l'expérience NEMO3 pour la recherche de la désintégration double bêta sans émission de neutrinos. Étude des biais systématiques du calorimètre et développement d'outils d'analyse, PhD thesis, Université Paris Sud, 2012.

[42] T. Junk, Nucl. Instrum. Meth. **A 434** (1999) 435–443. doi:10.1016/S0168-9002(99)00498-2. arXiv:hep-ex/9902006.

[43] M. Mirea, T. Pahomi, S. Stoica, Rom. Rep. Phys. **67** (2015) 872–889.

[44] F. Šimkovic, M. Nowak, W. A. Kamiński, A. A. Raduta and A. Faessler Phys. Rev. C **64** (2001) 035501.

[45] J. Menéndez, A. Poves, E. Caurier, F. Nowacki, Nucl. Phys. A **818** (2009) 139–151.

[46] J. Toivanen, J. Suhonen, Phys. Rev. C **55** (1997) 2314–2323.

[47] F. Perrot (on behalf of the SuperNEMO collaboration), POS (ICHEP 2016) (2016) 499.

Alimardon V. Rakhimov*, A. S. Barabash, A. Basharina-Freshville, S. Blot, M. Bongrand,
Ch. Bourgeois, D. Breton, R. Breier, E. Birdsall, V. B. Brudanin, H. Burešova, J. Busto,
S. Calvez, M. Cascella, C. Cerna, J. P. Cesar, E. Chauveau, A. Chopra, G. Claverie, S. De Capua,
F. Delalee, D. Duchesneau, V. G. Egorov, G. Eurin, J. J. Evans, L. Fajt, D. V. Filosofov, R. Flack,
X. Garrido, H. Gomez, B. Guillon, P. Guzowski, R. Hodák, K. Holý, A. Huber, C. Hugon,
A. Jeremie, S. Jullian, D. V. Karaivanov, M. Kauer, A. A. Klimenko, O. I. Kochetov, S. I. Konovalov,
V. Kovalenko, K. Lang, Y. Lemière, T. Le Noblet, Z. Liptak, X. R. Liu, P. Loaiza, G. Lutter, J. Maalmi,
M. Macko, F. Mamedov, C. Marquet, F. Mauger, A. Minotti, A. A. Mirsagatova, N. A. Mirzayev,
I. Moreau, B. Morgan, J. Mott, I. B. Nemchenok, M. Nomachi, F. Nova, H. Ohsumi, G. Oliviero,
R. B. Pahlka, J. R. Pater, V. Palušová, F. Perrot, F. Piquemal, P. Povinec, P. Pridal, Y. A. Ramachers,
A. Rebii, A. Remoto, B. Richards, J. S. Ricol, E. Rukhadze, N. I. Rukhadze, R. Saakyan, I. I. Sadikov,
R. Salazar, X. Sarazin, J. Sedgbeer, Yu. A. Shitov, F. Šimkovic, L. Simard, A. Smetana, K. Smolek,
A. A. Smolnikov, S. Snow, S. Söldner-Rembold, B. Soulé, M. Špavorova, I. Štekl, F. A. Tashimova,
J. Thomas, V. Timkin, S. Torre, Vl. I. Tretyak, V. I. Tretyak, V. I. Umatov, C. Vilela, V. Vorobel,
G. Warot, D. Waters, M. Zampaolo and A. Žukauskas

Development of methods for the preparation of radiopure ⁸²Se sources for the SuperNEMO neutrinoless double-beta decay experiment

Abstract: A radiochemical method for producing ⁸²Se sources with an ultra-low level of contamination of natural
radionuclides (⁴⁰K, decay products of ²³²Th and ²³⁸U) has been developed based on cation-exchange chromatographic purification with reverse removal of impurities. It includes chromatographic separation (purification), reduction, conditioning (which includes decantation,

*Corresponding author: Alimardon V. Rakhimov, Joint Institute for Nuclear Research (JINR), Dubna, 141980, Russian Federation; and Institute of Nuclear Physics of Uzbekistan Academy of Sciences, Tashkent, 100214, Uzbekistan, E-mail: alimardon@jinr.ru
A. S. Barabash, S. I. Konovalov and V. I. Umatov: NRC "Kurchatov Institute", ITEP, 117218 Moscow, Russia
A. Basharina-Freshville, M. Cascella, A. Chopra, R. Flack, M. Kauer, X. R. Liu, J. Mott, B. Richards, R. Saakyan, J. Thomas, S. Torre, C. Vilela and D. Waters: University College London, London WC1E 6BT, UK
S. Blot, E. Birdsall, S. De Capua, J. J. Evans, P. Guzowski, J. R. Pater and S. Söldner-Rembold: University of Manchester, Manchester M13 9PL, UK
M. Bongrand, Ch. Bourgeois, D. Breton, S. Calvez, X. Garrido, H. Gomez, S. Jullian, P. Loaiza, J. Maalmi and X. Sarazin: LAL, Université Paris-Sud, CNRS/IN2P3, Université Paris-Saclay, F-91405 Orsay, France
R. Breier, K. Holý, V. Palušová, P. Povinec, E. Rukhadze and F. Šimkovic: Faculty of Mathematics, Physics and Informatics, Comenius University, SK-842 48 Bratislava, Slovakia
V. B. Brudanin: Joint Institute for Nuclear Research (JINR), Dubna, 141980, Russian Federation; and National Research Nuclear University MEPhI, 115409 Moscow, Russia

H. Burešova: Nuvia a.s., Třebíč, Czech Republic
J. Busto: CPPM, Universite d'Aix Marseille, CNRS/IN2P3, F-13288 Marseille, France
C. Cerna, E. Chauveau, G. Claverie, F. Delalee, A. Huber, C. Hugon, G. Lutter, C. Marquet, I. Moreau, F. Perrot, F. Piquemal, A. Rebii, J. S. Ricol and B. Soulé: CENBG, Université de Bordeaux, CNRS/IN2P3, F-33175 Gradignan, France
J. P. Cesar, K. Lang, Z. Liptak, F. Nova, R. B. Pahlka and R. Salazar: University of Texas at Austin, Austin, TX 78712, USA
D. Duchesneau, A. Jeremie, T. Le Noblet, A. Minotti and A. Remoto: Univ. Grenoble Alpes, Univ. Savoie Mont Blanc, CNRS/IN2P3, LAPP, 74000 Annecy, France
V. G. Egorov, D. V. Filosofov, A. A. Klimenko, O. I. Kochetov, V. Kovalenko, I. B. Nemchenok, N. I. Rukhadze, Yu. A. Shitov, A. A. Smolnikov, V. Timkin and V. I. Tretyak: Joint Institute for Nuclear Research (JINR), Dubna, 141980, Russian Federation
G. Eurin: University College London, London WC1E 6BT, UK; and LAL, Université Paris-Sud, CNRS/IN2P3, Université Paris-Saclay, F-91405 Orsay, France
L. Fajt, R. Hodák, F. Mamedov, P. Pridal, A. Smetana, K. Smolek, M. Špavorova and I. Štekl: Institute of Experimental and Applied Physics, Czech Technical University in Prague, CZ-12800 Prague, Czech Republic

centrifugation, washing, grinding, and drying), and ^{82}Se foil production. The conditioning stage, during which highly dispersed elemental selenium is obtained by the reduction of purified selenious acid (H_2SeO_3) with sulfur dioxide (SO_2) represents the crucial step in the preparation of radiopure ^{82}Se samples. The natural selenium (600 g) was first produced in this procedure in order to refine the method. The technique developed was then used to produce 2.5 kg of radiopure enriched selenium (^{82}Se). The produced ^{82}Se samples were wrapped in polyethylene (12 μm thick) and radionuclides present in the sample were analyzed with the BiPo-3 detector. The radiopurity of the plastic materials (chromatographic column material and polypropylene chemical vessels), which were used at all stages, was determined by instrumental neutron activation analysis. The radiopurity of the ^{82}Se foils was checked by measurements with the BiPo-3 spectrometer, which confirmed the high purity of the final product. The measured contamination level for ^{208}Tl was 8–54 μBq/kg, and for ^{214}Bi the detection limit of 600 μBq/kg has been reached.

1 Introduction

Selenium-82 is one of the most suitable isotopes for studying double-beta decay (ββ decay) and searching for its neutrinoless mode (0νββ). Interest in studies of 0νββ decay has increased significantly in recent years since the discovery of neutrino oscillations. NEMO-3 was one of the leading underground experiments for ββ decay studies in different isotopes (^{48}Ca, ^{82}Se, ^{96}Zr, ^{100}Mo, ^{116}Cd, ^{130}Te, ^{150}Nd) with a total mass of about 10 kg. The experiment used a unique tracking-calorimetric technique to measure the full topology of ββ decay and obtained a number of important ββ decay results [1–3]. The SuperNEMO project extrapolates the successful NEMO-3 technique to a next-generation of 0νββ-experiments, planning to reach a sensitivity $t_{1/2}^{0\nu\beta\beta} \sim 10^{26}$ years with ~100 kg of enriched isotope (^{82}Se, ^{150}Nd) [4].

Use of ultrapure materials with respect to impurities of ^{40}K, ^{232}Th, ^{238}U is a key factor in the success of low-background underground experiments. Therefore, all materials used (e. g. construction materials, detector shielding, photomultipliers, cables, etc.) are carefully selected after screening for radioactive impurities. Inductively coupled plasma mass spectrometry (ICP-MS) [5], instrumental neutron activation analysis (INAA) [6, 7], and ultra-low background HPGe and BiPo-3 detectors have frequently been used [7–10] for the determination of the radiopurity of materials.

The most critical factor is the ultra-high radiopurity of the ββ source foils. The SuperNEMO spectrometer is designed in such a way that all radio-decays in source foils are registered with maximal efficiency. Unfortunately, this equally applies to the useful ββ signal and the background from radioactive impurities in foils. This background in the ROI can degrade critically the sensitivity of the experiment. In the SuperNEMO detector the ββ-sources, i. e. the enriched selenium (^{82}Se), are wrapped in 12 μm-thick polyethylene. The radiopurity of the NEMO-3 experiment's ^{82}Se foils was measured precisely: ^{208}Tl – 0.39 ± 0.01 mBq/kg, ^{214}Bi – 1.5 ± 0.04 mBq/kg (1σ statistical errors are given) [11]. A significant reduction (down to ~ μBq/kg level) in the radioactive contamination of the ^{82}Se was one of the main tasks of the SuperNEMO R&D.

B. Guillon, Y. Lemière, F. Mauger and G. Oliviero: LPC Caen, ENSICAEN, Université de Caen, CNRS/IN2P3, F-14050 Caen, France

D. V. Karaivanov: Joint Institute for Nuclear Research (JINR), Dubna, 141980, Russian Federation; and Institute for Nuclear Research and Nuclear Energy (INRNE), 72 Tzarigradsko chaussee, Blvd., BG-1784 Sofia, Bulgaria

M. Macko: Faculty of Mathematics, Physics and Informatics, Comenius University, SK-842 48 Bratislava, Slovakia; CENBG, Université de Bordeaux, CNRS/IN2P3, F-33175 Gradignan, France; and Institute of Experimental and Applied Physics, Czech Technical University in Prague, CZ-12800 Prague, Czech Republic

A. A. Mirsagatova, I. I. Sadikov and F. A. Tashimova: Institute of Nuclear Physics of Uzbekistan Academy of Sciences, Tashkent, 100214, Uzbekistan

N. A. Mirzayev: Joint Institute for Nuclear Research (JINR), Dubna, 141980, Russian Federation; and Institute of Radiation Problems of Azerbaijan National Academy of Sciences, AZ1143 B. Vahabzade 9, Baku, Azerbaijan

B. Morgan, Y. A. Ramachers and S. Snow: University of Warwick, Coventry CV4 7AL, UK

M. Nomachi: Osaka University, 1-1 Machikaney arna Toyonaka, Osaka 560-0043, Japan

H. Ohsumi: Saga University, Saga 840-8502, Japan

J. Sedgbeer: Imperial College London, London SW7 2AZ, UK

L. Simard: LAL, Université Paris-Sud, CNRS/IN2P3, Université Paris-Saclay, F-91405 Orsay, France; and Institut Universitaire de France, F-75005 Paris, France

Vl. I. Tretyak: Institute for Nuclear Research, 03028 Kyiv, Ukraine

V. Vorobel and A. Žukauskas: Charles University, Prague, Faculty of Mathematics and Physics, CZ-12116 Prague, Czech Republic

G. Warot and M. Zampaolo: Univ. Grenoble Alpes, CNRS, Grenoble INP, LPSC-IN2P3, 38000 Grenoble, France

The work presented here concentrates on the development of the radiochemical purification and conditioning) of enriched selenium (^{82}Se) samples produced in a "standard" state, and also on radioanalytical studies of radiopure (conditioned) ^{82}Se produced for the preparation of new ^{82}Se foils. For the "standard" state we mean samples with certain characteristics: isotopically enriched, chemically pure, radiochemically pure, in a physico-chemical state of elemental selenium, and with characteristic particle size of the powder of up to 5 μm.

This paper is a continuation of our previous work [12] concerning chromatographic separation of a small quantity (100 g) of selenium and preparation of selenium oxide (SeO$_2$) as the final product. In this paper we present the developed method for production of radiopure ^{82}Se in large quantities (1.5 kg and 1 kg batches from JINR Dubna and France, respectively) in the appropriate form (elemental selenium powder) required for the production of thin ^{82}Se foils. Therefore, special attention has been paid to a number of new aspects of the technology:

- Creation of a new chromatographic system with a new larger ion-exchange column optimized for obtaining kilogram quantities of highly radiopure selenium;
- Development of a technique and construction of a facility (system, equipment) for reduction of purified selenious acid to an elemental state;
- Preparation of the final product by decantation, centrifugation, washing, grinding and drying.

Particular attention has been paid to materials from which chemical vessels and instruments are made. These materials should be as pure as possible with respect to radioactive impurities (^{40}K, decay products of ^{232}Th and ^{238}U) and sufficiently resistant to chemical reagents. It should be noted that it is extremely difficult to find chemical vessels from materials which meet the requirements of modern low-background experiments.

The radiopurity of plastic materials of the chromatographic column (PEEK – chromatographic column material, Teflon – column filter) and polypropylene chemical vessels (glasses, bottles, centrifuge tubes) was determined by instrumental neutron activation analysis (INAA). The radiopurity of the final ^{82}Se wrapped in the foils was measured by the BiPo-3 spectrometer [10] (operating in the Canfranc underground laboratory in Spain).

The distribution coefficients of a series of lanthanides (^{88}Y, ^{139}Ce, ^{143}Pm, ^{167}Tm, ^{169}Yb, ^{173}Lu), ^{60}Co and ^{137}Cs (a potassium analog) on the DOWEX 50W×8 resin, used to produce the high radiopurity selenium, were also determined.

2 Experiment

2.1 Chemical reagents, materials and equipment

The following reagents, materials and equipment were used: bidistilled water; nitric acid (qualification "osch 18-4", GOST 11125-84); sulfur dioxide – SO$_2$ (GOST 2918-79, purity – 99.9 %); isopropyl alcohol (qualification "osch", STP TU COMR 2-018-06); natural technical selenium (^{nat}Se) CT-1 (GOST 10298-79); initial enriched selenium (^{82}SeO$_2$) was obtained in two batches. first part of ^{82}SeO$_2$ (isotope composition: ^{82}Se-99.88 %, ^{74}Se-0.01 %, ^{76}Se-0.01 %, ^{77}Se-0.01 %, ^{78}Se-0.04 %, ^{80}Se-0.05 %) purchased in JSC "PA Electrochemical Plant" (Russia) and labeled as "Dubna"; second part of ^{82}SeO$_2$ (isotope composition: ^{82}Se-96.1 %, ^{80}Se-3.9 %) purchased in "CHEMGAS" (France) and labeled as "France"; cation-exchange resin DOWEX 50W×8 (200–400 mesh, catalog No.217514, Fluka/Sigma-Aldrich, Germany); chemical vessels made of polypropylene (glasses, bottles, centrifuge tube); chromatographic column material: PEEK – polyether ether ketone (Elmica, Russia) – material of the chromatographic column (internal diameter of 28 mm and an operating length of 500 mm); three-way valves (stopcock 3-way PFA 6 mm OD, catalog No. 30503-10, Cole-Parmer, USA); peristaltic pumps (Masterflex L/S Computer-Compatible Digital Drive; 600 rpm, catalog No.07551-00, Cole-Parmer, USA); pump tubes (catalog No.77390-60, 4/6 mm Teflon (PFTE) tubing, Cole-Parmer, USA); magnetic stirrer with heating (MSH-30D, Daihan Scientific, Korea); Centrifuge (CL-40, Thermo scientific, USA); centrifuge tube with a volume of 750 mL (catalog No.75003699, Thermo scientific, USA); Homogenizer (HG-15D-Set-B, Daihan Scientific, Korea); vacuum drying cabinet (VDL 23, Binder, Germany); ICP mass spectrometer (x-7, Thermo elemental, USA); ICP atomic emission spectrometer (ICAP-6500, Thermo scientific, USA); AEROTRAK Handheld Particle Counter TSI 9303-01.

2.2 Production of radiopure selenium (purification of selenium)

The complete purification procedure consists of four main stages:

- Preparation of the initial solution of selenious acid (H$_2$SeO$_3$);
- Cation-exchange chromatographic separation (purification);

- Reduction of purified selenious acid to an elemental state (Se);
- Conditioning (decantation, centrifugation, washing, grinding and drying) of the final product.

All processes were conducted in a specially prepared clean room equipped with air supply, exhaust and recirculation ventilation systems, air intake devices, air distributors with final filters, air regulating devices, sensor equipment and automation elements, etc. The level of dust particles in the room was measured to be ~100 000 (≥0.5 µm) per m^3 and zero in the laminar box (measurement by the AERO-TRAK Handheld Particle Counter TSI 9303-01) where the chromatography stage was carried out.

2.2.1 Preparation of initial solution of H$_2$SeO$_3$

The selenium was divided into portions for purification. The volume of one portion of initial selenious acid solution was 5 L, with selenium concentration of 0.5 mol/L. In the case of natural selenium (^{nat}Se), the solution was prepared by dissolving 200 g of selenium in concentrated nitric acid, evaporating to SeO$_2$, followed by dissolution in water. In the case of enriched selenium (99.88 % of ^{82}Se), 285 g of selenium oxide (^{82}SeO$_2$) was dissolved in water (equivalent to 200 g of selenium, taking into account mass fraction corrections). The obtained solutions were then filtered.

2.2.2 Purification of selenium

The basic aspects of chromatographic purification of selenium for low-background measurements are described in our previous article [12]. Figure 1 shows the purification system with a reverse flow used in this work. The main changes from the previously used system relate to the components and the overall organization of the system. The unit is specially adapted for multiple repetitions of purification cycles for separate small portions in order to purify, in total, kilogram quantities of selenium.

A chromatographic column (item 10, Figure 1) is filled with cation exchange resin DOWEX 50W×8 (200–400 mesh). The purification system uses PTFE pumping tubes and connection hoses, and the flow of liquid is ensured by a peristaltic pump. Particular attention is paid to the selection of three-way valves, which must be sufficiently resistant to increased pressure (~5 atm) and to HNO$_3$ (5 mol/L). Before starting the work, the resin loaded in the column was thoroughly washed (reverse direction) with HNO$_3$ (2 L, 5 mol/L) and water (0.5 L).

Each purification cycle of a single portion of selenium (200 g) lasted about 3 h and included the following operations, presented in Figure 1:

1. Passing of unpurified selenious acid (5 L, 0.5 mol/L) solution through the column at a rate 40 mL/min in the forward direction (vessel 1→column→vessel 4).
2. Washing the column with HNO$_3$ (1 L, 0.1 mol/L) in the forward direction (vessel 2→column→vessel 4). The solutions from vessels 1 and 2 were eluted from the column and collected in a plastic vessel 4 for the purified H$_2$SeO$_3$ (6 L).
3. Elution of impurities adsorbed on the resin in the reverse direction (vessel 6→column→vessel 3) with HNO$_3$ (6 L, 5 mol/L).
4. Rinsing the resin from the HNO$_3$ (5 mol/L) residuals in the reverse direction (vessel 5→column→vessel 3) with HNO$_3$ (1 L, 0.1 mol/L).
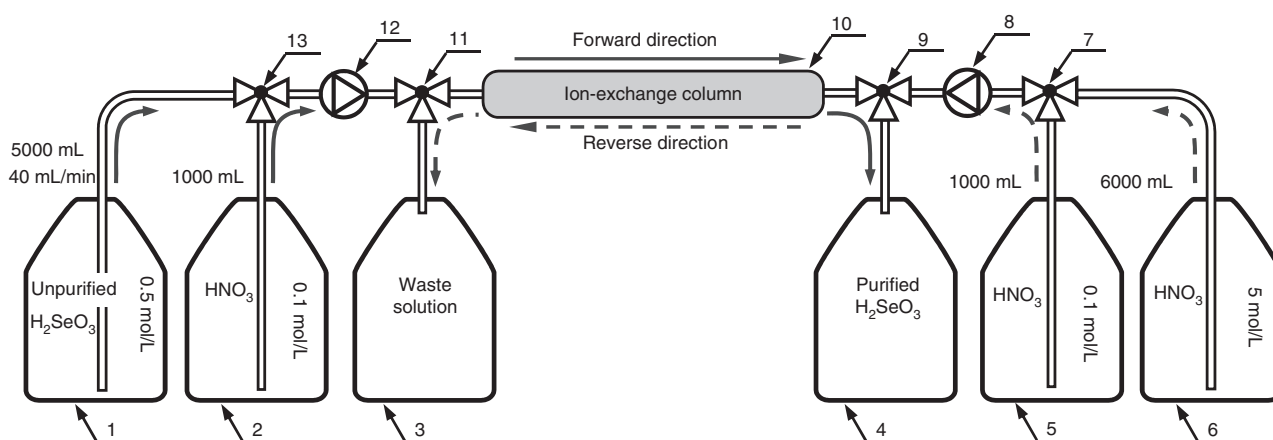

Figure 1: Chromatographic separation (purification) scheme of selenium by the reverse method.
1–6 – polypropylene vessels with the solutions; 7, 9, 11, 13 – triple valves; 8, 12 – peristaltic pumps; 10 – ion exchange column.

These solutions from vessels 6 and 5 were eluted through the column and collected in a separate vessel 3 (7 L waste (impurities) solution).

After the last operation, the purification system is ready to process the next portion of selenium.

2.2.3 Reduction of selenious acid to the elemental state

In order to obtain elemental selenium the purified selenious acid (vessel 4, Figure 1) was reduced with sulfur dioxide (SO_2) according to the reaction

$$H_2SeO_3 + 2\,SO_2 + H_2O \rightarrow Se + 2\,H_2SO_4. \tag{1}$$

Figure 2 shows the scheme of the reduction system used. A purified solution of H_2SeO_3 (vessel 4, Figure 1) was placed in vessel 6 (6 L; 5 L of original + 1 L of washing solution) and saturated through the surface with sulfur dioxide.

To increase the absorption of SO_2, the solution was agitated with a magnetic stirrer. The flow of SO_2 was regulated (valve 2 and rotameter 3, Figure 2) to provide almost complete absorption of SO_2 with a small excess of gas released by bubbles in vessel 8. The average flow of SO_2 was ≈10 L/h. The reduction of one portion took 6–7 h. The saturation of the solution through the surface is more convenient than bubbling due to the good solubility of SO_2, otherwise the tube is quickly clogged with reduced selenium. The use of gas (SO_2) in the recovery process is preferable for our purposes to using other reagents (liquid, solid) since it minimizes radioactive contamination of the final product.

2.2.4 Conditioning

The reduced elemental selenium was separated from the residual solution (Figure 2, vessel 6) by decanting and centrifugation, and then was collected in 750 mL centrifuge tubes. About 200 g of selenium (a single processed portion) was stored in each tube (~300 mL of the wet material). Even small residues of sulfuric acid formed in the process of selenium reduction create serious difficulties in the process of making the selenium source. Therefore, the selenium was further washed, first 10 times with distilled water, and then 5 times with isopropyl alcohol. For this purpose, water (or isopropyl alcohol) was added to the centrifuge tube with a single selenium portion until the tube was completely filled (750 mL mark), then gently blended with a Teflon stick, decanted and centrifuged.

During the reduction, elemental selenium was recovered in the form of tiny particles (<10 nm) which, over time, especially during centrifugation, coalesce into large crumbs and flakes of millimeter portions. They are not suitable for the production of thin ^{82}Se foils. Therefore, a final milling of the selenium was carried out with a homogenizer in isopropyl alcohol until a homogeneous suspension was obtained (~5 min, ~500 rpm). After grinding, the characteristic size of selenium particles was of the order of μm, which is suitable for the production of thin foils (average thickness of 300 μm). The use of surfactant isopropyl alcohol in the final stages of washing and grinding also reduces the adhesion of selenium. In addition, because of its good volatility, isopropyl alcohol facilitates the drying process.

Selenium drying was carried out for a day in a vacuum cabinet, without heating, at an average vacuum of ~5 mbar.

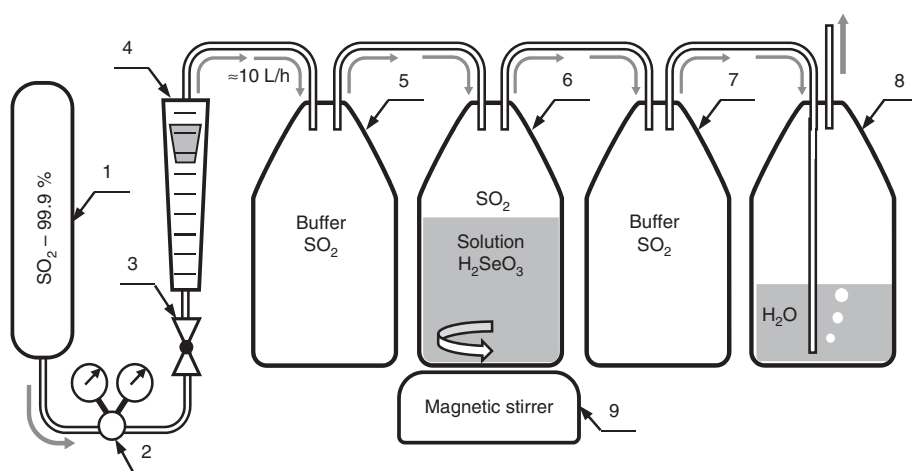**Figure 2:** The Scheme for the reduction system of selenious acid (H_2SeO_3) to an elemental state (Se). 1 – a cylinder with SO_2, 2 – a reducer, 3 – a control valve, 4 – a rotameter, 5–8 – polypropylene vessels (10 L), 9 – a magnetic stirrer.

For each selenium portion (200 g), all washing, grinding and drying processes were carried out in the same centrifuge tube.

During conditioning, we tried to reduce the speed and time of centrifugation (typical value ~1300 rpm for 2 min), and, if possible, to replace this procedure with settling the solution; this reduces the formation of coarse-grained selenium and reduces the grinding time. The grinding process can lead to contamination of selenium by the attrition products of the homogenizer nozzles made of stainless steel (Fe, Cr, Ni), which in turn can contain radioactive impurities.

It should be emphasized that reduction and washing leads to the removal of thorium, uranium, radium, actinium and potassium as they remain in solution.

A total of 600 g of natural selenium was purified and conditioned in order to test and refine the method. The resin in the column was then renewed and used to purify 2.5 kg of enriched selenium (^{82}Se).

2.3 Measurement of the distribution coefficients of radionuclides

The following radionuclides were used as indicators: ^{60}Co ($t_{1/2} = 5.27$ years), ^{88}Y ($t_{1/2} = 106.63$ days), ^{137}Cs ($t_{1/2} = 30.08$ years), ^{139}Ce ($t_{1/2} = 137.64$ days), ^{143}Pm ($t_{1/2} = 265$ days), ^{167}Tm ($t_{1/2} = 9.25$ days), ^{169}Yb ($t_{1/2} = 32.02$ days), ^{173}Lu ($t_{1/2} = 1.37$ years) [13]. Radionuclides ^{88}Y, ^{139}Ce, ^{143}Pm, ^{167}Tm, ^{169}Yb, and ^{173}Lu were obtained by irradiating a tantalum target with 660 MeV protons [14]. The ^{60}Co and ^{137}Cs radionuclides were of commercial origin.

To determine the distribution coefficients (K_D), the static adsorption method was used. Certain volumes of selenium acid solution, H_2O, and 10 μL of the prepared radionuclide cocktail were added to a sample of 50 mg resin (DOWEX 50W×8) and placed in a 1.5 mL centrifugation tube ("Eppendorf", Germany) so that the volume of each sample was 1 mL. The samples were then thoroughly mixed and left to stand for 24 h to achieve equilibrium. Then, centrifugation was carried out and the radioactivity of the solution was measured with a HPGe γ-spectrometer. The distribution coefficients were calculated using the equation:

$$K_D = \frac{A_{1\,g}(\text{resin})}{A_{1\,mL}(\text{solution})} = \frac{A_{50\,mg}(\text{resin})}{A_{50\,\mu L}(\text{solution})}, \qquad (2)$$

where $A_{50\,mg}$ (resin) is the radioactivity (Bq) of 50 mg of resin, and $A_{50\,\mu L}$ (solution) is the radioactivity (Bq) of 50 μL of the solution. To reduce uncertainties in the determination of these values, samples were weighed immediately after preparation and after fluid extraction.

2.4 Instrumental neutron activation analysis of plastic materials

Determination of thorium and uranium contamination in plastic materials of the chromatographic column (PEEK – column material, 2 Teflon samples – construction material and filter for the column) and polypropylene chemical vessels (glasses, bottles, centrifuge tubes) was carried out by INAA. Prepared samples of the plastic materials together with standard reference samples were irradiated at the IBR-2 reactor (JINR, Dubna) in a flux of epithermal neutrons of 2.2×10^{11} cm^{-2} s^{-1}. The standard materials IAEA 433 (marine sediment) and BCR 667 (estuarine sediment) were used as reference samples. The radioactivity of the samples and standards was measured with a HPGe detector GC5519 (Canberra, USA) with relative registration efficiency of 55 %. The collection and processing of gamma-spectra were carried out using Genie-2000 software [15].

2.5 Measurements with a BiPo-3 spectrometer

The BiPo-3 detector is a low radioactivity detector dedicated to the measurement of ^{208}Tl and ^{214}Bi in thin materials. The detector, running in the Canfranc Underground Laboratory since 2013, was initially developed to measure the radiopurity of the ββ-source foils for the SuperNEMO experiment. A comprehensive description of the design and performance of the detector, as well as the results of the radioactivity measurements of the first ^{82}Se foils prepared for the SuperNEMO experiment, can be found in [9]. The BiPo-3 detector represents at present the most sensitive radiometrics detector for radiopurity measurements of samples wrapped in foils. The obtained detection limits were 2 μBq/kg (90 % CL) for ^{208}Tl and 140 μBq/kg (90 % CL) for ^{214}Bi after 6 months of measurement.

2.6 Source foil production

The prepared source foils from the radiopure (conditioned) natural selenium (600 g) and enriched ^{82}Se (2.5 kg) were made in LAPP (Annecy, France); details of the foil production can be found in [16]. The surface density of the foil is ~55 mg/cm^2. The foils were carefully packed, transported

by car from Annecy to the Canfranc underground laboratory, unpacked and installed in the BiPo-3 detector. It is necessary to emphasize once again that all materials, substances, and tools used in the foil preparation procedures have been carefully screened using low-background HPGe spectrometers and the BiPo-3 (foil) detector in order to select samples with the best radiopurity. All the details of the foil production protocol will be presented in a dedicated publication.

3 Results and discussion

The radiopurity of the final product (at a given radiopurity of the initial selenium) depends on the following factors:
- The characteristics of the chromatographic process (distribution coefficients, parameters of the column, the flow of solutions, etc.). In such chromatographic separation systems, it is usually possible to achieve very high purification coefficients. Our experience shows that the obtained purification coefficients on thorium and uranium in the chromatographic system exceed 10^5.
- Radiopurity of the liquid chemical reagents (bi-distilled water, nitric acid and isopropyl alcohol).
- Radiopurity of plastic materials of the chromatographic column and polypropylene chemical vessels.
- General organization of the procedure; for example, one needs to minimize the number of operations with higher risk of contamination of the final product.

3.1 Chemical yield of selenium

The chemical yield of the selenium recovery in the chromatographic purification procedure is more than 99 %. The main losses occur during conditioning. The residue is collected for subsequent extraction of ^{82}Se. The losses during chromatography are negligible – less than 0.1 %, according to the ICP-AES/MS analysis of the (waste (impurities) solution (vessel 3 in Figure 1).

3.2 Distribution coefficients of radionuclides

The distribution coefficients (K_D) of lanthanides (^{88}Y, ^{139}Ce, ^{143}Pm, ^{167}Tm, ^{169}Yb, ^{173}Lu) and technogenic radionuclides – ^{60}Co and ^{137}Cs (a potassium analog) in the DOWEX 50W×8 – H_2SeO_3 system were determined experimentally (Table 1). It can be seen that the K_D values of rare-earth

Table 1: Distribution coefficients (K_D) of lanthanides, as well as cobalt and cesium on the cation – exchange resin DOWEX 50W×8 at various concentrations (C) of selenious acid in solutions.

C(H_2SeO_3), mol/L	Distribution coefficients (K_D) of radionuclides			
	^{60}Co	^{88}Y	^{137}Cs	^{139}Ce
4	400	>10^4	55	>10^4
3	1350	>10^4	160	>10^4
1	6700	>10^4	970	>10^4
0.5	~10^4	>10^4	1400	>10^4
	^{143}Pm	^{167}Tm	^{169}Yb	^{173}Lu
4	>10^4	>10^4	~10^4	~10^4
3	>10^4	>10^4	>10^4	>10^4
1	>10^4	>10^4	>10^4	>10^4
0.5	>10^4	>10^4	>10^4	>10^4

elements with decreasing concentration of H_2SeO_3 (from 4 to 0.5 mol/L) exceed 10^4.

The K_D values of cobalt and caesium are lower, but with a decrease in the concentration of selenious acid to a working concentration of 0.5 mol/L, the coefficients increase significantly, exceeding the critical values with respect to U. Thus, when the solution passes in the forward direction in a volume exceeding 100 times the volume of the column, the radionuclides and their analogs do not enter the purified solution.

3.3 Radiopurity of plastic materials

INAA was used to determine the radiopurity of the plastic materials used: the chromatographic column and polypropylene chemical vessels, as explained in the Section 2.4. Table 2 presents the INAA results for the plastic materials that are in direct contact with solutions: PEEK (chromatographic column material), Teflon (filter for the column and construction material), polypropylene vessels (glasses, bottles, centrifuge tubes) and polyethylene terephthalate (often used for making chemical vessels). The last two materials were not used in the setup but were measured for completeness and comparison.

The most radiopure plastic materials are usually Teflon and high-pressure polyethylene, although it should be noted that there can be exceptions to this rule. Typically, low-density polyethylene and polypropylene have approximately the same level of contamination in thorium and uranium. Polypropylene is still more mechanically resistant than polyethylene, and therefore in many cases its use is preferable. The obtained results show that the materials used are reliable for the whole

Table 2: Radiopurity of various plastic samples measured by INAA.

Samples	Mass, g	Irradiation/measurement time, h	Th content, g/g	U content, g/g
PEEK	0.49	93/0.5–1.5	$(3.8\pm0.7)\times10^{-8}$	$(4.3\pm0.2)\times10^{-8}$
Teflon (filter for column)	0.69	93/0.5–1.5	$(4.9\pm0.8)\times10^{-8}$	$(4.8\pm0.2)\times10^{-8}$
Teflon – material for construction	1.10	71/0.5–7	$<3\times10^{-10}$	$<9\times10^{-11}$
Glass, PP	0.37	93/0.5–1.5	$(5.5\pm1.0)\times10^{-8}$	$(1.3\pm0.1)\times10^{-7}$
Bottle 5 L, PP	0.17	71/0.5–10	$<2.9\times10^{-9}$	$<1.4\times10^{-9}$
Bottle 10 L, PP	0.19	71/0.5–10	$<2.6\times10^{-9}$	$<1.1\times10^{-9}$
Centrifuge tube, PP	2.76	71/0.5–10	$(6.9\pm0.4)\times10^{-9}$	$(2.7\pm0.2)\times10^{-9}$
Polyethylene terephthalate	0.18	71/0.5–10	$<2.4\times10^{-8}$	$<2.6\times10^{-8}$

PEEK, Polyether ether ketone; PP, polypropylene.

of our purification procedure. Of course, it is better to use the purest material (if available), however, the contamination levels in the selected plastic materials do not exceed ~10^{-8} g/g for uranium. From our point of view, such levels are not critical for vessels and materials that are used repeatedly, especially for a chromatographic column. The surface of such materials will be cleaned during multiple cycles and will be in balance with the solutions used in the purification process. The radiopurity of the materials will be reduced to the radiopurity of the water and chemicals used in the purification process. As a result, we used chemical vessels made of polypropylene (with the exception of pump hoses from teflon). According to Table 2, these were the purest products available to us from the relevant materials, and their use should not substantially affect the radiopurity of the resulting selenium samples. It should be noted that INAA is, because of good sensitivity and the ability to obtain results relatively quickly, one of the most successful methods for analysis of thorium, uranium and potassium in plastic materials.

3.4 Purity of liquid chemical reagents

Data on the purity of bi-distilled water and nitric acid can be found in our previous work [12]. The bi-distilled water does not contain thorium and uranium (detection limits were $<4.6\times10^{-13}$ g/g and $<1.7\times10^{-13}$ g/g, respectively). ICP-AES/MS analysis of isopropyl alcohol (1 L of isopropyl alcohol was evaporated in a Teflon vessel at a temperature of 50 °C; the residue remaining in the pot was analyzed with ICP-AES/MS) showed that the content of thorium and uranium was 6.7×10^{-14} g/g and 1.4×10^{-13} g/g, respectively. As can be seen, the content of Th and U is very low, therefore it should not affect the purity of the selenium samples produced.

3.5 Measurement of selenium foils with the BiPo-3 spectrometer

Unfortunately, the ICP-AES/MS analyses were not sensitive enough to determine K, Th and U levels in the initial and final (purified) selenium samples (both the natural and the enriched). Only detection limits for the K, Th and U were obtained. For thorium and uranium detection limits obtained by ICP-MS were 8×10^{-9} g/g and 3×10^{-10} g/g for the natural Se and for the enriched selenium (^{82}Se) samples, respectively. Further work is in progress to analyze these samples by ICP-MS and accelerator mass spectrometry. The obtained detection limit for K by ICP-AES was 10^{-7} g/g.

The source foils containing ~150 g of natural selenium (^{nat}Se) and 2.5 kg of purified (conditioned) ^{82}Se were measured, however, with the BiPo-3 spectrometer (Table 3).

Measurements (with interruptions) took place between December 2016 and August 2017, with a total exposure of ~130 days. The results obtained (Table 3) show lower ^{208}Tl (^{232}Th) and ^{214}Bi (^{238}U) levels for enriched selenium (^{82}Se) than for the natural (^{nat}Se) sample which was the first sample used for optimization of the method. This

Table 3: Results of ^{208}Tl and ^{214}Bi in the purified ^{82}Se samples wrapped in polyethylene foils measured by the BiPo-3 detector (90 % CL).

Origin of selenium foils	The specific activity, µBq/kg	
	^{228}Th (^{232}Th)/^{208}Tl	^{226}Ra/^{214}Bi
High radiopurity (conditioned) ^{nat}Se	19-336/7-121	<870/<870
High radiopurity (conditioned) ^{82}Se "Dubna"	22-150/8-54	<600/<600
High radiopurity (conditioned) ^{82}Se "France"	<294/<106	<1370/<1370

shows the suitability of the technique. The radionuclide levels in ^{82}Se (purified and conditioned in JINR Dubna) foils which will be used in the SuperNEMO experiment, are lower by factors of about 10 (^{208}Tl) and 3 (^{214}Bi) than in the ^{82}Se foil used in the NEMO-3 experiment [11].

4 Conclusions

The methods for the preparation of radiopure ^{82}Se sources for the SuperNEMO neutrinoless double-beta decay experiment have been developed. The chromatographic separation, reduction and conditioning have been used consistently to produce 2.5 kg (from total 6.23 kg) of highly dispersed, high radiopurity (conditioned) ^{82}Se. Grinding and washing were used additionally to obtain the highly dispersed powder (particle size ~1 μm) of elemental selenium as the final product, required for the production of thin source foils.

Key features of the proposed technology should be noted:

– use of ion-exchange chromatography for elution of impurities with reverse method;
– minimum number of chemical reagents (bidistilled water, nitric acid and isopropyl alcohol) used;
– use of sulfur dioxide (SO_2) as a reducing agent for obtaining of elemental selenium;
– high chemical yield (>99 %), unique radionuclide purity and high dispersion of final product.

The productivity of technology proposed is 300 g of ^{82}Se per day, which makes it possible to obtain tens and hundreds of kilograms of purified (conditioned) selenium.

Particular attention was paid to the selection of pure materials, liquid chemical reagents (water, nitric acid and isopropyl alcohol) and plastic vessels which were used at all stages. One needs also to highlight the methodological studies of the various plastic materials radiopurity (ultralow contaminations of thorium and uranium) performed by INAA method, which is found to be the best for these purposes. It has been shown, it is preferable to use products from Teflon and, if necessary, polypropylene.

The radiopurity of the final ^{82}Se foils has been measured by BiPo-3 spectrometer. The levels of impurities were found to be 8–54 μBq/kg level for ^{208}Tl (the ^{232}Th chain), and ≤600 μBq/kg for ^{214}Bi (the ^{238}U chain). This corresponds to an improvement in the radiopurity of the selenium foils by about a factor of 10 for ^{208}Tl and at least by about a factor of 3 for ^{214}Bi in comparison with the NEMO-3 experiment.

The ^{82}Se source foils produced by described techniques were approved for using in SuperNEMO, an experiment aimed to search for neutrinoless double-beta decay of ^{82}Se. The foils have been installed in the Demonstrator (the first module of the experiment) and data-taking will start at the end of 2019.

References

1. Arnold, R., Augier, C., Bakalyarov, A. M., Baker, J., Barabash, A., Bernaudin, Ph., Bouchel, M., Brudanin, V., Caffrey, A. J., Cailleret, J., Campagne, J.-E., Dassie, D., Egorov, V., Errahmane, K., Etienvre, A. I., Filipova, T., Forget, J., Guiral, A., Guiral, P., Guyonnet, J. L., Hubert, F., Hubert, Ph., Humbert, B., Igersheim, R., Imbert, P., Jollet, C., Jullian, S., Kisel, I., Klimenko, A., Kochetov, O., Kovalenko, V., Lalanne, D., Laplanche, F., Lavigne, B., Lebedev, V. I., Lebris, J., Leccia, F., Leconte, A., Linck, I., Longuemare, C., Marquet, Ch., Martin-Chassard, G., Mauger, F., Nemchenok, I., Nikolic-Audit, I., Ohsumi, H., Pecourt, S., Piquemal, F., Reyss, J. L., Richard, A., Riddle, C. L., Rypko, J., Sarazin, X., Simard, L., Scheibling, F., Shitov, Yu., Smolnikov, A., Stekl, I., Sutton, C. S., Szklarz, G., Timkin, V., Tretyak, V., Umatov, V., Vala, L., Vanushin, I., Vasiliev, S., Vasilyev, V., Vorobel, V., Vylov, Ts., Wurtz, J., Zhukov, S. V.: Technical design and performance of the NEMO 3 detector. Nucl. Instrum. Meth. Phys. Res. A. **536**, 79 (2005).
2. Arnold, R., Augier, C., Baker, J. D., Barabash, A. S., Basharina-Freshville, A., Blondel, S., Blot, S., Bongrand, M., Boursette, D., Brudanin, V., Busto, J., Caffrey, A. J., Calvez, S., Cascella, M., Cerna, C., Cesar, J. P., Chapon, A., Chauveau, E., Chopra, A., Duchesneau, D., Durand, D., Egorov, V., Eurin, G., Evans, J. J., Fajt, L., Filosofov, D., Flack, R., Garrido, X., G'omez, H., Guillon, B., Guzowski, P., Hod'ak, R., Huber, A., Hubert, P., Hugon, C., Jullian, S., Klimenko, A., Kochetov, O., Konovalov, S. I., Kovalenko, V., Lalanne, D., Lang, K., Lemiere, Y., Le Noblet, T., Liptak, Z., Liu, X. R., Loaiza, P., Lutter, G., Macko, M., Macolino, C., Mamedov, F., Marquet, C., Mauger, F., Morgan, B., Mott, J., Nemchenok, I., Nomachi, M., Nova, F., Nowacki, F., Ohsumi, H., Pahlka, R. B., Perrot, F., Piquemal, F., Povinec, P., Pridal, P., Ramachers, Y. A., Remoto, A., Reyss, J. L., Richards, B., Riddle, C. L., Rukhadze, E., Saakyan, R., Salazar, R., Sarazin, X., Shitov, Yu., Simard, L., Simkovic, F., Smetana, A., Smolek, K., Smolnikov, A., Soldner-Rembold, S., Soule, B., Stekl, I., Suhonen, J., Sutton, C. S., Szklarz, G., Thomas, J., Timkin, V., Torre, S., Tretyak, V. I., Tretyak, V. I., Umatov, V. I., Vanushin, I., Vilela, C., Vorobel, V., Waters, D., Zukauskas, A.: Measurement of the 2νββ decay half-life and search for the 0νββ decay of ^{116}Cd with the NEMO-3 detector. Phys. Rev. D **95**(1), 012007 (2017).

3. Arnold, R., Augier, C., Baker, J. D., Barabash, A. S., Basharina-Freshville, A., Blondel, S., Blot, S., Bongr, M., Boursette, D., Brudanin, V., Busto, J., Caffrey, A. J., Calvez, S., Cascella, M., Cerna, C., Cesar, J. P., Chapon, A., Chauveau, E., Chopra, A., Duchesneau, D., Dur, D., Egorov, V., Eurin, G., Evans, J. J., Fajt, L., Filosofov, D., Flack, R., Garrido, X., G'omez, H., Guillon, B., Guzowski, P., Hod'ak, R., Huber, A., Hubert, P., Hugon, C., Jullian, S., Klimenko, A., Kochetov, O., Konovalov, S. I., Kovalenko, V., Lalanne, D., Lang, K., Lemiere, Y., Le Noblet, T., Liptak, Z., Liu, X. R., Loaiza, P., Lutter, G., Macko, M., Macolino, C., Mamedov, F., Marquet, C., Mauger, F., Morgan, B., Mott, J., Nemchenok, I., Nomachi, M., Nova, F., Nowacki, F., Ohsumi, H., Pahlka, R. B., Perrot, F., Piquemal, F., Povinec, P., Pridal, P., Ramachers, Y. A. Remoto, A., Reyss, J. L., Richards, B., Riddle, C. L., Rukhadze, E., Saakyan, R., Salazar, R., Sarazin, X., Shitov, Yu., Simard, L., Simkovic, F., Smetana, A., Smolek, K., Smolnikov, A., Soldner-Rembold, S., Soule, B., Stekl, I., Suhonen, J., Sutton, C. S., Szklarz, G., Thomas, J., Timkin, V., Torre, S., Tretyak, V. I., Tretyak, V. I., Umatov, V. I., Vanushin, I., Vilela, C., Vorobel, V., Waters, D., Zukauskas, A.: Search for neutrinoless quadruple-β decay of Nd-150 with NEMO-3 detector. Phys. Rev. Lett. **119**, 041801 (2017).
4. Perrot, F.: Status of the SuperNEMO Demonstrator, 38th International Conference on High Energy Physics (ICHEP 2016), Chicago, USA, August 3–10, 2016, PoS (ICHEP2016) 499, https://doi.org/10.22323/1.282.0499.
5. Karandashev, V. K., Bezrukov, L. B., Kornoukhov, V. N., Nosenko, S. V., Glavin, G. G., Ovchinnikov, S. V.: Analysis of germanium and germanium dioxide samples by mass-spectrometry and atomic emission spectroscopy. J. Anal. Chem. **64**(3), 259 (2009).
6. Rakhimov, A. V., Brudanin, V. B., Filosofov, D. V., Loaiza, P., Marinov, G. M., Mirsagatova, A. A., Medvedev, D., Mukhamedshina, N. M., Rozov, S. V., Sadikov, I. I., Warot, G., Yakushev, E. A.: Neutron activation analysis of polyethylene from neutron shield of EDELWEISS experiment. Radiochim. Acta **109**(9), 673 (2015).
7. Leonard, D. S., Grinberg, P., Weber, P., Baussan, E., Djurcic, Z., Keefer, G., Piepke, A., Pocar, A., Vuilleumier, J.-L., Vuilleumier, J. M., Akimov, D., Bellerive, A., Bowcock, M., Breidenbach, M., Burenkov, A., Conley, R., Craddock, W., Danilov, M., DeVoe, R., Dixit, M., Dolgolenko, A., Ekchtout, I., Fairbank, W. Jr., Farine, J., Fierlinger, P., Flatt, B., Gratta, G., Green, M., Hall, C., Hall, K., Hallman, D., Hargrove, C., Herbst, R., Hodgson, J., Jeng, S., Kolkowitz, S., Kovalenko, A., Kovalenko, D., LePort, F., Mackay, D., Moe, M., Montero Díez, M., Neilson, R., Odian, A., O'Sullivan, K., Ounalli, L., Prescott, C. Y., Rowson, P. C., Schenker, D., Sinclair, D., Skarpaas, K., Smirnov, G., Stekhanov, V., Strickland, V., Virtue, C., Wamba, K., Wodin, J.: Systematic study of trace radioactive impurities in candidate construction materials for EXO-200. Nucl. Instrum. Meth. Phys. Res. A **591**. 490 (2008).
8. Budjás, D., Gangapshev, A. M., Gasparro, J., Hampel, W., Heisel, M., Heusser, G., Hult, M., Klimenko, A. A., Kuzminov, V. V., Laubenstein, M., Maneschg, W., Simgen, H., Smolnikov, A. A., Tomei, C., Vasiliev, S. I.: Gamma-ray spectrometry of ultra-low levels of radioactivity within the material screening program for the GERDA experiment. Appl. Radiat. Isot. **67**, 755 (2009).
9. Argyriades, J., Arnold, R., Augier, C., Baker, J., Barabash, A. S., Basharina-Freshville, A., Bongrand, M., Bourgeois, C., Breton, D., Brière, M., Broudinay, G., Brudanin, V. B., Caffrey, A. J., Carcel, S., Cebrián, S., Chapon, A., Chauveau, E., Dafni, Th., Díaz, J., Durand, D., Egorov, V. G., Evans, J. J., Flack, R., Fushima, K. I., Irastorza, I. G., Garrido, X., Gómez, H., Guillon, B., Holin, A., Hommet, J., Holy, K.,

Horkey, J. J., Hubert, P., Hugon, C., Iguaz, F. J., Ishihara, N., Jackson, C. M., Jenzer, S., Jullian, S., Kauer, M., Kochetov, O. I., Konovalov, S. I., Kovalenko, V., Lamhamdi, T., Lang, K., Lemière, Y., Lutter, G., Luzón, G., Mamedov, F., Marquet, Ch., Mauger, F., Monrabal, F., Nachab, A., Nasteva, I., Nemchenok, I. B., Nguyen, C. H., Nomachi, M., Nova, F., Ohsumi, H., Pahlka, R. B., Perrot, F., Piquemal, F., Povinec, P. P., Richards, B., Ricol, J. S., Riddle, C. L., Rodríguez, A., Saakyan, R., Sarazin, X., Sedgbeer, J. K., Serra, L., Shitov, Yu. A., Simard, L., Šimkovic, F., Söldner-Rembold, S., Štekl, I., Sutton, C. S., Tamagawa, Y., Szklarz, G., Thomas, J., Thompson, R., Timkin, V., Tretyak, V., Tretyak, V. I., Umatov, V. I., Vála, L., Vanyushin, I. A., Vasiliev, R., Vasiliev, V. A., Vorobel, V., Waters, D., Yahlali, N., Žukauskas, A.: Results of the BiPo-1 prototype for radiopurity measurements for the SuperNEMO double-beta decay source foils. Nucl. Instrum. Meth. Phys. Res. A **622**, 120 (2010).
10. Barabash, A. S., Basharina-Freshville, A., Birdsall, E., Blondel, S., Blot, S., Bongramd, M., Boursette, D., Brudanin, V., Busto, J., Caffrey, A. J., Calvez, S., Cascella, M., Cebrian, S., Cerna, C., Cesar, J. P., Chauveau, E., Chopra, A., Dafni, T., De Capua, S., Duchesneau, D., Durant, D., Egorov, V., Eurin, G., Evans, J. J., Fajt, L., Filosofov, D., Flack, R., Carrido, X., Gomes, H., Guillon, B., Guzovski, P., Holy, K., Hodak, R., Huber, A., Hugon, C., Iguaz, F. J., Irastorza, I. G., Jeremie, A., Jullian, S., Kauer, M., Klimenko, A., Kochetov, O., Konovalov, S. I., Kovalenko, V., Lang, K., Lemiere, Y., Npbiet, T. L., Liptak, Z., Liu, X. R., Loaiza, P., Lutter, G., Luzon, G., Macko, M., Mamedov, F., Marquet, C., Mauger, F., Morgan, B., Mott, J., Nemchenok, I., Nomachi, M., Nova, F., Osumi, Y., Oliviero, G., Ortiz de Solorzano, A., Pahlka, R. B., Pater, J., Perrot, F., Piquemal, F., Povinec, P., Pridal, P., Ramachers, Y. A., Remoto, A., Richards, B., Riddle, C. L., Ruchadze, E., Saakyan, R., Salazar, R., Sarazin, X., Shitov, Yu., Simard, L., Simkovic, F., Smetana, A., Smolek, K., Smolnikov, A., Soldner-Rembold, S., Soule, B., Stekl, I., Thomas, J., Timkin, V., Torre, S., Tretyak, V. I., Tretyak, V. I., Umatov, V. I., Volela, C., Vorobel, V., Waters, D., Zukauskas, A.: The BiPo-3 detector for the measurement of ultra low natural radioactivities of thin materials. JINST **12**, (2017) P06002.
11. Arnold, R., Augier, C., Barabash, A. S., Basharina-Freshville, A., Blondel, S., Blot, S., Bongrand, M., Boursette, D., Brudanin, V., Busto, J., Caffrey, A. J., Calvez, S., Cascella, M., Cerna, C., Cesar, J. P., Chapon, A., Chauveau, E., Chopra, A., Dawson, L., Duchesneau, D., Durand, D., Egorov, V., Eurin, G., Evans, J. J., Fajt, L., Filosofov, D., Flack, R., Garrido, X., Gómez, H., Guillon, B., Guzowski, P., Hodák, R., Huber, A., Hubert, P., Hugon, C., Jullian, S., Klimenko, A., Kochetov, O., Konovalov, S. I., Kovalenko, V., Lalanne, D., Lang, K., Lemière, Y., Le Noblet, T., Liptak, Z., Liu, X. R., Loaiza, P., Lutter, G., Macolino, C., Mamedov, F., Marquet, C., Mauger, F., Morgan, B., Mott, J., Nemchenok, I., Nomachi, M., Nova, F., Nowacki, F., Ohsumi, H., Pahlka, R. B., Patrick, C., Perrot, F., Piquemal, F., Povinec, P., Přidal, P., Ramachers, Y. A., Remoto, A., Reyss, J. L., Riddle, C. L., Rukhadze, E., Rukhadze, N. I., Saakyan, R., Salazar, R., Sarazin, X., Shitov, Yu., Simard, L., Šimkovic, F., Smetana, A., Smolek, K., Smolnikov, A., Söldner-Rembold, S., Soulé, B., Štekl, I., Suhonen, J., Sutton, C. S., Szklarz, G., Thomas, J., Timkin, V., Torre, S., Tretyak, V. I., Tretyak, V. I., Umatov, V. I., Vanushin, I., Vilela, C., Vorobel, V., Waters, D., Xie, F., Žukauskas, A.: Final results on [82]Se double-beta decay to the ground state of [82]Kr from the NEMO-3 experiment. Eur. Phys. J. C **78**, 821 (2018).

12. Rakhimov, A. V., Warot, G., Karaivanov, D. V., Kochetov, O. I., Lebedev, N. A., Mukhamedshina, N. M., Sadikov, I. I., Filosofov, D. V.: Purification of selenium from thorium, uranium, radium, actinium and potassium impurities for the low background measurements. Radiochim. Acta **101**(10), 653 (2013).
13. Available at http://www.nndc.bnl.gov.
14. Lebedev, N. A.: Poluchenie radioaktivnix preparatov redkoze-melnix elementov i istochnikov izlucheniya dlya yadernos-pectroskopicheskix issledovaniy. Dissertaciya na soiskanie uchyonoy stepeni candidata ximicheskix nauk. Ph.D. Thesis, Dubna (1973), p. 156 (in Russian).
15. Genie 2000 Software Family, Canberra, USA. Available at http://www.canberra.com/products/radiochemistry_lab/genie-2000-software.asp.
16. Jeremie, A., Remoto, A.: The SuperNEMO $\beta\beta$ source production. 38th International Conference on High Energy Physics (ICHEP 2016), Chicago, USA, August 3–10, 2016, PoS(ICHEP2016)1018. https://doi.org/10.22323/1.282.1018.